Performance Evaluation of IRS-Assisted Mixed FSO-RF Communication System

Thesis submitted for the award of the Degree

of

Doctor of Philosophy

in the Department of Electrical Engineering

by

Amina Girdher

(2019REE0013)

Under the supervision of

Dr. Ankur Bansal

and

Dr. Ankit Dubey

Indian Institute of Technology Jammu

Jammu 181221

June 2023

Amina Girdher: *Performance Evaluation of IRS-Assisted Mixed FSO-RF Communication System*

Dedicated to ***My Family***

and

My Teachers

Who are the inspiration and power behind the success of this work

Declaration of Originality

I hereby declare that the work which is being presented in the thesis entitled **Performance Evaluation of IRS-Assisted Mixed FSO-RF Communication System** has been solely authored by me. It presents the result of my own independent investigation/research conducted during the time period from August, 2019 to July, 2023 under the supervision of **Dr. Ankur Bansal** (Assistant Professor), and **Dr. Ankit Dubey** (Assistant Professor), Department of Electrical Engineering, IIT Jammu. To the best of my knowledge, it is an original work, both in terms of research content and narrative, and has not been submitted or accepted elsewhere, in part or in full, for the award of any degree, diploma, fellowship, associateship, or similar title of any university or institution. Further, due credit has been attributed to the relevant state-of-the-art with appropriate citations and acknowledgments, in line with established ethical norms and practices. I also declare that any idea/data/fact/source stated in my thesis has not been fabricated/ falsified/ misrepresented. All the principles of academic honesty and integrity have been followed. I fully understand that if the thesis is found to be unoriginal, fabricated, or plagiarized, the Institute reserves the right to withdraw the thesis from its archive and revoke the associated Degree conferred. Additionally, the Institute also reserves the right to appraise all concerned sections of society of the matter for their information and necessary action (if any). If accepted, I hereby consent for my thesis to be available online in the Institute's Open Access repository, inter-library loan, and the title & abstract to be made available to outside organizations.

Signature

Name: Amina Girdher

Entry Number: 2019REE0013

Program: Ph.D.

Department: Electrical Engineering

Indian Institute of Technology Jammu

Jammu, J&K 181221

Date: June 2023

Acknowledgement

First and foremost praise is to God, the most Gracious and the most Merciful, on whom ultimately we depend for sustenance and guidance. I am grateful to God for giving me strength and determination to complete my research.

This thesis has been seen through to completion with the continuous support of numerous people including my family, friends, colleagues and various institutions. First of all, I would like to thank my supervisors Dr. Ankur Bansal and Dr. Ankit Dubey for their guidance and encouragement which I received throughout my dissertation research journey. I am thankful to them for offering advice and encouragement with a perfect blend of insight and humor and for painstakingly reading my reports. Without their invaluable advice and support it would not have been possible for me to complete this dissertation.

I take this opportunity to express my sincere thanks to Dr. Manav Bhatnagar for his valuable discussions and suggestions for improving my research work. I would also like to thank all my fellow researchers of the Communication Group, who made this journey a memorable one. Further, I would like to extend them my best wishes for their future endeavors.

I express my heartfelt thanks to my parents who have been a constant source of inspiration to me all along and their encouraging words made this endeavor possible. Finally, I would like to thank my family, friends, and all others whose names are not mentioned here but have helped me to accomplish this work.

Certificate

This is to certify that the thesis entitled **Performance Evaluation of IRS-Assisted Mixed FSO-RF Communication System**, submitted by **Amina Girdher (2019REE0013)** for the award of the degree of **Doctor of Philosophy** of Indian Institute of Technology Jammu, is a record of bonafide research work carried out under my guidance and supervision. To the best of my knowledge and belief, the work presented in this thesis is original and has not been submitted, either in part or full, for the award of any other degree, diploma, fellowship, associateship or similar title of any university or institution.

In my opinion, the thesis has reached the standard fulfilling the requirements of the regulations relating to the Degree.

Dr. Ankur Bansal, and Dr. Ankit Dubey
Assistant Professor(s)
Department of Electrical Engineering
Indian Institute of Technology Jammu
Jammu, J&K 181221
Date: June 2023

Abstract

To meet the stringent requirements of future wireless communication networks such as eminent reliability, low latency, high data rates, high speed, and energy efficiency, etc., the integration of free-space optical (FSO) and radio frequency (RF) technologies has gained considerable attention. The concept of mixed FSO-RF communication systems offers the potential to combine the advantages of both technologies while overcoming their individual limitations. However, challenges such as atmospheric turbulence, limited coverage range, and the need for separate power sources still persist. Simultaneous lightwave information and power transfer (SLIPT) has emerged as a promising solution to address power constraints, enabling the coexistence of data transmission and wireless power transfer (WPT). This doctoral thesis presents a comprehensive performance evaluation of a mixed FSO-RF communication system that leverages the capabilities of various promising technologies to overcome the limitations of traditional FSO and RF systems. We first investigate the performance of a decode-and-forward (DF) relay-based mixed FSO-RF communication system with energy harvesting using SLIPT, where the relay node harvests power through the optical link and uses the harvested power to transmit across the RF hop and thus, makes the signal-to-noise ratio (SNR) of the RF hop dependent on the FSO channel coefficients. For the considered system, the statistical distribution of the end-to-end SNR is derived under Malaga ($\mathcal{M}$)-distributed atmospheric turbulence with non-zero boresight pointing error-based FSO link and Nakagami-m distributed RF link. Furthermore, the analytical expressions of an end-to-end outage, average bit-error-rate, ergodic capacity, and effective capacity are derived using non-coherent intensity modulation with direct detection (IMDD)-based FSO receiver and the energy harvesting relay node.

Further, the intelligent reflecting surface (IRS) is a promising hardware technology to cope with the challenges of atmospheric turbulence and multipath fading. The IRS, also known as reconfigurable meta-surfaces, can adaptively manipulate the signal propagation characteristics, thus enabling improved coverage, higher data rates, and enhanced link reliability. Thus, to improve the link performance of RF link (especially in urban areas where signals are unavailable due to blockage by buildings, trees, etc.) and enable more efficient utilization of the available energy at relay node, the IRS can be employed. Therefore, we investigated the performance of a mixed FSO-RF communication system utilizing on-off control IRS in the RF link. In particular, we derived expressions of outage probability, average bit-error rate, and ergodic capacity for the considered IRS-assisted

mixed FSO-RF network.

In addition to WPT and IRS, non-orthogonal multiple-access (NOMA) is another potential breakthrough technology to cope with high quality-of-service (QoS) requirements of future communication network applications. Thus, we aim to integrate these concepts and investigate their interactions, which can enable the design of more efficient communication systems. We propose a novel relay-based mixed FSO-RF communication system utilizing NOMA to assist two users in RF link. Assuming the non-availability of a direct FSO link, we consider the deployment of an optical IRS (OIRS). Moreover, we deploy an IRS in the vicinity of far user to improve its performance. We also adopt SLIPT technology to harvest energy at the relay node. For the proposed system with generalized $\mathcal{M}$-distributed FSO link with pointing error and Nakagami-m faded RF link, we evaluate the system's performance in terms of outage probability, throughput, and ergodic rate.

Conventionally, first-order statistics such as outage probability and bit-error rate has been considered as a useful metric to measure link performance and it has been thoroughly studied for a variety of system models under different fading statistics. However, it captures the static behavior of the system under consideration. To characterize the *dynamic behavior* of the system with multipath fading, the study of second-order statistics (SOS), i.e., level crossing rate (LCR) and average outage duration (AOD) have gained significant importance. In addition, the dynamic time-varying attributes of the various fading channels are well explored through SOS. Therefore, we studied the SOS for the OIRS-assisted FSO link in the presence of random fog, atmospheric turbulence and pointing error. In particular, we obtained the closed-form expressions of LCR and AOD for OIRS-assisted FSO network. Later on, the SOS for the IRS-assisted RF communication network with co-channel interference (CCI) is studied.

Keywords: Free space optical; performance analysis; Intelligent reflecting surfaces; non-orthogonal multiple access; second-order statistics;

List of Symbols

Symbol	Description
I	Channel coefficient of FSO link
h	Channel coefficient of RF link
x_m	message signal
$\mathcal{B}$	DC Bias
$\mathcal{B}_{\min}$	Minimum DC Bias
$\mathcal{B}_{\max}$	Maximum DC Bias
δ	electrical to optical conversion coefficient
ς	Electrical Power of modulating signal
η	optical to electrical conversion coefficient
R_{P}	Responsively of PD
A_{P}	Detection area of PD
L_i	Length of i-th FSO link
ϑ_o	Attenuation coefficient of optical signal
P_{S}	Transmit power of Source
P_{R}	Transmit power of relay
P_{H}	Instantaneous power harvested at Relay
I_a	Atmospheric turbulence coefficient of FSO link
I_p	pointing error coefficient of FSO link
I_l	path loss coefficient of FSO link
$\varkappa$	Electrical SNR of FSO link
σ^2	Noise power
σ_s	Jitter standard deviation
ϕ_L	Deterministic phase of the LOS terms
ϕ_S	Deterministic phase of scattered terms coupled-to-LOS component
Ω'	Average power of LOS component

Symbol	Description
α	Parameter related to effective number of large-scale cells of scattering process
β	is the amount of fading parameter
V	Visibility
N	Number of IRS elements
W_e	Equivalent beam width at the detector
A_o	Fraction of the optical power collected at the detector
m, Ω	Nakagami fading parameters
V_{T}	Thermal Voltage
V_{OC}	Open circuit Voltage
ϖ	Reflection coefficient of IRS
ρ	Transmit SNR
φ	Angle of arrival
f	Doppler frequency
χ	Degree of non-isotropic scattering
Γ	Signal-to-noise ratio
e	Path loss exponent
$\mathcal{P}_{\mathrm{out}}$	Outage probability
$\mathcal{P}_{\mathrm{e}}$	Bit-error-rate
$\mathcal{P}_{\mathrm{p}}$	Packet error rate
$\mathcal{C}_{\mathrm{erg}}$	Ergodic Capacity
$\mathcal{C}_{\mathrm{eff}}$	Effective capacity

List of Notations

In this dissertation, bold upper case and lower case letters denote matrices and vectors, respectively. The blackboard bold symbols, such as $\mathbb{A}$ refers to the set. The remaining notation and operators used in this thesis are listed below.

Notation	Description
$\mathcal{E}\{\cdot\}$	Expectation of operator
$\mathcal{V}\{\cdot\}$	Variance operator
$f_X(\cdot)$	Probability density function of Random variable X
$\mathcal{F}_X(\cdot)$	Cumulative distribution function of Random variable X
$\Pr\{\cdot\}$	Probability of an event
$\ln(\cdot)$	Natural logarithm function
$\Gamma(\cdot)$	Gamma function
$J_\nu(\cdot)$	Bessel function of first kind and order ν
$I_\nu(\cdot)$	Modified Bessel function of first kind and order ν
$K_\nu(\cdot)$	Modified Bessel function of second kind and order ν
$F(\cdot;\cdot;\cdot)$	Hypergeometric function
$Q_p(a,b)$	Marcum Q-function
$(\cdot)_\ell$	Pochhammer symbol
$G_{p,q}^{m,n}\left(y \,\middle\vert\, \begin{smallmatrix} a_1,\ldots,a_p \\ b_1,\ldots,b_q \end{smallmatrix}\right)$	Meijer's G-function
$\Gamma(\cdot,\cdot)$	Upper incomplete Gamma function
$\jmath$	imaginary number, $\jmath = \sqrt{-1}$
$\lvert\cdot\rvert$	Amplitude of complex number
$\angle\cdot$	Phase of complex number
$\lVert\cdot\rVert$	Norm of the Vector
$D_\upsilon(\cdot)$	Parabolic cylinder function
$\cap$	Intersection of Events

List of Abbreviations

Abbreviation	Description
AF	Amplify-and-forward
AO	Alternating optimization
AOA	Angle of arrival
AOD	Average outage duration
APD	Avalanche photo-diode
ARQ	Automatic repeat request
AWGN	Additive white Gaussian Noise
CDF	Cumulative distribution function
CLT	Central limit Theorem
D	Destination node
DC	Direct current
DF	Decode-and-forward
EGC	Equal gain combing
EH	Energy Harvesting
FSMC	Finite-state Markov channel
FSO	Free Space Optical
IMDD	Intensity modulation with direct detection
IRS	Intelligent reflecting surface
LED	Light emitting diode
LoS	Line of Sight
MIMO	Multiple input multiple output
MRC	Maximal ratio combing
NOMA	Non-orthogonal Multiple access
OFDMA	Orthogonal frequency division multiple access
OHD	Optical heterodyne detection

Abbreviation	Description
PD	Photo-detector
PDF	Probability density function
PER	Packet error rate
QoS	Quality of service
R	Relay node
RF	Radio frequency
RV	Random variable
RP	Random Process
S	Source node
SC	Selection combing
SCA	Successive convex approximation
SER	Symbol-error rate
SIM	Sub-carrier intensity modulation
SINR	Signal-to-interference plus noise Ratio
SNR	Signal-to-noise Ratio
SW	Stop-and-wait
SWIPT	Simultaneous wireless information and power transfer
SLIPT	Simultaneous lightwave information and power transfer
VLC	Visible light communication
WOC	Wireless optical communication
WPT	Wireless power transfer

Contents

List of Figures

List of Tables

Chapter 1

Introduction

1.1 Background: FSO Meets Next Generation Wireless Networks

The current fifth-generation (5G) wireless communication technology is based on mmWave frequencies and is expected to provide speeds of up to 10 gigabits per second (Gbps), which is 100 times faster than current fourth-generation (4G) networks [2]. As the use of data-intensive applications such as virtual and augmented reality, autonomous vehicles, and tele-medicine continues to grow, there will be a need for even faster and more reliable connectivity than what 5G can offer. Therefore, the need for sixth-generation (6G) technology is driven by the desire to improve upon the capabilities of 5G and simultaneously satisfy the high speed requirements of ground users in various applications and use cases [3].

The 6G networks may operate in the terahertz (THz) frequency band (300 GHz-3 THz), which offers significantly higher data rates than the millimeter wave (mmWave) frequency band used by 5G networks [2]. While 6G wireless networks are still in the research and development phase, some experts are already looking for beyond 6G (B6G) and envisioning what the future of wireless networks might look like. The potential research directions for 6G and B6G include quantum communication, artificial intelligence, wireless optics, intelligent reflecting surface (IRS), wireless power transfer (WPT), and hybrid/mixed networks, etc. [4, 5]. The 6G and B6G technologies are expected to incorporate optical wireless communication (OWC) to enable even higher data rates, lower latency, and greater security than traditional radio-based communication. Moreover, B6G technology is expected to integrate various wireless communication technologies, including satellite, cellular, Wi-Fi, and OWC, into a unified and seamless network.

The OWC refers to wireless connections using the optical spectrum ranging from 1 mm–10 nano-m (nm) and categorized into infrared (700 nm and 1 mm), visible light (400 nm and 700 nm), and ultraviolet (10 nm and 400 nm) spectrum [6]. The OWC is a high-speed technology utilized for short range communication since the advent of 4G communications. However, it is envisioned to be utilized broadly to meet the stringent requirements of B6G communication networks. Various popular OWC technologies utilizing the optical spectrum are optical camera communication (OCC), visible light communication (VLC), free space optical (FSO), and Light-fidelity (Lifi). The outdoor OWC, termed as FSO communication technology has been explored over the last few decades to utilize its several advantages in various applications in contrast to the radio frequency (RF) technology. The opportunities of the FSO communication technology along with the challenges are described in the next section.

1.2 Opportunities and Challenges

In comparison to the RF, FSO communication technology has the following advantages:

- High Data Rate: FSO communication can support much higher data rates than RF or microwave communication. This makes it a good option for applications where a large amount data is generated that needs to be transmitted quickly, such as in satellite communication, remote sensing, and high-speed internet. Moreover, FSO technology is highly suitable for establishing high speed access/backhaul connectivity for next generations wireless networks [7].

- Unlicensed spectrum: Unlike RF, FSO communication uses unlicensed spectrum, which means that there are no licensing requirements for using the FSO technology. Therefore, using FSO technology, a cost-efficient backhaul link for commercial and military applications can been established. Also, it is an attractive option for communication in remote areas or developing countries where the cost of licensing can be a barrier [8].

- Highly Secure: Since FSO communication uses light signals to transmit data, it is much more difficult to intercept the signal and eavesdrop on the communication. Thus, FSO technology can be used for transmitting sensitive information, such as military communication or financial transactions.

- Low interference: Unlike RF, FSO communication is not affected by electromagnetic interference, which can disrupt or block RF or microwave signals [9]. This makes it a good option for communication in areas with high levels of electromagnetic interference, such as in urban or industrial environments.

In recent years, FSO communication continues to be used for high-speed, point-to-point terrestrial links in urban areas, as well as for various applications. The current research on FSO technology focuses on how the reliability and the communication peformance can be enhanced by exploring new applications, such as inter-satellite communication and space-to-ground links. Thus, seen as a next frontier for high-speed 6G broadband connections.

However, despite the numerous advantages, there are various challenges that FSO communication faces.

- Weather and atmospheric effects: The Earth's atmosphere can distort and scatter the light signals used in FSO communication, which can reduce the signal strength and introduce errors in the transmission. This can be particularly problematic in adverse weather conditions, such as fog, rain, or snow. The presence of foggy conditions contributing to Mie scattering attenuates the signal and under dense fog with visibility (V) less than 50 m, the attenuation is higher than 350 dB/km [10]. Further, the inconsistent temperature variations on earth due to random wind fluctuations causes atmospheric turbulence which results in scintillation of laser beam propagating through it.

- Line-of-sight (LoS) requirements: Further, FSO requires a direct LoS between the transmitter and receiver, which is especially not available in scenarios, such as urban scenario with tall buildings or in mountainous regions [11].

- Misalignment error: Since FSO communication is only possible in the presence of LoS link, the transmitter and receiver must be precisely aligned in order to maintain a strong signal. A slight misalignment between the beam axis and receive aperture could lead to link failure, as a result, degrades the communication performance. Thus, it is crucial to maintain LoS connectivity between the transmitter and receiver. This requires sophisticated tracking mechanisms and can be difficult to maintain over long distances.

Due to these limitations, the range of FSO communication is limited. To overcome these limitations, relaying is the one of the possible solution which is an important concept in FSO communication that can help overcome some of the challenges associated with transmitting signals over long distances in the atmosphere.

1.3 Relay-based Mixed FSO-RF Communication Networks

The dual-hop relay-based mixed FSO-RF communication system combines FSO and RF technologies to establish a reliable and extended-range wireless link. In a dual-hop based network, the communication link is divided into two hops. In case of mixed FSO-RF network, the first hop employs FSO communication, which utilizes lasers or LED lights to transmit data through the atmosphere using optical signals. The FSO link offers high data rates and low latency over relatively short distances. However, FSO is susceptible to atmospheric conditions such as fog, rain, and atmospheric turbulence, which can degrade the signal quality. To overcome the limitations of FSO, the second hop of the system utilizes RF communication. The RF signals, such as microwave or mm-wave frequencies, are more resilient to atmospheric conditions and can propagate through obstacles. RF provides wider coverage and is less affected by weather conditions compared to FSO. However, RF typically has lower data rates and higher latency compared to FSO. By combining FSO and RF using relay node, the system leverages the advantages of both technologies while mitigating their individual limitations. It supports the high data rates and low latency of FSO for the initial hop and utilizes the robustness and wider coverage of RF for the extended hop with the help of relay node. This type of system can find applications in scenarios where a direct FSO link is limited by distance or LoS obstructions. It is commonly used in wireless backhaul for cellular networks, point-to-point communication between distant locations, rural connectivity, and disaster recovery networks. Such mixed FSO-RF relaying networks can be employed for establishing satellite-aerial-terrestrial, satellite-to-satellite, terrestrial-to-terrestrial, and vehicle-to-everything (V2X) communication links [12].

In this dissertation, we intend to investigate the mixed FSO-RF communication system and its performance. We also integrate various promising technologies to achieve energy-efficient and reliable network along with improved coverage and scalability. To fully leverage the advantages of FSO in wireless communication while also considering the above challenges, several research organizations, regulatory bodies, etc., are actively involved in conducting various trials and experiments. Therefore, we next introduce the industrial trends in FSO communication, for utilizing FSO in enhancing wireless connectivity.

1.4 Industrial Trends in FSO Communication

As described in the previous subsection, the opportunities in FSO communication has shifted the focus of researchers toward the development of communication technologies and protocols. In addition, the industry has already begun to test FSO into the current communication networks. For example, to address the RF spectrum scarcity issue and deliver a Terabit-per-second (Tb/s) data rate, optical transmission technology, in May 2018, the German Aerospace Center registered a world record of achieving 13.16 Tb/s using FSO transmissions in a GEO-equivalent turbulent channel [13].

As per a recent market analysis by Emergen Research, the global FSO technology market is projected to reach a staggering USD $4,675.89$ million by 2028, registering a revenue compounded annual growth rate (CAGR) of 33.3% during the forecast period [14]. Rising trends of work-from-home and online schooling amid the COVID-19 pandemic, growing trend of BYOD (bring-your-own-device) in the business sector, technological advances in telecommunications equipment, and increasing deployment of FSO communication systems in the aerospace & defense sector are among the major factors propelling the global market revenue growth.

The FSO communication market is primarily driven by the rising applications in enterprise connectivity, security, and surveillance, etc. Some of the key applications are last mile access, military applications due to the security capability and bandwidth of FSO, and many more. North America dominated the FSO communication market in 2021, as FSO communication technology is used by the US Military, primarily in naval and ship-to-ship communications. Moreover, the continuous expansion and upgrade of network facilities is also estimated to propel the FSO communication market in north America. Furthermore, increase in applications of FSO communication technology in the aerospace and defence sector is anticipated to propel the market in the next few years.

There are majority of key developments in the FSO communication system around the world. For example, in November 2017, L3 Technologies announced that it had received multiple contracts to develop FSO capabilities for the U.S. Department of Defense and space customers. In November 2020, IIT Guwahati developed FSO technology for information transfer [15]. In September 2021, Carillon Technologies bagged a US$ 6.4 Mn contract from the Defense Advanced Research Projects Agency to prototype next-generation satellite-to-satellite communication systems derived from cutting-edge commercial Holographic Optical Beam Steering (HOBS) technology. The new solid-state HOBS technology would offer a step change in weight, size, and cost for satellite FSO communication systems. Recently, in May 2022, Mitsubishi Electric Corporation announced that it had developed the world's first laser communication terminal integrating space optical communication and spatial laser acquisition in the photodetector [16]. It detects the direction of received beams in the 1.5-µm band, a general-purpose band used for terrestrial optical fiber communications and other applications.

1.5 Fundamental Key Technologies

In addition to optical wireless technology, some other important technologies that will be the driving force for 6G and B6G includes WPT, IRS [5].

1.5.1 Wireless Power Transfer

It is said that, in the future wireless networks, the large number of connected devices could be wirelessly charged with aid of WPT technology. Thus WPT is considered as an inventive technology for future genration communication. The WPT technologies are currently commercially available for a variety of applications, including charging smart phones and implantable medical devices, and are still being developed for a variety of applications.

The power-constraint wireless nodes can harvest energy through external ambient sources such as solar, heat, and wind etc. However, WPT technology has different advantages over traditional harvesting methods depending on the application. Some of them are listed below:

Reliability: WPT can be a more reliable source of energy because it is not dependent on the availability of sunlight. In contrast, the weather conditions would hinder the utilization of solar energy, and the density of ambient RF radiation entirely depends on human activity. In addition, these ambient sources are also scarce, which makes energy harvesting (EH) unsuitable for energy-hungry applications.

Flexibility: WPT can be used in a wider range of environments and settings, whereas solar EH requires a specific type of surface, such as a rooftop or open field, that is exposed to direct sunlight. WPT can also be used in areas where installing solar panels is not feasible or practical.

Efficiency: WPT can be more efficient than solar EH, especially in low-light conditions. While solar panels can generate power only during daylight hours, WPT can operate 24×7 as long as there is a power source to transmit the energy.

Scalability: WPT can be scaled up or down depending on the energy needs of a specific application. Solar EH systems require a certain amount of surface area to generate enough power, which may not be practical for smaller devices or in areas with limited space.

In the literature, the EH via RF-based WPT, commonly termed as simultaneous wireless information and power transfer (SWIPT), has been studied in [17, 18, 19, 20]. However, the use of RF-based WPT system raises various additional health issues due to intense electromagnetic radiation. Thus, EH using RF is not suitable in sensitive areas, such as hospitals. Moreover, as a result of the transmit power restrictions imposed by numerous safety issues, it is not viable to rely purely on RF-based EH [21]. Furthermore, energy conversion losses are also high because of the use of rectifiers for AC to DC conversion. Therefore, the actual gathered energy may be significantly lower than the beamed energy in practical settings. As a result, there always exists a trade-off with amount of average information rate and the energy harvested, hence, it is a crucial design element in RF-based EH system. To overcome these challenges, WPT through optical means is a promising solution. The optical signal carries a DC signal superimposed on an AC signal to operate the optical source in a linear region [22]. This DC signal allows the energy to be harvested at the receiver without any rectification. The twofold utilization of the optical signal for both communication and energy transfer can be advantageous for the practical system design. Moreover, the optical signal from the LED or laser source does not cause serious health hazards [21, 23].

The adoption of simultaneous lightwave information and power transfer (SLIPT) has been recently introduced in the past few years, both in indoor and outdoor applications through optical links [23, 22]. Further, to enhance the feasibility and efficacy of SLIPT technology, various transmission and receive SLIPT strategies have been adopted in literature such as *Time splitting* and *DC bias optimization*. In case of time splitting, time frame is split in two portions where transmitter switches between energy transfer mode and information transfer mode. In case of DC bias optimization, the DC component is optimized to achieve an appropriate trade-off in information rate and harvested energy. In the context of relay-aided networks, the main challenge is their limited/short operational lifetime which is primarily caused by the limited power available [24]. As a result, an EH facility can be added to these power-constrained relaying systems to improve energy sustainability.

1.5.2 Intelligent Reflecting Surface

IRS is a recent hardware technology that has emerged as a new paradigm for creating a reconfigurable wireless propagation environment[25, 26]. An IRS consists of a large number of low-cost programmable meta-surfaces as reflecting elements having the capability of adjusting the reflection amplitude and reflection phase of the incident signal. Some of the advantages of using IRS in wireless communications are:

- Improved signal strength: IRS can help improve the signal strength and quality by reflecting and manipulating the incoming signals in a way that reduces signal fading and interference. In case of OWC systems, an IRS can can enhance communication link by reducing the atmospheric turbulence and misalignment.
- Energy efficiency: As IRS are nearly passive and some energy is needed to operate the switches and receive control signals to configure them, once the metasurface is configured properly, a dedicated power source is not required for the signal transmission. Thus, this technology enhances the energy efficiency in upcoming 6G networks by reducing the power consumption.
- Increased capacity: IRS can increase the capacity of wireless networks by creating multiple signal paths for the same signal. Thus, it has the capability to improve the capacity of the system by coherently combining each signal at the receiver.
- Cost-effective: Compared to traditional wireless communication technologies, IRS can be cost-effective. For instance, instead of installing multiple antennas and equipment, a single IRS can be used to improve the wireless signal quality.
- Easy deployment: IRS can be easily deployed in various environments, such as indoor and outdoor, and can be mounted on walls or ceilings without requiring complex installation processes. Since, IRSs require very little direct current power supply and there is no need for any complex decoding/encoding logic, it is easy to integrate them with existing wireless infrastructures [26], [27].

IRS technology has been shown to mitigate the severe implications of the Doppler effect that arises due to the relative mobility between transmitter and receiver and also reduce the deep fades in the received signal [28]. Furthermore, it can also overcome the negative consequences of the time-varying wireless channels by making the wireless environment controllable. The IRS can be reconfigured dynamically in response to changes in the environment, such as the position and movement of users or changes in atmospheric conditions. This flexibility makes IRS well-suited for V2X communication, where the communication environment changes rapidly and unpredictably, thereby mitigating the effects caused by Doppler shift [28, 29]. Furthermore, the integration of IRS to existing wireless networks can support communication with mmWave and Terahertz frequencies, which makes IRS a promising technology for real-time applications.

IRS when integrated into the FSO network creates an attractive research opportunity to enhance the coverage and overcome the limitation of LoS communication for ubiquitous connectivity, especially in urban areas, where the signal is usually blocked by heavy vehicles or buildings [30]. Recent findings suggest that IRS have a lot of potential in 6G and B6G systems because of the promising gains they can make in spectral and energy efficiency without requiring more complicated and expensive hardware [27].

1.6 Motivation

The 6G and B6G technologies are expected to incorporate FSO to enable even higher data rates, lower latency, and greater security than traditional radio-based communication. As described in Section 1.2, mixed FSO-RF communication system leverages the benefits of both the technologies while mitigating their individual weaknesses. Moreover, some key technologies, such as WPT, IRS, and non-orthogonal multiple access (NOMA) will drive the communication requirements of the 6G and B6G networks. Thus, to better explain the motivation of our work, we first present some key benefits of the communication system obtained through integrating different technologies.

Improved Reliability and Coverage: It is well known that mixed FSO-RF systems can provide better reliability and improved data transfer even in challenging environments. By integrating IRS and NOMA, mixed FSO-RF systems can provide enhanced connectivity and coverage, particularly in outdoor environments. The integration of an optical IRS (OIRS) improves the connectivity of FSO hop and minimizes the misalignment errors, especially in situations where the LoS is blocked. Moreover, the IRS in RF hop can improve signal strength and quality at the cell edge user. The NOMA can enable multiple users to access the network simultaneously.

Enhanced Energy Efficiency: The integration of WPT technology (i.e., SLIPT) over the FSO hop leads to improved energy efficiency. The deployment of an OIRS (with sufficient size and desired orientation) can improve the amount of harvested power to enable the reliable data transfer over the next hop. Furthermore, the deployment of an IRS (of suitable size and optimized reflection coefficients) over RF hop ensures the sufficient received signal power, especially in the low transmit power conditions.

Accounting these benefits, in this dissertation, we consider the mixed FSO-RF network integrated with various technologies, such as EH using WPT, IRS, and NOMA.

Thereafter, we study the impact of utilizing each of these technologies into a mixed FSO-RF communication system on the communication performance (or performance metric, discussed in next section.) Some of the practical real-time scenarios where the NOMA-based IRS-assisted mixed FSO-RF system with EH can be realized include disaster response, secure military operations, and remote areas with limited infrastructure, where relay can harvest energy (through a dedicated and legitimate source) to ensure continuous and secure operations. Moreover, this system design can be applied in wireless sensor networks, where EH and efficient spectrum utilization are crucial. In such a scenario, the relay can harvest energy to power the sensors and act as a communication hub, enabling long-term and autonomous operation of the network. Similarly, it can also enhance the urban and rural connectivity.

1.7 Key Performance Metrics

1.7.1 First-Order Statistics

The first-order Statistics refer to the statistical properties of a random signal or process that are characterized by the average mean and variance. These statistics provide information about the central tendency and dispersion of the signal. The mean, also known as the expected value provides an indication of the typical value around which the signal fluctuates, whereas, variance measures the dispersion or spread of the signal values around the mean and quantifies the amount of random variation or noise present in the signal. By analyzing the first-order Statistics of a wireless signal, engineers can gain insights into its behavior and make predictions about its performance. These statistics are often employed in system design, modulation schemes, channel modeling, and signal processing techniques to optimize wireless communication performance and reliability. Some of the important first-order Statistics are described as follows:

Outage Probability

Outage probability is defined as the probability that the system will fail to meet a certain performance criterion. In particular, it refers to the probability that the received signal power will fall below a certain threshold, known as the outage threshold. For example, suppose we have a wireless communication system that is designed to maintain a certain level of signal quality, measured in terms of signal-to-noise (SNR), for such a system, if SNR falls below the outage threshold, we say that the signal is degraded to an unacceptable value. Through outage probability, engineers can design the system to meet specific performance requirements and optimize its performance in the face of noise, interference, and other sources of signal degradation. Mathematical the outage probability is represented as

$$\mathcal{P}_{\text{out}} = \Pr\{\Gamma \leq \gamma_{\text{Th}}\} = \mathcal{F}_{\Gamma}(\gamma_{\text{Th}}), \tag{1.1}$$

where Γ is the received SNR, $\Pr\{\cdot\}$ denotes the probability of an event, $\mathcal{F}_x(\cdot)$ is the cumulative distribution function (CDF), and γ_{Th} is the pre-defined SNR threshold.

Average Bit-Error-Rate

The average bit error rate is a measure of the error rate in a digital communication system. It is a statistical measure that quantifies the number of bit errors that occur in a transmission over time.

The bit-error-rate is calculated as the ratio of the number of errors to the total number of transmitted bits. This calculation is usually performed over a specific period of time, such as a second or a minute. The average bit-error-rate is an important parameter in digital communication systems because it affects the overall performance. A high bit-error-rate can result in lost data, reduced system capacity, and increased transmission errors, while a low bit-error-rate can ensure reliable transmission of data with minimal errors.

The average bit-error-rate for binary modulation schemes can be evaluated as

$$\mathcal{P}_{\text{e}} = \frac{b^a}{2\Gamma(a)} \int_0^{\infty} \frac{\gamma^{a-1} e^{-b\gamma}}{\sqrt{\gamma}} \mathcal{F}_{\Gamma}(\gamma) d\gamma, \tag{1.2}$$

where a and b represent different binary modulations schemes. For example, for coherent binary phase shift keying (CBPSK), $a = 1/2$ and $b = 1$. For coherent binary frequency shift keying (CBFSK), $a = 1/2$ and $b = 1/2$. For non-coherent BFSK (NCFSK), $a = 1$ and $b = 1/2$. Finally, for differential BPSK (DBPSK), $a = 1$ and $b = 1$.

Ergodic Capacity

Ergodic capacity is a measure of the maximum average data rate that can be reliably transmitted over the wireless channel, averaged over a large number of channel realizations. The term "ergodic" refers to the statistical properties of the channel, which are assumed to be stationary and ergodic. In an ergodic channel, the statistics of the channel do not change over time, and the channel realizations are statistically independent and identically distributed (IID) over time. The ergodic capacity depends on bandwidth of the channel, power constraints, modulation scheme used, the coding scheme used, and the channel characteristics (e.g., fading, interference, noise).

In general, the ergodic capacity in wireless communication is expressed as:

$$\mathcal{C}_{\text{erg}} = \frac{1}{\ln(2)} \int_0^\infty \ln(1+\gamma) f_\Gamma(\gamma) d\gamma, \tag{1.3}$$

where $f_\Gamma(\gamma)$ is the probability density function (PDF) of SNR Γ.

Effective Capacity

The effective capacity is a measure of the maximum average data rate that can be reliably transmitted over the wireless channel, while meeting a certain quality of service (QoS) requirement. The effective capacity takes into account the impact of channel fading and stochastic variations in the wireless channel, and provides a more realistic measure of the achievable data rate than the ergodic capacity, which assumes perfect channel state information (CSI) at the transmitter.

The effective capacity of a wireless communication system can be expressed mathematically as:

$$\mathcal{C}_{\text{eff}} = -\frac{1}{A_d} \log_2 \left(\mathcal{E} \left[\frac{1}{(1+\Gamma)^{A_d}} \right] \right), \tag{1.4}$$

where $A_d = \frac{\tau_d B_L B_w}{\ln 2}$, with τ_d denoting the asymptotic decay rate of buffer occupancy; B_L being the block length and B_w representing the bandwidth of the system.

1.7.2 Second-Order Statistics

Although, system performance in terms of first-order statistics is important, however, it captures the static behaviour of system under consideration [31]. To characterize the *dynamic behaviour* of the system with multipath fading, the study of second-order statistics (SOS) have gained significant importance [32, 33, 34, 35, 36, 37, 38].

The SOS refer to the statistical properties of a random signal or process that are characterized by the autocorrelation function (ACF) and the power spectral density (PSD). The ACF measures how similar the signal values are at different time instants or spatial locations and can be useful in analyzing the temporal or spatial characteristics of a signal, such as multipath fading in wireless channels or the presence of interference. On the other hand PSD provides information about the frequency content of the signal and the power distribution across different frequency components. It is often used to analyze the bandwidth requirements, channel capacity, and interference characteristics of wireless systems. These statistics are crucial for designing equalization techniques, error correction codes, interleaver size, packet length, and other signal processing algorithms that can mitigate the effects of fading, interference, and noise in wireless communication systems. The two important SOS are level crossing rate (LCR) and average outage duration (AOD) explained as follows:

Level Crossing Rate

The LCR is a measure of the rate at which the received signal falls below a given threshold in the downward direction subject to time-varying channel conditions. It can be used to quantify the frequency of signal fade events over time. In the case of wireless communication system, the LCR represents the temporal rate of signal fade events occurring when the received SNR at receiver falls below a predetermined threshold that determines the sensitivity of the receiver.

If γ is the received SNR, the LCR can be evaluated by Rice's formula [32] defined as

$$\mathcal{L}(\gamma_{\mathrm{Th}}) = \int_{0}^{\infty} \hat{\gamma} f_{\Gamma\hat{\Gamma}}(\gamma_{\mathrm{Th}}, \hat{\gamma}) d\hat{\gamma}, \tag{1.5}$$

where $f_{\Gamma\hat{\Gamma}}(\gamma, \hat{\gamma})$ is the joint PDF of Γ and its time derivative $\hat{\Gamma}$.

Average Outage Duration

The AOD is defined as the average time duration over which the received signal power falls below a certain threshold level. AOD is often used as a measure of the temporal variability of a wireless channel. For the considered system, the AOD can be mathematically defined as

$$\mathcal{T}(\gamma_{\mathrm{Th}}) = \frac{\mathcal{F}_{\Gamma}(\gamma_{\mathrm{Th}})}{\mathcal{L}(\gamma_{\mathrm{Th}})}. \tag{1.6}$$

1.8 Objectives

In this thesis, we focus on the performance analysis of IRS-assisted mixed FSO-RF communication system and provide important engineering insights. The performance analysis is an important and efficient approach, especially at the early stage of a system design to understand the system operations and to observe the impact of system parameters on the performance. The main objectives along with the brief descriptions are explained as hereunder:

- **Objective 1:** To investigate the performance of SLIPT-enabled drcode-and-forward (DF)-based mixed FSO-RF communication system.

  Under this objective, we consider a mixed FSO-RF communication system utilizing DF relay. The FSO subsystem exploits SLIPT technology to harvest energy at relay node which is utilized for information transmission over the RF hop. Under the effect of atmospheric turbulence and non-zero boresight pointing error for the FSO link and multipath fading for the RF link, we obtain the end-to-end SNR statistics. In particular, analytical expressions of outage probability, average bit-error-rate, ergodic capacity, and effective capacity are derived in terms of Meijer's G-function. To gain additional insights, we also derive the asymptotic expressions of outage, average bit-error-rate, and effective capacity and estimate the diversity order mathematically.

- **Objective 2:** To investigate the performance of an IRS-assisted one-bit control based mixed FSO-RF communication system.

  Further to enhance the performance of mixed FSO-RF system, we integrate IRS into the RF link. For the considered IRS-assisted mixed FSO-RF system, we employ a one-bit controlling mechanism of IRS for passive beamforming optimization. In particular, unified closed-form expressions for the outage, bit-error-rate, and ergodic rate are derived for optical heterodyne detection (OHD) and intensity modulation with direct detection (IMDD) techniques. We also derive the achievable diversity order of the considered IRS-assisted system by obtaining the asymptotic outage and bit-error-rate, and ergodic rate performance.

- **Objective 3:** To investigate the performance of SLIPT-enabled IRS-assisted mixed FSO-RF communication system using NOMA.

  Under this objective, we consider multiuser scenario using NOMA technique that provide high spectral efficiency. Thus, we propose a novel relay-based mixed FSO-RF communication system utilizing NOMA to assist two users (i.e., near user and far user) in RF link. Assuming the non-availability of direct FSO link, we consider the deployment of an optical IRS (OIRS). Moreover, we deploy an conventional RF-based IRS in the vicinity of far user to improve its performance. We adopt SLIPT technology to harvest energy at the relay node, which is utilized to forward the information signal over the RF hop and thus, makes the SNR of the RF hop dependent on the FSO channel coefficients. For the proposed network, we evaluate the performance in terms of outage, throughput, and ergodic rate. We also derive asymptotic analytical outage at high SNR to get more insights and obtain the diversity order analytically.

- **Objective 4:** To analyze the SOS for OIRS-assisted FSO communication network.

  Further, to characterize the *dynamic behaviour* of the a system under time-varying channel fading, we analyze SOS for OIRS-assisted FSO communication system utilizing multi-aperture receiver that performs selection combining (SC) to achieve spatial diversity. The SOS analysis for the considered system is carried out in the presence of atmospheric turbulence, foggy conditions, and misalignment error. We specifically develop the closed-form analytical expressions of SOS, i.e., LCR and AOD of SNR at the output of the SC receiver under non-isotropic scattering environment. Further, by using finite-state Markov channel (FSMC) model, we derive packet-error-rate (PER) using the derived LCR expression. In order to have optimum packet length using FSMC model, we employ stop-and-wait automatic repeat request (SW-ARQ) protocol. The optimized packet length, which provides the maximum throughput under the SW-ARQ protocol, is also determined.

- **Objective 5:** To analyze second-order statistics for an IRS-Assisted multi-user RF communication system with co-channel interference.

  Finally, we analyze the SOS for an IRS-assisted RF-based communication system. For this, we consider a downlink multi-user communication network empowered by an IRS with the BS employing the orthogonal frequency division multiple access (OFDMA) scheme. The performance of the considered system is evaluated in the presence of multiple co-channel interferers with varying powers and speeds. In particular, we develop the analytical expressions of LCR and AOD of the received signal envelope at a desired user by considering a generalized fading model as κ-μ distribution. Moreover, we derive an expression for asymptotic LCR under high transmit power conditions. In addition, we consider a SW-ARQ protocol for reliable data packet transmission and derive the expressions for PER and throughput by utilizing the FSMC model. The optimal packet length is also determined which maximizes the throughput under SW-ARQ protocol.

1.9 Thesis Outline

The organization of this dissertation is as follows.

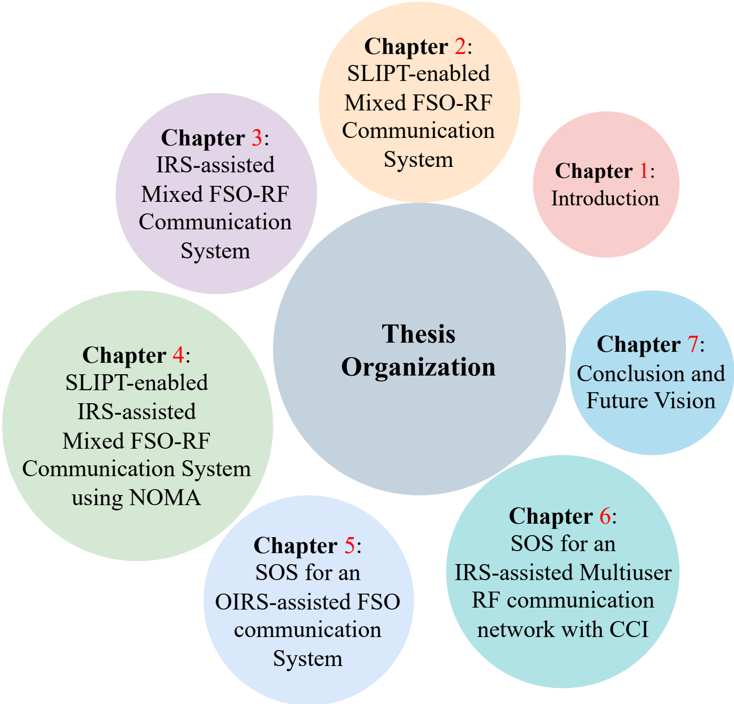

Figure 1.1: Thesis organization.

- **Chapter 1: Introduction -** This chapter introduces how the FSO communication meets next generation wireless communication networks, various challenges and opportunities of FSO communication systems, and the need for mixed FSO-RF communications systems. Further, we introduce the various breakthrough technologies that can be integrated into the current wireless networks and then we define some of the key performance metrics used in later chapters.

- **Chapter 2: SLIPT-Enabled Mixed FSO-RF Communication System -** In this chapter, we consider a dual-hop mixed FSO-RF communication network with DF relay that harvest power using SLIPT technology. For the considered system, the statistical distribution of the end-to-end SNR is derived under $\mathcal{M}$-distributed atmospheric turbulence with non-zero boresight pointing error based FSO link and Nakagami-m distributed RF link. In particular, analytical expressions of outage probability, bit-error-rate, ergodic capacity, and effective capacity are derived in terms of Meijer's G-function. Thereafter, we derived the asymptotic expressions of average bit-error-rate, outage probability, and effective capacity. Furthermore, we also derive the diversity order mathematically. The impact of various system and channel parameters like DC bias, turbulence, weather conditions, and visibility is explored on the system performance.

- **Chapter 3: IRS-Assisted Mixed FSO-RF Communication System -** In this chapter, we consider a dual-hop mixed FSO-RF communication system assisted by an IRS. Further, we employ a one-bit controlling mechanism of IRS for passive beamforming optimization, which selects some of the reflecting elements in such a way that the SNR at the receiver is maximized. Considering generalized $\mathcal{M}$-distribution with non-zero bore-sight pointing error for the FSO link and Nakagami-m distribution for the RF link, we derive the closed-form expressions for the unified end-to-end outage probability, bit-error-rate, and ergodic capacity for an IRS-assisted mixed FSO-RF communication system by considering both IMDD and OHD schemes. We also derive the achievable diversity order of the considered IRS-assisted system by obtaining the asymptotic outage probability and bit-error-rate performance, and it has been shown that the number of elements of one-bit control IRS has an impact on the diversity order. In addition, we derive the asymptotic ergodic capacity of the considered system. The numerical results have been provided to show the performance of the proposed IRS-assisted system. Moreover, the impact of the number of reflecting elements, practical reflection amplitude, and controlling mechanism at the IRS is studied on the system performance.

- **Chapter 4: SLIPT-Enabled IRS-Assited Mixed FSO-RF Communication System -** In this chapter, we consider NOMA-based SLIPT-enabled mixed FSO-RF communication network assisted two users (i.e., near and far user) in the RF link. We assume the LoS communication link from source to relay is not present; therefore, we employ single-element OIRS between source and relay. Since far user experiences poor channel conditions, we deploy IRS consisting of multiple reflecting elements in the vicinity of the far user to further enhance its channel quality. For the considered system, we derive closed-form analytical expressions of outage probability, throughput, and ergodic rate for NOMA-based SLIPT-enabled IRS-aided mixed FSO-RF communication system. We also derive asymptotic analytical outage at high SNR to get more insights and obtain the diversity order analytically. Numerical results with useful observations are provided to see the impact of system and channel parameters on the system's performance. The integration of IRS exhibits significant improvement in the performance of the considered system with NOMA.

- **Chapter 5: SOS for OIRS-Assisted FSO Communication System -** In this chapter, we consider a downlink OIRS-assisted FSO communication network, where a single aperture transmitter communicates with a multi-aperture receiver through an OIRS. Under the impact of random fog, Gamma-Gamma distributed atmospheric turbulence and zero-boresight misalignment errors, we derive the closed-form analytical expressions for LCR and AOD for the considered OIRS-assisted FSO communication network under the non-isotropic scattering environment. Further, using FSMC model, we derive an expression for the PER utilizing the derived LCR expression. To achieve optimum packet length using the FSMC model, we employ a SW-ARQ protocol at the link layer. The optimized packet length, which provides the maximum throughput under the SW-ARQ protocol, is also determined. Extensive numerical results have been provided to show the effect of various system and channel parameters on the system's performance.

- **Chapter 6: SOS for IRS-Assisted Multiuser RF Communication System -** In this chapter, we consider a OFDMA-based multi-user downlink RF communication network assisted by an IRS. We derive the analytical expressions for the SOS in terms of LCR and AOD for the considered IRS-assisted RF communication system under interference-limited scenario by following the κ-μ fading distribution for all the desired as well interfering links. Moreover, we derive the analytical expressions for asymptotic LCR for high transmit power. For reliable packet transmission, we employ the SW-ARQ scheme at the link layer of the considered IRS-assisted RF communication system and derive the expressions for PER and throughput using the FSMC model. Furthermore, the optimal packet length of the data packet is determined which maximizes the throughput under SW-ARQ protocol. Through numerical results, we have shown the impact of various system and channel parameters on system's performance.

- **Chapter 7: Conclusion and Future scope -** This chapter summarizes and provides additional perspective on the results obtained in previous chapters. We also provide a number of topics for possible future work on the grounds of the research presented in this dissertation.

Chapter 2

SLIPT-Enabled Mixed FSO-RF Communication System

2.1 Introduction

The advantages of both the FSO and RF technologies are merged to achieve superior performance in the mixed FSO-RF relaying system [39]. The two most prevalent protocols for relaying are amplify-and-forward (AF) and DF. The primary goal of an AF-relay is to forward the received signal after amplifying its power. The DF relay, on the other hand, decodes the incoming signal before passing it on to the next hop. In comparison to AF relaying, [40, 41] shows that DF relaying improves overall SNR. Further, the main challenge with these relay-aided mixed FSO-RF networks is their limited/short operational lifetime which is primarily caused by power constraints [24]. As a result, an EH facility can be added to these power-constrained relaying systems to improve energy sustainability.

Thus, in this chapter, we consider a DF relay-based mixed FSO-RF network, where the FSO subsystem exploits simultaneous transfer of energy and information to increase the system's lifespan. For the proposed DF relay-assisted FSO-RF system, $\mathcal{M}$-distribution with non-zero boresight pointing/misalignment error is considered to model the FSO channel, and Nakagami-m model is assumed for the RF channel. To investigate the system performance, the end-to-end SNR statistics are derived using the optical energy transfer at the DF relay. In particular, analytical expressions of outage probability, average bit error rate, ergodic capacity, and effective capacity are derived in terms of Meijer's G-function. To gain additional insights, we also derive the asymptotic expressions of outage probability, average bit-error-rate, and effective capacity and estimate the diversity order mathematically. The impact of various system and channel parameters like DC bias, atmospheric turbulence, weather conditions, and visibility is explored on the system performance. Through numerical results, we show that the proposed DF relay-aided and SLIPT-enabled mixed FSO-RF system surpasses its AF-based counterpart. The superiority of the proposed system over non-EH and RF-EH based mixed FSO-RF system is also shown. The analytical formulations are validated with Monte-Carlo simulations.

2.1.1 State-of-the-Art

Over the last few years, several mixed RF-FSO as well as FSO-RF systems have been studied [42, 43, 44, 45, 46, 47, 48, 49, 50, 51, 52, 53, 54]. In [42], the authors have examined the outage performance of multiple DF relay based mixed RF-FSO systems using relay selection. The mixed RF-FSO network with asymmetric channel distribution utilizing multiple input multiple output (MIMO) technology with DF relaying is investigated in [43]. The authors in [43] have obtained the diversity multiplexing trade-off with different number of antennas at each node. In [44], the outage probability, bit-error-rate, and ergodic capacity of a hybrid RF-FSO network with both fixed and variable gain AF-relay are investigated. The work in [44] is further extended for mixed FSO-RF network in [45]. The authors in [46] have proposed both AF and DF relaying for a mixed FSO-RF system. In [46], the FSO link undergoes double generalized Gamma distribution whereas the RF link is modelled by the extended generalized-K shadowed fading. In [47], the authors have investigated the end-to-end performance of a hybrid FSO-mmWave system where the FSO channel is modelled as the Gamma-Gamma and the mmWave channel undergoes the fluctuating two-ray fading. Also, the outage probability, average bit-error-rate, and ergodic and effective capacities are obtained for both the relaying protocols. Further, a parallel FSO/RF system, where the FSO channel follows the Gamma-Gamma distribution and RF channel follows the Rayleigh distribution, is studied in [48]. The outage probability for an adaptive mixed FSO-RF system with DF relaying is derived in [49], where RF and FSO links are modelled by the Rayleigh and the K-distribution, respectively. The authors in [50] have studied the hybrid FSO/RF system, where the relay (utilizing both AF and DF) receives the signal from the Gamma-Gamma distributed FSO link with the impact of zero-boresight misalignment error and transmits the signal through the $\alpha - \mathcal{F}$ distributed RF link.

The performance of a fixed gain AF relay-assisted mixed RF-FSO communication system is analyzed in [51] over Nakagami-m-Gamma-Gamma (GG) links. Further, a multi-antenna based DF relay is considered in [52] to analyze the performance of a mixed RF-FSO communication system. In [53], authors have considered η-μ distributed RF link and $\mathcal{M}$-distributed FSO link to analyze the performance of the mixed RF-FSO system. The secrecy performance of mixed RF-FSO is analyzed in [54].

Table 2.1: Comparison of Existing Works with the Proposed Work

Ref.	Performance metric	FSO link	RF link	Pointing error	Energy Harvesting
[45]	Outage, bit-error-rate, and ergodic capacity	Gamma-Gamma	Nakagami-m	Zero boresight	×
[46]	Outage, bit-error-rate, and ergodic capacity	Double Generalized Gamma	Generalized-K	Zero boresight	×
[47]	Outage, bit-error-rate, ergodic rate, and effective capacity	Gamma-Gamma	Fluctuating two ray (FTR)	Zero boresight	×
[48]	Outage and bit-error-rate	Gamma-Gamma	Rayleigh	Zero boresight	×
[49]	Outage	K-distribution	Rayleigh	Zero boresight	×
[50]	Outage, bit-error-rate, ergodic rate, and effective capacity	Gamma-Gamma	α-$\mathcal{F}$ fading	Zero boresight	×
[55]	Outage	Gamma-Gamma	Rayleigh	Zero boresight	✓*
[56]	Outage	Gamma-Gamma	Rayleigh	Zero boresight	✓
Our work	Outage, bit-error-rate, ergodic rate, and effective capacity	$\mathcal{M}$-distribution	Nakagami-m	Non-zero boresight	✓ (SLIPT)

*For harvesting the energy, an RF based external power beacon is utilized.

The adoption of SLIPT has been recently introduced in the past few years, both in indoor and outdoor applications through optical links [23, 22]. In [22], the SLIPT protocol in the VLC system is analyzed. Moreover, for harvesting the energy in the dual-hop FSO-RF network, an RF based external power beacon is utilized in [55]. In addition, [56] considers a mixed FSO-RF system with an AF relay with EH and analyzes the outage performance under the Gamma-Gamma-Rayleigh fading model.The short summary and the comparison of the existing works that have considered the similar mixed FSO-RF communication system is shown in Table 2.1.

2.1.2 Novelty and Contributions

To the author's knowledge, SLIPT with a DF relay-aided mixed FSO-RF network has not been explored in the literature since it makes the system's performance analysis more complex. Moreover, majority of the existing works have considered the Rayleigh fading distribution for RF links when considering EH in the mixed FSO-RF system. In addition, the complicated performance metrics, such as average bit-error-rate, ergodic capacity, and effective capacity, have not been investigated for the aforementioned model. Motivated by the above discussion, in this chapter, we consider a novel DF relay-aided mixed FSO-RF system that utilizes SLIPT over $\mathcal{M}$-distributed FSO link with non-zero boresight pointing error. Apart from this, we model the RF channel using Nakagami-m fading as it is a more generalized model.

The key contributions of this chapter are described as follows:

- We consider a DF relay-aided mixed FSO-RF communication system in which the relay node harvests power through the optical link and uses the harvested power to transmit across the RF hop.

- For the considered system, the statistical distribution of the end-to-end SNR is derived under $\mathcal{M}$-distributed atmospheric turbulence with non-zero boresight pointing error based FSO link and Nakagami-m distributed RF link.
- Furthermore, the analytical expressions of end-to-end outage probability, average bit-error-rate, ergodic capacity, and effective capacity are derived using non-coherent IMDD based FSO receiver and the EH relay node.
- To gain further insights, we also provide the asymptotic analysis of outage probability, average bit-error-rate, and effective capacity and evaluate the diversity order mathematically.
- Through numerical results, the effect of various system and channel parameters like DC bias, atmospheric turbulence, misalignment error coefficients, attenuation, and visibility parameter has been revealed on the performance of SLIPT-enabled DF relay-aided mixed FSO-RF communication system.
- The performance of the proposed DF relay-aided mixed FSO-RF communication network with EH relay node has been compared with a similar SLIPT-enabled AF-based mixed FSO-RF communication system [56]. In addition to this, the proposed system has also been compared with the non-EH as well as RF-EH based mixed FSO-RF communication systems. It has been shown through numerical results that the proposed EH based mixed FSO-RF system significantly outperforms the other systems.

2.2 System Model

We consider a mixed FSO-RF communication network as shown in Fig. 2.1. It comprises of an optical source node (S), an RF destination node (D) and a DF relay node (R). In this model, the node S communicates to D through R and we assume all nodes operate in a half-duplex mode and are equipped with a single aperture/antenna. Assuming that R can process both optical and RF signals, we use a non-coherent IMDD receiver at R to detect the optical signal received from S over the FSO link. Usually, the avalanche photodoide (APD) is employed as an FSO receiver for direct detection of the received optical signal. APD offers high responsivity (approximately 1) due to the internal carrier gain through the avalanche process. Moreover, it provides a large collection area for the

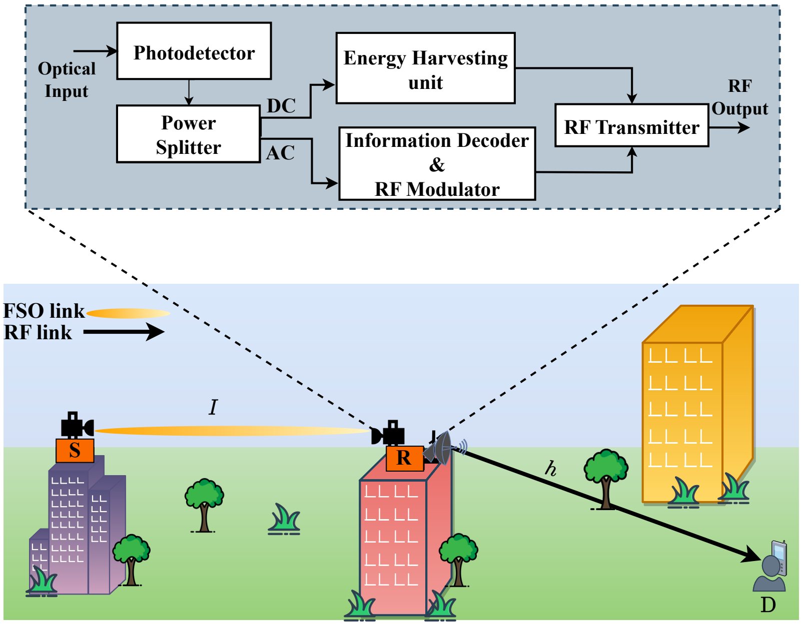

Figure 2.1: Block diagram of SLIPT-enabled DF relay-aided mixed FSO-RF communication system.

incoming optical signal [57]. After the incoming optical signal is converted to an electrical signal at R, a power splitter is used to segregate the AC and DC components. Thereafter, the unwanted DC component is fed to the EH unit to drive the RF transmitter. The AC component of information signal is decoded, re-modulated, and then forwarded through the RF transmitter.

2.2.1 Transmission Protocol

The communication between S and D takes place in two time slots that are orthogonal to each other, denoted by T_1 and T_2. The node R simultaneously harvests energy and decodes the information signal during entire time slot T_1. The node S uses sub-carrier intensity modulation (SIM) to convert digitally modulated information signal x_m with electrical power ς to an optical signal. A DC bias $\mathcal{B} \in (\mathcal{B}_{\min}, \mathcal{B}_{\max})$ is added to $x_m(t)$ to ensure a non-negative optical signal, where $\mathcal{B}_{\min}$ and $\mathcal{B}_{\max}$ are the minimum and the maximum DC bias values, respectively. Let P_{S} be the electrical power of S to transmit the optical signal s_m, then s_m is written as

$$s_m = \sqrt{P_{\mathrm{S}}}[\delta x_m + \mathcal{B}], \tag{2.1}$$

where δ is defined as the electrical-to-optical conversion coefficient. The following constraint on δ must be satisfied in order to avoid clipping due to the non-linearity of the laser-diode. [56]

$$\delta \leq \min\left(\frac{\mathcal{B}-\mathcal{B}_{\min}}{\varsigma}, \frac{\mathcal{B}_{\max}-\mathcal{B}}{\varsigma}\right). \tag{2.2}$$

The electrical signal y_{R} obtained at the output of the APD having responsivity R_{P} and detection area A_{P} at R is given by

$$y_{\mathrm{R}} = \eta R_{\mathrm{P}} A_{\mathrm{P}} I s_m + e_{\mathrm{R}}, \tag{2.3}$$

where η is the optical-to-electrical conversion coefficient. Here $I = I_a I_p I_l$ denotes the channel gain of FSO link (i.e., SR link), where I_a and I_p represents the gains due to atmospheric turbulence and non-zero boresight misalignment error, respectively. The term $I_l = \exp(-\vartheta L_{\mathrm{SR}})$ is the path loss factor over SR link with link distance L_{SR} and the attenuation coefficient ϑ. For given visibility (V) and wavelength λ, the attenuation coefficient is given by $\vartheta = \frac{3.91}{V}\left(\frac{\lambda}{550}\right)^{-f_{\mathrm{K}}}$, where the value of parameter f_{K} is given by Kim's model depending on the distribution of size of atmospheric particles. $e_{\mathrm{R}} \sim \mathcal{CN}(0, \sigma_{\mathrm{R}}^2)$ denotes the complex zero mean additive white Gaussian noise (ZM-AWGN) at R. Let x_d denote the signal transmitted by the node R, then the received signal y_{D} at D is given as

$$y_{\mathrm{R}} = h\sqrt{P_{\mathrm{R}}} x_d + e_{\mathrm{D}}, \tag{2.4}$$

where h is the channel gain of RD link, P_{R} is the re-transmission power available at R, and $e_{\mathrm{D}} \sim \mathcal{CN}(0, \sigma_{\mathrm{D}}^2)$ denotes the ZM-AWGN at D;.

2.2.2 Channel Model

Atmospheric Turbulence Model

The atmospheric turbulence channel gain I_a follows $\mathcal{M}$-distribution given by [53, 58, 59]

$$f_{I_a}(I_a) = \mathcal{A}\sum_{r=1}^{\infty} s_r\, I_a^{\frac{\alpha+r}{2}-1}\, K_{\alpha-r}\left(2\sqrt{\frac{\alpha\, I_a}{g}}\right), \quad I_a > 0, \tag{2.5}$$

$$\text{wherein} \quad \mathcal{A} \triangleq \frac{2\,\alpha^{\alpha/2}}{g^{1+\alpha/2}\Gamma(\alpha)}\left(\frac{g\,\beta}{g\,\beta+\Omega''}\right)^{\beta}, \quad s_r \triangleq \frac{(\beta)_{r-1}\,(\alpha g)^{r/2}}{[(r-1)!]^2\, g^{r-1}\,(g\,\beta+\Omega'')^{r-1}}, \tag{2.6}$$

where K_ℓ is the ℓ-th order modified Bessel function of the second kind and $\Gamma(\cdot)$ is the gamma function defined in [60, (6.1.1)]. The parameter α is the distance-dependent fading positive parameter associated with the effective number of large-scale cells characterizing the scattering process, β is a real number and defines the amount of fading parameter

Table 2.2: Various Models obtained through $\mathcal{M}$-distribution.

Parameters	Distribution
$\varepsilon = 0$ and $g = 0$	Lognormal distribution
$\Omega' = 0$, $\varepsilon = 0$, and $\beta = 1$	K-distribution
$\Omega' = 0$ and $\varepsilon = 0$	Homodyned K-distribution
$\varepsilon = 1$, $g = 0$, and $\Omega'' = 1$	Gamma-Gamma distribution

and $g = 2p_o(1-\varepsilon)$ [58]. The values of p_0 and ε depend on the total scatter components, while $\Omega'' = \Omega' + 2\varepsilon p_o + 2\sqrt{2p_o\Omega'\varepsilon}\cos(\phi_a - \phi_b)$ is the average optical power of the coherent contribution, wherein Ω' is the average power of LoS component, and ϕ_a and ϕ_b are deterministic phases of LoS and scattering terms coupled to the LoS term, respectively. Specifically, the parameter ε, where $0 \leq \varepsilon \leq 1$, represents the amount of scattering power coupled to the LoS component. Further, $(\cdot)_k$ represents the Pochhammer symbol. Table 2.2 describes various known FSO channel distribution models obtained from the $\mathcal{M}$-distribution [61].

Non-zero Boresight Pointing Error

The radial displacement p due to horizontal and vertical deviation of the axes of (PD) plane can be represented by approximated Rayleigh distribution as [58]

$$f_p(p) = \frac{p}{\sigma_s^2}\exp\left(-\frac{p}{2\sigma_s^2}\right), \quad p \geq 0, \quad \text{with} \tag{2.7}$$

$$\sigma_s^2 = \left(\frac{3\mu_x^2\sigma_x^4 + 3\mu_y^2\sigma_y^4 + \sigma_x^6 + \sigma_y^6}{2}\right)^{1/3}, \tag{2.8}$$

where the parameters μ_x, μ_y denote the mean values, and σ_x, σ_y symbolize the standard deviation for the horizontal and elevation displacements, respectively. The PDF of irradiance depending on non-zero boresight can be written as

$$f_{I_p}(I_p) = \frac{\xi^2}{(A_o\varrho)^{\xi^2}} I_p^{\xi^2-1}, \quad 0 \leq I_p \leq A_o\varrho, \tag{2.9}$$

where q is given by

$$\varrho = \exp\left(\frac{1}{\xi^2} - \frac{1}{2\xi_x^2} - \frac{1}{2\xi_y^2} - \frac{\mu_x^2}{2\sigma_x^2\xi_x^2} - \frac{\mu_y^2}{2\sigma_y^2\xi_y^2}\right), \tag{2.10}$$

and $\xi_x = \frac{W_e}{2\sigma_x}$, $\xi_y = \frac{W_e}{2\sigma_y}$, and $\xi = \frac{W_e}{2\sigma_s}$, where W_e is the equivalent radius of beam. Moreover, the constant term A_o is the fraction of power received by PD in the absence of pointing error[62].

Composite Atmospheric Turbulence and Pointing Error Distribution

The composite PDF of $I = I_a I_p I_l$ can be obtained by the following integral

$$\begin{aligned} f_I(I) &= \int_{I/(I_l\ A_o\varrho)}^{\infty} f_{I_a}(I_a)\ f_{I|I_a}(I|I_a)\ dI_a \\ &= \int_{I/(I_l\ A_o\varrho)}^{\infty} f_{I_a}(I_a)\frac{I}{I_a I_l} f_{I_p}\left(\frac{I}{I_a I_l}\right) dI_a. \end{aligned} \tag{2.11}$$

Following the similar procedure discussed in [59], the composite PDF of I is given by

$$f_I(I) = \frac{\xi^2 \mathcal{A}}{4I}\sum_{r=1}^{\infty} s_r \left(\frac{\alpha}{g}\right)^{-\frac{\alpha+r}{2}} G_{1,3}^{3,0}\left(\frac{\alpha I}{g I_l A_o \varrho}\middle| \begin{matrix} \xi^2+1 \\ \xi^2, \alpha, r \end{matrix}\right), \tag{2.12}$$

where $G_{p,q}^{m,n}\left(y \middle| \begin{smallmatrix} a_1,\ldots,a_p \\ b_1,\ldots,b_q \end{smallmatrix}\right)$ is the Meijer's-G function defined in [63, (07.34.02.0001.01)].

The instantaneous SNR at R, γ_{R}, can now be defined from (2.3) as

$$\gamma_{\mathrm{R}} = \bar{\gamma}_o I_a^2 I_p^2, \tag{2.13}$$

where $\bar{\gamma}_o = (\eta R_{\mathrm{P}} A_{\mathrm{P}} I_l \sqrt{P_{\mathrm{S}}}\delta)^2/\sigma_{\mathrm{R}}^2$. Considering IMDD receiver at R, the PDF of γ_{R} can be expressed as

$$f_{\gamma_{\mathrm{R}}}(z) = \frac{\xi^2 \mathcal{A}}{4z}\sum_{r=1}^{\infty} s_r \left(\frac{\alpha}{g}\right)^{-\frac{\alpha+r}{2}} G_{1,3}^{3,0}\left(\Psi\sqrt{\frac{z}{\varkappa_{FSO}}}\middle| \begin{matrix} \xi^2+1 \\ \xi^2, \alpha, r \end{matrix}\right), \tag{2.14}$$

where $\Psi = \xi^2\alpha\beta(g+\Omega')/[\left(\xi^2+1\right)(g\beta+\Omega')]$ and $\varkappa_{FSO}$ is the electrical SNR defined as [64, (34)]

$$\varkappa_{FSO} = \frac{\bar{\gamma}_o A_o^2 \varrho^2 \xi^4 g^2}{(\xi^2+1)^2}\left(\frac{g\beta}{g\beta+\Omega'}\right)^{2\beta} {}_2F_1^2\left(2,\beta;1;\frac{\Omega'}{g\beta+\Omega'}\right), \tag{2.15}$$

where ${}_2F_1(\cdot;\cdot;\cdot)$ is the Gauss hypergeometric function defined in [63, (07.23.02.0001.01)]. The average value of γ_{R} is given b

$$\bar{\gamma}_{\mathrm{R}} = \mathcal{E}\left\{\gamma_{\mathrm{R}}\right\} = \frac{(\alpha+1)\left[2g\left(g+2\Omega'\right)+\Omega'^2\left(\beta+1\right)\right](1+\xi^2)^2\varkappa_{FSO}}{\alpha\beta\xi^2(\xi^2+2)(g+\Omega')}, \tag{2.16}$$

where $\mathcal{E}\left\{\cdot\right\}$ is the expectation operator. Then, the CDF of γ_{R} can be derived by using [63, (07.34.21.0084.01)] as

$$F_{\gamma_{\mathrm{R}}}(z) = K\sum_{r=1}^{\infty}\Upsilon_r G_{3,7}^{6,1}\left(\frac{\Psi^2}{16\varkappa_{FSO}}z\middle| \begin{matrix} 1, \mathbb{A} \\ \mathbb{B}, 0 \end{matrix}\right), \tag{2.17}$$

where $K = \frac{\xi^2 \mathcal{A}}{8\pi}$, $\Upsilon_r = s_r \left(\frac{\alpha}{g}\right)^{-\frac{\alpha+r}{2}} 2^{\alpha+r-2}$, $\mathbb{A} = \left\{\frac{\xi^2+1}{2}, \frac{\xi^2+2}{2}\right\}$, and $\mathbb{B} = \left\{\frac{\xi^2}{2}, \frac{\xi^2+1}{2}, \frac{\alpha}{2}, \frac{\alpha+1}{2}, \frac{r}{2}, \frac{r+1}{2}\right\}$.

Further, the instantaneous SNR at D can be defined from (2.4) as

$$\gamma_{\mathrm{D}} = \frac{P_{\mathrm{R}}}{\sigma_{\mathrm{D}}^2} h^2. \tag{2.18}$$

By assuming that the channel gain h follows Nakagami-m fading with $\mathcal{E}\left\{h^2\right\} = 1$, γ_{D} follows Gamma distribution with PDF [65]

$$f_{\gamma_{\mathrm{D}}}(z) = \frac{m^m}{\Gamma(m)\bar{\gamma}_{\mathrm{D}}^m} z^{m-1} \exp\left(-\frac{m}{\bar{\gamma}_{\mathrm{D}}} z\right), \tag{2.19}$$

with parameter $\bar{\gamma}_{\mathrm{D}} = P_{\mathrm{R}}/\sigma_{\mathrm{D}}^2$.

2.2.3 EH at Relay Node

This subsection provides a mathematical framework to evaluate the energy harvested at the relay node. Given the DC component supplied to the EH unit is $I_{\mathrm{DC}} = \eta R_{\mathrm{P}} A_{\mathrm{P}} I \sqrt{P_{\mathrm{S}}} \mathcal{B}$ and the open circuit voltage of the photovoltaic (PV) cell is V_{OC}, the power harvested at R is given by [66]

$$P_{\mathrm{H}} = 0.75 V_{\mathrm{OC}} I_{\mathrm{DC}}, \tag{2.20}$$

where $V_{\mathrm{OC}} = V_{\mathrm{T}} \ln\left((I_{\mathrm{DC}}/I_o) + 1\right)$. Here, I_o and V_{T} represent the dark saturation current and the thermal voltage of the PV cell, respectively. Therefore, the instantaneous value of power harvested at R can be rewritten as

$$P_{\mathrm{H}} = 0.75 \eta R_{\mathrm{P}} A_{\mathrm{P}} I \sqrt{P_{\mathrm{S}}} \mathcal{B} V_{\mathrm{T}} \ln\left(\frac{\eta R_{\mathrm{P}} A_{\mathrm{P}} I \sqrt{P_{\mathrm{S}}} \mathcal{B}}{I_o} + 1\right). \tag{2.21}$$

The harvested power can be approximated utilizing [56] as

$$P_{\mathrm{H}} \approx \frac{0.75 V_{\mathrm{T}} \eta^2 R_{\mathrm{P}}^2 A_{\mathrm{P}}^2 I^2 P_{\mathrm{S}} \mathcal{B}^2}{I_o}. \tag{2.22}$$

Since P_{H} is used by R to transmit signal over the RF hop for a duration of T_2, the transmit power which is needed at R can be achieved as $P_{\mathrm{R}} = P_{\mathrm{H}} T_1 / T_2$. For a special case of equal time duration i.e., $T_1 = T_2$, we get $P_{\mathrm{R}} = P_{\mathrm{H}}$. Moreover using (2.16), the average value of power harvested at R can be as

$$\bar{P}_{\mathrm{R}} = \mathcal{E}\left\{P_{\mathrm{R}}\right\} = \frac{0.75 V_{\mathrm{T}} (\eta R_{\mathrm{P}} A_{\mathrm{P}} I_l^2 \sqrt{P_{\mathrm{S}}} \mathcal{B})^2 \bar{\gamma}_{\mathrm{R}}}{I_o \bar{\gamma}_o}. \tag{2.23}$$

2.3 Performance Analysis

This section describes the performance of the considered system. Here, we will discuss the end-to-end SNR characterization, then utilizing this, we derive the analytical expressions for outage probability, average bit-error-rate, ergodic capacity, and effective capacity. Later, to get better insights, we derive the asymptotic analysis and achievable diversity order valid for high SNR conditions.

2.3.1 End-to-End SNR Characterization

Let γ_{R} be the instantaneous SNR over SR link and γ_{D} be the instantaneous SNR over RD link, respectively. Then, the end-to-end instantaneous SNR Γ_{E} for DF relaying system can be expressed as $\Gamma_{\mathrm{E}} = \min(\gamma_{\mathrm{R}}, \gamma_{\mathrm{D}})$. For $T_1 = T_2$, we can rewrite γ_{D} described in (2.18), using P_{H} from (2.22) as

$$\gamma_{\mathrm{D}} = \frac{(\eta R_{\mathrm{P}} A_{\mathrm{P}} \sqrt{P_{\mathrm{S}}}\mathcal{B})^2 I^2 h^2 0.75 V_{\mathrm{T}}}{I_o \sigma_{\mathrm{D}}^2} \triangleq \gamma_{\mathrm{R}} \gamma'_{\mathrm{D}}, \tag{2.24}$$

where $\gamma'_{\mathrm{D}} = \bar{\gamma}'_{\mathrm{D}} h^2$ with the average value

$$\bar{\gamma}'_{\mathrm{D}} = \frac{0.75 V_{\mathrm{T}} \rho_{\mathrm{RD}} \mathcal{B}^2}{\delta^2 I_o \rho_{\mathrm{SR}}}, \tag{2.25}$$

where $\rho_{\mathrm{SR}} = \frac{P_{\mathrm{S}}}{\sigma_{\mathrm{R}}^2}$ and $\rho_{\mathrm{RD}} = \frac{P_{\mathrm{S}}}{\sigma_{\mathrm{D}}^2}$ represent the transmit SNR of SR and RD links, respectively. The PDF of $\gamma'_{\mathrm{D}} = \bar{\gamma}'_{\mathrm{D}} h^2$ can be computed in a similar way as shown in (2.19) with parameter $\bar{\gamma}'_{\mathrm{D}}$. It can be observed from (2.24) that γ_{R} and γ_{D} are dependent random variables, as a result, the CDF of Γ_{E} can be expressed as

$$\mathcal{F}_{\Gamma_{\mathrm{E}}}(\gamma) = \Pr[\min(\gamma_{\mathrm{R}}, \gamma_{\mathrm{R}}\gamma'_{\mathrm{D}}) \le \gamma] = \int_0^\infty \mathcal{F}_{\Gamma_{\mathrm{E}}}(\gamma \mid \gamma'_{\mathrm{D}} = u) f_{\gamma'_{\mathrm{D}}}(u) du. \tag{2.26}$$

Note that when $0 \le \gamma'_{\mathrm{D}} < 1$, then $\Gamma_{\mathrm{E}} = \gamma_{\mathrm{R}}\gamma'_{\mathrm{D}}$, whereas, when $\gamma'_{\mathrm{D}} \ge 1$, then $\Gamma_{\mathrm{E}} = \gamma_{\mathrm{R}}$. Accounting this, we can transform (2.26) as

$$\mathcal{F}_{\Gamma_{\mathrm{E}}}(\gamma) = \underbrace{\int_0^1 \mathcal{F}_{\gamma_{\mathrm{R}}}\left(\frac{\gamma}{u}\right) f_{\gamma'_{\mathrm{D}}}(u) du}_{\mathcal{J}_1(\gamma)} + \underbrace{\int_1^\infty \mathcal{F}_{\gamma_{\mathrm{R}}}(\gamma) f_{\gamma'_{\mathrm{D}}}(u) du}_{\mathcal{J}_2(\gamma)}. \tag{2.27}$$

Substituting (2.17) along with the PDF of γ'_{D} in (2.27), we get

$$\mathcal{J}_1(\gamma) = \frac{K m^m}{\Gamma(m)\bar{\gamma}_D'^m} \sum_{r=1}^{\infty} \Upsilon_r \int_0^1 u^{m-1} \exp\left(-\frac{m}{\bar{\gamma}'_{\mathrm{D}}} u\right) G_{3,7}^{6,1}\left(\frac{(\alpha\beta\Psi)^2}{16\varkappa_{FSO}}\left(\frac{\gamma}{u}\right) \middle| \begin{matrix} 1, \mathbb{A} \\ \mathbb{B}, 0 \end{matrix}\right) du, \tag{2.28}$$

$$\text{and}\quad \mathcal{J}_2(\gamma) = \frac{Km^m}{\Gamma(m)\bar{\gamma}_D'^m}\sum_{r=1}^{\infty}\Upsilon_r\int_1^{\infty}u^{m-1}\exp\left(-\frac{m}{\bar{\gamma}_{\mathrm{D}}'}u\right)G_{3,7}^{6,1}\left(\frac{(\alpha\beta\Psi)^2}{16\varkappa_{FSO}}\gamma\,\middle|\,\begin{matrix}1,\mathbb{A}\\ \mathbb{B},0\end{matrix}\right)du. \tag{2.29}$$

Using $e^x=\sum_{n=0}^{\infty}\frac{x^n}{n!}$ in (2.28) and using [67, (8.2.2,14)], [63], we have

$$\mathcal{J}_1(\gamma)= \frac{K}{\Gamma(m)}\sum_{n=0}^{\infty}\frac{(-1)^n}{n!}\left(\frac{m}{\bar{\gamma}_{\mathrm{D}}'}\right)^{m+n}\sum_{r=1}^{\infty}\Upsilon_r G_{4,8}^{7,1}\left(\frac{(\alpha\beta\Psi)^2\gamma}{16\varkappa_{FSO}}\,\middle|\,\begin{matrix}1,\mathbb{A},m+n+1\\ m+n,\mathbb{B},0\end{matrix}\right). \tag{2.30}$$

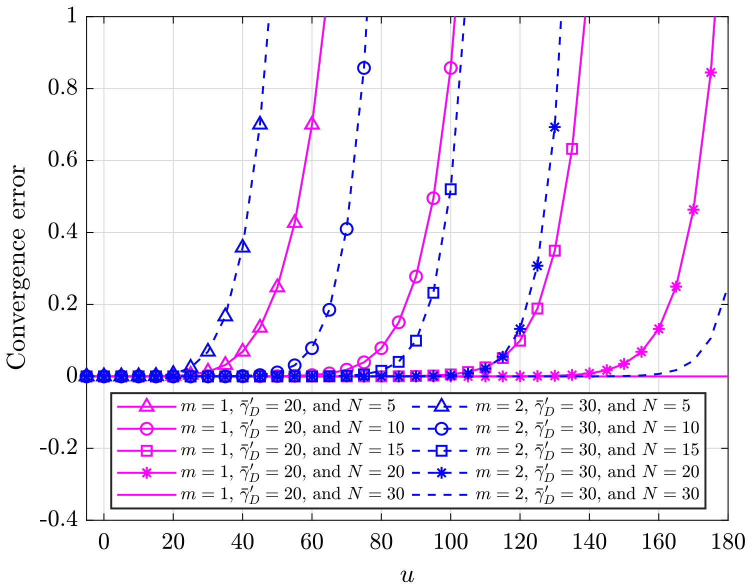

Figure 2.2: Variations of convergence error for different m, N, and $\bar{\gamma}_D'$.

Remark 2.1: *For numerical purpose, the infinite series in* (2.30) *(obtained by using the power series expansion of the exponential term in* (2.28)*) can be truncated to first N terms such that the convergence error is minimized. The convergence error $\epsilon(u)$, due to the truncation, can be defined as*

$$\epsilon(u) = \left|\exp\left(-\frac{m}{\bar{\gamma}_D'}u\right) - \sum_{n=0}^{N}\frac{(-1)^n m^n u^n}{n!(\bar{\gamma}_D')^n}\right|, \tag{2.31}$$

where $|\cdot|$ denotes the absolute value. An appropriate value of N can be chosen in order to have a negligible convergence error. For this, we have plotted the convergence error in Fig. 2.2 for different values of m, N, and $\bar{\gamma}_D'$. It is clear from Fig. 2.2 that for small values of N, the convergence error deviates from zero error line at low values of u, whereas for higher values of N, the convergence error remains at zero for larger range of u. For example with $N = 30$, the convergence error is zero for almost entire range of u considered *in the figure. Thus, we consider $N = 30$ for all the analytical curves presented in Section IV.*

Similar to (2.30), we can obtain $\mathcal{J}_2(\gamma)$ in (2.29) with the help of [63, (07.34.21.0085.01)] as

$$\mathcal{J}_2(\gamma) = \frac{K}{\Gamma(m)}\Gamma\left(m, \frac{m}{\bar{\gamma}'_{\mathrm{D}}}\right)\sum_{r=1}^{\infty}\Upsilon_r G_{3,7}^{6,1}\left(\frac{(\alpha\beta\Psi)^2\gamma}{16\varkappa_{FSO}}\middle|\begin{matrix}\mathbb{A}\\ \mathbb{B}\end{matrix}\right), \tag{2.32}$$

where $\Gamma(\cdot,\cdot)$ denotes the upper incomplete Gamma function [68, (8.350,2)]. Using (2.30) and (2.32) in (2.27), the CDF of end-to-end SNR can be obtained.

2.3.2 Outage Probability and Diversity Analysis

Outage probability, P_{out}, is defined as the probability when the instantaneous SNR falls below a pre-defined SNR threshold γ_{Th}, i.e.,

$$\mathcal{P}_{\mathrm{out}} = \Pr[\Gamma_{\mathrm{E}} \leq \gamma_{\mathrm{Th}}] = \mathcal{F}_{\Gamma_{\mathrm{E}}}(\gamma_{\mathrm{Th}}). \tag{2.33}$$

P_{out} can be obtained by substituting $\gamma = \gamma_{\mathrm{Th}}$ in (2.27).

To get more insights into the performance, we consider a high SNR condition. For this, we assume equal noise power at R and D such that $\rho_{\mathrm{SR}} = \rho_{\mathrm{RD}} = \rho$ and the asymptotic outage is derived as $\tilde{\mathcal{P}}_{\mathrm{out}} = \lim_{\rho\to\infty} \mathcal{P}_{\mathrm{out}}$. Intuitively, for high SNR conditions, i.e., $\rho \to \infty$, the term corresponding to $n = 0$ in the exponential series of (2.30) will have major dominance over the other terms. Thus, we obtain the asymptotic outage probability $\tilde{\mathcal{P}}_{\mathrm{out}}$ by applying the asymptotic expansion for Meijer-G function given in [63, (7.34.06.0006.01)] as

$$\begin{aligned}\tilde{\mathcal{P}}_{\mathrm{out}} = \frac{K}{\Gamma(m)}\Bigg[&\left(\frac{m}{\bar{\gamma}'_{\mathrm{D}}}\right)^{m}\sum_{r=1}^{\infty}\Upsilon_r\sum_{\ell=1}^{7}\frac{\prod\limits_{\substack{i=1\\ i\neq\ell}}^{7}\Gamma(b_i-b_\ell)\Gamma(b_\ell)\left(\frac{\Psi^2\gamma_{\mathrm{Th}}}{16\varkappa_{FSO}}\right)^{b_\ell}}{\prod\limits_{i=2}^{4}\Gamma(a_i-b_\ell)\Gamma(1+b_\ell)}\\ &+\Gamma\left(m,\frac{m}{\bar{\gamma}'_{\mathrm{D}}}\right)\sum_{r=1}^{\infty}\Upsilon_r\sum_{k=1}^{6}\frac{\prod\limits_{\substack{j=1\\ j\neq k}}^{6}\Gamma(d_j-d_k)\Gamma(d_k)\left(\frac{\Psi^2\gamma_{\mathrm{Th}}}{16\varkappa_{FSO}}\right)^{d_k}}{\prod\limits_{j=2}^{3}\Gamma(c_j-d_k)\Gamma(1+d_k)}\Bigg],\end{aligned} \tag{2.34}$$

where $c_j \in \{1, \mathbb{A}\}$, $d_j \in \mathbb{B}$, $a_i \in \{1, \mathbb{A}, m+1\}$, and $b_i \in \{m, \mathbb{B}\}$.

Remark 2.2: *It should be noted from* (2.25) *that for $\rho_{SR} = \rho_{RD}$, the $\bar{\gamma}'_D$ is a constant. As a result, the asymptotic outage probability can be given as $\tilde{\mathcal{P}}_{out} \propto \left(\frac{1}{\rho}\right)^{\mathcal{G}_d}$, where $\mathcal{G}_d$*

represents the analytical achievable diversity order and is given by

$$\mathcal{G}_d = \min\left\{m, \frac{\xi^2}{2}, \frac{\alpha}{2}, \frac{r}{2}\right\}. \tag{2.35}$$

It can be noted from (2.35) *that for both the systems i.e., SLIPT-enabled DF relay-aided mixed FSO-RF and similar setup without utilizing SLIPT, the diversity order is same. Since, the diversity order of a mixed FSO-RF system is a function of channel parameters i.e., fading parameters of RF link and the atmospheric and misalignment parameters of the FSO link, it is independent of energy harvested at the relay. Therefore, for mixed FSO-RF system with SLIPT and without SLIPT, the diversity order will be same.*

2.3.3 Ergodic Capacity Analysis

The ergodic capacity of the mixed FSO-RF system under IMDD technique is given by [47]

$$\mathcal{C}_{\text{erg}} = \frac{1}{\ln(2)} \int_0^\infty \ln(1+\Lambda\gamma) f_{\Gamma_{\text{E}}}(\gamma) d\gamma, \tag{2.36}$$

where $\Lambda = \frac{e}{2\pi}$ and $f_{\Gamma_{\text{E}}}(\gamma)$ is the PDF of Γ_{E}.

Lemma 2.1: *The end-to-end ergodic capacity of the considered mixed FSO-RF system with SLIPT can be expressed as*

$$\begin{aligned}\mathcal{C}_{\text{erg}} = \frac{K}{\Gamma(m)\ln(2)}\Bigg[&\sum_{n=0}^{\infty}\frac{(-1)^n}{n!}\left(\frac{m}{\bar{\gamma}'_{\text{D}}}\right)^{m+n}\sum_{r=1}^{\infty}\Upsilon_r G_{7,11}^{9,3}\left(\frac{\Psi^2}{16\varkappa_{FSO}\Lambda}\middle|\begin{matrix}0,1,0,1,\mathbb{A},m+n+1\\ m+n,\mathbb{B},0,0,1,0\end{matrix}\right)\\ &+\Gamma\left(m,\frac{m}{\bar{\gamma}'_{\text{D}}}\right)\sum_{r=1}^{\infty}\Upsilon_r G_{6,10}^{8,3}\left(\frac{\Psi^2}{16\varkappa_{FSO}\Lambda}\middle|\begin{matrix}0,1,0,1,\mathbb{A}\\ \mathbb{B},0,0,1,0\end{matrix}\right)\Bigg].\end{aligned} \tag{2.37}$$

Proof. See Appendix A.1.1 for the proof. □

2.3.4 Effective Capacity Analysis

The concept of effective capacity outlines the maximum arrival rate that a time-varying fading channel can sustain depending upon the quality-of-service requirements of the system[47, 69]. The effective capacity for the considered system can be defined as

$$\begin{aligned}\mathcal{C}_{eff} &= -\frac{1}{A_d}\log_2\left(\mathcal{E}\left\{\frac{1}{(1+\gamma)^{A_d}}\right\}\right),\\ &= -\frac{1}{A_d}\log_2\left(1 - A_d\int_0^\infty \frac{1-F_{\Gamma_{\text{E}}}(\gamma)}{(1+\gamma)^{A_d+1}}d\gamma\right),\end{aligned}$$

$$= -\frac{1}{A_d}\log_2\left(A_d\int_0^{\infty}\frac{F_{\Gamma_{\rm E}}(\gamma)}{(1+\gamma)^{A_d+1}}d\gamma\right), \tag{2.38}$$

where $A_d = \frac{\tau_d B_L B_w}{\ln 2}$, with τ_d denoting the asymptotic decay rate of buffer occupancy; B_L being the block length and B_w representing the bandwidth of the system. Substituting the CDF of $\Gamma_{\rm E}$ in (2.38) and using [63, (07.34.21.0086.01)], the effective capacity of DF relay-aided mixed FSO-RF with SLIPT will be given as

$$\mathcal{C}_{\rm eff} = -\frac{1}{A_d}\log_2\left(\frac{KA_d\mathcal{S}}{\Gamma(m)\Gamma(A_d+1)}\right), \tag{2.39}$$

where

$$\begin{aligned}\mathcal{S} = &\sum_{n=0}^{\infty}\frac{(-1)^n}{n!}\left(\frac{m}{\bar{\gamma}'_{\rm D}}\right)^{m+n}\sum_{r=1}^{\infty}\Upsilon_r G_{5,9}^{8,2}\left(\frac{\Psi^2}{16\varkappa_{FSO}}\middle|\begin{matrix}0,1,\mathbb{A},m+n+1\\ A_d,m+n,\mathbb{B},0\end{matrix}\right)\\ &+\Gamma\left(m,\frac{m}{\bar{\gamma}'_{\rm D}}\right)\sum_{r=1}^{\infty}\Upsilon_r G_{4,8}^{7,2}\left(\frac{\Psi^2}{16\varkappa_{FSO}}\middle|\begin{matrix}0,1,\mathbb{A}\\ A_d,\mathbb{B},0\end{matrix}\right).\end{aligned} \tag{2.40}$$

Furthermore, the asymptotic effective capacity can be obtained for high SNR conditions (i.e., $\rho_{\rm SR}=\rho_{\rm RD}=\rho\to\infty$) as $\tilde{C}_{\rm eff} = \lim_{\rho\to\infty} C_{\rm eff}$ and can be evaluated by replacing $\mathcal{S}=\tilde{\mathcal{S}}$ in (2.39) with $\tilde{\mathcal{S}} = \lim_{\rho\to\infty}\mathcal{S}$. By using [63, (7.34.06.0006.01)] in (2.40), we can get $\tilde{\mathcal{S}}$ as

$$\begin{aligned}\tilde{S} = &\left(\frac{m}{\bar{\gamma}'_{\rm D}}\right)^{m}\sum_{r=1}^{\infty}\Upsilon_r\sum_{\ell=1}^{8}\frac{\prod_{\substack{i=1\\ i\neq\ell}}^{8}\Gamma(b'_i-b'_\ell)\prod_{i=1}^{2}\Gamma(1-a''_i+b'_\ell)\left(\frac{(\alpha\beta\Psi)^2}{16\varkappa_{FSO}}\right)^{b'_\ell}}{\prod_{i=3}^{5}\Gamma(a''_i-b'_\ell)\Gamma(1+b'_\ell)}\\ &+\Gamma\left(m,\frac{m}{\bar{\gamma}'_{\rm D}}\right)\sum_{r=1}^{\infty}\Upsilon_r\sum_{k=1}^{7}\frac{\prod_{\substack{j=1\\ j\neq k}}^{7}\Gamma(d'_j-d'_k)\prod_{j=1}^{2}\Gamma(1-c''_j+d'_k)\left(\frac{(\alpha\beta\Psi)^2}{16\varkappa_{FSO}}\right)^{d'_k}}{\prod_{j=3}^{4}\Gamma(c''_j-d'_k)\Gamma(1+d'_k)},\end{aligned} \tag{2.41}$$

where $c''_j\in\{0,1,\mathbb{A}\}$, $d'_j\in\{A_d,\mathbb{B}\}$, $a''_i\in\{0,1,\mathbb{A},m+1\}$, and $b'_i\in\{A_d,m,\mathbb{B}\}$.

2.3.5 Average and Asymptotic Bit-Error-Rate Analysis

In this subsection, we evaluate the analytical expression of the end-to-end average bit-error-rate and it's asymptote for the system under consideration. The average bit-error-rate for BPSK modulation schemes can be evaluated as [45]

$$\mathcal{P}_{\rm e} = \frac{1}{2\sqrt{\pi}} \int_0^\infty \frac{e^{-\gamma}}{\sqrt{\gamma}} F_{\Gamma_{\rm E}}(\gamma) d\gamma. \tag{2.42}$$

Substituting the CDF $\mathcal{F}_{\Gamma_{\rm E}}(\gamma)$ from (2.27) in (2.42) and using [63, 07.34.21.0088.01], the average bit-error-rate of DF relay-aided mixed FSO-RF with SLIPT is given by

$$\mathcal{P}_{\rm e} = \frac{K}{2\sqrt{\pi}\Gamma(m)} \Bigg[\sum_{n=0}^{\infty} \frac{(-1)^n}{n!} \left(\frac{m}{\bar{\gamma}'_{\rm D}}\right)^{m+n} \sum_{r=1}^{\infty} \Upsilon_r G_{5,8}^{7,2} \left(\frac{\Psi^2}{16\varkappa_{FSO}} \middle| \begin{matrix} 0.5, 1, \mathbb{A}, m+n+1 \\ m+n, \mathbb{B}, 0 \end{matrix} \right) \\ + \sum_{r=1}^{\infty} \Upsilon_r \Gamma\left(m, \frac{m}{\bar{\gamma}'_{\rm D}}\right) G_{4,7}^{6,2} \left(\frac{\Psi^2}{16\varkappa_{FSO}} \middle| \begin{matrix} 0.5, 1, \mathbb{A} \\ \mathbb{B}, 0 \end{matrix} \right) \Bigg]. \tag{2.43}$$

Further, we derive the expression for asymptotic bit-error-rate at high SNR conditions by assuming $\rho_{\rm SR} = \rho_{\rm RD} = \rho$. The asymptotic bit-error-rate can be evaluated as $\tilde{\mathcal{P}}_{\rm e} = \lim_{\rho \to \infty} \mathcal{P}_{\rm e}$. It is clear from (2.43) that for $\rho \to \infty$, only the term corresponding to $n = 0$ will dominate in the infinite summation. By utilizing the expansion of Meijer's-G function from [63, (7.34.06.0006.01)] in (2.43), we get

$$\tilde{\mathcal{P}}_{\rm e} = \frac{K}{2\sqrt{\pi}\Gamma(m)} \Bigg[\left(\frac{m}{\bar{\gamma}'_{\rm D}}\right)^m \sum_{r=1}^{\infty} \Upsilon_r \times \sum_{\ell=1}^{7} \frac{\prod_{\substack{i=1 \\ i\neq\ell}}^{7} \Gamma(b_i - b_\ell) \prod_{i=1}^{2} \Gamma(1 - a'_i + b_\ell) \left(\frac{\Psi^2}{16\varkappa_{FSO}}\right)^{b_\ell}}{\prod_{i=3}^{5} \Gamma(a'_i - b_\ell) \Gamma(1 + b_\ell)} \\ + \Gamma\left(m, \frac{m}{\bar{\gamma}'_{\rm D}}\right) \sum_{r=1}^{\infty} \Upsilon_r \sum_{k=1}^{6} \frac{\prod_{\substack{j=1 \\ j\neq k}}^{6} \Gamma(d_j - d_k) \prod_{j=1}^{2} \Gamma(1 - c'_j + d_k) \left(\frac{\Psi^2}{16\varkappa_{FSO}}\right)^{d_k}}{\prod_{j=3}^{4} \Gamma(c'_j - d_k) \Gamma(1 + d_k)} \Bigg], \tag{2.44}$$

where $c'_j \in \{0.5, 1, \mathbb{A}\}$, $d_j \in \mathbb{B}$, $a'_i \in \{0.5, 1, \mathbb{A}, m+1\}$, and $b_i \in \{m, \mathbb{B}\}$. It is evident from (2.44) that the achievable diversity order for the considered system is same as obtained in (2.35).

2.4 Numerical Results

This section presents the analytical and simulation results for outage probability, average bit-error-rate, ergodic capacity, and effective capacity of the SLIPT enabled mixed FSO-RF network utilizing DF relay. Table 2.3 [56] depicts the system parameters that were taken into account for obtaining numerical results. The threshold SNR for all the figures in this Section is set as $\gamma_{\rm Th} = 0.1$. Table 2.4 shows the atmospheric turbulence

Table 2.3: System Specifications

Parameter	Symbol	Value
Operating wavelength of laser	λ	1550 nm
Optical to electrical conversion coefficient	η	0.7
Diameter of APD	$2a$	20 cm
Responsivity of APD	R_{P}	0.9
FSO link distance	L_{SR}	1 Km
Equivalent beam radius	W_e	0.1733
Jitter deviation at APD	σ_s	0.1, 0.01
Dark saturation current	I_o	10 nA
Thermal voltage	V_{T}	25 mV
Noise variance	σ_i^2	1

Table 2.4: Weather and Turbulence Parameters

Turbulence Conditions of FSO link				
	Parameters			
Moderate turbulence	$\beta = 3.78$, $\alpha = 5.41$			
Strong turbulence	$\beta = 1.70$, $\alpha = 3.99$,			
Weather conditions of FSO link				
	Visibility	ϑ	Attenuation	I_l
Light fog scenario	0.5 km	4.839	21 dB/km	0.0079
	1 km	2.0724	9 dB/km	0.1259
Clear sky scenario	10 km	0.1017	0.43 dB/km	0.9033
	26 km	0.0392	0.17 dB/km	0.9617

and weather conditions taken to obtain the numerical results [70, 11]. Unless mentioned specifically, we have assumed $\rho_{\mathrm{SR}} = \rho_{\mathrm{RD}} = \rho$.

Fig. 2.3 illustrates the effect of DC bias $\mathcal{B}$ on the average SNR of SR link denoted by $\bar{\gamma}_{\mathrm{R}}$ and average harvested power denoted by $\bar{P}_{\mathrm{R}}$ at the node R. The value of $\mathcal{B}_{\min}$ and $\mathcal{B}_{\max}$ are taken as 0 mA and 20 mA, respectively, and DC bias $\mathcal{B}$ must be between $\mathcal{B}_{\min}$ and $\mathcal{B}_{\max}$. The value of ρ_{SR} is kept constant at 40 dB. It is intuitive that as $\mathcal{B}$ is increased from $\mathcal{B}_{\min}$ to $\mathcal{B}_{\max}$, $\bar{P}_{\mathrm{R}}$ monotonically increases for all turbulence and misalignment error conditions. When $\mathcal{B}$ is equal to $\mathcal{B}_{\min}$ or $\mathcal{B}_{\max}$, $\delta = 0$ or i.e., amplitude of message signal is 0 and therefore the average SNR at relay becomes 0. It is clear from Fig. 2.3, that as $\mathcal{B}$ approaches to 0 or 20 mA, the value of average SNR, $\bar{\gamma}_{\mathrm{R}}$ at relay approaches to $-\infty$ dB. Also, it is observed that $\bar{\gamma}_{\mathrm{R}}$ at R acquires a maximal value at $\mathcal{B} = 10$ mA. As a result, there exists a trade-off between $\bar{\gamma}_{\mathrm{R}}$ and $\bar{P}_{\mathrm{R}}$ at R. We must sacrifice the $\bar{\gamma}_{\mathrm{R}}$ at node R to enhance the average gathered power. Moreover, it is observed that the optimal value of $\mathcal{B}$ (to achieve maximum SNR) determined numerically is consistent with the theoretical optimum as $\mathcal{B} = \frac{\mathcal{B}_{\max}+\mathcal{B}_{\min}}{2}$. Depending upon the results obtained in Fig. 2.3, for all the

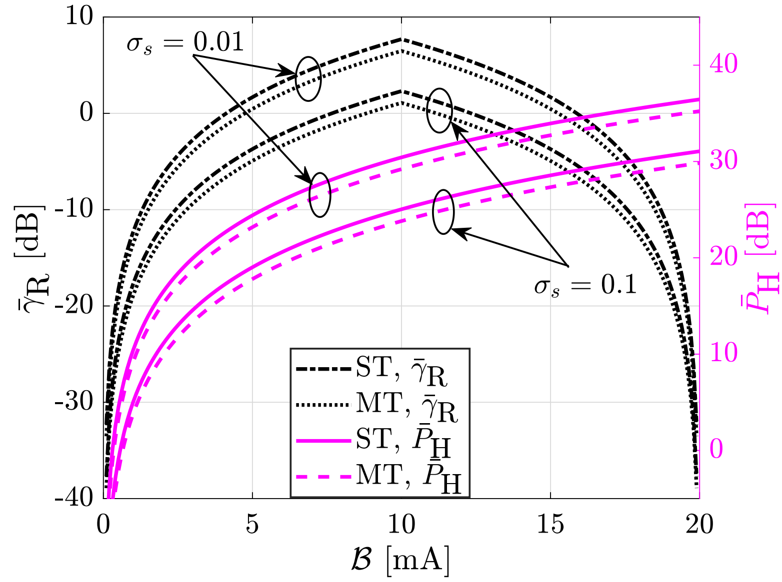

Figure 2.3: Variations of $\bar{\gamma}_{\mathrm{R}}$ and $\bar{P}_{\mathrm{R}}$ at node R with DC bias $\mathcal{B}$ ($\varepsilon = 1$ and $\Omega' = 1$).

remaining results, we consider $\mathcal{B} = 10$ mA.

In Figs. 2.4(a)-(b), the outage probability is varied with respect to transmit SNR of the proposed system for Gamma-Gamma distribution (i.e., $\varepsilon = 1$, $g = 0$, and $\Omega' = 1$) under different turbulence conditions. In Figs. 2.4(a)-(b), we consider 10 km visibility with 0.43 dB/km attenuation which can be assumed to be clear sky. The curves in Fig. 2.4(a) have been plotted for $m = 1$, $\xi = 0.8863$ and for Fig. 2.4(b), we have assumed $m = 2$, $\xi = 8.8627$. We have considered two different conditions for transmit SNRs of FSO and RF hops (and hence, for average received SNRs at nodes R and D) as (i) $\rho_{\mathrm{SR}} = \rho_{\mathrm{RD}}$ such that $\bar{\gamma}_{\mathrm{D}} > \bar{\gamma}_{\mathrm{R}}$, and (ii) $\rho_{\mathrm{SR}} > \rho_{\mathrm{RD}}$ such that $\bar{\gamma}_{\mathrm{D}} < \bar{\gamma}_{\mathrm{R}}$. For condition (ii), ρ_{SR} is chosen as ρ_{SR} [dB]= ρ_{RD} [dB]+23 dB, in accordance with Observation 2.2. It is observed from Fig. 2.4(a) that under both the considered transmit SNR conditions, the outage probability performance of the proposed SLIPT enabled mixed FSO-RF system for both turbulences varies with almost same rate. However, for negligible misalignment error conditions as shown in Fig. 2.4(b), the outage probability of proposed system for moderate turbulence decays rapidly as compared to that for strong turbulence under both transmit SNR conditions (i) and (ii). From Fig. 2.4(b) it is observed that the outage performance under strong turbulence condition and better FSO link SNR (i.e., $\rho_{\mathrm{SR}} > \rho_{\mathrm{RD}}$) decays at a lower rate as compared to the outage performance under moderate turbulence condition with equal SNRs of two hops (i.e., $\rho_{\mathrm{SR}} = \rho_{\mathrm{RD}}$). Therefore, for low values of ρ_{RD}, the outage probability values are lower for strong turbulence case, whereas after certain value of ρ_{RD}, the outage performance for values for moderate turbulence condition become much smaller in comparison to the strong turbulence condition.

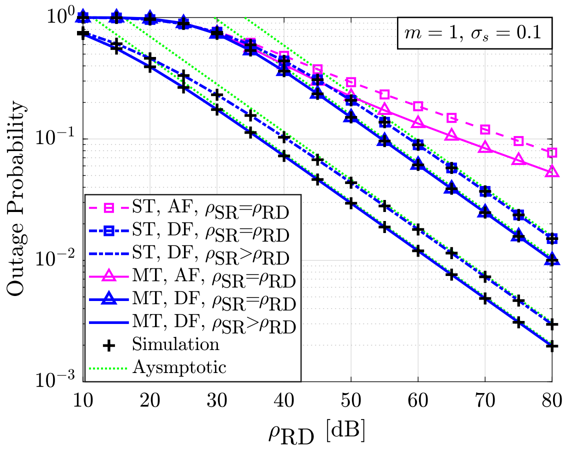

(a) Outage probability versus transmit SNR performance for $\sigma_s = 0.1$ and $m = 1$.

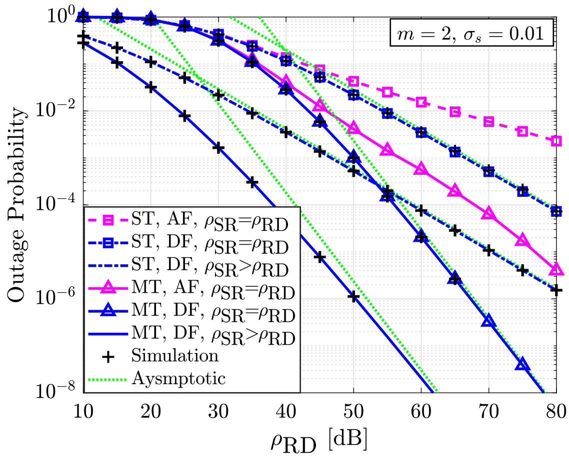

(b) Outage probability versus transmit SNR performance for $\sigma_s = 0.01$ and $m = 2$.

Figure 2.4: Comparison of outage probability performances of proposed DF relay-aided SLIPT enabled mixed FSO-RF communication system and its AF based counterpart under various channel and weather conditions.

Table 2.5: Theoretical and numerical values of diversity order.

Distribution	α	ξ	m	Diversity Order	
				$\mathcal{G}_d$ Theoretical	$\mathcal{G}_d$ Numerical
K ($\beta = 1$)	5.41	8.8627	1	0.5	0.5041
	5.41	0.8863	2	0.3927	0.3881
Log-normal ($\beta = 3.78$)	5.41	8.8627	1	1	1.0103
	5.41	0.8863	2	0.3927	0.3894
Gamma-Gamma ($\beta = 1.70$)	3.99	8.8627	1	0.8500	0.8444
	3.99	0.8863	2	0.3927	0.3894
Gamma-Gamma ($\beta = 3.78$)	5.41	8.8627	1	1	1.100
	5.41	0.8863	2	0.3927	0.3780

Further, the outage probability performance comparison for the considered SLIPT-enabled DF relay-aided mixed FSO-RF system with its AF-counterpart is shown in Figs. 2.4(a)-(b). It is noticed from both Figs. 2.4(a)-(b) that the proposed system provides remarkable enhancement in the outage probability performance as compared to the its corresponding AF-based system (both utilizing SLIPT at node R) under all atmospheric turbulence, jitter, and transmit SNR values. Apart from this, we have also shown the asymptotic outage probability (as derived in (2.34)) in Figs. 2.4(a)-(b). It is clear from Figs. 2.4(a)-(b) that for high transmit SNR values, the resulting analytical asymptotic results follow the exact outage obtained from simulations, which also validates the accuracy of the derived asymptotic expressions.

Observation 2.1: *Table 2.5 shows the theoretical and numerical diversity order of the proposed DF relay-aided SLIPT-enabled mixed FSO-RF communication system for*

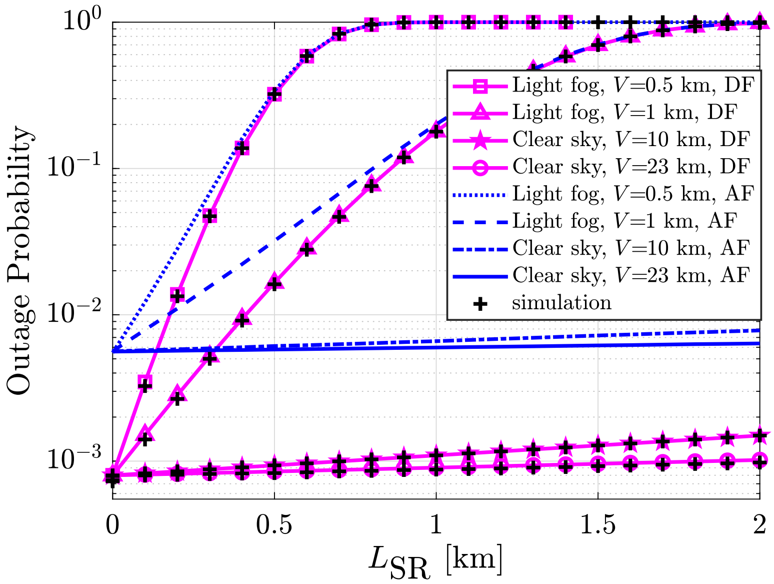

Figure 2.5: Outage probability variations for different link lengths of SR link.

different channel conditions. It can be easily verified from Table 2.5 that the analytically derived diversity order values (utilizing asymptotic outage probability as given in (2.35)*) are very close to the diversity order values obtained numerically for all the channel parameters considered.*

Observation 2.2: *From* (2.24), (2.25) *along with the system parameters given in Table 2.3, it can be observed that* $\bar{\gamma}_D = 187.5\,\bar{\gamma}_R \frac{\rho_{RD}}{\rho_{SR}}$*, where it is assumed that* $\mathcal{B} = 10$ *mA,* $\delta = 1$*, and* $\mathcal{E}\left\{h^2\right\} = 1$*. With this, it is evident that if* $\rho_{SR} = \rho_{RD}$*,* $\bar{\gamma}_D > \bar{\gamma}_R$*, i.e., average SNR of RF hop is higher compared to that of FSO hop. However, to examine the system performance for better SR link scenario, one can have* $\rho_{SR} > 187.5\,\rho_{RD}$*, i.e.,* ρ_{SR} *[dB]>* ρ_{RD} *[dB]+22.73 dB* such that $\bar{\gamma}_{\mathrm{R}} > \bar{\gamma}_{\mathrm{D}}$.

Fig. 2.5 shows the variations of outage probability with respect to SR link length under various weather conditions for both proposed DF relay-aided and corresponding AF-based mixed FSO-RF communication systems with EH relay node. It can be noticed from Fig. 2.5 that under fog conditions, the outage probability increases significantly as compared to the clear sky condition for AF as well DF relay-aided communication systems. For example, to achieve a target outage probability of 0.01 under the light fog conditions, the proposed DF relay-aided system can have a SR link length of approximately 0.41 km and 0.179 km for a visibility of 1 km and 0.5 km, respectively. However, for the same target outage probability performance with light fog, the AF-based counterpart can deploy a relay node R having $L_{\mathrm{SR}} = 0.179$ km and $L_{\mathrm{SR}} = 0.075$ km only with visibility 1 km 0.5 km, respectively. Under clear sky conditions, the outage probability for both AF and DF relaying remains almost constant for all SR link length values studied in the figure. It can

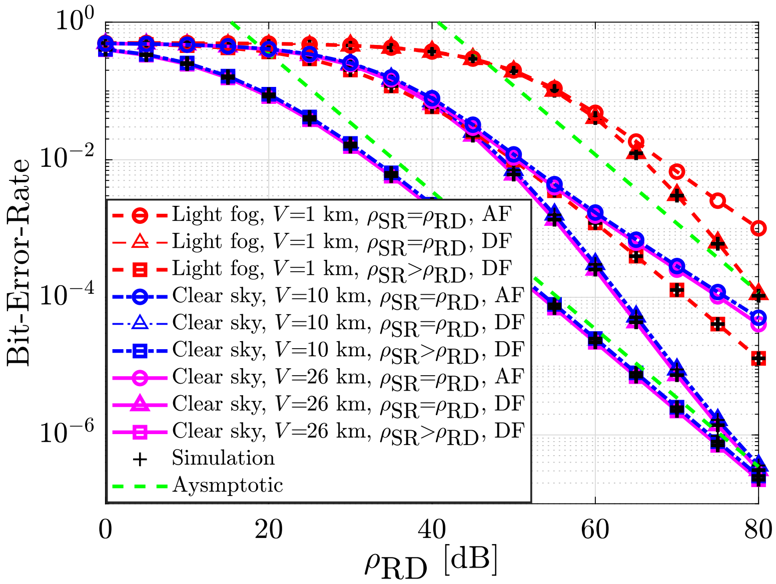

Figure 2.6: Average bit-error-rate variations for varying values of RF hop transmit SNR with $m = 1$, $\alpha = 5.41$, $\beta = 3.78$, and $\xi = 8.8627$.

be also seen from Fig. 2.5 that the outage curve for a DF relaying case with $V = 0.5$ km crosses the outage curves for its AF counterpart with $V = 1$ km, $V = 10$ km, and $V = 23$ km at $L_{\mathrm{SR}} = 0.12$ km, $L_{\mathrm{SR}} = 0.12$ km, and $L_{\mathrm{SR}} = 0.19$ km, respectively. This refers that for very small link lengths, the DF relaying with poor visibility can outperform the AF relaying based system having higher visibility and clear sky conditions.

In Fig. 2.6 and Fig. 2.7, we have shown the average bit-error-rate performance of the proposed DF relay-aided mixed FSO-RF communication systems for Gamma-Gamma turbulence ($\varepsilon = 1$, $g = 0$, and $\Omega' = 1$) under various weather conditions with $m = 1$, $\alpha = 5.41$, $\beta = 3.78$, and $\xi = 8.8627$. For Fig. 2.6, we have considered two different transmit SNR conditions as considered in Fig. 2.4 (i.e., $\rho_{\mathrm{SR}} = \rho_{\mathrm{RD}}$ and $\rho_{\mathrm{SR}} > \rho_{\mathrm{RD}}$). It can be seen from Fig. 2.6 that the average bit-error-rate performance is superior under clear sky conditions as compared to light fog for both the considered transmit SNR scenarios. It should also be noted that improvement in the visibility range with clear sky does not really improve the bit-error-rate performance. Moreover, the average bit-error-rate performance is significantly enhanced for the case when $\rho_{\mathrm{SR}} > \rho_{\mathrm{RD}}$, (i.e., better SR link condition) under all weather conditions. We have also compared the effectiveness of average bit-error-rate of the proposed model with its AF relay based system in Fig. 2.6. It can be clearly deduced from Fig. 2.6 that the proposed communication system completely outperforms the AF counterpart for all channel parameters considered in the figure. The asymptotic bit-error-rate curves, plotted in Fig. 2.6, approach to the actual bit-error-rate values at high transmit SNR, thus validating the accuracy of the derived expressions.

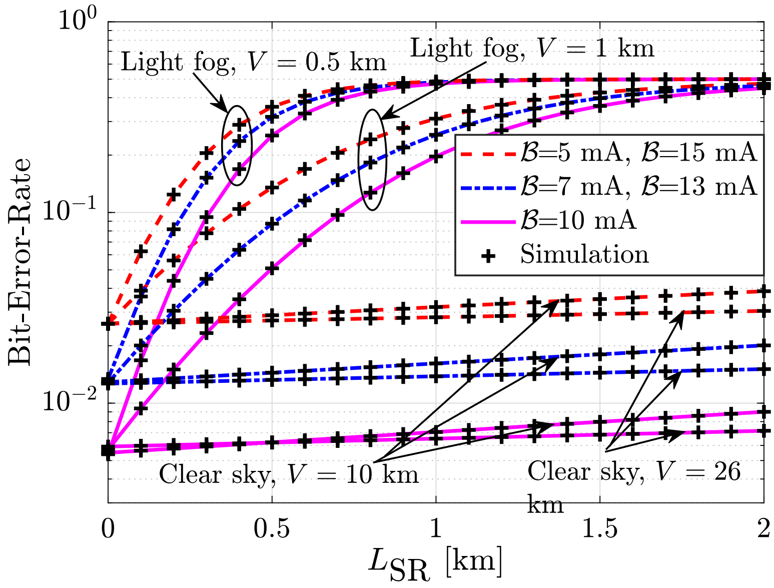

Figure 2.7: Average bit-error-rate versus L_{SR} performance for various weather conditions and different DC bias values with $m = 1$, $\alpha = 5.41$, $\beta = 3.78$, and $\xi = 8.8627$.

Fig. 2.7 depicts the impact of SR link length on the average bit-error-rate performance of the considered system under various weather conditions and DC bias. It can be seen from Fig. 2.7 that the bit-error-rate performance quickly deteriorates with respect to L_{SR} under light fog condition contrary to very slow deterioration under clear sky scenario for all values of DC bias considered in the figure. Further, it has been revealed from Fig. 2.7 that $\mathcal{B} = 10$ mA (i.e., optimum DC bias as discussed in Fig. 2.3) provides the best bit-error-rate performance under all the weather scenarios. It is intuitive to note that an equal amount of positive or negative deviation in DC bias value from $\mathcal{B} = 10$ mA results in equal degradation in the bit-error-rate performance of the considered network for all weather conditions.

Fig. 2.8, shows the average bit-error-rate versus transmit SNR performance comparison for the proposed SLIPT-enabled mixed FSO-RF system with the conventional non-EH based mixed FSO-RF system and an RF EH based mixed FSO-RF system (considering Gamma-Gamma turbulence ($\varepsilon = 1$, $g = 0$, and $\Omega' = 1$) for the FSO link). For all the curves in Fig. 2.8, the total available external power is kept constant for all cases. It can be observed from Fig. 2.8 that the proposed system outperforms the other two systems (considered in this figure) in terms of average bit-error-rate performance. For low jitter deviation, i.e., $\sigma_s = 0.01$, the performance of proposed SLIPT-enabled mixed FSO-RF system improves significantly and the gain in the improvement increases with the increase in SNR. For example, to achieve a target average bit-error-rate performance of 0.003, the proposed SLIPT-based mixed FSO-RF system requires $\rho_{\text{RD}} = 60$ dB, whereas, the non-EH

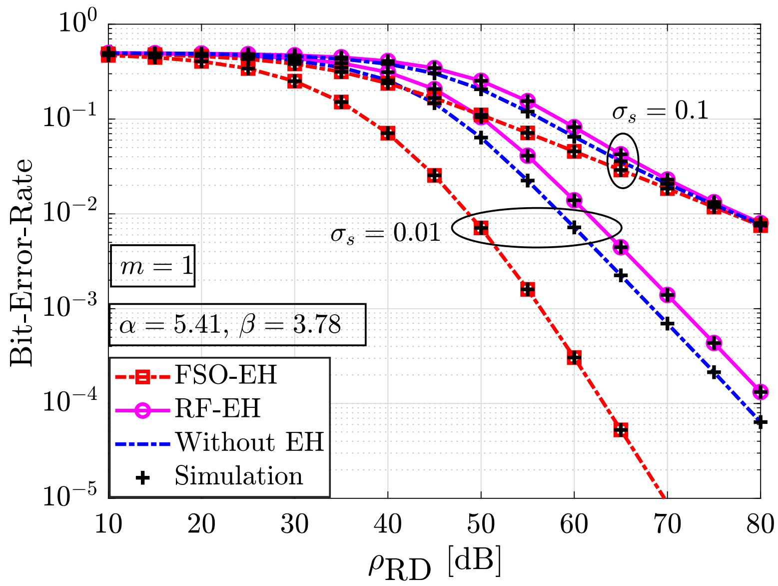

Figure 2.8: Comparison of average bit-error-rate performance for DF relay-aided mixed FSO-RF system utilizing SLIPT (FSO-EH) with conventional non-EH based mixed FSO-RF system (Without SLIPT) as well as RF EH based mixed FSO-RF system (RF-EH).

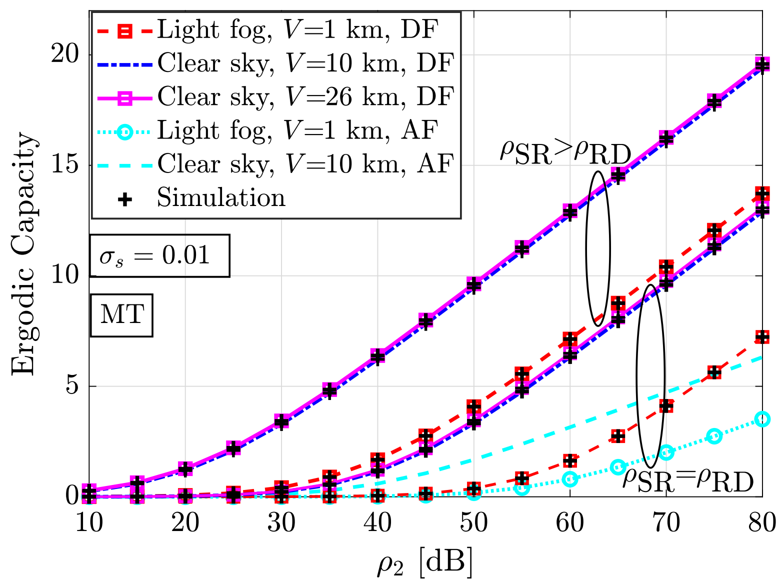

Figure 2.9: Ergodic capacity performance for different weather conditions with moderate turbulence and $\sigma_s = 0.01$.

mixed FSO-RF system and RF EH based mixed FSO-RF require approximately $\rho_{\mathrm{RD}} = 74$ dB and $\rho_{\mathrm{RD}} = 77$ dB, respectively.

In Figs. 2.9 and 2.10, we have presented the capacity behaviour of the proposed SLIPT enabled DF relay-aided mixed FSO-RF communication system for Gamma-Gamma turbulence ($\varepsilon = 1$, $g = 0$, and $\Omega' = 1$) and have compared the same with a similar system employing AF at the relay node. Fig. 2.9 shows the variations of ergodic capacity for varying RF hop transmit SNR under different visibility conditions with moderate

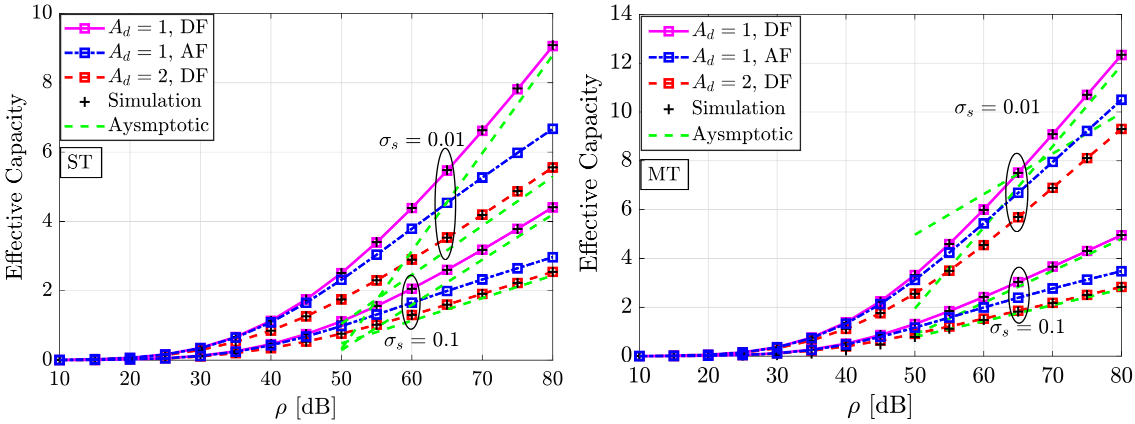

(a) Effective capacity performance for different values of A_d and σ_s with strong turbulence.

(b) Effective capacity performance for different values of A_d and σ_s with moderate turbulence.

Figure 2.10: Capacity with respect to transmit SNR performance comparison of the proposed DF relay-aided mixed FSO-RF communication system and its AF counterpart with $m = 1$.

turbulence and negligible misalignment error (i.e., $\sigma_s = 0.01$). It can be observed from Fig. 2.9 that under clear sky scenario with both $V = 10$ km and $V = 26$ km, the proposed DF relay-aided communication system achieves a desired capacity performance at around 17.5 dB lesser SNR as compared to that obtained under light fog conditions with $V = 1$ km. Furthermore, on comparing the ergodic capacity of the proposed system with AF-based SLIPT-enabled mixed FSO-RF system, we have noticed that the proposed system not only provides high capacity but also offers a rapid rise in the capacity values with transmit SNR ρ_{RD}.

Observation 2.3: *For ergodic capacity performance, the performance gap of approximately 17.5 dB between clear sky and light fog conditions remains unaltered under both transmit SNR conditions, i.e., $\rho_{SR} = \rho_{RD}$ and $\rho_{SR} > \rho_{RD}$. However, the absolute capacity values for $\rho_{SR} > \rho_{RD}$ are sufficiently higher (approximately by 7 b/s/Hz) in comparison to the same for $\rho_{SR} = \rho_{RD}$.*

Next, we have shown the variation of effective capacity of the proposed DF relay-aided mixed FSO-RF system using SLIPT with respect to transmit SNR ($\rho_{\text{SR}} = \rho_{\text{RD}} = \rho$) for strong and moderate turbulence conditions in Fig. 2.10(a) and Fig. 2.10(b), respectively. For both these figures, we have considered different values of A_d and σ_s. We have set path loss coefficient $I_l = 0.933$ with clear sky condition having $V = 10$ km. It can be observed from Figs. 2.10(a) and (b) that for low jitter deviation (i.e., $\sigma_s = 0.01$), the effective capacity increases more rapidly for moderate turbulence as compared to strong turbulence. However, the effective capacity performance for high jitter deviation (i.e., $\sigma_s = 0.1$) is nearly same for both turbulence conditions. Furthermore, it is clear from

Figs. 2.10(a) and (b) that increasing A_d results in decreasing the effective capacity by a significant margin for all atmospheric and misalignment error conditions with the largest reduction under strong turbulence with $\sigma_s = 0.01$. Figs. 2.10(a) and (b) clearly shows that the asymptotic effective capacity curves are sufficiently tight and approaches to exact values at high transmit SNRs. All the analytical results shown in Fig. 2.10 almost overlap to Monte Carlo simulations, indicating the accuracy of the derived expressions.

2.5 Summary

This chapter investigated a DF relay-aided mixed FSO-RF communication network that uses EH at relay node through SLIPT technology. To determine the system's efficiency, analytical expressions have been derived for outage probability, average bit-error-rate, ergodic capacity, and effective capacity. Furthermore, we analyzed the network's high SNR behavior and derived the diversity order analytically. We compared the performance of our system to that of an AF-based SLIPT-enabled mixed FSO-RF communication system to demonstrate the efficiency of the proposed system. It has been shown that the proposed system by using SLIPT gives better performance its AF-based counterpart, conventional mixed FSO-RF system without EH, and RF EH based mixed FSO-RF network. The analytical formulations of the performance metric has also been validated with simulation runs and the numerical results illustrates that the integrating SLIPT with a DF relay-aided mixed FSO-RF communication system is a feasible approach to enhance the energy sustainability.

This chapter employs SLIPT technogly to harvest power at relay node which is further utilized to transmit information over the RF link. However, in some cases the power harvested at relay may not be sufficient due to the poor channel conditions of RF link or unavailability of direct RF link. In such cases, power requirements of RF link can be managed by integration of IRS. The IRS plays a crucial role in enhancing the system performance by enabling more efficient utilization of the available energy. As described in Chapter 1, the deployment of an IRS of suitable size and optimized reflection coefficients over RF hop ensures the sufficient received signal power, especially in the low transmit power conditions. Thus, in the next chapter, we proposed mixed FSO-RF communication system where RF link is assisted by IRS to enhance the link performance. Moreover, we utilized practical on-off control mechanism at IRS that simplifies the problem of designing the IRS passive beamformers.

Chapter 3

IRS-Assisted Mixed FSO-RF Communication System

3.1 Introduction

With the potential of reconfiguring the wireless environment, an IRS has been proven to be a viable solution for the next generation 6G wireless communication networks. In this chapter, we investigate the performance of the novel one-bit control IRS-assisted mixed FSO-RF communication system, where an IRS is utilized over the RF hop to empower the end-to-end system performance. The FSO link is assumed to be affected by path loss, non-zero boresight pointing error, and atmospheric turbulence, which is modeled by generalized $\mathcal{M}$-distribution with non-zero bore-sight pointing error, whereas the multipath fading in RF link is modeled by Nakagami-m distribution. In particular, unified closed-form expressions for the outage probability, bit-error-rate, and ergodic capacity are derived for OHD and IMDD techniques. We also derive the achievable diversity order of the considered IRS-assisted system by obtaining the asymptotic outage and bit-error-rate performance, and it has been shown that the number of elements of one-bit control IRS has an impact on the diversity order. In addition, we derive the asymptotic ergodic capacity of the considered system. The numerical results show that the proposed IRS-assisted system significantly outperforms the conventional mixed FSO-RF system without IRS. Moreover, the impact of the number of reflecting elements, practical reflection amplitude, and controlling mechanism at the IRS is studied on the system performance.

3.1.1 State-of-the-Art

Many researchers have investigated IRS-assisted communication systems over the last few years to enhance spectral efficiency and coverage of wireless communications. The authors in [27] have discussed a few important open research problems of IRS-assisted communications, while index modulation for IRS is proposed in [71] to improve the spectral efficiency at the receiver. The authors in [72] have considered a multi-user multiple-input single-output (MISO) communication system with IRS to propose a beamforming algorithm, while a resource allocation strategy has been discussed in [73] for IRS-assisted MISO wireless communication systems. The authors in [74] considered an IRS-assisted dowlink multi-user communication system based on the practical phase shift model for the IRS and justified its accuracy through extensive experimentation. Furthermore, IRS has been studied along with the MIMO/MISO system to optimize beamforming and maximize the achievable ergodic rate in [75, 76]. In [77, 78], the authors analyzed the performance of an IRS-assisted system with CCI in terms of first-order statistics such as outage and average bit-error-rate. Further, the authors in [79, 80] analyzed the end-to-end SINR statistics of an IRS-assisted multiuser vehicular communication network in the presence of multiple co-channel interferers.

The appealing advantage of IRS to intelligently improve the wireless link can be utilized in various communication networks. The assistance of IRS technology into the mixed FSO-RF communication networks in [81, 82, 83, 84] has enhanced the system's performance to certain extent. A mixed FSO-RF (or RF-FSO) communication system with IRS under Gamma-Gamma atmospheric turbulence and zero-boresight pointing error in the FSO link is analyzed in terms of outage probability and bit-error rate and the impact of using an IRS (along the RF hop) on the system performance is shown [81]. Further, the performance of the IRS-assisted mixed FSO-RF communication system with CCI under Gamma-Gamma atmospheric turbulence and zero-boresight pointing error in the FSO link is analyzed in [82]. In [83], the performance of the IRS-assisted mixed FSO-RF system considering phase error was analyzed in terms of outage and PER under Gamma-Gamma atmospheric turbulence and Rayleigh fading. Recently a mixed RF-FSO network where the IRS link is integrated into the RF link is invested in [84] and the authors derived symbol-error rate (SER) considering Gamma-Gamma distributed FSO link Nakagami-m distributed RF link.

3.1.2 Novelty and Contributions

To the best of our knowledge, there are few works that have utilized IRS with the mixed FSO-RF communication system. Moreover, the analytical expressions obtained by the authors in [81, 83, 84, 82] are approximate and are valid only for a large number of reflecting elements as the channel statistics for the IRS-assisted RF link is based on the

Table 3.1: Comparison of Existing Works IRS-assisted FSO-RF network with the Proposed Work. Here ZB represents the zero boresight.

Ref.	Performance metric	FSO link	RF link	Pointing error	Channel statistics	Phase Error	IRS Control Mechanism
[81]	Outage, bit-error-rate	Gamma-Gamma	Rayleigh	ZB	Approx. (CLT)	No	No
[82]	Outage, bit-error-rate	Gamma-Gamma	Rayleigh	ZB	Approx. (CLT)	No	No
[83]	Outage, PER	Gamma-Gamma	Rayleigh	ZB	Approx. (CLT)	Yes	No
[84]	SER	Gamma-Gamma	Nakagami-m	ZB	Approx.	No	No
Our work	Outage, bit-error-rate, ergodic capacity	Malaga ($\mathcal{M}$)	Nakagami-m	Non-ZB	Exact	Yes	Yes

*The CLT-based channel statistics is valid for large number of IRS elements and cannot be used to analyze the diversity order.

central-limit theorem (CLT). For an IRS with a limited number of elements, the CLT, however, does not deliver correct results and cannot effectively estimate the diversity order. Furthermore, the existing works [81, 84, 82] do not consider phase noise in their analysis. Motivated by the above mentioned facts, we investigate the performance of an IRS-assisted mixed FSO-RF communication system with phase noise to achieve improved system performance and coverage.

The main differences between [81, 83, 82, 84] and our work are listed below:

- We derive the closed-form expressions for unified end-to-end outage probability, bit-error-rate, and ergodic capacity for an IRS-assisted mixed FSO-RF communication system by considering both IMDD and OHD schemes, whereas the analytical expressions in [81, 83, 84, 82] are obtained for IMDD scheme only. Apart from this, we consider generalized $\mathcal{M}$-distribution with non-zero bore-sight pointing error for the FSO link whereas the works in [81, 83, 84, 82] consider system channel models with zero bore-sight pointing errors.

- Contrary to the works in [81, 83, 84, 82], we consider a one-bit controlling mechanism of IRS for passive beamforming optimization which selects some of the reflecting elements in such a way that the SNR at the receiver is maximized.

- The analytical framework considered in [81, 83, 82, 84] is based on some approximations (such as the central limit theorem based or moment generating function based), whereas we derive the exact statistical distributions for the SNR of the IRS-assisted RF hop with phase error.

- To gain additional understanding, we derive asymptotic analysis of outage, average bit-error-rate and ergodic capcity at high SNR. In addition to this, we obtain the

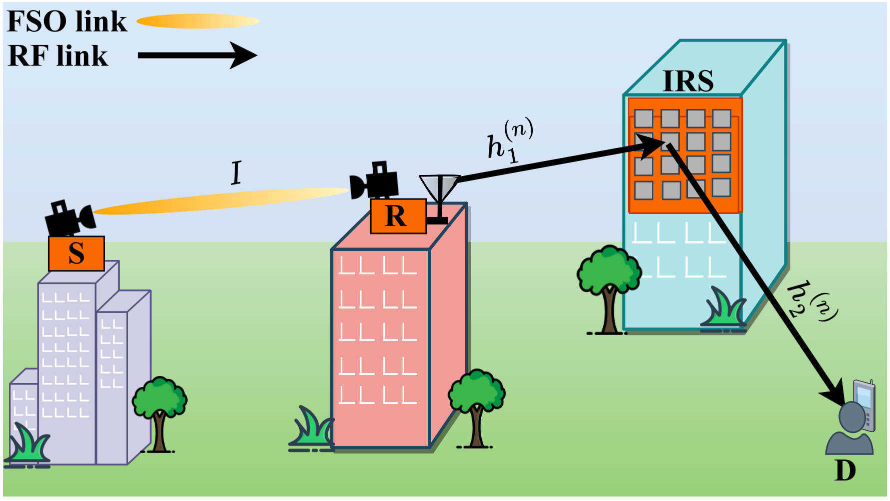

Figure 3.1: System Model for the IRS-assisted mixed FSO-RF communication system.

diversity order analytically using asymptotic expressions of outage and bit-error-rate. It shall be noted that CLT-based channel statistics for composite channel can not be utilized to obtain diversity order.

- It is shown through numerical results that for very few reflecting elements at IRS, the outage performance of the proposed IRS-assisted mixed FSO-RF communication system with one-bit control is superior than the analytical outage performance given in [81], which utilized CLT approximations.

Note: Through the remaining part of the chapter, the IRS-assisted mixed FSO-RF system of [81] will be referred as *existing* FSO-RF system with IRS.

3.2 System Model

Let us consider a dual-hop mixed FSO-RF communication system consisting of an optical source node (S), an RF and FSO compatible relay node (R), and a single IRS assisting the destination node (D) as depicted in Fig. 3.1. It is assumed that the node S and node R are equipped with a single transmit and a single receive apertures, respectively. Further, node R also has one transmit antenna and communicates with the single antenna based RF node D through an IRS equipped with N reflecting elements. Due to large distance and possible blockage, it is assumed that the direct path between R and D is unavailable.

This type of framework is practically possible in many scenarios. For example, a residential society or a commercial zone with many high-rise buildings and towers. Let the optical laser source is mounted on the roof top of a tower. Due to the various other towers available in the society/zone, the direct connection between the laser source and the end user is not possible. Therefore, an intermediate relay node (with FSO-RF compatibility) may be installed at the roof top of another tower (near to the source) so that a direct LoS path is available. Due to large distance between the relay node and the end user, it is difficult for the relay node to have a reliable communication with the end user. Thus, an IRS can be installed on the wall of a tower to assist the communication. Such a system exploits the high data rate advantages of FSO link along with the long distance reliability of the IRS-assisted RF link.

3.2.1 Transmission Scheme

We assume that all the active nodes work in half duplex mode. Therefore, the transmission of data from the node S to the node D takes place in two orthogonal time slots.

First Time Slot (FSO Transmission)

In the first time slot, the optical source node S utilizes SIM scheme [85] to transmit the optical data x_m over the FSO link. The received electrical signal at node R can be written as

$$y_{\mathrm{R}} = \eta R_{\mathrm{P}} A_{\mathrm{P}} I \delta x_m + \eta R_{\mathrm{P}} A_{\mathrm{P}} \mathcal{B} + e_{\mathrm{R}}, \tag{3.1}$$

where η denotes the optical-to-electrical conversion coefficient; P_{S} is the transmit power at optical source S; $I = I_a I_p$ represents the optical channel coefficient with I_a, I_p representing the components due to atmospheric turbulence induced fading and misalignment error, respectively; and $e_{\mathrm{R}} \sim \mathcal{CN}(0, \sigma_{\mathrm{R}}^2)$ denotes the thermal and shot noise at R modelled as complex ZM-AWGN.

Second Time Slot (RF Transmission Through IRS)

In the second time slot, node R first utilizes either OHD or IMDD technique to detect the optical data (s_m) and then re-modulates the detected symbol ($\hat{x}_m$) over an RF carrier. This modulated RF data (x_d) is then transmitted to the IRS which digitally controls the phase of the impinging signal and reflects the same towards node D. It is assumed that the perfect CSI are available at IRS. Thus, the received signal at node D can be written as

$$y_{\mathrm{D}} = \sqrt{P_{\mathrm{R}}} \mathbf{h}_2^{\mathrm{H}} \boldsymbol{\Theta} \mathbf{h}_1 s + e_{\mathrm{D}}, \tag{3.2}$$

where $\mathbf{h}_2$ represents the $N \times 1$ channel vector between node IRS and D, $\mathbf{h}_1$ is the $1 \times N$ channel vector between R and node IRS; $e_D \sim \mathcal{CN}(0, \sigma_{\mathrm{D}}^2)$ denotes the ZM-AWGN at D;

P_{R} is the transmit power at node R, and the matrix $\mathbf{\Theta}$ is an $N \times N$ diagonal matrix containing the reflected amplitude and phase shift values at the IRS defined as $\mathbf{\Theta} = \mathrm{Diag}\left[\varpi_{\mathrm{R}}^{(1)}, \varpi_{\mathrm{R}}^{(2)} \cdots, \varpi_{\mathrm{R}}^{(N)}\right]$, where reflection coefficient of n-th reflecting element is given by $\varpi_{\mathrm{R}}^{(n)} = \left|\varpi_{\mathrm{R}}^{(n)}\right| e^{-\jmath\angle\varpi_{\mathrm{R}}^{(n)}}$ with $\left|\varpi_{\mathrm{R}}^{(n)}\right| \in [0,1]$ and $\angle\varpi_{\mathrm{R}}^{(n)} \in [0, 2\pi]$. The phase-dependent practical reflection amplitude is given by [74, (5)]

$$\left|\varpi_{\mathrm{R}}^{(n)}\right| = (1 - \varpi_{\min}) \left(\frac{\sin\left(\angle\varpi_{\mathrm{R}}^{(n)} - \bar{\theta}\right) + 1}{2}\right)^{\P} + \varpi_{\min}, \tag{3.3}$$

$\varpi_{min} \geq 0$ is the minimum amplitude of reflection, $\bar{\theta} \geq 0$ is the horizontal distance between $-\pi/2$ and ϖ_{min}, and $\P \geq 0$ controls the steepness of the function curve. The ideal reflection conditions are represented by $\varpi_{min} = 1$ (or $\P = 0$). It is assumed that the phase shift of each reflection coefficient takes a discrete value from a set $\mathbb{S} = \{0, \Delta\theta, \cdots, (Q-1)\Delta\theta\}$, where $\Delta\theta = 2\pi/Q$, where Q is the number of quantization levels.

3.2.2 Channel Model

The statistical models of all the channel coefficients under consideration are given as hereunder.

Optical Channel Modelling

Considering $\mathcal{M}$-distribution for atmospheric turbulence induced fading I_a with non-zero bore-sight misalignment error model for I_p, the composite PDF of $I = I_a I_p$ is given by

$$f_I(I) = \frac{\xi^2 \mathcal{A}}{4I} \sum_{r=1}^{\infty} s_r \left(\frac{\alpha}{g}\right)^{-\frac{\alpha+r}{2}} G_{1,3}^{3,0}\left(\frac{\alpha I}{g A_o \varrho} \middle| \begin{matrix} \xi^2+1 \\ \xi^2, \alpha, r \end{matrix}\right), \quad I > 0, \tag{3.4}$$

where $G_{c,d}^{a,b}\left(\cdot \middle| \vdots\right)$ is the Meijer's-G function [63]. Depending upon the type of detection technique employed at node R, the instantaneous received SNR of FSO hop can be written as

$$\gamma_{\mathrm{R}}^{(q)} = \frac{(\eta R_{\mathrm{P}} A_{\mathrm{P}} \delta)^q}{\sigma_{\mathrm{R}}^2} I^q, \tag{3.5}$$

where $q = 1, 2$ correspond to the OHD and IMDD techniques, respectively. Following the discussion in [44, 86], the unified PDF of $\gamma_{\mathrm{R}}^{(q)}$ can be written as

$$f_{\gamma_{\mathrm{R}}^{(q)}}(\gamma) = \frac{\gamma_q^{-1} \xi^2 \mathcal{A}}{4q} \sum_{r=1}^{\infty} s_{\mathrm{R}} \left(\frac{\alpha}{g}\right)^{-\frac{\alpha+r}{2}} G_{1,3}^{3,0}\left(\Psi\left(\frac{\gamma}{\varkappa_{\mathrm{FSO}}^{(q)}}\right)^{\frac{1}{q}} \middle| \begin{matrix} \xi^2+1 \\ \xi^2, \alpha, r \end{matrix}\right), \tag{3.6}$$

where $\Psi = \xi^2\alpha\beta(g+\Omega')/[\left(\xi^2+1\right)(g\beta+\Omega')]$; α, g, β, and s_r are defined under (2.5) and discussion thereafter. The parameter $\varkappa_{\mathrm{FSO}}^{(q)}$ denotes the average electrical SNR which can be defined for OHD and IMDD as

$$\varkappa_{\mathrm{FSO}}^{(1)} = \varkappa_{\mathrm{FSO}}^{\mathrm{OHD}} = \bar{\gamma}_{\mathrm{R}}^{(1)} \tag{3.7}$$

and

$$\varkappa_{\mathrm{FSO}}^{(2)} = \varkappa_{\mathrm{FSO}}^{\mathrm{IMDD}} = \frac{\bar{\gamma}_{\mathrm{R}}^{(2)} A_o^2 \varrho^2 \xi^4 g^2}{(\xi^2+1)^2} \left(\frac{g\beta}{g\beta+\Omega'}\right)^{2\beta} {}_2F_1^2\left(2,\beta;1;\frac{\Omega'}{g\beta+\Omega'}\right), \tag{3.8}$$

respectively, where $\bar{\gamma}_{\mathrm{R}}^{(q)} = \frac{(\eta R_{\mathrm{P}} A_{\mathrm{P}} \delta)^q}{\sigma_{\mathrm{R}}^2}$, $q = 1, 2$, is the corresponding average SNR for the OHD and IMDD techniques, respectively; ${}_2F_1(\cdot;\cdot;\cdot)$ is the Gauss hyper-geometric function defined in [63, (07.23.02.0001.01)].

RF Channel Modelling

Let the RF channel coefficients between R to the n-th IRS element and between n-th IRS element to D are denoted as $h_1^{(n)} = |h_1^{(n)}|e^{\jmath\angle h_1^{(n)}} \in \mathbf{h}_1$ and $h_2^{(n)} = |h_2^{(n)}|e^{\jmath\angle h_2^{(n)}} \in \mathbf{h}_2^{\mathrm{H}}$. The coefficients $|h_1^{(n)}|$ and $|h_2^{(n)}|$ are assumed to be independent and identically distributed (IID) following Nakagami-m distributed with parameters $(m_2, \Omega_2/m_2)$ and $(m_1, \Omega_1/m_1)$, respectively. Following (3.2), the transmit SNR of RD link can be defined as $\rho_{\mathrm{RD}} = \frac{P_{\mathrm{R}}}{\sigma_{\mathrm{D}}^2}$. Assuming the unity signal power, the instantaneously received SNR at node D will be given by

$$\gamma_{\mathrm{D}} = \rho_{\mathrm{RD}} \left|\mathbf{h}_2^{\mathrm{H}} \boldsymbol{\Theta} \mathbf{h}_1\right|^2 = \rho_{\mathrm{RD}} \left|\boldsymbol{\theta}^{\mathrm{H}} \mathbf{G} \mathbf{h}_1\right|^2, \tag{3.9}$$

where the second line is written by using some vector algebra as $\boldsymbol{\theta}^{\mathrm{H}}$ is $1 \times N$ vector containing main diagonal elements of matrix $\boldsymbol{\Theta}$ and $\mathbf{G}$ is an $N \times N$ diagonal matrix with diagonal elements obtained from $\mathbf{h}_2^{\mathrm{H}}$.

3.3 SNR Characterization

In this Section, we present the end-to-end outage analysis of the considered IRS-assisted FSO-RF communication system. However, it should be noted that the performance of an IRS-assisted system depends on the choice and control of the IRS reflection matrix $\boldsymbol{\Theta}$. Depending upon the complexity of the design, there are different controlling mechanisms that are available in the literature for IRS [27]-[87] as discussed below.

3.3.1 Design and Control of IRS

The ideal design for an IRS needs the infinite resolution reflecting elements which refers to the hardware support for an arbitrary choice of the reflection coefficients. A typical example for an ideal design may utilize Zero Forcing (ZF) mechanism at IRS [87]. But, it is not practically feasible due to the limitations of the circuitry involved. Then, one has to go for a finite resolution based design. A typical finite resolution design is proposed in [88] by utilizing lens antenna arrays for millimeter wave communication system, where a discrete Fourier transform (DFT) based design is used to maximize the SNR. The discrete values of phase shifts can be realized by finite-resolution phase shifters.

Alternatively, a cost effective solution to design the finite resolution based reflecting surface is proposed in [87], known as one-bit control or on-off control. The one-bit control is a near-optimal and scalable solution (especially for large number of reflecting element) for configuring and controlling of an IRS. In this scheme, it is considered that each element of vector $\boldsymbol{\theta}^{\mathrm{H}}$ can will either be 0 (OFF) or can take a non-zero finite value (ON).

Let the total number of reflecting elements at IRS is factored as $N = MD$, such that M and D are positive integers. Here, D is the number of active elements and M signifies the number of disjoint combinations with D active elements, then we define an $M \times N$ matrix, $\mathbf{F}$ as

$$\mathbf{F} = \begin{bmatrix} \mathbf{u}_1 & \mathbf{0} & \mathbf{0} & \cdots & \mathbf{0} \\ \mathbf{0} & \mathbf{u}_2 & \mathbf{0} & \cdots & \mathbf{0} \\ \mathbf{0} & \mathbf{0} & \mathbf{u}_3 & \cdots & \mathbf{0} \\ \vdots & \vdots & \vdots & \ddots & \vdots \\ \mathbf{0} & \mathbf{0} & \mathbf{0} & \cdots & \mathbf{u}_M \end{bmatrix} \tag{3.10}$$

where $\mathbf{u}_\ell = \left\{ \frac{|\varpi_{\mathrm{R}}^{(n)}|}{\sqrt{\bar{\varpi}}} e^{-\jmath \angle \varpi_{\mathrm{R}}^{(n)}} \right\}_{n=(\ell-1)D+1}^{\ell D}$ is $1 \times D$ vector that contains practical reflection coefficients of D active elements with $\bar{\varpi}_{\mathrm{R}} = \sum\limits_{n=(\ell-1)D+1}^{D\ell} |\varpi_{\mathrm{R}}^{(n)}|^2$ and $\mathbf{0}$ is the $1 \times D$ vector containing all zeros. It should be noted that $\mathbf{F}$ contains orthonormal row vectors. Let $\mathbf{f}_\ell$, $\ell = 1, 2, \ldots, M$, denotes the ℓ-th row vector of $\mathbf{F}$, then we choose $\boldsymbol{\theta}^{\mathrm{H}} = \mathbf{f}_\ell$, in a way that maximizes the SNR in (3.9). Therefore, the optimum SNR of the RF hop will be given as

$$\gamma_{\mathrm{D}}^{\mathrm{opt}} \triangleq \max\left[\gamma_{\mathrm{D}}(\mathbf{f}_1), \gamma_{\mathrm{D}}(\mathbf{f}_2), \ldots, \gamma_{\mathrm{D}}(\mathbf{f}_M)\right], \quad \text{where,} \tag{3.11}$$

$$\gamma_{\mathrm{D}}(\mathbf{f}_\ell) = \rho_{\mathrm{RD}} |\mathbf{f}_\ell \mathbf{G} \mathbf{h}|^2. \tag{3.12}$$

It is intuitive to note that random variables (RVs) $\gamma_{\mathrm{D}}(\mathbf{f}_1), \gamma_{\mathrm{D}}(\mathbf{f}_2), \ldots, \gamma_{\mathrm{D}}(\mathbf{f}_M)$ are independent to each other. The structure of ℓ-th row vector of $\mathbf{F}$ can be defined as

$$\mathbf{f}_\ell = [\mathbf{0}_{1\times(\ell-1)D}, \mathbf{u}_\ell, \mathbf{0}_{1\times(M-\ell)D}], \tag{3.13}$$

where $\mathbf{0}_{1\times M}$ represents an all zero row vector of size M, we can write $\gamma_{\mathrm{D}}(\mathbf{f}_\ell)$

$$\gamma_{\mathrm{D}}(\mathbf{f}_\ell) = \rho_{\mathrm{RD}} \left| \frac{1}{\sqrt{\bar{\varpi}_{\mathrm{R}}}} \underbrace{\sum_{n=(\ell-1)D+1}^{\ell D} |\varpi_{\mathrm{R}}^{(n)}| H^{(n)} e^{j\psi^{(n)}}}_{D \text{ Terms}} \right|^2, \tag{3.14}$$

where $H^{(n)} = \left|h_1^{(n)}\right| \left|h_2^{(n)}\right|$ and $\psi^{(n)} = \angle h_1^{(n)} + \angle h_2^{(n)} - \angle \varpi_{\mathrm{R}}^{(n)}$ is the random phase error. In order to maximize the received SNR, IRS set the phase $\angle \varpi_{\mathrm{R}}^{(n)}$ to cancel phase introduced by channel coefficients $h_1^{(n)}$ and $h_2^{(n)}$ (i.e., $\psi^{(n)} = 0$). However, practically the residual phase error exist at IRS (i.e., $\psi^{(n)} \neq 0$).

3.3.2 End-to-End SNR Statistics

The end-to-end SNR of the considered mixed FSO-RF system with IRS under decode and forward relaying is given by $\Gamma_{\mathrm{E}} = \min\left(\gamma_{\mathrm{R}}^{(q)}, \gamma_{\mathrm{D}}^{\mathrm{opt}}\right)$. As a result, the CDF is given by

$$\mathcal{F}_{\Gamma_{\mathrm{E}}}(\gamma) = \Pr\left\{\min\left(\gamma_{\mathrm{R}}^{(q)}, \gamma_{\mathrm{D}}^{\mathrm{opt}}\right) < \gamma\right\}, \tag{3.15}$$

where $\mathcal{F}_X(\cdot)$ denotes the cumulative distribution function (CDF) of RV X; $\Pr\{\cdot\}$ represents the probability of an event. Using the simple RV transformation [89], the CDF of end-to-end SNR in (3.15) can be further simplified as,

$$\mathcal{F}_{\Gamma_{\mathrm{E}}}(\gamma) = \mathcal{F}_{\gamma_{\mathrm{R}}^{(q)}}(\gamma) + \mathcal{F}_{\gamma_{\mathrm{D}}^{\mathrm{opt}}}(\gamma) - \mathcal{F}_{\gamma_{\mathrm{R}}^{(q)}}(\gamma)\mathcal{F}_{\gamma_{\mathrm{D}}^{\mathrm{opt}}}(\gamma), \tag{3.16}$$

Following (3.11), the CDF of $\gamma_{\mathrm{D}}^{\mathrm{opt}}$ can be evaluated as

$$\mathcal{F}_{\gamma_{\mathrm{D}}^{\mathrm{opt}}}(\gamma) = \prod_{\ell=1}^{M} \mathcal{F}_{\gamma_{\mathrm{D}}(\mathbf{f}_\ell)}(\gamma). \tag{3.17}$$

Lemma 3.1: *For any given $\boldsymbol{\theta}^{\mathrm{H}} = \mathbf{f}_\ell$, the CDF of SNR for IRS-assisted RF hop (defined* *in* (3.12)*) in the presence of phase error can be evaluated as*

$$\mathcal{F}_{\gamma_{\mathrm{D}}(\mathbf{f}_\ell)}(\gamma)=\sum_{u_0=0}^{m_1-1}\cdots\sum_{u_{D-1}=0}^{m_1-1}\prod_{j=0}^{D-1}Z_j\left[1-\frac{2\left(\frac{Dm_1m_2}{\Omega_1\Omega_2\rho_{\mathrm{RD}}}\right)^{\frac{\nu}{2}}}{(\nu-1)!}\gamma^{\frac{\nu}{2}}K_\nu\left(2\sqrt{\frac{Dm_1m_2}{\Omega_1\Omega_2\rho_{\mathrm{RD}}}\gamma}\right)\right]. \tag{3.18}$$

where $\nu = D(m_1+m_2-1)-\sum_{j=0}^{D-1}u_j$ aand $Z_j = \frac{(m_2)_{m_1-1-u_j}(1-m_2)_{u_j}}{(m_1-1-u_j)!u_j!}$.
Proof: See Appendix A.2.1 for the proof.

It can be noticed from the discussion in Appendix that $\mathcal{E}\left\{|\mathbf{f}_\ell\mathbf{Gh}|^2\right\} = \Omega_1\Omega_2$. Hence, we have $\mathcal{E}\{\gamma_{\mathrm{D}}(\mathbf{f}_\ell)\} = \Omega_1\Omega_2\rho_{\mathrm{RD}}$ for all ℓ. With this observation, we can obtain the CDF of SNR of IRS-assisted RF hop by substituting (3.18) in (3.17) as

$$\mathcal{F}_{\gamma_{\mathrm{D}}^{\mathrm{opt}}}(\gamma)=\left\{\sum_{u_0=0}^{m_1-1}\cdots\sum_{u_{D-1}=0}^{m_1-1}\prod_{j=0}^{D-1}Z_j\left[1-\frac{2\left(\frac{Dm_1m_2}{\Omega_1\Omega_2\rho_{\mathrm{RD}}}\right)^{\frac{\nu}{2}}}{(\nu-1)!}\gamma^{\frac{\nu}{2}}K_\nu\left(2\sqrt{\frac{Dm_1m_2}{\Omega_1\Omega_2\rho_{\mathrm{RD}}}\gamma}\right)\right]\right\}^M. \tag{3.19}$$

Further, the unified CDF of $\gamma_{\mathrm{R}}^{(q)}$ can be obtained by using (3.6) in $\mathcal{F}_{\gamma_{\mathrm{R}}^{(q)}}(\gamma)=\int_0^\gamma f_{\gamma_{\mathrm{R}}^{(q)}}(z)\,dz$, followed by the use of [63, (07.34.21.0084.01)] as

$$\mathcal{F}_{\gamma_{\mathrm{R}}^{(q)}}(\gamma)=\frac{\xi^2\mathcal{A}}{4(2\pi)^{q-1}}\sum_{r=1}^{\infty}s_r\left(\frac{\alpha}{g}\right)^{-\frac{\alpha+r}{2}}q^{\alpha+r-2}G_{q+1,3q+1}^{3q,1}\left(\frac{\Psi^q}{q^{2q}\varkappa_{\mathrm{FSO}}^{(q)}}\gamma\middle|\begin{matrix}1,\mathbb{A}_q\\ \mathbb{B}_q,0\end{matrix}\right), \tag{3.20}$$

where $\mathbb{A}_q=\Delta(q,\xi^2+1)$, $\mathbb{B}_q=\Delta(q,\xi^2),\Delta(q,\alpha),\Delta(q,r)$ and $\Delta(a,b)=b/a,\ldots,(b+a-1)/a$.

3.4 Performance Evaluation

This Section presents the performance evaluation of considered IRS-assisted one-bit control mixed FSO-RF network. Utilizing end-to-end SNR statistics, we derive analytical expressions of outage probability, bit-error-rate, and ergodic capacity. In addition, we perform high SNR analysis of the considered system.

3.4.1 End-to-End Outage Analysis

The end-to-end outage event of the considered mixed FSO-RF system with IRS will occur iff the minimum[1] of instantaneous SNRs over two hops falls below a certain threshold (equivalently, the required QoS or the targeted data rate). Hence, the end-to-end outage

[1]Due to the assumption of decode-and-forward strategy at the relay node

probability of an IRS-assisted mixed FSO-RF communication system is written as,

$$\mathcal{P}_{\text{out}} = \Pr\{\Gamma_{\text{E}} < \gamma_{\text{Th}}\} = \mathcal{F}_{\Gamma_{\text{E}}}(\gamma_{\text{Th}}), \tag{3.21}$$

where $\gamma_{\text{Th}} = 2^{\bar{\mathcal{R}}} - 1$ is the threshold SNR with $\bar{\mathcal{R}}$ being the targeted data rate. The end-to-end outage probability for the considered IRS-assisted mixed FSO-RF system employing one-bit control at IRS can thus be evaluated by using $\gamma = \gamma_{\text{Th}}$ in (3.16).

Remark 3.1: *Through numerical results, it is shown that the one-bit control at IRS with $M = N$ achieves the best end-to-end outage performance under given system parameters. Also, it is intuitive from* (3.32) *as the minimum possible value of exponent M (i.e., $M = 1$) will achieve the maximum possible outage probability over RF hop. It is interesting to visualize the physical significance of the above fact in the context of IRS control.*

- *For $M = N$ and $D = 1$, one-bit control at IRS maximizes the RF hop SNR by considering single reflecting element at a time.*
- *However, for $M = 1$ and $D = N$, one-bit controlling provides the worst end-to-end performance of mixed FSO-RF communication system allowing the reflection from all IRS elements.*

3.4.2 Diversity Order Analysis

In order to get an insight of the end-to-end outage performance, we present the asymptotic analysis for high average SNR conditions. This asymptotic analysis also helps in developing the diversity order of the considered IRS-assisted mixed FSO-RF communication system.

Lemma 3.2: *For high average SNR of IRS-assisted RF hop, i.e., $\rho_{RD} \to \infty$, and a known reflection vector $\boldsymbol{\theta}^{\text{H}} = \mathbf{f}_{\ell}$, the CDF given in* (3.18) *can be approximated as $\lim\limits_{\rho_{RD}\to\infty} \mathcal{F}_{\gamma_D(\mathbf{f}_\ell)}(\gamma) = \tilde{\mathcal{F}}_{\gamma_D(\mathbf{f}_\ell)}(\gamma)$, where*

$$\tilde{\mathcal{F}}_{\gamma_D(\mathbf{f}_\ell)}(\gamma) = \begin{cases} \sum\limits_{u_0=0}^{m_1-1} \cdots \sum\limits_{u_{D-1}=0}^{m_1-1} \prod\limits_{j=0}^{D-1} Z_j \dfrac{D m_1 m_2}{\Omega_1 \Omega_2 \rho_{RD}} \gamma \ln\left(\dfrac{\rho_{RD}}{\Xi\gamma}\right), & For\, \nu = 1, \\ \sum\limits_{u_0=0}^{m_1-1} \cdots \sum\limits_{u_{D-1}=0}^{m_1-1} \prod\limits_{j=0}^{D-1} Z_j \dfrac{D m_1 m_2}{\Omega_1 \Omega_2 \rho_{RD}} \left(\dfrac{1}{\nu - 1}\right), & For\, \nu > 1. \end{cases} \tag{3.22}$$

Proof: See Appendix A.2.2 for the proof.

Corollary 3.1: *By applying the L'Hôpital's rule in* (3.22)*, we can show that for all values* *of* D *with* $\rho_{RD} \to \infty$,

$$\tilde{\mathcal{F}}_{\gamma_{D(\mathbf{f}_\ell)}}(\gamma) \propto \frac{1}{\rho_{RD}}. \tag{3.23}$$

Following Lemma 3.2, we can write the asymptotic outage probability of IRS-assisted RF hop by applying high SNR conditions in (3.17) *as*

$$\lim_{\rho_{RD}\to\infty} \mathcal{F}_{\gamma_D}(\gamma_{Th}) = \tilde{\mathcal{F}}_{\gamma_D}(\gamma_{Th}) = \prod_{\ell=1}^{M} \tilde{\mathcal{F}}_{\gamma_{D(\mathbf{f}_\ell)}}(\gamma_{Th}), \tag{3.24}$$

where $\tilde{\mathcal{F}}_{\gamma_{D(\mathbf{f}_\ell)}}(\gamma_{Th})$ *is obtained by substituting* $\gamma = \gamma_{Th}$ *in* (3.22)*.*

Remark 3.2: *With the help of the result in Corollary 3.1, it can be deduced from* (3.24) *that for high SNR conditions, the outage probability of IRS-assisted RF hop utilizing one-bit control achieves a diversity order of* M*, i.e.,*

$$\tilde{\mathcal{F}}_{\gamma_D}(\gamma_{Th}) \propto \frac{1}{\rho_R^M}. \tag{3.25}$$

Now, utilizing the asymptotic expression of Meijer's-G function from [63, (07.34.06.0006.01)] in (3.20), we can find the unified asymptotic outage probability of FSO hop for high average SNR conditions (i.e., $\bar{\gamma}_{\mathrm{R}}^{(q)} \to \infty$ or equivalently $\varkappa_{\mathrm{FSO}}^{(q)} \to \infty$) as

$$\begin{aligned}\tilde{\mathcal{F}}_{\gamma_{\mathrm{R}}^{(q)}}(\gamma_{\mathrm{Th}}) = & \frac{\xi^2 \mathcal{A}}{4(2\pi)^{q-1}} \sum_{r=1}^{\infty} s_r \left(\frac{\alpha}{g}\right)^{-\frac{\alpha+r}{2}} q^{\alpha+r-2} \\ & \times \sum_{m=1}^{3q} \left(\left(\frac{\Psi}{q^2}\right)^q \frac{\gamma_{\mathrm{Th}}}{\varkappa_{\mathrm{FSO}}^{(q)}}\right)^{b_{q,m}} \frac{\Gamma(b_{q,m}) \prod_{\substack{n=1\\n\neq m}}^{3q} \Gamma(b_{q,n} - b_{q,m})}{\Gamma(1+b_{q,m}) \prod_{n=2}^{q+1} \Gamma(a_{q,n} - b_{q,m})},\end{aligned} \tag{3.26}$$

where $a_{q,n}$ denotes the n-th element of $\mathbb{A}_q' = \{1, \mathbb{A}_q\}$ and $b_{q,m}$ denotes the m-th element of $\mathbb{B}_q$.

Remark 3.3: *It can be easily noticed from* (3.26) *that for high SNR conditions, the outage probability of FSO hop achieves a diversity order of* $\min\{\mathbb{B}_q\}$*, i.e.,*

$$\tilde{\mathcal{F}}_{\gamma_R^{(q)}}(\gamma_{Th}) \propto \left(\frac{1}{\bar{\gamma}_R^{(q)}}\right)^{\min\{\mathbb{B}_q\}}. \tag{3.27}$$

If we assume high SNR conditions over both the FSO and the RF hop, i.e., $\bar{\gamma}_{\mathrm{R}}^{(q)} \to \infty$ and $\rho_{\mathrm{RD}} \to \infty$, then the asymptotic end-to-end outage probability of the considered IRS-assisted mixed FSO-RF communication system can be evaluated from (3.16) as

$$\tilde{\mathcal{P}}_{\mathrm{out}} = \tilde{\mathcal{F}}_{\gamma_{\mathrm{R}}^{(q)}}(\gamma_{\mathrm{Th}}) + \tilde{\mathcal{F}}_{\gamma_{\mathrm{D}}^{\mathrm{opt}}}(\gamma_{\mathrm{Th}}) - \tilde{\mathcal{F}}_{\gamma_{\mathrm{R}}^{(q)}}(\gamma_{\mathrm{Th}}) \tilde{\mathcal{F}}_{\gamma_{\mathrm{D}}^{\mathrm{opt}}}(\gamma_{\mathrm{Th}}), \tag{3.28}$$

where $\tilde{\mathcal{F}}_{\gamma_{\mathrm{R}}^{(q)}}(\gamma_{\mathrm{Th}})$ and $\tilde{\mathcal{F}}_{\gamma_{\mathrm{D}}^{\mathrm{opt}}}(\gamma_{\mathrm{Th}})$ are obtained from (3.24) and (3.26), respectively.

Remark 3.4: *Using (3.25) and (3.27) in (3.28), it can be revealed that for $\bar{\gamma}_R^{(q)} = \rho_{RD} = \bar{\gamma}$(say), the end-to-end outage probability of considered IRS-assisted mixed FSO-RF communication system behaves as $\tilde{\mathcal{P}}_{out} \propto \bar{\gamma}^{-\mathcal{G}_d}$ with $\mathcal{G}_d = \min\{M, \mathbb{B}_q\}$ is the achievable diversity order. For OHD scheme ($q = 1$) employed at node R, the diversity order is $\mathcal{G}_d = \min\{M, \xi^2, \alpha, r\}$, whereas for $q = 2$, i.e., IMDD scheme, we get $\mathcal{G}_d = \min\{M, \xi^2/2, \alpha/2, r/2\}$. This is why, for large number of reflecting elements at IRS, the performance is mainly determined by the FSO link parameters.*

3.4.3 Bit-Error-Rate Analysis

The bit-error-rate for the proposed IRS-assisted mixed FSO-RF system can be obtained as [84]

$$\mathcal{P}_{\mathrm{e}} = \mathcal{P}_{\mathrm{FSO}} + \mathcal{P}_{\mathrm{RF}} - 2\mathcal{P}_{\mathrm{FSO}}\mathcal{P}_{\mathrm{RF}} \tag{3.29}$$

where $\mathcal{P}_{\mathrm{FSO}}$ and $\mathcal{P}_{\mathrm{RF}}$ are the bit-error-rates of FSO and RF links, respectively. The average bit-error-rate $\mathcal{P}_i$ of i-th hop, $i \in \{\mathrm{FSO}, \mathrm{RF}\}$ considering BPSK modulation is given by

$$\mathcal{P}_i = \frac{1}{2\sqrt{\pi}} \int_0^\infty \frac{\exp(-\gamma)}{\sqrt{\gamma}} \mathcal{F}_{\gamma_i}(\gamma) d\gamma. \tag{3.30}$$

The closed-form analytical expression of bit-error-rate of the FSO link $\mathcal{P}_{\mathrm{FSO}}$ can be obtained by substituting $\mathcal{F}_{\gamma_{\mathrm{R}}^{(q)}}(\gamma)$ from (3.20) in (3.30) and utilizing [63, (07.34.21.0088.01)]

$$\mathcal{P}_{\mathrm{FSO}} = \frac{\xi^2 \mathcal{A}}{2^{q+2}(\pi)^{q-1/2}} \sum_{r=1}^{\infty} s_r \left(\frac{\alpha}{g}\right)^{-\frac{\alpha+r}{2}} q^{\alpha+r-2} G_{q+2,3q+1}^{3q,2}\left(\frac{\Psi^q}{q^{2q}\varkappa_{\mathrm{FSO}}^{(q)}} \middle| \begin{matrix} 0.5, 1, \mathbb{A}_q \\ \mathbb{B}_q, 0 \end{matrix} \right). \tag{3.31}$$

Further, bit-error-rate of IRS-assisted RF hop $\mathcal{P}_{\mathrm{RF}}$ can be obtained by substituting $\mathcal{F}_{\gamma_{\mathrm{D}}^{\mathrm{opt}}}(\gamma)$ from (3.19) in (3.30) as

$$\begin{aligned} \mathcal{P}_{\mathrm{RF}} = \frac{1}{2\sqrt{\pi}} \int_0^\infty \frac{\exp(-\gamma)}{\sqrt{\gamma}} \Bigg\{ \sum_{u_0=0}^{m_1-1} \cdots \sum_{u_{D-1}=0}^{m_1-1} \prod_{j=0}^{D-1} Z_j \Bigg[1 - \frac{2\left(\frac{D m_1 m_2}{\Omega_1 \Omega_2 \rho_{\mathrm{RD}}}\right)^{\frac{\nu}{2}}}{(\nu-1)!} \\ \times \gamma^{\frac{\nu}{2}} K_\nu \left(2\sqrt{\frac{D m_1 m_2}{\Omega_1 \Omega_2 \rho_{\mathrm{RD}}} \gamma} \right) \Bigg] \Bigg\}^M d\gamma. \end{aligned} \tag{3.32}$$

To the author's knowledge the above integral cannot be solved analytically in a closed form. Hence, we derive the asymptotic expression of bit-error-rate at high SNR conditions ($\bar{\gamma}_{\mathrm{R}}^{(q)} \to \infty$ and $\rho_{\mathrm{RD}} \to \infty$) as $\lim_{\bar{\gamma}\to\infty} \mathcal{P}_{\mathrm{e}} = \tilde{\mathcal{P}}_{\mathrm{e}}$. The approximate expressions are more tractable and computationally efficient.

Lemma 3.3: *Assuming high SNR conditions over both the FSO and the RF hop, i.e., $\bar{\gamma}_R^{(q)} \to \infty$ and $\rho_{RD} \to \infty$, then the asymptotic high average SNR analysis of bit-error-rate given in* (3.29) *can be approximated as*

$$\tilde{\mathcal{P}}_e = \tilde{\mathcal{P}}_{FSO} + \tilde{\mathcal{P}}_{RF} - 2\tilde{\mathcal{P}}_{FSO}\tilde{\mathcal{P}}_{RF} \tag{3.33}$$

where $\tilde{\mathcal{P}}_{FSO} = \lim_{\rho_{SR}\to\infty} \mathcal{P}_{FSO}$ *and* $\tilde{\mathcal{P}}_{RF} = \lim_{\rho_{RD}\to\infty} \mathcal{P}_{RF}$ *are given as*

$$\begin{aligned}\tilde{\mathcal{P}}_{FSO} =& \lim_{\bar{\gamma}_R^{(q)}\to\infty} \mathcal{P}_{FSO} = \frac{\xi^2\mathcal{A}}{2^{q+2}(\pi)^{q-1/2}} \sum_{r=1}^{\infty} s_r \left(\frac{\alpha}{g}\right)^{-\frac{\alpha+r}{2}} q^{\alpha+r-2} \\ &\times \sum_{m=1}^{3q} \left(\left(\frac{\Psi}{q^2}\right)^q \frac{1}{\varkappa_{FSO}^{(q)}} \right)^{b_{q,m}} \frac{\Gamma(b_{q,m}) \prod_{\substack{n=1\\ n\neq m}}^{3q} \Gamma(b_{q,n} - b_{q,m})}{\Gamma(1+b_{q,m}) \prod_{n=3}^{q+2} \Gamma\left(a'_{q,n} - b_{q,m}\right)},\end{aligned} \tag{3.34}$$

where $a'_{q,n}$ *denotes the* n*-th element of* $\mathbb{A}''_q = \{0.5, \mathbb{A}'_q\}$ *and*

$$\tilde{\mathcal{P}}_{RF} = \begin{cases} \left\{ \sum_{u_0=0}^{m_1-1} \cdots \sum_{u_{D-1}=0}^{m_1-1} \prod_{j=0}^{D-1} Z_j \frac{\Xi^2}{\rho_{RD}} \right\}^M \frac{\sqrt{\pi}}{2^{2L}} (4M-1)!!, & For\, \nu = 1, \\ \left\{ \sum_{u_0=0}^{m_1-1} \cdots \sum_{u_{D-1}=0}^{m_1-1} \prod_{j=0}^{D-1} Z_j \frac{D m_1 m_2}{\Omega_1 \Omega_2 \rho_{RD}} \left(\frac{1}{\nu-1}\right) \right\}^M \frac{\sqrt{\pi}}{2^M} (2L-1)!!, & For\, \nu > 1. \end{cases} \tag{3.35}$$

where $x!!$ *is the double factorial function.*[2]

Proof: See Appendix A.2.3 for the proof.

Remark 3.5: *From* (3.34) *and* (3.35)*, it can be noted that* $\tilde{\mathcal{P}}_{FSO} \propto \bar{\gamma}^{-\mathbb{B}_q}$ *and* $\tilde{\mathcal{P}}_{RF} \propto \bar{\gamma}^{-L}$*. Therefore bit-error-rate of considered IRS-assisted mixed FSO-RF communication system at high SNR defined in* (3.33) *behaves as* $\tilde{\mathcal{P}}_e \propto \bar{\gamma}^{-\mathcal{G}'_d}$ *with* $\mathcal{G}'_d = \min\{M, \mathbb{B}_q\}$ *is the achievable diversity order. It can also be noted that the system under consideration achieves the same diversity order as that obtained from* (3.28)*.*

3.4.4 Ergodic Capacity Analysis

The ergodic capacity of the IRS-assisted mixed FSO-RF system is given by [86]

$$\mathcal{C}_{\text{erg}} = \int_0^\infty \log_2(1 + \Lambda\gamma) f_{\Gamma_{\text{E}}}(\gamma) d\gamma. \tag{3.36}$$

[2]Some useful results of double factorial function for computing the coefficients: $(2x-1)!! = 1 \cdot 3 \cdot 5 \ldots (2x-1)$, $(2x)!! = 2 \cdot 4 \cdot 6 \ldots (2x)$, $0!! = 1$, and $(-1)!! = 1$ [68].

where $\Lambda = 1$ for OHD and $\Lambda = \frac{e}{2\pi}$ for IMDD technique. Using the integration by parts and some manipulations (3.36) can be simplified as

$$\mathcal{C}_{\text{erg}} = \frac{\Lambda}{2\ln(2)} \int_0^\infty \frac{1-\mathcal{F}_{\Gamma_{\text{E}}}(\gamma)}{1+\Lambda\gamma} d\gamma. \tag{3.37}$$

Since $\gamma_{\text{R}}^{(q)}$ and $\gamma_{\text{D}}^{\text{opt}}$ are independent, (3.37) can be written as

$$\mathcal{C}^{\text{erg}} = \frac{\Lambda}{2\ln(2)} \left[\underbrace{\int_0^\infty \frac{\mathcal{F}'_{\gamma_{\text{R}}^{(q)}}(\gamma)}{1+\Lambda\gamma} d\gamma}_{\mathcal{Q}_1} - \underbrace{\int_0^\infty \frac{\mathcal{F}'_{\gamma_{\text{R}}^{(q)}}(\gamma)\mathcal{F}_{\gamma_{\text{D}}^{\text{opt}}}(\gamma)}{1+\Lambda\gamma} d\gamma}_{\mathcal{Q}_2} \right], \tag{3.38}$$

where $\mathcal{F}'_{\gamma_{\text{R}}^{(q)}}(\gamma)$ is the complementary CDF (CCDF). Therefore, the CCDF of $\gamma_{\text{R}}^{(q)}$ can be obtained by $\int_\gamma^\infty f_{\gamma_{\text{R}}^{(q)}}(\gamma)d\gamma$ along with use of [63, (07.34.21.0085.01)] as

$$\mathcal{F}'_{\gamma_{\text{R}}^{(q)}}(\gamma) = \frac{\xi^2\mathcal{A}}{4(2\pi)^{q-1}} \sum_{r=1}^{\infty} s_r \left(\frac{\alpha}{g}\right)^{-\frac{\alpha+r}{2}} q^{\alpha+r-2} G_{q+1,3q+1}^{3q+1,0}\left(\frac{\Psi^q\gamma}{q^{2q}\varkappa_{\text{FSO}}^{(q)}} \middle| \begin{matrix} \mathbb{A}_q, 1 \\ 0, \mathbb{B}_q \end{matrix} \right). \tag{3.39}$$

Substituting (3.17) along with $\mathcal{F}'_{\gamma_{\text{R}}^{(q)}}(\gamma)$ in (3.38), we get $\mathcal{F}_1$ and $\mathcal{Q}_2$ as

$$\mathcal{Q}_1 = \frac{\xi^2\mathcal{A}}{4(2\pi)^{q-1}} \sum_{r=1}^{\infty} s_r \left(\frac{\alpha}{g}\right)^{-\frac{\alpha+r}{2}} q^{\alpha+r-2} \int_0^\infty \frac{1}{1+\Lambda\gamma} G_{q+1,3q+1}^{3q+1,0}\left(\frac{\Psi^q}{q^{2q}\varkappa_{\text{FSO}}^{(q)}}\gamma \middle| \begin{matrix} \mathbb{A}_q, 1 \\ 0, \mathbb{B}_q \end{matrix} \right) d\gamma, \tag{3.40}$$

and

$$\mathcal{Q}_2 = \frac{\xi^2\mathcal{A}}{4(2\pi)^{q-1}} \sum_{r=1}^{\infty} s_r \left(\frac{\alpha}{g}\right)^{-\frac{\alpha+r}{2}} q^{\alpha+r-2} \int_0^\infty \frac{1}{1+\Lambda\gamma} G_{q+1,3q+1}^{3q+1,0}\left(\frac{\Psi^q\gamma}{q^{2q}\varkappa_{\text{FSO}}^{(q)}} \middle| \begin{matrix} \mathbb{A}_q, 1 \\ 0, \mathbb{B}_q \end{matrix} \right)$$
$$\times \left\{ \sum_{u_0=0}^{m_1-1} \cdots \sum_{u_{D-1}=0}^{m_1-1} \prod_{j=0}^{D-1} Z_j \left[1 - \frac{2\left(\frac{Dm_1m_2}{\Omega_1\Omega_2\rho_{\text{RD}}}\right)^{\frac{\nu}{2}}}{(\nu-1)!} \gamma^{\frac{\nu}{2}} K_\nu\left(2\sqrt{\frac{Dm_1m_2}{\Omega_1\Omega_2\rho_{\text{RD}}}\gamma}\right)\right]\right\}^M d\gamma. \tag{3.41}$$

Utilizing [63, (07.34.21.0086.01)] in (3.40), we get

$$\mathcal{Q}_1 = \frac{\xi^2\mathcal{A}\Lambda^{-1}}{4(2\pi)^{q-1}} \sum_{r=1}^{\infty} s_r \left(\frac{\alpha}{g}\right)^{-\frac{\alpha+r}{2}} q^{\alpha+r-2} G_{q+2,3q+2}^{3q+2,1}\left(\frac{\Psi^q\Lambda^{-1}}{q^{2q}\varkappa_{\text{FSO}}^{(q)}} \middle| \begin{matrix} 0, \mathbb{A}_q, 1 \\ 0, 0, \mathbb{B}_q \end{matrix} \right). \tag{3.42}$$

The integral $\mathcal{Q}_2$ cannot be solved analytically. Therefore, we derive the asymptotic ergodic capacity at high SNR conditions ($\bar{\gamma}_{\text{R}}^{(q)} \to \infty$ and $\rho_{\text{RD}} \to \infty$) as $\lim_{\bar{\gamma}\to\infty} \mathcal{C}^{\text{erg}} = \tilde{\mathcal{C}}^{\text{erg}}$.

Lemma 3.4: *Assuming high SNR conditions over both the FSO and the RF hop, i.e.,*

$\bar{\gamma}_R^{(q)} \to \infty$ *and* $\rho_{RD} \to \infty$*, then the asymptotic ergodic capacity is given by*

$$\tilde{\mathcal{C}}^{erg} = \frac{\Lambda}{2\ln(2)}\left(\tilde{\mathcal{Q}}_1 - \tilde{\mathcal{Q}}_2\right), \tag{3.43}$$

where $\tilde{\mathcal{Q}}_1$ *and* $\tilde{\mathcal{Q}}_2$ *are given by*

$$\tilde{\mathcal{Q}}_1 = \ln(\bar{\gamma}_R^{(q)}) + \frac{\xi^2\mathcal{A}\Lambda^{-1}}{4(2\pi)^{q-1}}\sum_{r=1}^{\infty} s_r\left(\frac{\alpha}{g}\right)^{-\frac{\alpha+r}{2}} q^{\alpha+r-2} G_{q+2,3q+2}^{3q+2,1}\left(\frac{\Psi^q\bar{\gamma}_R^{(q)}}{q^{2q}\varkappa_{FSO}^{(q)}}\middle|\begin{matrix}0,\mathbb{A}_q,1\\0,0,\mathbb{B}_q\end{matrix}\right), \tag{3.44}$$

and

$$\tilde{\mathcal{Q}}_2 = \begin{cases} \dfrac{\xi^2\mathcal{A}}{4(2\pi)^{q-1}}\displaystyle\sum_{r=1}^{\infty} s_r\left(\frac{\alpha}{g}\right)^{-\frac{\alpha+r}{2}} q^{\alpha+r-2}\left\{\sum_{u_0=0}^{m_1-1}\cdots\sum_{u_{D-1}=0}^{m_1-1}\prod_{j=0}^{D-1} Z_j\left(\frac{Dm_1m_2}{\Omega_1\Omega_2}\right)^2\right\}^M \\ \times\displaystyle\sum_{m=1}^{3q+2}\frac{\Gamma(d_{q,m})\prod_{\substack{n=1\\n\neq m}}^{3q+2}\Gamma(d_{q,n}-d_{q,m})\left(\frac{q^{2q}\varkappa_{FSO}^{(q)}\rho_R^M}{\Psi^q}\right)^{-d_{q,m}}}{\Gamma(1+d_{q,m})\prod_{n=2}^{q+2}\Gamma(c_{q,n}-d_{q,m})}, \quad For\,\nu = 1, \\ \dfrac{\xi^2\mathcal{A}}{4(2\pi)^{q-1}}\displaystyle\sum_{r=1}^{\infty} s_r\left(\frac{\alpha}{g}\right)^{-\frac{\alpha+r}{2}} q^{\alpha+r-2}\left\{\sum_{u_0=0}^{m_1-1}\cdots\sum_{u_{D-1}=0}^{m_1-1}\prod_{j=0}^{D-1}\frac{Z_j}{(\nu-1)}\frac{Dm_1m_2}{\Omega_1\Omega_2\rho_{RD}}\right\}^M \\ \times\displaystyle\sum_{m=1}^{3q+2}\frac{\Gamma(d'_{q,m})\prod_{\substack{n=1\\n\neq m}}^{3q+2}\Gamma(d'_{q,n}-d'_{q,m})\left(\frac{q^{2q}\varkappa_{FSO}^{(q)}\rho_R^M}{\Psi^q}\right)^{-d'_{q,m}}}{\Gamma(1+d'_{q,m})\prod_{n=2}^{q+2}\Gamma\left(c'_{q,n}-d'_{q,m}\right)}, \quad For\,\nu > 1, \end{cases} \tag{3.45}$$

where $c_{q,n} \in \{-2L, \mathbb{A}_q, 1\}$, $d_{q,m} \in \{-2L, 0, \mathbb{B}_q\}$, $c'_{q,n} \in \{-L, \mathbb{A}_q, 1\}$, *and* $d'_{q,m} \in \{-L, 0, \mathbb{B}_q\}$.

Proof: See Appendix A.2.4 for the proof.

3.5 Numerical Results

The results for exact (simulated) and analytical end-to-end outage probability of the considered IRS-assisted mixed FSO-RF communication system are presented in this Section. Unless mentioned explicitly, it is assumed that average SNR of FSO hop (under both OHD and IMDD schemes) is equal to transmit SNR of RF hop, i.e., $\bar{\gamma}_{\mathrm{R}}^{(1)} = \bar{\gamma}_{\mathrm{R}}^{(2)} = \rho_{\mathrm{RD}}$. The turbulence conditions for FSO channel are considered as strong ($\alpha = 4.2, \beta = 1.4$), moderate ($\alpha = 4.0, \beta = 1.9$), and weak ($\alpha = 11.6, \beta = 10.4$) [52]. The other parameters related to $\mathcal{M}$-distribution given by ε, p_o, θ_A, θ_B, and Ω are taken as 0.9, 0.597, $\pi/2$, 0, and 1.32, respectively. The equivalent detector beam width W_e is taken as 0.1 m. For exact non-zero boresight pointing error model, we have assumed $(u_x, u_y, \sigma_x, \sigma_y)$

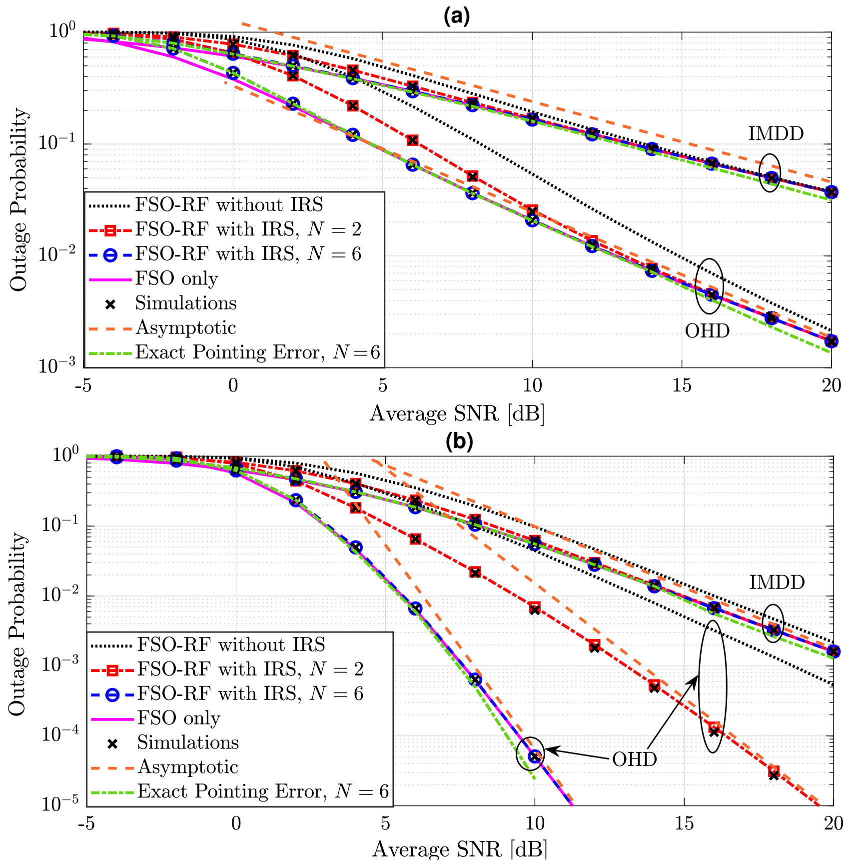

Figure 3.2: End-to-end outage performance of an IRS-assisted mixed FSO-RF system with $\alpha = 11.6, \beta = 10.4, \xi = 1.5$, $m_2 = m_1 = 2$ under OHD and IMDD techniques (a) $\varepsilon = 0.7$, (b) $\varepsilon = 1$.

as $(0.01, 0.01, 0.06, 0.06)$ and $(0.001, 0.001, 0.01, 0.01)$ under high and low pointing error conditions, respectively. Also the corresponding values of ξ for high and low pointing error are obtained as 1.5 and 8.8627, respectively. For all numerical results given in this Section, the threshold SNR is taken as unity, i.e., $\gamma_{\text{Th}} = 0$ dB (corresponding to a targeted data rate of $\bar{\mathcal{R}} = 1$ BPCU) and $M = N$ (except in Fig. 3.7). Monte carlo simulation are performed to verify that accuracy of the analytical results.

3.5.1 Comparison with Equal SNRs of FSO and RF Hops

Fig. 3.2 shows the end-to-end outage probability versus average SNR performance of the considered IRS-assisted mixed FSO-RF communication system with (a) $\varepsilon = 0.7$ (b) $\varepsilon = 1$. Here, ε is the factor that defines the amount of power coupled to LoS component of the optical wave propagating through the turbulent atmosphere and the value of ε lies between 0 and 1, where $\varepsilon = 0$ signifies absence of LoS component and $\varepsilon = 1$ means absence of scattered components. Fig. 3.2 considers both OHD and IMDD schemes under weak turbulence conditions with misalignment error coefficient $\xi = 1.5$ and the results

Table 3.2: Comparison of theoretical and numerical diversity order under different system parameters

Distribution	q	α/q	ξ^2/q	M	Diversity Order	
					$\mathcal{G}_d$ Theoretical	$\mathcal{G}_d$ Numerical
K [86] ($\beta = 1$)	1	11.6	2.25	2	1	0.9944
	2	5.2	1.125	2	0.5	0.49
	1	11.6	2.25	4	1	0.98
	2	5.2	1.125	4	0.5	0.459
Gamma-Gamma ($\beta = 3.78$)	1	11.6	2.25	2	2	1.95
	2	5.2	1.125	2	1.125	1.114
	1	11.6	2.25	4	2.25	2.23
	2	5.2	1.125	4	1.125	1.114

are compared with the conventional mixed FSO-RF communication system without IRS, where the node R directly communicates with node D. It can be observed from Fig. 3.2 that use of an IRS enhances the outage performance of the mixed FSO-RF system in comparison to the system with no IRS under both type of detection schemes. It can be observed that as ε increases, end-to-end outage probability decreases because of the availability of strong LoS component. However, the impact of ε is more pronounced for OHD compared to IMDD technique. For example, at average SNR=10 dB and $N = 4$, with increase in $\varepsilon = 0.7$ to 1, the outage probability reduces from 2.06×10^{-2} to 5.08×10^{-5} for OHD, whereas outage probability for IMDD decreases from 0.19 to 0.0554. Further, it can be seen from Fig. 3.2 that the asymptotic outage derived in (3.28) at high SNR (using asymptotic expansion of Meijer-G function and Bessel function) converges to the derived analytical results at high SNR values for both IMDD and OHD schemes. This also validates the diversity order analysis given in Section 4-B and confirms the tightness between the theoretically and numerically obtained diversity order. We have also simulated outage performance of the proposed system considering exact non-zero bore-sight pointing error model with $N = 6$ for IMDD as well as OHD scheme. It can be seen from Fig. 3.2 that the derived outage performance (by approximating the non-zero boresight pointing error coefficients with an equivalent zero boresight pointing error values) is very close to that with exact pointing error model for low to moderate values of average SNR.

Discussion 1: *Although the performance gain is more under the OHD scheme as compared to the IMDD scheme (for the system parameters considered in Fig. 3.2), the end-to-end outage probability under both the detection techniques approaches to the best possible outage performance (i.e., the performance under the FSO hop only) with only four reflecting elements at IRS, i.e., $N = 4$. Due to the deployment of an IRS over RF hop,*

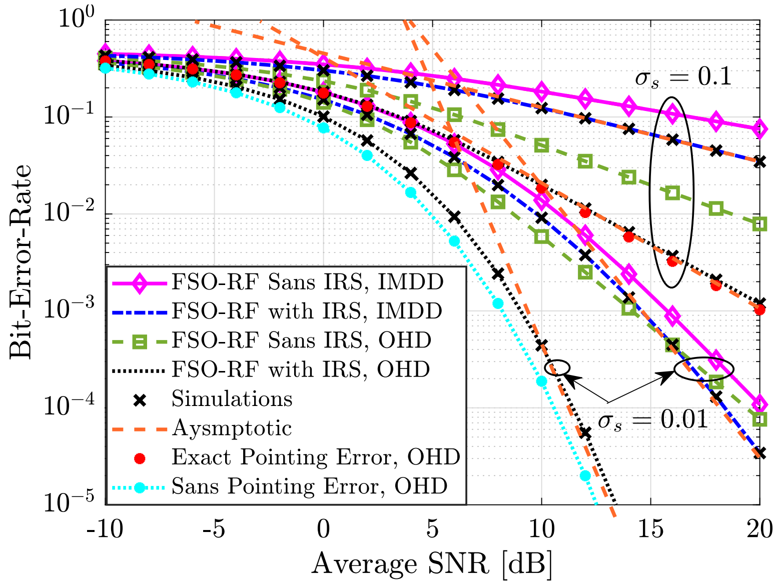

Figure 3.3: Bit-error-rate performance of an IRS-assisted mixed FSO-RF system with $\alpha = 11.6, \beta = 10.4, N = 4, p_o = 0.5, m_1 = m_2 = 2$ under OHD and IMDD techniques.

the instantaneous SNR of FSO hop is primarily responsible for the system performance, especially at high average SNRs. It can be noticed from Fig. 3.2 that the exact (simulated) values of end-to-end outage probability perfectly matches with the analytically obtained outage probability values, which validates the accuracy of the presented analysis.

Observation 3.1: *It can be observed from Fig. 3.2 that for IMDD scheme, the rate of decay of end-to-end outage probability curves is similar for $N = 2$ and $N = 4$. This is due to the fact that for $\alpha = 11.6, \beta = 10.4, \xi = 1.5$, the diversity order under IMDD scheme is $\mathcal{G}_d = \min\{N, \xi^2/2, \alpha/2, \beta/2\} = 1.125$ for both $N = 2$ and $N = 4$. However, for OHD scheme, the diversity order for $N = 2$ and $N = 4$ are different as $\mathcal{G}_d = \min\{N, \xi^2, \alpha, \beta\} = 2$ for $N = 2$ and $\mathcal{G}_d = \min\{N, \xi^2, \alpha, \beta\} = 2.25$ for $N = 6$. This also justifies that increasing N beyond a certain limit will not enhance the system performance. The theoretical and numerically obtained values of $\mathcal{G}_d$ for different curves in Fig. 3.2 are given in Table 3.2. It is clear from Table 3.2 that numerically obtained diversity order is very close to it's theoretical value and hence confirms the correctness of asymptotic analysis.*

Fig. 3.3 shows the average bit-error-rate performance versus average SNR performance of the considered IRS-assisted mixed FSO-RF communication system under both OHD and IMDD schemes. Under weak turbulence conditions Fig. 3.3 shows the impact of ξ, where $\xi = \frac{W_e}{2\sigma_s}$ is the coefficient of error due to misalignment between optical source and optical receiver. The value of ξ lies between 0 and ∞. When $\xi \to 0$, the source and receiver are highly mismatched and pointing error is high, whereas, $\xi \to \infty$ means that source and receiver are properly aligned and pointing error is negligible. Therefore, we consider two values of misalignment error coefficient as $\xi = 1.5$ (severe pointing error) and $\xi = 8.8627$ (low pointing error). The bit-error-rate performance improves with an increase in ξ from 1.5 to 8.8627 because of a decrease in misalignment error.

We have also plotted the simulated bit-error-rate [3] versus average SNR performance of a mixed FSO-RF system Sans pointing error under both detection schemes in Fig. 3.3. It can be noticed from Fig. 3.3 that bit-error-rate performance of the proposed system with small pointing error values approaches to the exact bit-error-rate values of a system without pointing error. Moreover, for significant pointing error conditions, we have plotted the simulated bit-error-rate performance of the proposed system with exact non-zero boresight pointing error model in Fig. 3.3. It can be observed from Fig. 3.3 that the derived analytical bit-error-rate performance (with approximate pointing error model) is very close to the exact non-zero boresight pointing error model bases simulated values for IMDD as well as OHD schemes.

It can be noted that the gain in bit-error-rate performance with the integration of IRS to the mixed FSO-RF system is significant for the OHD detection scheme. Further, It can be observed from Fig. 3.3 that the use of an IRS enhances the bit-error-rate performance of the mixed FSO-RF system in comparison to the system sans IRS under both types of detection schemes. Further, we can see from Fig. 3.3 that the high SNR asymptotic bit-error-rate derived in (40) using asymptotic expansion of Meijer-G function and Bessel function converges to the analytically obtained bit-error-rate values at high SNR values for both IMDD and OHD schemes and all values of ξ considered in the figure.

Observation 3.2: *It can be observed that bit-error-rate improvement with integration of IRS is significant under OHD scheme for low pointing error. For example, under OHD scheme at* 10 *dB, the bit-error-rate reduces from* 0.035 *to* 0.0137 *for* $\xi = 1.5$*, whereas bit-error-rate reduces from* 2.5×10^{-3} *to* 5.54×10^{-5} *for* $\xi = 8.8627$*. Further, it can be noted that at low pointing error conditions, average SNR required for the IRS-assisted mixed FSO-RF system to achieve bit-error-rate of* 10^{-2} *is approximately* 3 *dB less than that required for mixed FSO-RF system without IRS. However, to achieve the same bit-error-rate performance at high pointing error conditions average SNR required for the IRS-assisted mixed FSO-RF system is approximately* 7 *dB less compared to mixed FSO-RF system without IRS.*

Fig. 3.4 demonstrates ergodic rate [4] versus average SNR performance of the considered

[3]Here, the analytical values of $\mathcal{P}_{\mathrm{RF}}$ have been obtained by numerically integrating (3.32).

[4]Here, the analytical values of $\mathcal{Q}_2$ term in the expression of $\mathcal{C}_{\mathrm{erg}}$ (defined in (3.38)) have been obtained by numerically integrating (3.41).

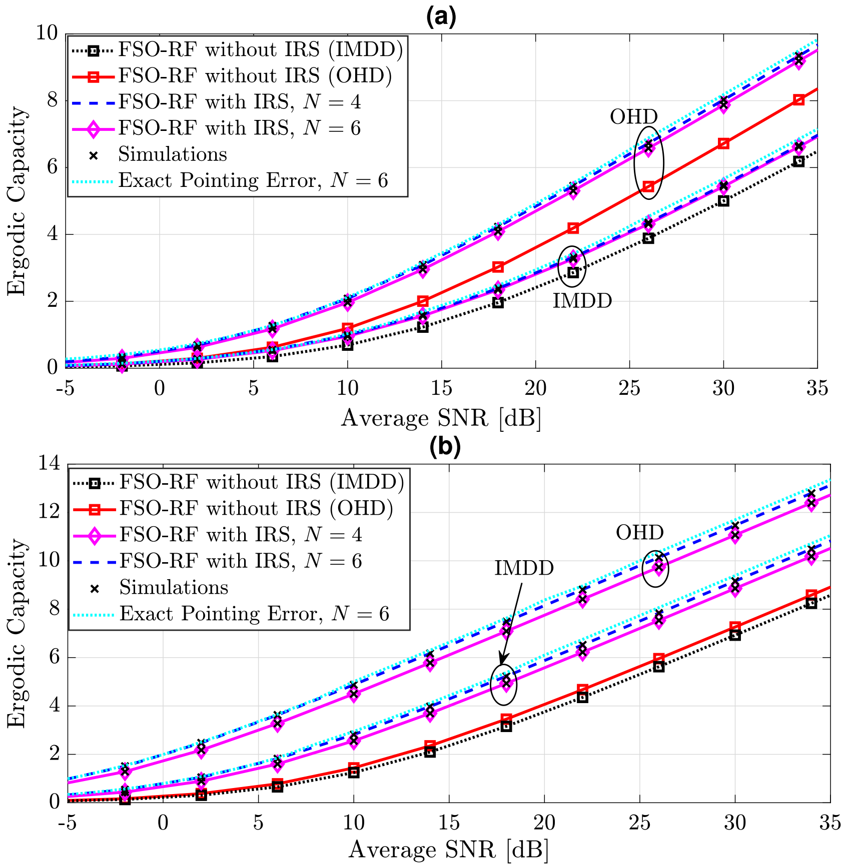

Figure 3.4: Ergodic capacity of an IRS-assisted mixed FSO-RF system with $\alpha = 4, \beta = 1.9, N = 4$, $p_o = 0.5$, $\Omega = 1$, $\varepsilon = 1$, $m_1 = m_2 = 2$ under OHD and IMDD techniques a) $\sigma_s = 0.1$, b) $\sigma_s = 0.01$.

IRS-assisted mixed FSO-RF system with IMDD and OHD detection scheme under (a) high misalignment error ($\xi = 0.8863$) (b) low misalignment error ($\xi = 8.8627$). It can be seen from Figs. 3.4(a) and 3.4(b) that ergodic capacity performance is better under the OHD scheme compared to IMDD under all for high as well as low pointing error conditions. For instance at average SNR of 18 dB and $\xi = 0.8863$ (strong pointing error), OHD scheme results in approximately 73% improvement compared to IMDD scheme. Furthermore, it can be seen that as the pointing error becomes severe, the ergodic capacity decreases. The ergodic capacity performance of the considered system is also compared with the existing FSO-RF system sans IRS. The ergodic capacity performance of the proposed IRS-assisted FSO-RF system is better compared to the existing FSO-RF system without IRS. Moreover, the gain in performance with integration of IRS is significant at low pointing error conditions for IMDD as well as OHD schemes. For example, under OHD and at average SNR of 10 dB, the performance gain is approximately 0.774 under high pointing error, whereas performance gain is approximately 3.058 under low pointing error. Further, the performance gain is negligible as N increases from 4 to 6. This implies that the system has the best achievable capacity with few reflecting elements.

Additionally, in Fig. 3.4, the simulation of ergodic capacity is provided for proposed system considering exact non-zero bore-sight pointing error model with $N = 6$ under IMDD and OHD schemes. It can be clearly observed that the derived ergodic capacity performance using the approximation of the non-zero boresight pointing error coefficients with an equivalent zero boresight pointing error values is very close to that with exact pointing error model for low as well as high pointing error conditions.

Observation 3.3: *It can be observed from Fig.3.4 that low pointing error, gain in ergodic capcity by implementing OHD is significant for IRS-assisted mixed FSO-RF whereas it is negligible for mixed FSO-RF system without IRS. For instance , at average SNR of* 10 *dB, the performance gain of IRS-assisted system ($N = 6$) in implementing OHD is approximately* 74%, *whereas performance gain is only* 16% *for system without IRS.*

3.5.2 Comparison with Fixed FSO-Hop SNR

In Fig. 3.5, the outage performance of the considered IRS-assisted mixed FSO-RF system is compared with that of the conventional FSO-RF system (without IRS) and the existing IRS-assisted mixed FSO-RF system of [81] for varying transmit SNR of RF hop (while keeping the average SNR of FSO hop fixed) under (a) IMDD scheme and (b) OHD scheme. It can be seen from Fig. 3.5 that the proposed system with one-bit control at IRS outperforms the conventional mixed FSO-RF system with $N = 2$ (for IMDD) and $N = 4$ (for OHD) only, for all the SNR values considered in the figure. Further, the outage probability reduces with increase in the number of reflecting elements at IRS. However, the analytical outage results of IRS-assisted mixed FSO-RF system of [81] with $N = 2$ and 4 outperforms the conventional FSO-RF system only up to 14 dB and 31 dB, respectively, under IMDD scheme. A similar behavior of analytical outage of existing IRS-assisted FSO-RF system of [81] is observed under OHD scheme[5], where the analysis of [81] with $N = 4$ and $N = 6$ outperforms the conventional system up to 31 dB and 46 dB, respectively. Moreover, From Fig. 3.5(a) under the IMDD technique, it is observed that the outage performance under the proposed mixed FSO-RF system for $N = 2$ and $N = 4$ decays at a higher rate as compared to the analytical outage performance under existing IRS-assisted mixed FSO-RF system for low to moderate values of average SNR. Similarly, in Fig. 3.5(b), under the OHD case, it is observed that the outage performance under the proposed IRS-assisted mixed FSO-RF system for $N = 4$, $N = 6$ (i.e., $\rho_1 > \rho_2$)

[5] Although, the authors in [81] have not considered OHD scheme at FSO receiver, we have simulated the existing IRS-assisted FSO-RF model with OHD scheme for the purpose of comparison.

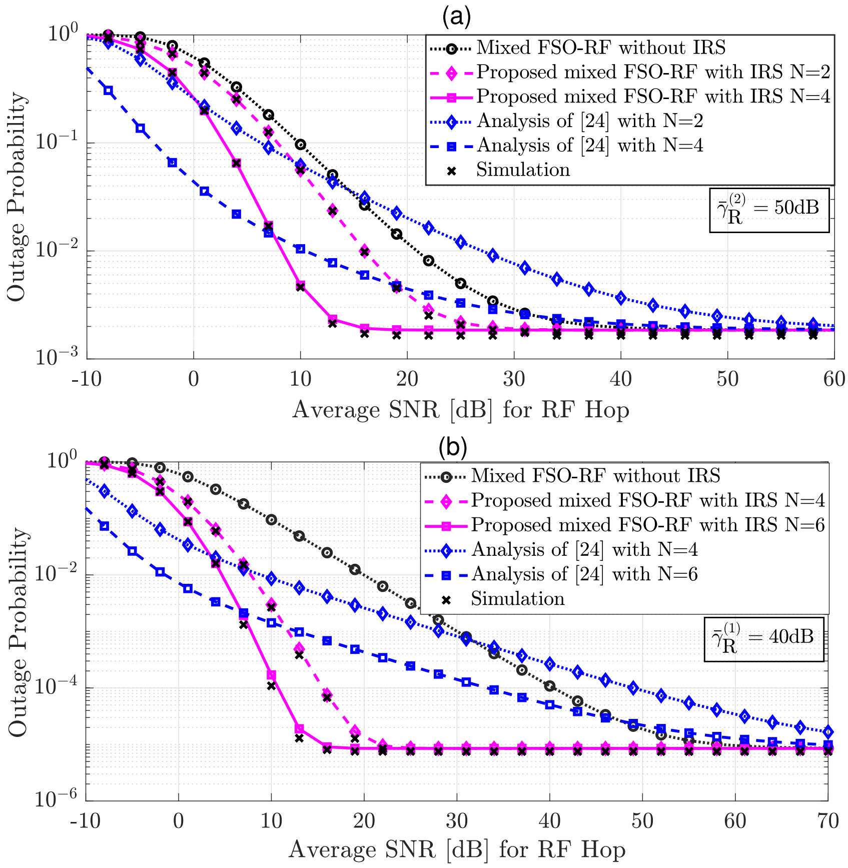

Figure 3.5: Comparison of outage probability versus RF transmit SNR performance for the proposed system with conventional and existing systems under $\alpha = 4.2, \beta = 1.4, \xi = 1.9$, $m_2 = m_1 = 1$ for (a) IMDD scheme having $\bar{\gamma}_R^{(2)} = 50$ dB and (b) OHD scheme having $\bar{\gamma}_R^{(1)} = 40$ dB.

decays at a higher rate as compared to the outage performance under existing IRS-assisted mixed FSO-RF system for low to moderate values of average SNR.

Discussion 2: *The results presented in this subsection implies that the analysis of [81] requires large number of reflecting elements at IRS to achieve the desired performance under both IMDD and OHD schemes at high SNR of RF hop. In addition, it can be noticed from Fig. 3.5 that the outage performance of proposed system is better than the analytical outage performance of [81] for $\rho_{RD} > 10$ dB (for $N = 2$) and $\rho_{RD} > 7$ dB (for $N = 4, 6$) under both type of optical detection schemes. However, for transmit SNR values below this, the existing system of [81] behaves well due to the use of CLT approximation. Further, It can also be observed from Fig. 3.5 that after a particular value of RF hop SNR, the outage probability of a conventional system without IRS is better than the analytical outage probability of [81]. This is because the analysis presented in [81] is based on CLT approximations, due to which analytical outage probability curves deviates from the exact outage probability values for low values of N and high values of RF hop SNR.*

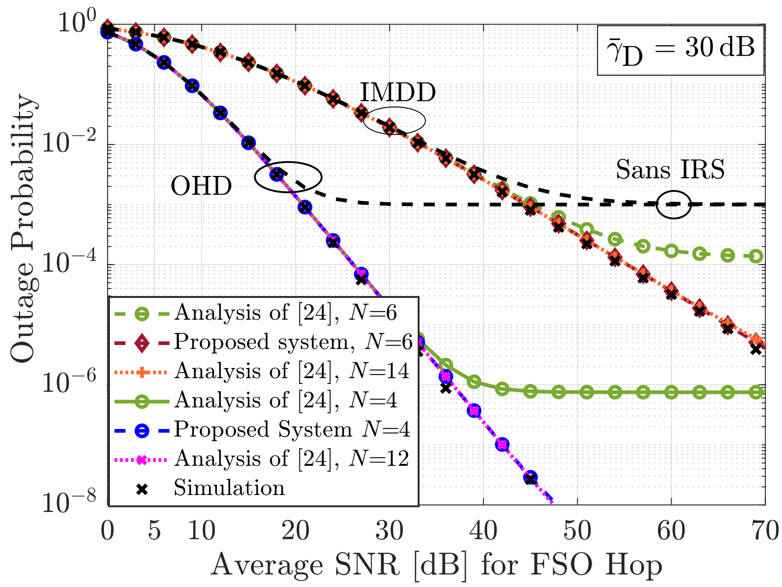

Figure 3.6: Outage performance comparison among the conventional (non-IRS), existing (with IRS), and the proposed (IRS-assisted) mixed FSO-RF communication systems with respect to average SNR of FSO hop with $\alpha = 4.0$, $\beta = 1.9$, $\xi = 1.5$, $m_1 = m_2 = 1$, $\rho_{\mathrm{RD}} = 30$ dB.

3.5.3 Comparison with Fixed Transmit SNR of RF Hop

An outage performance comparison among the conventional (without IRS), the existing (IRS based), and the proposed (IRS-assisted) mixed FSO-RF communication systems is performed in Fig. 3.6 with respect to the average SNR of FSO hop. The RF hop transmit SNR is fixed at 30 dB. It can be observed from Fig. 3.6 that the end-to-end outage probability of the conventional FSO-RF communication system saturates to 0.001 at $\rho_{\mathrm{RD}} = 30$ dB under both OHD and IMDD schemes. It can be clearly noted from Fig. 3.6 that analytical outage performance of [81] performs poor for low values of N in the high SNR regime. Thus, the proposed IRS-assisted mixed FSO-RF system with one-bit control requires very few reflecting elements as compared to that needed in analysis of [81] to achieve a specific desired performance under high SNR conditions of FSO hop. For example, under IMDD scheme, the proposed system requires only 6 reflecting elements in comparison to the 14 needed by the analysis of [81]. Similarly, 4 reflecting elements are sufficient with the proposed system under OHD scheme contrary to the requirement of 12 in the analysis of existing FSO-RF system of [81].

3.5.4 Impact of M on the System Performance

Fig. 3.7 shows the impact of parameter M on the end-to-end outage probability of the considered IRS-assisted mixed FSO-RF communication system under weak turbulence

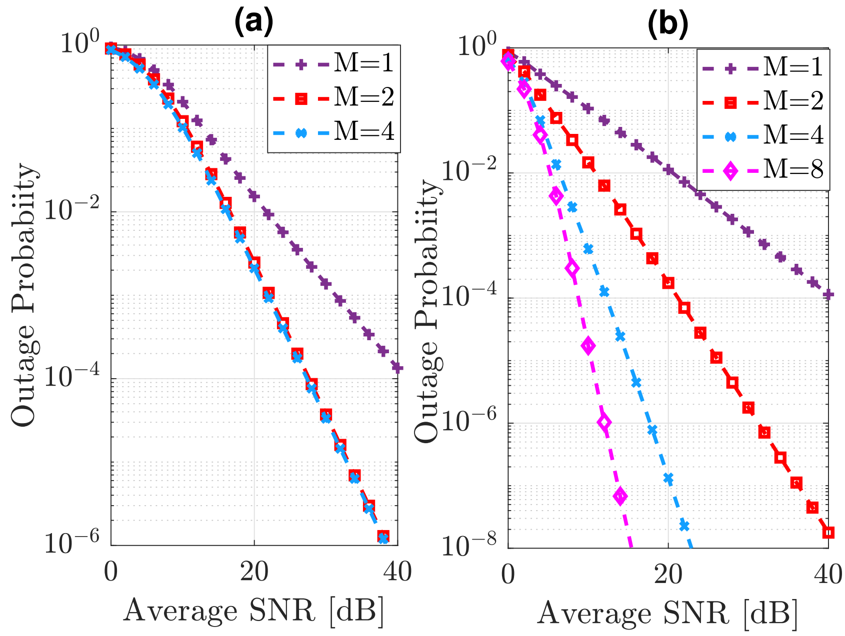

Figure 3.7: Impact of M on the end-to-end outage performance of the proposed IRS-assisted mixed FSO-RF system under weak turbulence condition and $m_2 = m_1 = 1$ with (a) IMDD scheme, $\xi = 1.9$ and (b) OHD scheme, $\xi = 8.86$.

condition with (a) IMDD, $\xi = 1.9$, $N = 4$ and (b) OHD, $\xi = 8.86$, $N = 8$. It can be observed from Fig. 3.7 that for all the SNR values considered in the figure, the end-to-end outage performance enhances with M and the best performance is obtained at $M = N$ (as explained in the Remark 3.1). It can be seen from Fig. 3.7 (a) that for IMDD scheme and weak turbulence condition with $\xi = 1.9$, the achievable diversity order remains same for $M = 2$ and $M = 4$ as $\mathcal{G}_d = \min\{M, \xi^2/2, \alpha/2, \beta/2\} = \xi^2/2 = 1.805$ for $M > 1$. However, for OHD scheme with $\xi = 8.86$ and $N = 8$, it can be noticed from Fig. 3.7 (b) that the diversity order increases with M as $\mathcal{G}_d = \min\{M, \xi^2, \alpha, \beta\} = M$.

Fig. 3.8 shows the average bit-error-rate performance versus M for the considered IRS-assisted mixed FSO-RF communication system under both OHD and IMDD schemes. The average SNR of each hop is taken as $\bar{\gamma}_{\mathrm{R}}^{(1)} = \bar{\gamma}_{\mathrm{R}}^{(2)} = \bar{\gamma}_{\mathrm{D}}^{\mathrm{opt}} = 15$ dB. It can be observed from Fig. 3.8 that there is significant improvement in bit-error-rate performance with an increase in M under OHD and IMDD detection techniques. As M increases, bit-error-rate performance approaches the best possible bit-error-rate performance (i.e., the performance under the FSO hop only) with only a few reflecting elements at IRS (i.e., $M = 4$ for IMDD and $M = 7$ for the OHD scheme). It can also be noted from Fig. 3.8, that the bit-error-rate performance of the considered IRS-assisted FSO-RF system improves with an increase in $\varpi_{\min}$ from 0.7 to 0.9. Further, if the average SNR of IRS-assisted RF hop is increased to 10 times the average SNR of FSO hop, bit-error-rate performance saturates with very few

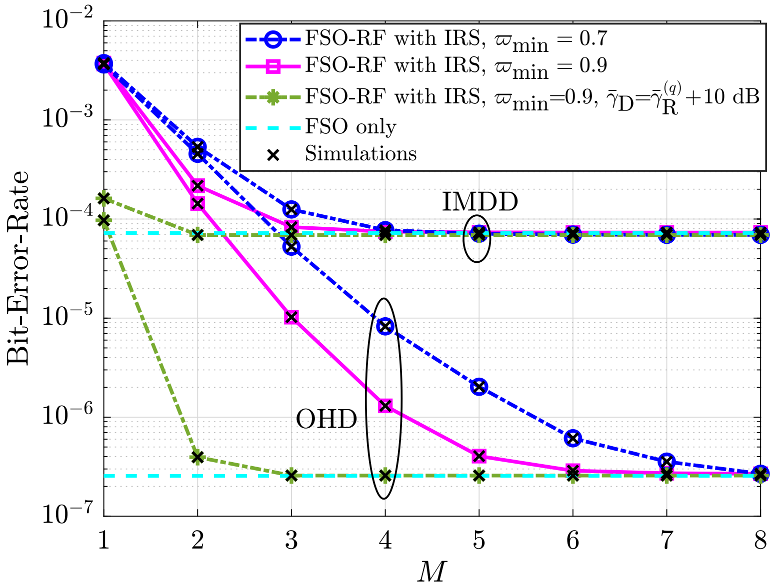

Figure 3.8: Bit-error-rate performance versus number of reflecting elements (M) of an IRS-assisted mixed FSO-RF system with $\alpha = 11.6$, $\beta = 10.4$, $\gamma = 15$ dB, $p_o = 0.5$, $m_1 = m_2 = 2$, under OHD and IMDD techniques.

reflecting elements. Since the overall bit-error-rate performance depends on the minimum of the two SNRs (i.e., SNR of FSO and RF hop), increasing the average SNR of RF hop beyond a specific value (average SNR of FSO hop) do not affect the bit-error-rate performance.

Observation 3.4: *It can be observed that the improvement in bit-error-rate performance with increase in value of ϖ_{min} is significant for OHD scheme compared to IMDD. For example, at $M = 3$, the bit-error-rate decreases from 1.25×10^{-4} to 0.828×10^{-4} with increase in ϖ_{min} from 0.7 to 0.9 for IMDD, whereas bit-error-rate decreases from 5.266×10^{-5} to 1.023×10^{-5}.*

3.5.5 Impact of Practical Reflection Coefficient

Fig. 3.9 illustrates the impact of practical phase shift model (as given in [74]) on the performance of IRS-assisted mixed FSO-RF communication system. For $\varpi_{\min} = 1$ or $\P = 0$, we get $|\varpi_{\mathrm{R}}^{(n)}| = 1$, which corresponds to the ideal reflection scenario. For all the plots in Fig. 3.9, we have set $\P = 1.6$, $\bar{\theta} = 0.43\pi$, $M = N = 4$, and $\xi = 1.9$. In Fig. 3.9(a), the outage probability versus average RF hop SNR performance of the considered system is shown under moderate turbulence conditions with both IMDD and OHD schemes. We also assume that average SNR of FSO hop is 10 times the average SNR of RF hop. It can be observed from Fig. 3.9(a) that the performance loss due to practical reflection model is relatively higher for OHD scheme as compared to IMDD scheme. Moreover, we have

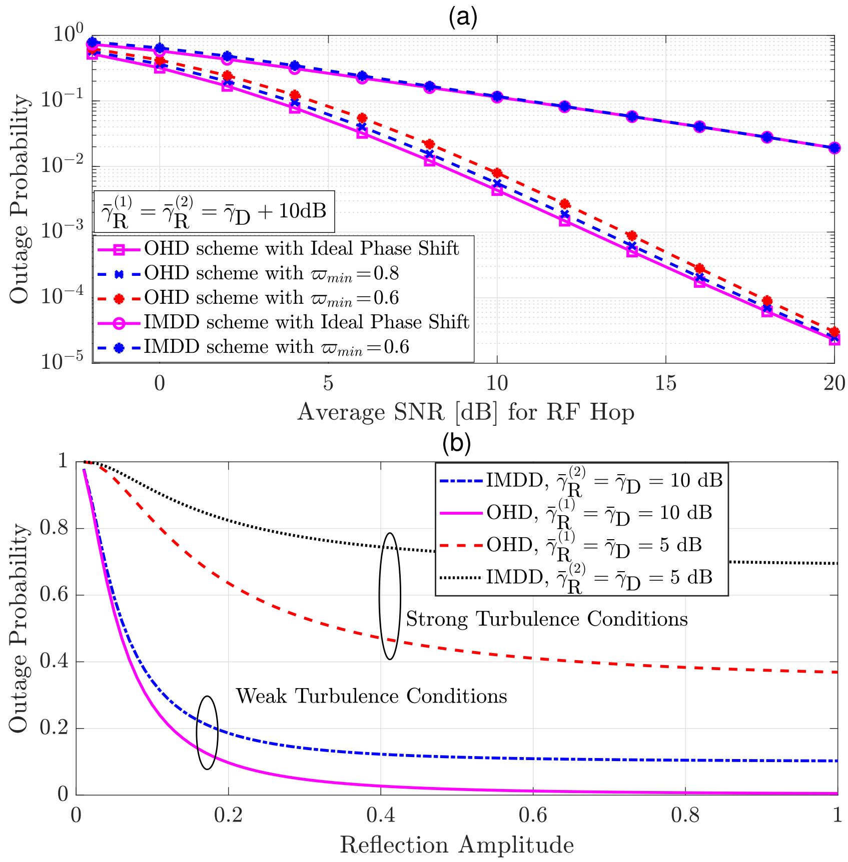

Figure 3.9: Impact of practical reflection amplitude and phase shifts on the end-to-end outage performance of the proposed IRS-assisted mixed FSO-RF system with $N = 4$, $\xi = 1.9$, $m_1 = m_2 = 1$.

shown the variations of end-to-end outage probability with respect to $|\varpi_n|$ in Fig. 3.9(b) for varying average SNR conditions. It can be noticed from the figure that under strong as well as weak turbulence, outage probability increases more rapidly for OHD scheme rather than for IMDD scheme with a small deviation in reflection amplitude from the ideal conditions.

3.6 Summary

In this chapter, we have analyzed a mixed FSO-RF communication system utilizing an IRS over the RF hop. The use of the IRS enhances the end-to-end outage performance and thus widens the coverage. The closed-form expressions for the outage probability, bit-error-rate, and ergodic capacity are derived for both OHD and IMDD techniques. Further, we analyzed the system's high SNR behavior and the diversity order of the considered system is obtained analytically. It is shown that the one-bit control at IRS in mixed FSO-RF communication system significantly outperforms the conventional and existing mixed

FSO-RF systems. It has been further revealed that for very few reflecting elements at IRS, the outage performance of the proposed IRS-assisted mixed FSO-RF communication system with one-bit control is superior than the analytical outage performance based on CLT approximation. In the end, the impact of practical reflection amplitude and phase shift of IRS elements has been observed on the system performance. It has been found that the performance loss due to practical reflection model is small for IMDD as compared to OHD scheme.

Chapter 4

SLIPT-Enabled IRS-Assited Mixed FSO-RF Communication System

4.1 Introduction

IRSs are also a promising technology for improving quality of FSO-based communication networks [90]. An OIRS is a planar array of passive elements, such as mirrors or lenses, that can be electronically controlled to manipulate the phase and the direction of the incident light signal. By adjusting the angle and phase shift of the reflected light, an OIRS can enhance the signal strength and reduce interference from other sources. The integration of OIRS into FSO communication networks have significant advantages. First, the introduction of OIRS to the FSO communication network creates an attractive research opportunity to enhance the coverage and overcome the limitation of LoS communication for ubiquitous connectivity, especially in urban areas, where the signal is usually blocked by heavy vehicles or buildings [91]. Second, in FSO-based communication network, OIRSs can be used to improve the SNR and reduce the effects of atmospheric turbulence and fading caused by obstacles. Overall, the use of OIRSs for FSO-based system has the potential to improve the performance and reliability of FSO communication systems.

In addition to WPT and IRS, NOMA is the another potential breakthrough technology to cope with high QoS requirements of 6G applications. Considering the huge connection density of users in 6G networks, it is viable to utilize channel access schemes that provide high spectral efficiency such as NOMA [92]. The system performance of SLIPT-enabled mixed FSO-RF network and IRS-assisted mixed FSO-RF have been individually well investigated in the previous chapters. Thus this chapter aims to provide a comprehensive framework that integrates these concepts and their interactions, which can enable the design of more efficient communication systems. Integrating different technologies, such as IRS and NOMA into mixed FSO-RF communication can provide enhanced connectivity and coverage, particularly in outdoor environments. The integration of an OIRS improves the connectivity of FSO hop and minimizes the misalignment errors, especially in situations where the LoS is blocked. The integration of SLIPT over OIRS-assisted FSO hop can lead to improved energy efficiency and the use of RIRS can improve signal strength and quality at the cell edge user, particularly under the low transmit power conditions at the relay. Motivated by this, we consider a novel NOMA-based IRS-assisted mixed FSO-RF communication system with SLIPT which can be realized in disaster response, secure military operations, and remote areas with limited infrastructure, where relay can harvest energy to enable long-term and autonomous operation of the network. This setup can be also be applied to enhance the urban and rural connectivity.

In this chapter, we propose a novel relay-based mixed FSO-RF communication system utilizing NOMA to assist two users over RF-hop. Assuming non-availability of direct FSO-link, we consider the deployment of an OIRS. Moreover, we deploy an RIRS in the vicinity of far user to improve its performance. We adopt SLIPT technology to harvest energy at relay node, which is utilized to forward the information signal over RF-hop and thus, makes the SNR of RF-hop dependent on the FSO-channel coefficients. For the proposed system with $\mathcal{M}$-distributed FSO-link with pointing error and Nakagami-m faded RF-link, we evaluate the system's performance in terms of outage probability, throughput, and ergodic capacity. We also derive asymptotic outage at high SNR and obtain diversity order analytically. Moreover, we propose an efficient algorithm for designing of reflection coefficients of RIRS elements to maximize the downlink SNR of far user. Numerical results are provided to see impact of system and channel parameters on system's performance. The Integration of OIRS and RIRS exhibits significant improvement in the performance of the NOMA-based considered system.

4.2 State-of-the Art

The FSO communication system integrating IRS is still in its infancy and is gaining significant attention in recent years. Till now, only a handful of research is available for the free-space environment. For instance, the authors in [90] have considered transmission in IRS-aided FSO system. This work presents the system and channel models for IRS-aided FSO system and analyzed pointing displacement while focusing on both the 2D and 3D representations. Moreover, they show the conditional geometric and misalighment errors by varying the IRS sizes. Further, [91] extended the work presented in [90], where they put insights on deriving the PDF for the geometric and misalignment errors for the same considered system setup. Moreover, they provide the expressions to compute the PDF of pointing misalignment along with the IRS phase-shift matrix. The PDF of pointing misalignment is combined for log-normal and Gamma-Gamma (i.e., for turbulence models) to provide the outage analysis. In [93] the authors considered a IRS-aided FSO system for unmanned aerial vehicles applications, whereas in [94], based on the Huygens-Fresnel principle, the authors developed an analytical end-to-end channel model. Further, the authors in [30] considered single element OIRS-assisted terrestrial FSO communication network and derived the closed-form expressions of outage, ergodic rate, and bit-error-rate under Gamma-Gamma atmospheric turbulence and misalignment error at OIRS as well as the receiver. In [95], the authors integrated OIRS to the FSO communication setup with the goal of expanding the communication coverage and enhancing the system performance. Under the assumption of Gamma-Gamma atmospheric turbulence with pointing error, the authors in [95] obtained the statistical channel model for multiple element IRS using the CLT.

The IRS-assisted NOMA network has been well-invested in [87, 96, 97, 98]. The authors in [87] proposed the IRS-assisted NOMA and it is shown that system can serve more number of user in the orthogonal spatial direction in comparison to spatial division multiple access scheme. In [96], the performance of an IRS-assisted multi-input single-output system employing NOMA was investigated in which the authors minimized the transmission power by optimizing the beamforming vectors and the phase shift matrix of IRS elements. Further, the authors in [98] maximized the throughput of the IRS-assisted NOMA system by optimizing decoding order, power allocation, channel assignment, and IRS reflection coefficients using alternating optimization technique.

NOMA has been integrated over cooperative networks to improve system performance in terms of coverage and reliability [99, 100, 101, 102]. The NOMA-based downlink mixed FSO-RF system under AF relaying was first time considered in [99] and the authors derived closed-form expressions of outage probability and ergodic rate. In [100], the authors investigated the performance of NOMA-based uplink AF relaying mixed RF-FSO system in the presence of interference resulting from multiple users. In particular, the authors in [100] obtained closed-form expressions of the outage and ergodic rate, and findings demonstrate that FSO backhauling is preferable to RF backhauling for high-throughput and high-reliability NOMA systems. The authors in [101] considered the NOMA-based mixed RF-FSO network and optimized the power allocation factors and duration of RF-based EH at the relay. Recently, the secrecy performance analysis of NOMA-based mixed FSO-RF was presented in [102].

Table 4.1: Comparison of Existing mixed FSO-RF communication network with the Proposed Work. ZB here stands for zero boresight.

Ref.	Performance Metric	FSO link	RF link	Pointing error	NOMA	IRS	Energy Harvesting
[99]	Outage, ergodic rate	$\mathcal{M}$-distribution	Nakagami-m	ZB	✓	×	×
[100]	Outage, ergodic rate	Gamma-Gamma	Rayleigh	ZB	✓	×	×
[101]	Outage, throughput	Gamma-Gamma	Rayleigh	×	✓	×	✓[†]
[102]	Secrecy outage	Gamma-Gamma	Rayleigh	ZB	✓	×	×
Our Work	Outage, throughput, ergodic rate	$\mathcal{M}$-distribution	Nakagami-m	Non-ZB	✓	✓	✓ (SLIPT)

[†]Energy is harvested from the signal received through RF link using SWIPT.

4.3 Motivation and Contribution

As discussed in the previous section, there are many works that utilized NOMA to assist multiple users in a mixed FSO-RF network. Also, there are works which considered IRS in the RF link to improve the wireless channel. But, majority of works with IRS-assisted RF link utilized CLT for composite channel statistics, which cannot effectively provide the diversity order, especially for small number of IRS elements. Moreover, there are very few studies that utilized SLIPT to mixed FSO-RF network. Table 3.1 provides a comprehensive study and comparison of several existing works on mixed FSO-RF communication network and highlights the importance of the proposed work. It is clear from Table 3.1 that no work has been reported so far which integrates NOMA with IRS-assisted mixed FSO-RF communication system. Integrating different technologies, such as IRS and NOMA into mixed FSO-RF communication can provide enhanced connectivity and coverage, particularly in outdoor environments. The integration of an OIRS improves the connectivity of FSO hop and minimizes the misalignment errors, especially in situations where the LoS is blocked. The integration of SLIPT over OIRS-assisted FSO hop can lead to improved energy efficiency and the use of RIRS can improve signal strength and quality at the cell edge user, particularly under the low transmit power conditions at the relay. Motivated by this, we consider a novel NOMA-based IRS-assisted mixed FSO-RF communication system with SLIPT which can be realized in disaster response, secure military operations, and remote areas with limited infrastructure, where relay can harvest energy to enable long-term and autonomous operation of the network. This setup can be also be applied to enhance the urban and rural connectivity. However, to perfectly utilize the benefits of both the technologies, we need to integrate NOMA and IRS into the mixed FSO-RF network to develop a network, where multiple users can be served with better channel conditions. Table 4.1 gives the comparison of the existing works on mixed FSO-RF communication network with the proposed work.

The main contributions of our work are as follows:

- We propose a novel OIRS and RIRS based mixed FSO-RF network with SLIPT which enables (i) the improvement in coverage and reliability of FSO link in the presence of atmospheric turbulence and pointing error, (ii) the enhancement in the end-user performance under NOMA technique, and (iii) the harvesting of energy at relay through optical signal.

- For the proposed network, we consider the instantaneously harvested power at the relay node to be used for RF hop transmission, thus, making the SNR of the RF hop dependent on the FSO channel coefficients. With this considerations, we derive the analytical expressions for outage, throughput, and ergodic rate of both the users in the form of bi-variate Fox-H function under generalized $\mathcal{M}$-distributed turbulence with non-zero boresight pointing error in FSO link, and Nakagami-m faded RF links.

- To gain more insights into the system's performance, we derive asymptotic outage performance of the users and obtain the achievable diversity order analytically.

- Through numerical results, the effect of various system and channel parameters like DC bias, atmospheric turbulence, misalignment error coefficients, attenuation, and visibility parameters of FSO link has been revealed on the performance of considered SLIPT-enabled NOMA based mixed FSO-RF communication system. Moreover, we have shown the impact of imperfect channel state information (CSI) of RIRS-aided RF channel on the outage performance of far user. Also, the impact of NOMA power allocation factors over both the FSO and RF hops have been discussed and highlighted numerically.

- To clearly highlight the advantages of deploying RIRS and NOMA, we have compared the ergodic sum rate performance of the proposed system with that of benchmark schemes such as orthogonal multiple access (OMA) based system (with and without RIRS) and NOMA sans RIRS.

- Finally, we propose a framework to optimize the reflection coefficients of RIRS elements to maximize the downlink SNR of the far user and propose an iterative algorithm utilizing the alternating optimization (AO) approach.

4.4 System Model and Transmission Protocol

We consider an OIRS-RIRS-assisted mixed FSO-RF communication network with SLIPT as shown in Fig. 4.1, where an optical source node S first communicates with a DF relay node R through an OIRS. The R then utilizes the harvested power to forward the decoded data of the two users [1] denoted by U_1 and U_2, using power domain NOMA. We assume U_1 is near to R compared to U_2. We assume LoS communication link from S to R is not present, therefore, we employ single-element OIRS between S and R. We assume all nodes operate in a half-duplex mode and are equipped with a single aperture/antenna. Assuming that R can process both optical and RF signals, we use a non-coherent IMDD receiver at R to detect the optical signal received from S over the optical link. Usually, the APD is employed as an optical receiver for direct detection of the received optical signal. After the incoming optical signal is converted to an electrical signal at R, a power splitter is used to segregate the AC and DC components. Thereafter, the undesirable DC component is received by the EH unit to drive the RF transmitter. The AC component of information signal is decoded, re-modulated, and then forwarded through the RF transmitter to both the users U_1 and U_2. Since U_2 is located far compared to U_1 and experiences poor channel conditions, we deploy RIRS in the vicinity of the weak user (U_2) to further enhance its channel quality. We assume that the RIRS consists of N elements and the RIRS is connected to a micro-controller that can adjust the phase and amplitude of each element.

The communication between S and U_j, $j \in \{1, 2\}$ takes place in two time slots that are orthogonal to each other, denoted by T_1 and T_2.

4.4.1 First Time Slot (FSO Transmission)

The node S forms a NOMA signal by superimposing the two independent symbols in power-domain as $x_m = \sqrt{w_1}x_1 + \sqrt{w_2}x_2$, where x_j represents the information symbol of U_j and w_j is power allocation coefficient for x_j. The S uses SIM to convert the superimposed data symbol to optical information signal. A DC bias $\mathcal{B} \in (\mathcal{B}_{\min}, \mathcal{B}_{\max})$ is added to x_m to ensure a non-negative optical signal, where $\mathcal{B}_{\min}$ and $\mathcal{B}_{\max}$ are the minimum and the maximum DC bias values, respectively. Let P_{S} be the electrical power of S to transmit the optical symbol, then s_m is written as $s_m = \sqrt{P_{\mathrm{S}}}[\delta x_m + \mathcal{B}]$, where δ is peak amplitude of

[1]Since the CCI is strong in NOMA system as multiple users share the same spectrum and implementation complexity is increased with increase in number of user, we consider only two users in our system model.

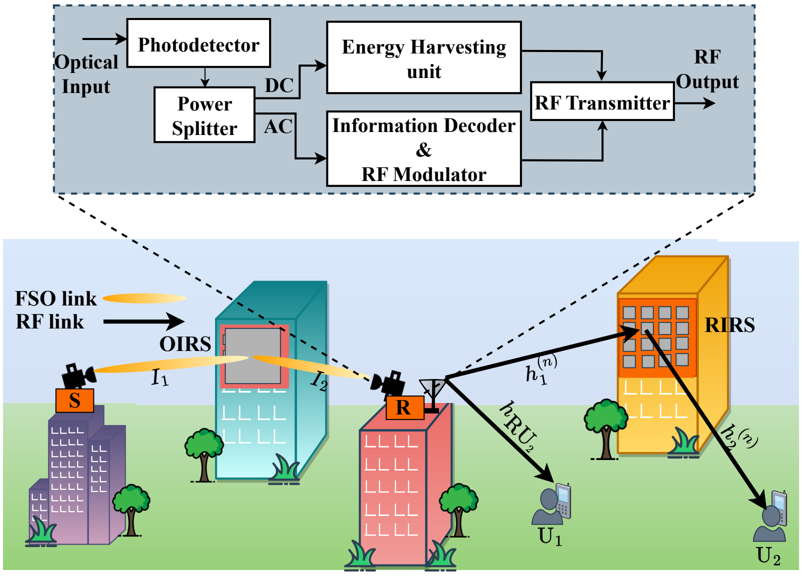

Figure 4.1: Block diagram of SLIPT-enabled IRS-assisted mixed FSO-RF communication system.

modulating signal. In order to avoid clipping due to the non-linearity of the laser-diode, δ must satisfy $\delta \leq \min(\mathcal{B} - \mathcal{B}_{\min}, \mathcal{B}_{\max} - \mathcal{B})$ [56]. The electrical signal y_{R} obtained at the output of the PD having responsivity R_{P} and detection area A_{P} at R is given by

$$y_{\mathrm{R}} = \eta R_{\mathrm{P}} A_{\mathrm{P}} I_{\mathrm{SR}} s_m + e_{\mathrm{R}} = \underbrace{\eta R_{\mathrm{P}} A_{\mathrm{P}} I_{\mathrm{SR}} \sqrt{P_{\mathrm{S}}} \delta x_m}_{I_{\mathrm{AC}}} + \underbrace{\eta R_{\mathrm{P}} A_{\mathrm{P}} I_{\mathrm{SR}} \sqrt{P_{\mathrm{S}}} \mathcal{B}}_{I_{\mathrm{DC}}} + e_{\mathrm{R}}, \tag{4.1}$$

where η is the optical-to-electrical conversion coefficient, $I_{\mathrm{SR}} = I_1 \varpi_{\mathrm{O}} I_2$, with I_1 and I_2 being the channel coefficients of S-OIRS and OIRS-R links, respectively. The term $\varpi_{\mathrm{O}} = |\varpi_{\mathrm{O}}| e^{\jmath \angle \varpi_{\mathrm{O}}}$ is reflection coefficient of OIRS; e_{R} is the ZM-AWGN noise at R with noise power σ_{R}^2. Considering DF relay, the node R employ SIC to decode the data of two users. Assuming $w_2 > w_1$, R first decodes x_2 considering x_1 as interference. Considering the perfect SIC conditions at R, the signal corresponding to x_2 is removed from the received signal and x_1 is decoded. Therefore, signal-to-interference plus noise ratio (SINR) for decoding x_2 and SNR for decoding x_1 at R is given by

$$\Gamma_{\mathrm{R},x_2} = \frac{w_2 \bar{\gamma}_o I_1^2 I_2^2}{w_1 \bar{\gamma}_o I_1^2 I_2^2 + 1} \triangleq \frac{w_2 \gamma_{\mathrm{R}}}{w_1 \gamma_{\mathrm{R}} + 1}, \tag{4.2}$$

and

$$\Gamma_{\mathrm{R},x_1} = w_1 \gamma_{\mathrm{R}} \tag{4.3}$$

where $\bar{\gamma}_o = \frac{(\eta R_{\mathrm{P}} A_{\mathrm{P}} \sqrt{P_{\mathrm{S}}} \delta)^2 |\varpi_{\mathrm{O}}|^2}{\sigma_1^2}$ and $\gamma_{\mathrm{R}} = \bar{\gamma}_o I_1^2 I_2^2$.

4.4.2 Second Time Slot (RF Transmission)

After decoding the information symbols x_1 and x_2, R remodulates them and transmit over the next hop by utilizing NOMA. Let $x_d = \sqrt{\hat{w}_1}\hat{x}_1 + \sqrt{\hat{w}_2}\hat{x}_2$ denotes the superimposed signal transmitted by the node R, where $\hat{x}_j$ is the decoded data of U_j and $\hat{w}_j$ is the corresponding power allocation coefficient over RF hop. Considering the channel gain of R-U_1 link as h_{RU_1}, the signal received by U_1 can be written as

$$y_{\mathrm{U}_1} = \sqrt{P_{\mathrm{R}}} h_{\mathrm{RU}_1} x_d + e_{\mathrm{U}_1}, \tag{4.4}$$

where P_{R} is the re-transmission power available at R and e_{U_1} is zero mean AWGN at U_1 with average power $\sigma^2_{\mathrm{U}_1}$. Let $\mathbf{h}_1 \in \mathbb{C}^{1\times N}$ and $\mathbf{h}_2 \in \mathbb{C}^{1\times N}$ denote the channel vectors of R-RIRS and IRS-U_2 links, respectively, then signal received by U_2 can be expressed as

$$y_{\mathrm{U}_2} = \sqrt{P_{\mathrm{R}}} \mathbf{h}_2^{\mathrm{H}} \mathbf{\Theta} \mathbf{h}_1 x_d + e_{\mathrm{U}_2}, \tag{4.5}$$

where e_{U_2} is the ZM-AWGN at U_2 with average power $\sigma^2_{\mathrm{U}_2}$. The matrix $\mathbf{\Theta}$ is an $N \times N$ diagonal matrix containing the reflection coefficients of RIRS, defined as $\mathbf{\Theta} = \mathrm{diag}\left[\varpi_{\mathrm{R}}^{(1)}, \varpi_{\mathrm{R}}^{(2)}, \cdots, \varpi_{\mathrm{R}}^{(N)}\right]$, where reflection coefficient of n-th reflecting element is given by $\varpi_{\mathrm{R}}^{(n)} = \left|\varpi_{\mathrm{R}}^{(n)}\right| e^{-\jmath\angle\varpi_{\mathrm{R}}^{(n)}}$ with $\left|\varpi_{\mathrm{R}}^{(n)}\right| \in [0,1]$ and $\angle\varpi_{\mathrm{R}}^{(n)} \in [0, 2\pi]$. The value of $\left|\varpi_{\mathrm{R}}^{(n)}\right|$ related to a practical phase shift is given in [74, Eq.5]. It is assumed that the phase shift of each reflection coefficient takes a discrete value from a set $\mathbb{L} = \{0, \Delta\theta, \cdots, (Q-1)\Delta\theta\}$, where $\Delta\theta = 2\pi/Q$. Let the n-th element of vector $\mathbf{h}_j^{\mathrm{H}}$, $j = 1, 2$, is defined as $h_j^{(n)} = \left|h_j^{(n)}\right| e^{\jmath\angle h_j^{(n)}}$, then we can rewrite (4.5) as

$$y_{\mathrm{U}_2} = \sqrt{P_{\mathrm{R}}} h_{\mathrm{RU}_2} x_d + e_{\mathrm{U}_2}, \tag{4.6}$$

where $h_{\mathrm{RU}_2} = \sum_{n=1}^{N} \left|\varpi_{\mathrm{R}}^{(n)}\right| \left|h_1^{(n)}\right| \left|h_2^{(n)}\right| e^{\jmath\psi^{(n)}}$ is the overall cascaded channel gain between R and U_2 with $\psi^{(n)} = \angle h_1^{(n)} + \angle h_2^{(n)} - \angle\varpi_{\mathrm{R}}^{(n)}$ representing the net phase error. Assuming $\hat{w}_2 > \hat{w}_1$, U_1 employs SIC to detect $\hat{x}_2$ by considering $\hat{x}_1$ as interference and after considering perfect SIC, U_1 detects its own symbols. Therefore SINR and SNR at U_1 to detect $\hat{x}_2$ and $\hat{x}_1$, respectively, is given by

$$\Gamma_{\mathrm{U}_1,\hat{x}_2} = \frac{\hat{w}_2 \gamma_{\mathrm{U}_1}}{\hat{w}_1 \gamma_{\mathrm{U}_1} + 1} \quad \text{and} \tag{4.7}$$

$$\Gamma_{\mathrm{U}_1,\hat{x}_1} = \hat{w}_1 \gamma_{\mathrm{U}_1} \tag{4.8}$$

where $\gamma_{\mathrm{U}_1} = \bar{\gamma}_{\mathrm{U}_1} |h_{\mathrm{RU}_1}|^2$ with $\bar{\gamma}_{\mathrm{U}_1} = \frac{P_{\mathrm{R}}}{\sigma^2_{\mathrm{U}_1}}$. Similarly, the SINR at U_2 to detect its own symbols $\hat{x}_2$ can be writtem as

$$\Gamma_{\mathrm{U}_2,\hat{x}_2} = \frac{\hat{w}_2 \gamma_{\mathrm{U}_2}}{\hat{w}_1 \gamma_{\mathrm{U}_2} + 1}, \tag{4.9}$$

where $\gamma_{\mathrm{U}_2} = \bar{\gamma}_{\mathrm{U}_2} |h_{\mathrm{RU}_2}|^2$ with $\bar{\gamma}_{\mathrm{U}_2} = \frac{P_{\mathrm{R}}}{\sigma^2_{\mathrm{U}_2}}$.

4.5 Channel Model and Statistical Characterization of SINRs

In this section, we present the considered FSO and RF channel models and derive the statistical distributions of SINRs at R, U_1 and U_2.

4.5.1 Optical Channel Model: S-R

The optical link is generally affected by attenuation, atmospheric turbulence and the misalignment error caused by the building sway due to thermal expansion or minor earthquake vibrations. Therefore channel coefficient of the FSO link is given by $I_i = I_i^l I_i^a I_i^p$, $i \in \{1, 2\}$, where I_i^l, I_i^a, and I_i^p denotes the path loss, atmospheric turbulence, and misalignment error, respectively. The path loss of optical signal in the i^{th} link is quantified by Beer Lambert's law as $I_i^l = e^{-\vartheta_i L_i}$ [70], where ϑ_i is the attenuation coefficient and L_i is the link distance. Let us consider $\mathcal{M}$-distributed atmospheric turbulence as $I_i^a \sim \mathcal{M}(\alpha_i, \beta_i, \Omega_i', g_i)$, where $\alpha_i, \beta_i, \Omega_i'$, and g_i are the fading parameters of $\mathcal{M}$-distribution [86]. Assuming approximated non-zero boresight misalignment error with parameters $(\xi_i, \sigma_{s,i}, A_{o,i}, \varrho_i)$ [86], the composite PDF[2] of I_i can be given by [86, Eq. (12)]

$$f_{I_i}(I) = \frac{\xi_i^2 \mathcal{A}_i}{4I} \sum_{r_i=1}^{\infty} s_{r_i} \left(\frac{\alpha_i}{g_i}\right)^{-\frac{\alpha_i + r_i}{2}} G_{1,3}^{3,0}\left(\frac{\alpha_i I}{g_i I_i^l A_{o,i} \varrho_i} \middle| \begin{matrix} \xi_i^2 + 1 \\ \xi_i^2, \alpha_i, r_i \end{matrix}\right), \quad I \geq 0 \tag{4.10}$$

$$\text{wherein} \quad \mathcal{A}_i \triangleq \frac{2\, \alpha_i^{\alpha_i/2}}{q_i^{1+\alpha_i/2} \Gamma(\alpha_i)} \left(\frac{g_i\, \beta_i}{g_i\, \beta_i + \Omega_i'}\right)^{\beta_i}, \quad s_{r_i} \triangleq \frac{(\beta_i)_{r_i - 1} (\alpha_i g_i)^{r_i/2}}{[(r_i - 1)!]^2 q_i^{r_i - 1} (g_i\, \beta_i + \Omega_i')^{r_i - 1}}, \tag{4.11}$$

where $A_{o,i} = [\mathrm{erf}(v_i)]^2$ is the fraction of power received with $\mathrm{erf}(\cdot)$ being the error function [68]. Further, $v_i = d_i \sqrt{\pi}/W_{z,i}$ with d_i and $W_{z,i}$ being the radius and the beam waist, respectively, of the receiver aperture; $\xi_i = \frac{W_{e,i}}{2\sigma_{s,i}}$ is the ratio of equivalent beam radius $(W_{e,i})$ and jitter deviation $(\sigma_{s,i})$. The parameter ξ_i is pointing error factor, where $\xi_i \to 0$ corresponds to very high pointing error and $\xi_i \to \infty$ corresponds to very low pointing

[2]It can be noted that (4.10) contains infinite summation. For analytical tractability, it can be truncated to 10 terms with a convergence error of approximately 10^{-4}.

error. The equivalent beam radius is defined by $W_{e,i} = \frac{(W_{z,i})^2\sqrt{\pi}\mathrm{erf}(r_i)}{2r_i e^{-(r_i)^2}}$. Considering the link distances of S-OIRS and OIRS-R links, beam divergences, and incident angle of beam, we define beam waist at OIRS and R as follows.

- **Beam waist at the OIRS:** Considering elliptical beam footprint at OIRS, the beam waist is expressed as [30]

$$W_{z,1} = \frac{L_1\theta_{\mathrm{S}}}{2}\sqrt{\frac{\cos(\theta_{\mathrm{S}}/2)}{\cos(\phi_{\mathrm{OIRS}} + \theta_{\mathrm{S}}/2)}} \tag{4.12}$$

  where θ_{S} is the beam divergence angle at S and ϕ_{OIRS} is the incident angle of beam at OIRS.

- **Beam waist at the R:** The optical beam is perceived by R as if it was transmitted by OIRS with divergence angle $\theta_{\mathrm{OIRS}} = \theta_{\mathrm{S}}\,(1 + L_1/L_2)$. Considering elliptical beam footprint at R , the beam waist at R is given as [30]

$$W_{z,2} = \frac{L_2\theta_{\mathrm{OIRS}}}{2}\sqrt{\frac{\cos(\theta_{\mathrm{S}}/2)}{\cos(\phi_{\mathrm{D}_j} + \theta_{\mathrm{S}}/2)}} \triangleq \frac{(L_1 + L_2)\,\theta_{\mathrm{S}}}{2}\sqrt{\frac{\cos(\theta_{\mathrm{S}}/2)}{\cos(\phi_{\mathrm{R}} + \theta_{\mathrm{S}}/2)}} \tag{4.13}$$

  where ϕ_{R} is the angle of incidence beam at R.

It is important to note that modelling of irradiance fluctuations through a turbulent medium by the $\mathcal{M}$ distribution is applicable for all range of turbulence conditions and it is found to provide an excellent fit to the experimental data. Moreover, it unifies most of the statistical models for the irradiance fluctuations available in the literature as described in [86, Table II].

Following (4.10), PDF of I_i^2 can be expressed as

$$f_{I_i^2}(z) = \frac{\xi_i^2\mathcal{A}_i}{4z}\sum_{r_i=1}^{\infty} s_{r_i}\left(\frac{\alpha_i}{g_i}\right)^{-\frac{\alpha_i+r_i}{2}} G_{1,3}^{3,0}\left(\Psi_i\sqrt{\frac{z}{\varkappa_i}}\,\middle|\, \begin{matrix}\xi_i^2+1\\ \xi_i^2, \alpha_i, r_i\end{matrix}\right), \tag{4.14}$$

where $\Psi_i = \xi_i^2\alpha_i\beta_i(g_i + \Omega_i')/[(\xi_i^2+1)\,(g_i\beta_i + \Omega_i')]$ and $\varkappa_i = \frac{A_{o,i}^2\varrho_i^2\xi_i^4}{(\xi_i^4+1)^2}$ is the electrical SNR obtained as [86, Eq. 34]. The average value of I_i^2 can be given by

$$\mathcal{E}\left\{I_i^2\right\} = \frac{(\alpha_i+1)\left[2g_i\,(g_i + 2\Omega_i') + \Omega_i'^2\,(\beta_i+1)\right](1+\xi_i^2)^2\varkappa_i}{\alpha_i\beta_i\xi_i^2(\xi_i^2+2)(g_i+\Omega_i')}. \tag{4.15}$$

Therefore, the expected value of γ_{R} is given by

$$\bar{\gamma}_{\mathrm{R}} = \mathcal{E}\{\gamma_{\mathrm{R}}\} = \bar{\gamma}_o\mathcal{E}\{I_1^2\}\,\mathcal{E}\{I_2^2\}\,. \tag{4.16}$$

Now, we can obtain the CDF of γ_{R} by utilizing the product of two RVs [89] along with the use of PDF of I_i^2 from (4.14) followed by the use of [63, 07.34.21.0084.01)], as

$$\mathcal{F}_{\gamma_{\mathrm{R}}}(\gamma) = K_{\mathrm{eq}} \sum_{r_1=1}^{\infty} \sum_{r_2=1}^{\infty} \Upsilon_r G_{5,13}^{12,1} \left(\frac{\Psi_{\mathrm{eq}}}{\varkappa_{\mathrm{eq}}} \gamma \middle| \begin{matrix} 1, \mathbb{P} \\ \mathbb{Q}, 0 \end{matrix} \right), \tag{4.17}$$

where $K_{\mathrm{eq}} = \frac{\xi_1^2 \xi_2^2 \mathcal{A}_1 \mathcal{A}_2}{64\pi^2}$, $\Upsilon_r = \prod_{i=1}^{2} s_{r_i} \left(\frac{\alpha_i}{g_i}\right)^{-\frac{\alpha_i + r_i}{2}} 2^{\alpha_i + r_i - 1}$, $\Psi_{\mathrm{eq}} = \frac{\Psi_1 \Psi_2}{2^8}$, $\mathbb{P} = \left\{\frac{\xi_1^2+1}{2}, \frac{\xi_1^2+2}{2}, \frac{\xi_2^2+1}{2}, \frac{\xi_2^2+2}{2}\right\}$, $\varkappa_{\mathrm{eq}} = \bar{\gamma}_o \varkappa_1 \varkappa_2$, and $\mathbb{Q} = \left\{\frac{\xi_1^2}{2}, \frac{\xi_1^2+1}{2}, \frac{\alpha_1}{2}, \frac{\alpha_1+1}{2}, \frac{r_1}{2}, \frac{r_1+1}{2}, \frac{\xi_2^2}{2}, \frac{\xi_2^2+1}{2}, \frac{\alpha_2}{2}, \frac{\alpha_2+1}{2}, \frac{r_2}{2}, \frac{r_2+1}{2}\right\}$.

4.5.2 RF channel Model: R-U$_1$ and R-U$_2$

All the RF links available in the network are assumed to follow Nakagami-m distribution and are independent of each other. If we define $|h_{\mathrm{RU}_1}|$ ~Nakagami(m_0, Ω_0), where m_0 and $\Omega_0 = \mathcal{E}\left\{|h_{\mathrm{RU}_1}|^2\right\}$ denote the channel parameters of h_{RU_1}, then we can write γ_{U_1} ~Gamma$\left(m_0, \frac{\Omega_0 \bar{\gamma}_{\mathrm{U}_1}}{m_0}\right)$ and its PDF can be written as

$$f_{\gamma_{\mathrm{U}_1}}(z) = \frac{m_0^{m_0}}{\Gamma(m_0) \bar{\gamma}_{\mathrm{U}_1}^{m_0} \Omega_0^{m_0}} z^{m_0 - 1} \exp\left(-\frac{m_0}{\bar{\gamma}_{\mathrm{U}_1} \Omega_0} z\right). \tag{4.18}$$

Similarly, if we define $\left|h_j^{(n)}\right|$ ~Nakagami(m_j, Ω_j), $j \in \{1, 2\}$, with m_j and $\Omega_j = \mathcal{E}\left\{\left|h_j^{(n)}\right|^2\right\}$ being the fading parameters, the PDF of SNR γ_{U_2} (defined in Subsection 4.4.2) can be be obtained from [103, (4)] by considering uniform phase error (i.e., $\psi^{(n)} \sim U(0, 2\pi)$) as

$$f_{\gamma_{\mathrm{U}_2}}(z) = \sum_{u_1=0}^{m_1-1} \cdots \sum_{u_N=0}^{m_1-1} \prod_{n=1}^{N} \frac{2Z_n}{\Gamma(\nu)} \left(\frac{m_1 m_2}{\left|\varpi_{\mathrm{R}}^{(n)}\right| \bar{\gamma}_{\mathrm{U}_2} \Omega_1 \Omega_2} \right)^{\frac{\nu+1}{2}} z^{\frac{\nu-1}{2}} K_{\nu-1} \left(2 \sqrt{\frac{m_1 m_2}{\left|\varpi_{\mathrm{R}}^{(n)}\right| \bar{\gamma}_{\mathrm{U}_2} \Omega_1 \Omega_2} z} \right), \tag{4.19}$$

where $\nu = N(m_1 + m_2 - 1) - \sum_{n=1}^{N} u_n$ and $Z_n = \frac{(m_2)_{m_1-1} (1-m_2)_{u_n}}{(m_1-1-u_n)! u_n!}$.

4.5.3 EH at Relay Node

This subsection provides a mathematical framework to evaluate the energy harvested at the relay node. The DC component supplied to the EH unit can be written as $I_{\mathrm{DC}} = \eta R_{\mathrm{P}} A_{\mathrm{P}} I_{\mathrm{SR}} \sqrt{P_{\mathrm{S}}} \mathcal{B}$ from (2.3). If the open circuit voltage of the photovoltaic (PV) cell is V_{OC}, the power harvested at R can be given by $P_{\mathrm{H}} = 0.75 V_{\mathrm{OC}} I_{\mathrm{DC}}$, where $V_{\mathrm{OC}} = V_{\mathrm{T}} \ln\left[(I_{\mathrm{DC}}/I_{\mathrm{o}}) + 1\right]$ [56] with I_{o} and V_{T} representing the dark saturation current and the thermal voltage of the PV cell, respectively. Utilizing the above discussion followed by the use of logarithmic approximation [56], the instantaneous harvested power can be approximated as

$$P_{\mathrm{H}} \approx \frac{0.75 V_{\mathrm{T}} \eta^2 R_{\mathrm{P}}^2 A_{\mathrm{P}}^2 \left|I_{\mathrm{SR}}\right|^2 P_{\mathrm{S}} \mathcal{B}^2}{I_{\mathrm{o}}}. \tag{4.20}$$

Moreover, using (4.16) and some algebraic manipulations, the average value of power harvested at R can be calculated as

$$\bar{P}_{\mathrm{H}} = \mathcal{E}\left\{P_{\mathrm{H}}\right\} = \frac{0.75 V_{\mathrm{T}} (\eta R_{\mathrm{P}} A_{\mathrm{P}} \sqrt{P_{\mathrm{S}}} \mathcal{B})^2 |\varpi_{\mathrm{O}}|^2 \gamma_{\mathrm{R}}}{I_{\mathrm{o}} \bar{\gamma}_o}. \tag{4.21}$$

Since P_{H} is utilized by R to transmit signal over the RF hop for a duration of T_2, the transmit power needed at R will be $P_{\mathrm{R}} = P_{\mathrm{H}} T_1 / T_2$. Now, we can rewrite SNR γ_{U_1} (described in (4.7) and (4.8)) by substituting the expression for P_{R} as

$$\gamma_{\mathrm{U}_1} = \frac{(\eta R_{\mathrm{P}} A_{\mathrm{P}} \sqrt{P_{\mathrm{S}}} \mathcal{B})^2 \left|I_{\mathrm{SR}}\right|^2 \left|h_{\mathrm{RU}_1}\right|^2 0.75 V_{\mathrm{T}} T_1}{I_{\mathrm{o}} \sigma_{\mathrm{U}_1}^2 T_2} \triangleq \gamma_{\mathrm{R}} \gamma'_{\mathrm{U}_1}, \tag{4.21}$$

where $\gamma'_{\mathrm{U}_1} = \bar{\gamma}'_{\mathrm{U}_1} \left|h_{\mathrm{RU}_1}\right|^2$ and $\bar{\gamma}'_{\mathrm{U}_1} = \frac{0.75 V_{\mathrm{T}} \rho_{\mathrm{RU}_1} \mathcal{B}^2 T_1}{\delta^2 I_{\mathrm{o}} \rho_{\mathrm{SR}} T_2}$ with $\rho_{\mathrm{SR}} = \frac{P_{\mathrm{S}}}{\sigma_{\mathrm{R}}^2}$ and $\rho_{\mathrm{RU}_1} = \frac{P_{\mathrm{S}}}{\sigma_{\mathrm{U}_1}^2}$ denoting the transmit SNR at R and U_1, respectively. Similarly, we can rewrite the SNR γ_{U_2} (described in (4.9)) with the substitution of P_{R} as

$$\gamma_{\mathrm{U}_2} = \frac{(\eta R_{\mathrm{P}} A_{\mathrm{P}} \sqrt{P_{\mathrm{S}}} \mathcal{B})^2 \left|I_{\mathrm{SR}}\right|^2 \left|h_{\mathrm{RU}_2}\right|^2 0.75 V_{\mathrm{T}} T_1}{I_{\mathrm{o}} \sigma_{\mathrm{U}_2}^2 T_2} \triangleq \gamma_{\mathrm{R}} \gamma'_{\mathrm{U}_2}, \tag{4.22}$$

where $\gamma'_{\mathrm{U}_2} = \bar{\gamma}'_{\mathrm{U}_2} \left|h_{\mathrm{RU}_2}\right|^2$ and $\bar{\gamma}'_{\mathrm{U}_2} = \frac{0.75 V_{\mathrm{T}} \rho_{\mathrm{RU}_2} \mathcal{B}^2 T_1}{\delta^2 I_{\mathrm{o}} \rho_{\mathrm{SR}} T_2}$ with $\rho_{\mathrm{RU}_2} = \frac{P_{\mathrm{S}}}{\sigma_{\mathrm{U}_2}^2}$ representing transmit SNR at U_2. It can be noted that the PDF of RVs γ'_{U_1} and γ'_{U_2} can be written in a similar fashion as given in (4.18) and (4.19), respectively, by simply changing the parameters.

4.6 Performance Analysis

In this section, the performance of both users under the considered OIRS-RIRS-assisted mixed FSO-RF network is analyzed in terms of useful first-order statistics. In particular, we derive the closed-form analytical expressions for outage probability along with the high SNR asymptotic outage analysis. Next, the throughput and the ergodic capacity expressions of each user is derived.

4.6.1 Outage Probability Analysis

Outage probability is defined as a probability that end-to-end SNR or SINR falls below certain threshold. According to NOMA protocol, the signal received by U_j is in outage when R cannot decode x_j correctly or U_j cannot decode $\hat{x}_j$ correctly. Let $\Xi_{\mathrm{A},z_j} \equiv \left\{\Gamma_{\mathrm{A},z_j} \geq \gamma_{\mathrm{Th}_j}\right\}$, (where $\mathrm{A} \in \{\mathrm{R}, \mathrm{U}_1, \mathrm{U}_2\}$, $z \in \{x, \hat{x}\}$) denotes an event such that SNR or SINR for successful decoding of symbol z_j at node A is greater than SINR threshold γ_{Th_j}, where $\gamma_{\mathrm{Th}_j} = 2^{\bar{\mathcal{R}}_j} - 1$ and $\bar{\mathcal{R}}_j$ be the target rate of U_j.

Outage Probability of $\mathbf{U}_1$

The U_1 will said to be in outage if either R or U_1 is unable to successfully decode the data of any of the two users. This can be mathematically defined as $\mathcal{P}_{\mathrm{out},1} = 1 - \Pr\left[\Xi_{\mathrm{R},x_2} \cap \Xi_{\mathrm{R},x_1} \cap \Xi_{\mathrm{U}_1,\hat{x}_2} \cap \Xi_{\mathrm{U}_1,\hat{x}_1}\right]$. Substituting Γ_{R,x_2}, Γ_{R,x_1}, $\Gamma_{\mathrm{U}_1,\hat{x}_2}$, and $\Gamma_{\mathrm{U}_1,\hat{x}_1}$ from (4.2), (4.3), and (4.9), respectively, followed by few mathematical rearrangements, we can write $\mathcal{P}_{\mathrm{out},1}$ as

$$\mathcal{P}_{\mathrm{out},1} = 1 - \Pr\left[\gamma_{\mathrm{R}} \geq C_1, \gamma_{\mathrm{R}}\gamma'_{\mathrm{U}_1} \geq C_2\right] = \Pr\left[\gamma_{\mathrm{R}} < \max\left(C_1, \frac{C_2}{\gamma'_{\mathrm{U}_1}}\right)\right], \tag{4.23}$$

where $C_1 = \max\left(\frac{\gamma_{\mathrm{Th}_2}}{w_2 - w_1\gamma_{\mathrm{Th}_2}}, \frac{\gamma_{\mathrm{Th}_1}}{w_1}\right)$ and $C_2 = \max\left(\frac{\gamma_{\mathrm{Th}_2}}{\hat{w}_2 - \hat{w}_1\gamma_{\mathrm{Th}_2}}, \frac{\gamma_{\mathrm{Th}_1}}{\hat{w}_1}\right)$.

Theorem 4.1: *The outage probability of the near user under the proposed OIRS-RIRS-aided NOMA based mixed FSO-RF communication system with EH at the relay node is given by*

$$\mathcal{P}_{out,1} = \mathcal{D}_1 + \mathcal{D}_2, \tag{4.24}$$

where $\mathcal{D}_1$ is obtained in terms of Bi-variate Fox-H function [104], as

$$\mathcal{D}_1 = \frac{K_{eq} m_0^{m_0}}{\bar{\gamma}_{U_1}^{\prime m_0} \Omega_0^{m_0} \Gamma(m_0)} \left(\frac{C_2}{C_1}\right)^{m_0} \times \sum_{r_1=1}^{\infty} \sum_{r_2=1}^{\infty} \Upsilon_r H_{1,1;0,1;13,5}^{0,1;1,0;1,12} \left[\begin{matrix} \frac{m_0}{\bar{\gamma}'_{U_1}\Omega_0}\frac{C_2}{C_1} \\ \frac{\varkappa_{eq}}{\Psi_{eq}}\frac{1}{C_1} \end{matrix} \middle| \begin{matrix} (1-m_0,1,1) \\ (-m_0,1,1) \end{matrix} \middle| \begin{matrix} - \\ (0,1) \end{matrix} \middle| \begin{matrix} \{(1-a_l,1)\}_{l=1}^{12}, (1,1) \\ (0,1), \{(1-b_k,1)\}_{k=1}^{4} \end{matrix} \right], \tag{4.25}$$

with $a_l \in \mathbb{Q}$, $b_k \in \mathbb{P}$ and

$$\mathcal{D}_2 = \frac{K_{eq}}{\Gamma(m_0)} \sum_{r_1=1}^{\infty} \sum_{r_2=1}^{\infty} \Upsilon_r \Gamma\left(m_0, \frac{m_0 C_2}{\bar{\gamma}'_{U_1}\Omega_0 C_1}\right) G_{5,13}^{12,1}\left(\frac{\Psi_{eq}}{\varkappa_{eq}} C_1 \middle| \begin{matrix} 1, \mathbb{P} \\ \mathbb{Q}, 0 \end{matrix}\right). \tag{4.26}$$

Proof. See Appendix A.3.1 for proof. □

Outage Probability of $\mathbf{U}_2$

The U_2 will said to be in outage if either R or U_2 cannot successfully decode the data of U_2, i.e., far user. This can be mathematically defined as $\mathcal{P}_{\mathrm{out},2} = 1 - \Pr\left[\Xi_{\mathrm{R},x_2} \cap \Xi_{\mathrm{U}_2,\hat{x}_2}\right]$.

Substituting Γ_{R,x_2} and $\Gamma_{\mathrm{U}_2,x_2}$ from (4.2) and (4.9) respectively, we can write $\mathcal{P}_{\mathrm{out},2}$ as

$$\mathcal{P}_{\mathrm{out},2} = 1 - \Pr\left[\gamma_{\mathrm{R}} \geq C_3, \gamma_{\mathrm{R}}\gamma'_{\mathrm{U}_2} \geq C_4\right] = \Pr\left[\gamma_{\mathrm{R}} < \max\left(C_3, \frac{C_4}{\gamma'_{\mathrm{U}_2}}\right)\right], \tag{4.27}$$

where $C_3 = \frac{\gamma_{\mathrm{Th}_2}}{w_2 - w_1\gamma_{\mathrm{Th}_2}}$ and $C_4 = \frac{\gamma_{\mathrm{Th}_2}}{\hat{w}_2 - \hat{w}_1\gamma_{\mathrm{Th}_2}}$.

Theorem 4.2: *The outage probability of the far user under the proposed OIRS-RIRS-aided NOMA based mixed FSO-RF communication system with EH at the relay node can be given by*

$$\mathcal{P}_{out,2} = \mathcal{H}_1 + \mathcal{H}_2, \tag{4.28}$$

where $\mathcal{H}_1$ is given as

$$\begin{aligned}\mathcal{H}_1 = {} & 2K_{eq}\sum_{r_1=1}^{\infty}\sum_{r_2=1}^{\infty}\Upsilon_r\sum_{u_1=0}^{m_1-1}\cdots\sum_{u_N=0}^{m_1-1}\prod_{n=1}^{N}\frac{Z_n\mathcal{C}_o}{\Gamma(\nu)}\\ & \times H^{0,1;2,0;1,12}_{1,1;0,2;13,5}\left[\begin{matrix}\frac{\mathcal{C}_oC_4}{C_3}\\ \frac{\varkappa_{eq}}{\Psi_{eq}C_3}\end{matrix}\left|\begin{matrix}(0,1,1)\\(-1,1,1)\end{matrix}\right|\begin{matrix}-\\(\nu-1,1),(0,1)\end{matrix}\left|\begin{matrix}\{(1-a_l,1)\}_{l=1}^{12},(1,1)\\(0,1),\{(1-b_k,1)\}_{k=1}^{4}\end{matrix}\right.\right],\end{aligned} \tag{4.29}$$

with $a_l \in \mathbb{Q}$, $b_k \in \mathbb{P}$, $\mathcal{C}_o = \frac{m_1m_2}{\left|\varpi_R^{(n)}\right|\bar{\gamma}'_{U_2}\Omega_1\Omega_2}$ and

$$\begin{aligned}\mathcal{H}_2 = {} & K_{eq}\sum_{r_1=1}^{\infty}\sum_{r_2=1}^{\infty}\Upsilon_rG^{12,1}_{5,13}\left(\frac{\Psi_{eq}}{\varkappa_{eq}}C_3\left|\begin{matrix}1,\mathbb{P}\\ \mathbb{Q},0\end{matrix}\right.\right)\\ & \times\left[1-\sum_{u_1=0}^{m_1-1}\cdots\sum_{u_N=0}^{m_1-1}\prod_{n=1}^{N}Z_n\left(1-\frac{\left(\mathcal{C}_o\frac{C_4}{C_3}\right)^{\frac{\nu}{2}}K_{\nu-1}\left(2\sqrt{\mathcal{C}_o\frac{C_4}{C_3}}\right)}{\Gamma(\nu)}\right)\right].\end{aligned} \tag{4.30}$$

Proof. See Appendix A.3.2 for proof. □

4.6.2 Asymptotic Outage Analysis

The closed-form analytical expressions of outage probability of U_1 and U_2 defined in (4.24) and (4.28) are in the form of bi-variate Fox-H function and are quite complex. These analytical results reveal the limited physical insights of the system and channel parameters. Therefore, we derive asymptotic analytical expressions at high SNR conditions which are tractable.

Lemma 4.1: *Assuming equal noise power at R and U_1 under high SNR conditions over both the S-R and R-U_1 link, i.e., $\rho_{SR} \to \infty$ and $\rho_{RU_1} \to \infty$, the asymptotic outage* *probability of* U_1 *is given by* $\tilde{\mathcal{P}}_1 = \tilde{\mathcal{D}}_1 + \tilde{\mathcal{D}}_2$ *where*

$$\tilde{\mathcal{D}}_1 = \frac{K_{eq}}{\Gamma(m_0)} \sum_{r_1=1}^{\infty}\sum_{r_2=1}^{\infty} \Upsilon_r \frac{\Gamma(m_0-\tilde{a}_l) \prod\limits_{l=1,\tilde{a}_l\neq a_l}^{12} \Gamma(-a_l+\tilde{a}_l)}{\tilde{a}_l \prod\limits_{k=1}^{4} \Gamma(b_k-\tilde{a}_l)} \left(\frac{\bar{\gamma}'_{U_1}\Omega_0 \varkappa_{eq}}{m_0 \Psi_{eq} C_2}\right)^{-\tilde{a}_l}, \quad and \tag{4.31}$$

$$\tilde{\mathcal{D}}_2 = \frac{K_{eq}}{\Gamma(m_0)} \Gamma\left(m_0, \frac{m_0}{\bar{\gamma}'_{U_1}\Omega_0} \frac{C_2}{C_1}\right) \sum_{r_1=1}^{\infty}\sum_{r_2=1}^{\infty} \Upsilon_r \sum_{l=1}^{12} \frac{\prod_{p=1, p\neq l}^{12} \Gamma(a_p-a_l)\Gamma(a_l)}{\prod_{k=1}^{4}\Gamma(b_k-a_l)\Gamma(1+a_l)} \left(\frac{\varkappa_{eq}}{\Psi_{eq} C_1}\right)^{-a_l}, \tag{4.32}$$

with $a_l \in \mathbb{Q}$ *and* $\tilde{a}_l = \min\{\mathbb{Q}\}$.

Proof. See Appendix A.3.3 for proof. □

For a special case of $\zeta = 1, q = 0, \Omega' = 1$ (i.e., Gamma-Gamma distribution) for FSO link and $m_0 = 1$ (i.e., Rayleigh fading) for RF link, we can write the asymptotic outage of U_1 as $\tilde{\mathcal{P}}_{\mathrm{out},1} = \tilde{\mathcal{J}}_1 + \tilde{\mathcal{J}}_1$, where

$$\tilde{\mathcal{J}}_1 = \frac{K'_{\mathrm{eq}} \Gamma(1-\tilde{a}'_l) \prod_{l=1,\tilde{a}'_l\neq a'_l}^{12} \Gamma(-a_l+\tilde{a}_l)}{\tilde{a}'_l \prod_{k=1}^{4}\Gamma(b_k-\tilde{a}_l)} \left(\frac{\bar{\gamma}'_{\mathrm{U}_1}\Omega_0 \mu_{\mathrm{eq}}}{\kappa'_{\mathrm{eq}} C_2}\right)^{-\tilde{a}_l}, \quad \text{and} \tag{4.33}$$

$$\tilde{\mathcal{J}}_2 = K'_{\mathrm{eq}} e^{-\frac{1}{\bar{\gamma}'_{\mathrm{U}_1}\Omega_0}\frac{C_2}{C_1}} \sum_{l=1}^{12} \frac{\prod_{p=1, p\neq l}^{12} \Gamma(a'_p-a'_l)\Gamma(a_l)}{\prod_{k=1}^{4}\Gamma(b_k-a'_l)\Gamma(1+a'_l)} \left(\frac{\mu_{\mathrm{eq}}}{\kappa'_{\mathrm{eq}} C_1}\right)^{-a'_l}, \tag{4.34}$$

where $K'_{\mathrm{eq}} = \frac{1}{64\pi^2} \frac{\xi_1^2\xi_2^2 2^{\alpha_1+\beta_2+\alpha_1+\beta_2}}{\Gamma(\alpha_1)\Gamma(\beta_1)\Gamma(\alpha_2)\Gamma(\beta_2)}$, $\kappa'_{\mathrm{eq}} = \frac{1}{2^8}\frac{\xi_1^2\xi_2^2\alpha_1\beta_1\alpha_2\beta_2}{(\xi_1^2+1)(\xi_2^2+1)}$, $a'_l \in \mathbb{Q}'$, $\tilde{a}'_l = \min\{\mathbb{Q}'\}$, and $\mathbb{Q}' = \left\{\frac{\xi_1^2}{2}, \frac{\xi_1^2+1}{2}, \frac{\alpha_1}{2}, \frac{\alpha_1+1}{2}, \frac{\beta_1}{2}, \frac{\beta_1+1}{2}, \frac{\xi_2^2}{2}, \frac{\xi_2^2+1}{2}, \frac{\alpha_2}{2}, \frac{\alpha_2+1}{2}, \frac{\beta_2}{2}, \frac{\beta_2+1}{2}\right\}$.

Lemma 4.2: *Assuming equal noise power at R and* U_2 *under high SNR conditions over both the S-R and R-*U_2 *links, i.e.,* $\rho_{SR} \to \infty$ *and* $\rho_{RU_2} \to \infty$*, the asymptotic outage probability of* U_2 *is given by* $\tilde{\mathcal{P}}_{out,2} = \tilde{\mathcal{H}}_1 + \tilde{\mathcal{H}}_2$ *where*

$$\tilde{\mathcal{H}}_1 = 2K_{eq} \sum_{r_1=1}^{\infty}\sum_{r_2=1}^{\infty} \Upsilon_r \sum_{u_1=0}^{m_1-1}\cdots\sum_{u_N=0}^{m_1-1} \prod_{n=1}^{N} \frac{Z_n}{\Gamma(\nu)} \frac{\Gamma(\nu-\tilde{a}_l)\Gamma(\tilde{a}_l) \prod\limits_{l=1,\tilde{a}_l\neq a_l}^{12} \Gamma(-a_l+\tilde{a}_l)}{\tilde{a}_l \prod_{k=1}^{4}\Gamma(b_k-\tilde{a}_l)} \left(\frac{\varkappa_{eq}}{\mathcal{C}_o \Psi_{eq} C_4}\right)^{-\tilde{a}_l}, \tag{4.35}$$

and

$$\tilde{\mathcal{H}}_2 = \left[1 - \sum_{u_1=0}^{m_1-1}\cdots\sum_{u_N=0}^{m_1-1} \prod_{n=1}^{N} Z_n \left(1 - \frac{\left(\mathcal{C}_o \frac{C_4}{C_3}\right)^{\frac{\nu}{2}} K_{\nu-1}\left(2\sqrt{\frac{\mathcal{C}_o C_4}{C_3}}\right)}{\Gamma(\nu)}\right)\right]$$

$$\times \frac{K_{eq}}{\Gamma(m_0)} \sum_{r_1=1}^{\infty} \sum_{r_2=1}^{\infty} \Upsilon_r \sum_{l=1}^{12} \frac{\prod_{\substack{p=1 \\ p \neq l}}^{12} \Gamma(a_p -! a_l)\Gamma(a_l) \left(\frac{\varkappa_{eq}}{\Psi_{eq} C_3}\right)^{-a_l}}{\prod_{k=1}^{4} \Gamma(b_k - a_l)\Gamma(1 + a_l)}, \tag{4.36}$$

with $a_l \in \mathbb{Q}$ *and* $\tilde{a}_l = \min\{\mathbb{Q}\}$.

Proof. See Appendix A.3.4 for proof. □

Similar to (4.33) and (4.34), the simplified expression of $\tilde{\mathcal{P}}_{\text{out},2}$ for a special case of Gamma-Gamma distribution for FSO link and Rayleigh distribution for RF link is given by $\tilde{\mathcal{P}}_{\text{out},2} = \tilde{\mathcal{H}}_1 + \tilde{\mathcal{H}}_1$, where

$$\tilde{\mathcal{H}}_1 = 2K'_{\text{eq}} \frac{1}{\Gamma(N)} \frac{\Gamma(N - \tilde{a}_l)\Gamma(\tilde{a}'_l) \prod_{l=1, \tilde{a}'_l \neq a_l}^{12} \Gamma(-a'_l + \tilde{a}'_l)}{\tilde{a}'_l \prod_{k=1}^{4} \Gamma(b_k - \tilde{a}'_l)} \left(\frac{\mu_{\text{eq}}}{\mathcal{C}'_o \kappa'_{\text{eq}} C_4}\right)^{-\tilde{a}'_l}, \quad \text{and} \tag{4.37}$$

$$\tilde{\mathcal{H}}_2 = 2K'_{\text{eq}} \frac{\left(\mathcal{C}'_o \frac{C_4}{C_3}\right)^{\frac{N}{2}} K_{N-1}\left(2\sqrt{\frac{\mathcal{C}'_o C_4}{C_3}}\right)}{\Gamma(N)} \sum_{r_1=1}^{\infty} \sum_{l=1}^{12} \frac{\prod_{p=1, p \neq l}^{12} \Gamma(a'_p - a'_l)\Gamma(a'_l) \left(\frac{\mu_{\text{eq}}}{\kappa'_{\text{eq}} C_3}\right)^{-a'_l}}{\prod_{k=1}^{4} \Gamma(b_k - a'_l)\Gamma(1 + a'_l)}; \tag{4.38}$$

where $\mathcal{C}'_o = \frac{1}{\left|\varpi_{\text{R}}^{(n)}\right| \bar{\gamma}'_{\text{U}_2} \Omega_1 \Omega_2}$.

Remark 4.1: *For equal transmit SNR conditions, i.e.,* $\rho_{SR} = \rho_{RU_1} = \rho_{RU_2} = \rho$ *(say), the end-to-end asymptotic outage probability of* U_1 *and* U_2 *under the proposed NOMA based OIRS-RIRS-assisted mixed FSO-RF communication system with SLIPT behaves as* $\tilde{\mathcal{P}}_{out,j} \propto \rho^{-\mathcal{G}_d}$, $j \in \{1, 2\}$, *where* $\mathcal{G}_d$ *is the achievable diversity order given by*

$$\mathcal{G}_d = \min\left\{\frac{\xi_1^2}{2}, \frac{\alpha_1}{2}, \frac{r_1}{2}, \frac{\xi_2^2}{2}, \frac{\alpha_2}{2}, \frac{r_2}{2}\right\}. \tag{4.39}$$

Further, for a special case of Gamma-Gamma distribution for FSO link and Rayleigh distribution for RF link, the achievable diversity order can be obtained from (4.33), (4.34), (4.37), *and* (4.38) *as*

$$\mathcal{G}_d = \min\left\{\frac{\xi_1^2}{2}, \frac{\alpha_1}{2}, \frac{\beta_1}{2}, \frac{\xi_2^2}{2}, \frac{\alpha_2}{2}, \frac{\beta_2}{2}\right\}. \tag{4.40}$$

4.6.3 Throughput Analysis

Under delay limited transmission, the throughput of j^{th} user (i.e., U_j) can be obtained from the analytical expressions of their corresponding outage probabilities as $\mathcal{U}_j = (1 - \mathcal{P}_{\text{out},j})\,\bar{\mathcal{R}}_j$ with $\bar{\mathcal{R}}_j$ be the target rate of U_j.

4.6.4 Ergodic Capacity Analysis

As the considered mixed FSO-RF system model employs a DF relaying approach, the achievable rate is constrained by the weakest link. As a result, taking both S-R and R-U_j links into account, the attainable (Shannon) rate of U_j is given as [86]

$$\mathcal{R}_j = \frac{1}{2}\log_2\left(1+\Lambda\min\left\{\Gamma_{\mathrm{R},x_j},\Gamma_{\mathrm{U}_j,x_j}\right\}\right), \tag{4.41}$$

where $\Lambda = 1$ corresponds to coherent detection and $\Lambda = \frac{e}{2\pi}$ corresponds to the direct detection scheme. The ergodic capacity of U_j can be obtained by evaluating the statistical average of $\mathcal{R}_j$ over the end-to-end instantaneous SINR as

$$\mathcal{C}_{\mathrm{erg},j} = \mathcal{E}\left\{\mathcal{R}_j\right\} = \frac{1}{2}\int_0^\infty \log_2\left(1+\Lambda\gamma\right) f_{\Gamma_{\mathrm{E}_j}}(\gamma)d\gamma, \tag{4.42}$$

where Γ_{E_j}=min $\left\{\Gamma_{\mathrm{R},x_j},\Gamma_{\mathrm{U}_j,x_j}\right\}$ and $f_{\Gamma_{\mathrm{E}_j}}(\gamma)$ is the PDF of Γ_{E_j}.

Lemma 4.3: *The unified (for coherent and direct detection schemes) anlytical expressions for the end-to-end achievable ergodic rate of the near and far users (i.e., U_1 and U_2, respectively) under the proposed NOMA based OIRS-RIRS-assisted mixed FSO-RF system with SLIPT can be written as $\mathcal{C}_{erg,j} = \mathcal{L}_{j1}+\mathcal{L}_{j2}$, where $j\in\{1,2\}$, $\mathcal{L}_{11}$, $\mathcal{L}_{12}$, $\mathcal{L}_{21}$ and $\mathcal{L}_{22}$ are given as*

$$\begin{aligned}\mathcal{L}_{11} = {} & \frac{K_{eq} m_0^{m_0}}{\hat{w}_1 \bar{\gamma}'^{m_0}_{U_1}\Omega_0^{m_0}\Gamma(m_0)} \sum_{r_1=1}^{\infty}\sum_{r_2=1}^{\infty}\Upsilon_r \\ & \times H^{0,1;1,0;1,13}_{1,1;0,1;13,5}\left[\begin{array}{c} \frac{w_1 m_0}{\hat{w}_1\bar{\gamma}'_{U_1}\Omega_0} \\ \frac{w_1\varkappa_{eq}\Lambda}{\Psi_{eq}} \end{array}\middle| \begin{array}{c} (2-m_0,1,1) \\ (1-m_0,1,1) \end{array}\middle| \begin{array}{c} - \\ (0,1) \end{array}\middle| \begin{array}{c} \{(2-a_l,1)\}_{l=1}^{12},(2,1) \\ (1,1),\{(2-b_k,1)\}_{k=1}^{4} \end{array}\right],\end{aligned} \tag{4.43}$$

$$\mathcal{L}_{12} = \frac{K_{eq}}{w_1\Gamma(m_0)}\sum_{r_1=1}^{\infty}\sum_{r_2=1}^{\infty}\Upsilon_r\Gamma\left(w_1 m_0, \frac{w_1 m_0}{\hat{w}_1\bar{\gamma}'_{U_1}\Omega_0}\right) G^{14,1}_{6,14}\left(\frac{\Psi_{eq}}{w_1\varkappa_{eq}\Lambda}\middle| \begin{array}{c} -1,0,\mathbb{P}-1 \\ \mathbb{Q}-1,-1 \end{array}\right), \tag{4.44}$$

$$\begin{aligned}\mathcal{L}_{21} = {} & 2K_{eq}\sum_{r_1=1}^{\infty}\sum_{r_2=1}^{\infty}\Upsilon_r\sum_{u_1=0}^{m_1-1}\cdots\sum_{u_N=0}^{m_1-1}\prod_{n=1}^{N}\frac{Z_n\mathcal{C}_o}{\Gamma(\nu)}\int_0^\infty \frac{\ln(1+\Lambda\gamma)\hat{w}_2}{(\hat{w}_2-\hat{w}_1\gamma)^2} \\ & \times H^{0,1;2,0;0,12}_{1,1;0,2;12,4}\left[\begin{array}{c} \mathcal{C}_o\frac{\omega_2(\gamma)}{\omega_1(\gamma)} \\ \frac{\varkappa_{eq}}{\Psi_{eq}}\frac{1}{\omega_1(\gamma)} \end{array}\middle| \begin{array}{c} (1,1,1) \\ (0,1,1) \end{array}\middle| \begin{array}{c} - \\ (\nu-1,1),(0,1) \end{array}\middle| \begin{array}{c} \{(1-a_l,1)\}_{l=1}^{12} \\ \{(1-b_k,1)\}_{k=1}^{4} \end{array}\right],\end{aligned} \tag{4.45}$$

Algorithm 1 Alternating Optimization to solve P1

Input: $\angle\varpi_{\mathrm{R}}^{(n)}, \forall n \in \{1, \cdots, N\}$.

Repeat

for $n = 1 : N$ **do**

  Find $\angle\varpi_{\mathrm{R}}^{(n)}$ by fixing others $\angle\varpi_{\mathrm{R}}^{(m)}, m \neq n$ and solve P1 using the SCA approach.

Obtain $\angle\varpi_{\mathrm{R}}^{(n)}, \forall n$ and $\varpi_{\mathrm{R}}^{(n)} = \left|\varpi_{\mathrm{R}}^{(n)}\right| e^{-\iota\angle\varpi_{\mathrm{R}}^{(n)}}$.

until objective function in P1 converges.

and

$$\mathcal{L}_{22} = K_{eq} \sum_{r_1=1}^{\infty} \sum_{r_2=1}^{\infty} \Upsilon_r \int_0^{\infty} \frac{\ln(1+\Lambda\gamma)w_2}{(w_2 - w_1\gamma)^2} G_{4,12}^{12,0}\left(\frac{\Psi_{eq}}{\varkappa_{eq}} \frac{\gamma}{w_2 - w_1\gamma}\middle| \begin{matrix} \mathbb{P}-1 \\ \mathbb{Q}-1 \end{matrix}\right)$$
$$\times \left[1 - \sum_{u_1=0}^{m_1-1} \cdots \sum_{u_N=0}^{m_1-1} \prod_{n=1}^{N} Z_n \left(1 - \frac{1}{\Gamma(\nu)} \left(\mathcal{C}_o \frac{w_2 - w_1\gamma}{\hat{w}_2 - \hat{w}_1\gamma}\right)^{\frac{\nu}{2}} K_{\nu-1}\left(2\sqrt{\mathcal{C}_o \frac{w_2 - w_1\gamma}{\hat{w}_2 - \hat{w}_1\gamma}}\right)\right)\right] d\gamma. \quad (4.46)$$

Proof. See Appendix A.3.5 for proof. □

Remark 4.2: *To the best of author's knowledge,* (4.45) *and* (4.46) *cannot be solved further analytically. However, numerical tools can be used to quickly evaluate* $\mathcal{L}_{21}$ *and* $\mathcal{L}_{22}$*. Furthermore, we can obtain an upper bound (UB) on the achievable rate of* U_2 *by considering high transmit SNR conditions. For* $\rho_{SR} \to \infty$ *and* $\rho_{RU_2} \to \infty$*, it follows from* (4.2) *and* (4.9) *that* $\Gamma_{R,x_2} \approx \frac{w_2}{w_1}$ *and* $\Gamma_{U_2,\hat{x}_2} \approx \frac{\hat{w}_2}{\hat{w}_1}$*. Thus, using* (4.41)*, we can obtain an upper bound on* $\mathcal{R}_2$ *as*

$$\mathcal{R}_2^{UB} \approx \frac{1}{2}\log_2\left(1 + min\left\{\frac{w_2}{w_1}, \frac{\hat{w}_2}{\hat{w}_1}\right\}\right). \quad (4.47)$$

It can also be noted that $\mathcal{C}_{erg,2}^{UB} = \mathcal{R}_2^{UB}$.

4.6.5 Design of Reflection Coefficients of RIRS

In this section, we design the reflection coefficients of RIRS elements in order to maximize the SNR at U_2. More specifically, we optimize the reflection phase of n-th RIRS element (i.e., $\angle\varpi_{\mathrm{R}}^{(n)}$) such that the net phase error of the n-th composite RF link (i.e., $\psi^{(n)} = \angle h_1^{(n)} + \angle h_2^{(n)} - \angle\varpi_{\mathrm{R}}^{(n)}$) approaches to zero. Furthermore, iterative algorithms are proposed to obtain the sub-optimal solutions to this problem by utilizing the low-complexity AO approach. The problem to design the reflection coefficients is given as follows.

Table 4.2: Weather and Turbulence Parameters

Parameter	λ	η	A_{P}	R_{P}	L_{SR}	σ_s	V_{T}	I_{o}	$\gamma_{\mathrm{Th1}} = \gamma_{\mathrm{Th2}}$
Value	1550 nm	0.8	314 cm^2	0.9	1000 m	0.1, 0.01	25 mV	10^{-8} A	0.2

Table 4.3: System Specifications

<table>
<tr><td colspan="10">Weather conditions of FSO link</td></tr>
<tr><td>Scenario</td><td>Visibility</td><td>ϑ</td><td>Attenuation</td><td>h_i^l</td><td>Scenario</td><td>Visibility</td><td>ϑ</td><td>Attenuation</td><td>h_i^l</td></tr>
<tr><td rowspan="2">Foggy</td><td>0.5 km</td><td>4.839</td><td>21 dB/km</td><td>0.0079</td><td rowspan="2">Clear sky</td><td>10 km</td><td>0.102</td><td>0.43 dB/km</td><td>0.903</td></tr>
<tr><td>1 km</td><td>2.072</td><td>9 dB/km</td><td>0.1259</td><td>26 km</td><td>0.039</td><td>0.17 dB/km</td><td>0.962</td></tr>
<tr><td colspan="10">Turbulence Conditions</td></tr>
<tr><td colspan="5">MT: $\beta = 3.78$, $\alpha = 5.41$</td><td colspan="5">ST: $\beta = 1.70$, $\alpha = 3.99$</td></tr>
</table>

$$\mathbf{P1}: \max_{\angle \varpi_{\mathrm{R}}^{(n)}} \quad \gamma_{\mathrm{U}_2}, \qquad \text{s.t.} \quad S_1 : \angle \varpi_{\mathrm{R}}^{(n)} \in \{0, \Delta\theta, \cdots, (Q-1)\Delta\theta\}.$$

where $\Delta\theta = 2\pi/L$ and γ_{U_2} is defined in (4.22). Since (4.22) includes the terms associated with $\angle \varpi_{\mathrm{R}}^{(n)}$, the problem **P1** becomes a non-convex optimization problem.

To solve this problem, we consider an iterative approach based on successive convex approximation (SCA) and AO (as given in Algorithm 1), where the objective function is maximized over individual sub-problems successively, and the algorithm iterates until a feasible solution is obtained. In other words, the phase shift of one reflecting element is optimized in each iteration by keeping the others fixed, resulting in the suboptimal solution.

Since the proposed algorithm depends on SCA and AO approaches, the convergence of proposed algorithm can be verified with the convergence of these approaches. As shown in [105], the AO algorithm converges when each iteration involves a convex optimization problem. Moreover, SCA, being based on the first-order Taylor series approximation, converges to a convex problem [106]. Thus, Algorithm 1 guarantees convergence.

4.7 Numerical Results

In this section, we present the analytical and simulation results for the outage probability, throughput, and ergodic capacity at each user under the considered NOMA-based IRS-assisted mixed FSO-RF system utilizing SLIPT. The important system parameters considered for numerical results are given in Table 4.2, and the parameters corresponding to atmospheric and weather conditions used in this section are mentioned in Table 4.3. For numerical results, it is assumed that the channel conditions of S-OIRS and OIRS-R links are identical to each other. Since U_1 is closer to R as compared to U_2, we have taken average channel gain of R-U_1 link to be higher than that for R-RIRS and RIRS-U_2 links, i.e., $\Omega_0 > \Omega_1, \Omega_2$. Unless otherwise mentioned, the channel fading parameters for

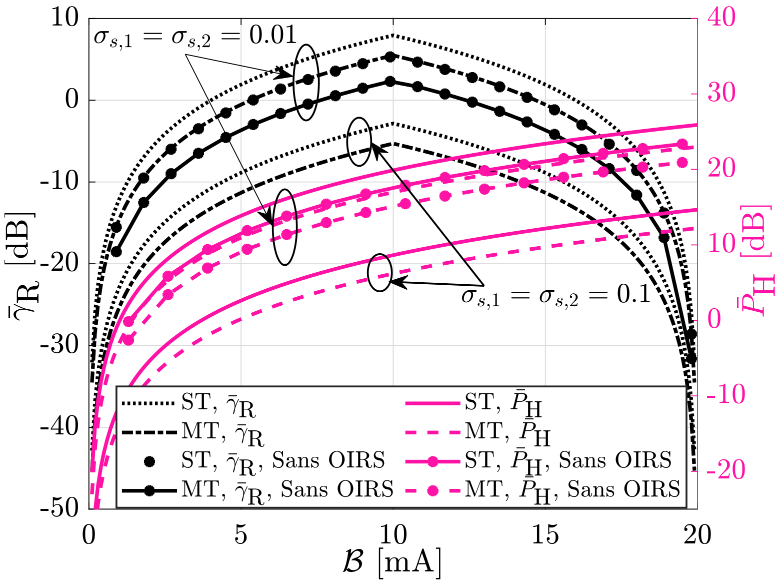

Figure 4.2: Impact of DC bias on the received average SNR and harvested power at R.

R-U$_1$, R-IRS, and IRS-U$_2$ links are taken as $(m_0, \Omega_0) = (2, 1)$, $(m_1, \Omega_1) = (1, 0.01)$ and $(m_2, \Omega_2) = (2, 0.01)$, respectively. Further, the value of beam divergence at S, angle of incident at OIRS, and angle of beam incidence at R are chosen as $\theta_{\mathrm{S}} = 0.175$ mili-radian (mrad), $\phi_{\mathrm{S}} = 0°$, and $\phi_{\mathrm{R}} = 68.45°$, respectively. The minimum reflection amplitude ($\varpi_{\min}$) for the RIRS is set as 0.8, unless defined otherwise. The noise variance at R, U$_1$, and U$_2$ is assumed as unity such that the transmit SNRs $\rho_{\mathrm{SR}} = \rho_{\mathrm{RU}_1} = \rho_{\mathrm{RU}_2} = \rho$. Unless mentioned specifically, we have considered clear sky conditions with a visibility (V) of 10 km (i.e., 0.43 dB/km).

Fig. 4.2 illustrates the impact of DC bias $\mathcal{B}$ on the average SNR of OIRS-assisted FSO link denoted by $\bar{\gamma}_{\mathrm{R}} = \mathcal{E}\{\gamma_{\mathrm{R}}\}$ and the average harvested power at the node R, denoted by $\bar{P}_{\mathrm{H}} = \mathcal{E}\{P_{\mathrm{H}}\}$. In this figure, the DC bias $\mathcal{B}$ is varied between $\mathcal{B}_{\min} = 0$ mA and $\mathcal{B}_{\max} = 20$ mA. We have fixed the transmit SNR ρ at 30 dB and have observed the variations in $\bar{\gamma}_{\mathrm{R}}$ and $\bar{P}_{\mathrm{H}}$ for varying turbulence and pointing error conditions. Intuitively, increasing $\mathcal{B}$ increases the $\bar{P}_{\mathrm{H}}$ monotonically under all turbulence and pointing displacement conditions. However, the information-bearing signal vanishes as $\mathcal{B}$ is approaches to $\mathcal{B}_{\min}$ or $\mathcal{B}_{\max}$, i.e., $\delta = 0$ and thus, the average SNR at R approaches 0. We have also shown the harvested energy and received average SNR at R without the OIRS in Fig. 2.3. It can be seen from the figure that harvested power through the FSO link without the use of OIRS is less in comparison to that of OIRS-assisted FSO link. This is because of the reduced effective misalignment by the OIRS due to its large beam waist. Moreover, it can be observed from Fig. 4.2 that the $\bar{\gamma}_{\mathrm{R}}$ is maximized at $\mathcal{B} = 10$ mA, which is consistent with the theoretical optimum of DC bias at $\mathcal{B} = \frac{\mathcal{B}_{\max}+\mathcal{B}_{\min}}{2}$. As a result, there exists a trade-off between $\bar{\gamma}_{\mathrm{R}}$

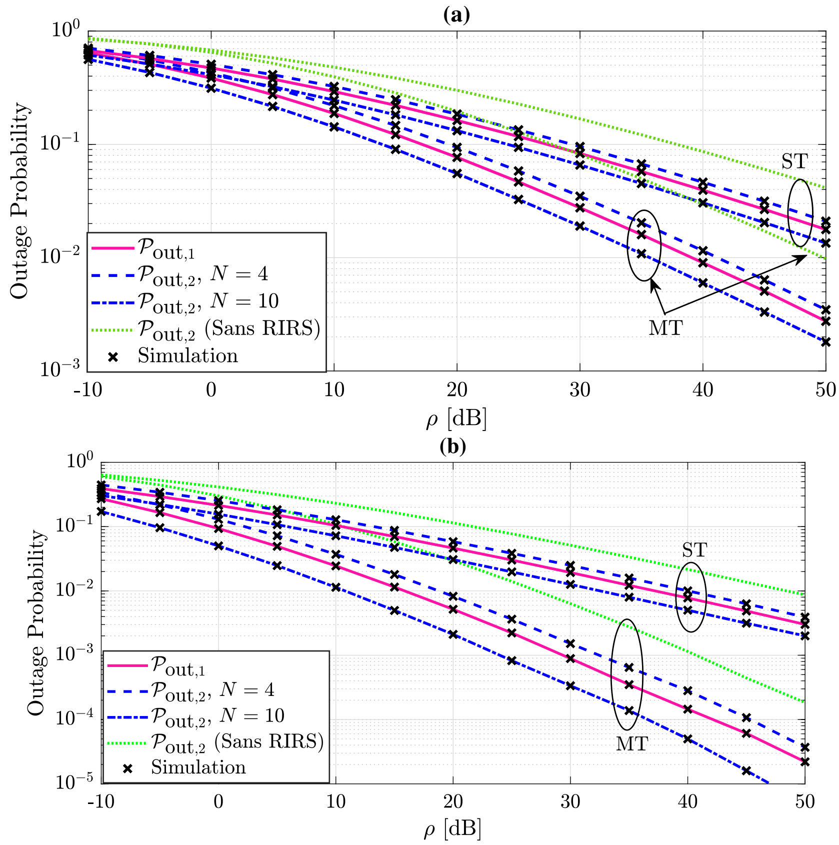

Figure 4.3: Variation of outage probability w.r.t transmit SNR with $w_2 = \hat{w}_2 = 0.7$ under a) $\sigma_{s,1} = \sigma_{s,2} = 0.1$ and (b) $\sigma_{s,1} = \sigma_{s,2} = 0.01$.

and $\bar{P}_{\text{H}}$ at node R. To improve the average harvested power, one might need to sacrifice the average SNR at node R. Considering the information SNR on priority, we have taken optimum DC bias (that maximizes the average SNR) of 10 mA for all the subsequent results, in this section.

Fig. 4.3 shows the outage performance of the proposed IRS-assisted mixed FSO-RF network utilizing downlink NOMA with SLIPT under different jitter deviation conditions as a) $\sigma_{s,1} = \sigma_{s,2} = 0.1$, and b) $\sigma_{s,1} = \sigma_{s,2} = 0.01$. It is clear from the figure that the outage performance of both the users under the considered system deteriorates significantly for strong turbulence (ST) and high jitter conditions over the FSO links. For example, at $\rho = 40$ dB, the values of $\mathcal{P}_{\text{out},1}$ for MT are 1.45×10^{-4} and 9.01×10^{-3} under a jitter deviation of 0.01 and 0.1, respectively, whereas for same ρ with ST, the $\mathcal{P}_{\text{out},1}$ increases to 7.7×10^{-3} and 4.1×10^{-2} for a jitter deviation of 0.01 and 0.1, respectively. The outage performance of U_2 is affected by the size of the IRS.

Observation 4.1: *It can be noticed from Fig. 4.3 that for achieving the desired outage performance of U_2, we need significantly less transmit SNR for large size IRS. For example, to attain the outage performance of 10^{-3} at low jitter deviation and MT, the considered*

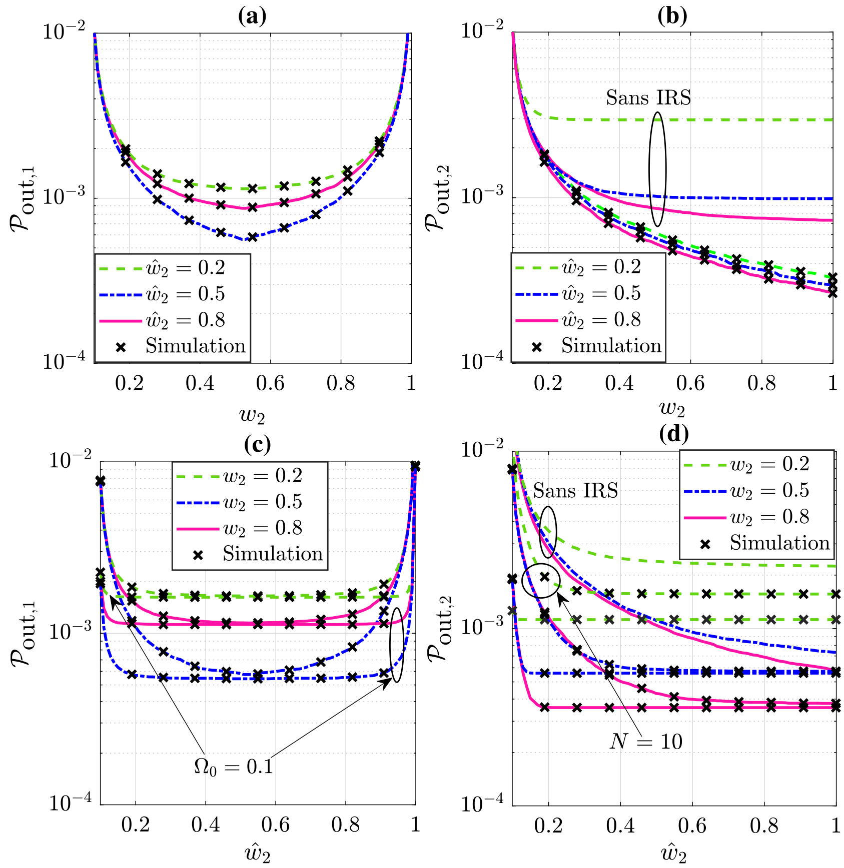

Figure 4.4: Impact of power allocation factors on the outage performance under MT and weak pointing error, $\rho = 30$ dB $N = 10$.

system requires a transmit SNR of 24 *dB and* 32 *dB for* $N = 10$ *and* $N = 4$, *respectively. Similarly, for high jitter conditions with MT, the transmit SNR requirements to achieve an outage probability of* 0.01 *are* 10 *dB and* 19 *dB for* $N = 10$ *and* $N = 4$, *respectively. As a benchmark, the outage performance of* U_2 *is also compared with a system sans IRS, where the R directly communicates with* U_2. *It can be seen from Fig. 4.3 that the system without RIRS requires very high transmit power to obtain a sufficiently small outage probability under all the turbulence and jitter conditions considered in the figure.*

Since the considered IRS-aided mixed FSO-RF system employs a power-domain NOMA strategy in both the hops, it is critical to investigate the impact of the user's power allocation on the system's performance. Fig. 4.4 shows the variations of outage probability of both users w.r.t power allocation factors of both hops. In Figs. 4.4(a) and (b), we have demonstrated the outage behavior U_1 and U_2, respectively, with varying power allocation factor w_2 of FSO link. It can be observed from Fig. 4.4(a) that $\mathcal{P}_{\text{out},1}$ is minimized for $w_2 \approx 0.5$ for different settings of $\hat{w}_2$ considered in the figure, whereas Fig. 4.4(b) depicts that $\mathcal{P}_{\text{out},2}$ decreases monotonically with an increase in w_2 for all values of $\hat{w}_2$. The intuitive reasoning for $\mathcal{P}_{\text{out},1}$ minimizing at nearly equal power allocation to both the users is the dependence of $\mathcal{P}_{\text{out},1}$ on the successful decoding of the data of both the users and the single destination node R to receive the data over cascaded FSO link. We have also plotted the $\mathcal{P}_{\text{out},2}$ versus w_2 performance for the benchmark system (sans RIRS) for comparison in Fig. 4.4(b). It can be observed from Fig. 4.4(b) that for a given $\hat{w}_2$, the outage probability of U_2 (in the absence of RIRS) saturates for small values of w_2. However, using an RIRS with $N = 20$ provides a significant gain in the outage performance of U_2.

In Figs. 4.4(c) and (d), we have shown the variations of $\mathcal{P}_{\text{out},1}$ and $\mathcal{P}_{\text{out},2}$, respectively, for varying $\hat{w}_2$ (power allocation factor over RF link) and fixed w_2. It can be seen from Fig. 4 (c) that $\mathcal{P}_{\text{out},1}$ is minimized at $\hat{w}_2 = 0.5$ especially for $w_2 = 0.5$ under poor channel condition of R-U_2 link (i.e., $\Omega_0 = 0.01$). However, if the channel conditions of R-U_1 link are improved (i.e., $\Omega_0 = 0.1$), $\mathcal{P}_{\text{out},1}$ is hardly affected by the power allocation factor $\hat{w}_2$. This is because for the DF relay assisted dual hop mixed FSO-RF network, the overall outage performance depends on the minimum of the SINRs/SNRs of FSO and RF hop. Since for given value of w_2, the average SNR of FSO hop is constant, increasing the average SNR of RF hop beyond a specific value does not affect the outage performance. Similarly, It can be seen from Figs. 4.4(d) that for $N = 10$, the outage probability of U_2 decreases exponentially with $\hat{w}_2$. However, if the channel conditions are improved by an increase in number of RIRS elements, outage performances of U_2 is almost unchanged for a large range of $\hat{w}_2$ for all the values of w_2 considered in the figures. Moreover, it can be noticed from Fig. 4.4(d) that $\mathcal{P}_{\text{out},2}$ is minimized for large values of w_2, whereas Fig. 4.4(c) shows that $\mathcal{P}_{\text{out},1}$ is minimized at $w_2 = 0.5$. All the analytical results are verified through simulations. With the help of these results, one can select the appropriate power allocation factors for both the hops under given system parameter conditions to develop a reliable communication system.

Fig. 4.5 depicts the impact of the length of the cascaded FSO link (i.e., S-OIRS-R) on the outage performance of the far and IRS-assisted user U_2 under various weather conditions and DC bias settings. It can be noted from Fig. 4.5 that for all the values of DC bias considered in this figure, the outage performance of U_2 degrades rapidly with L_{SR} under light fog conditions contrary to the very slow degradation under clear sky scenario. For example, at $L_{\text{SR}} = 1$ km with light fog and $\mathcal{B} = 10$ mA, the $\mathcal{P}_{\text{out},2}$ values increase drastically from 0.0096 to 0.25 for a decrease in the visibility from 1 km and 0.5 km. Whereas, under clear sky conditions, even if the visibility changes from 26 km to 10 km, the outage probability of U_2 increase slightly from 4.5×10^{-4} to 5.2×10^{-4}. Furthermore, it

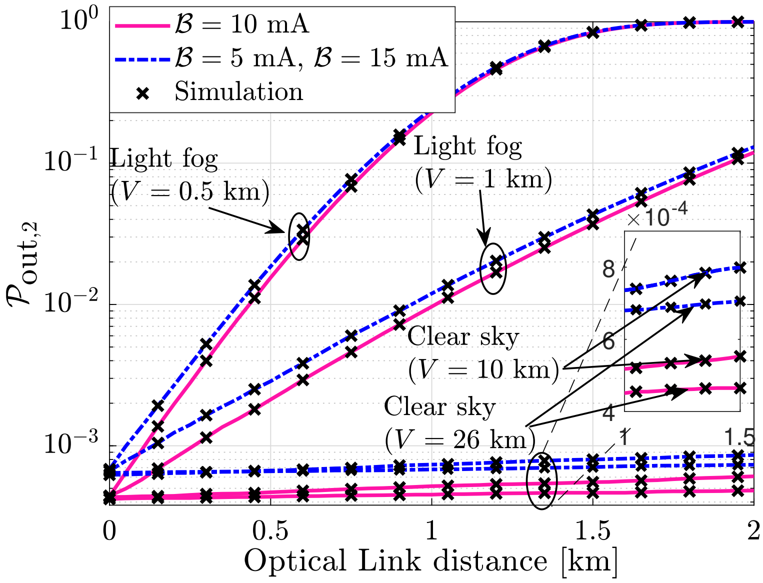

Figure 4.5: Variations of outage probability of far user U_2 with FSO link distance at MT and low jitter deviation with $w_2 = \hat{w}_2 = 0.7$, $\rho = 30$ dB, and $N = 10$.

has again been verified from Fig. 4.5 that $\mathcal{B} = 10$ mA (i.e., optimum DC bias as discussed in Fig. 4.2) provides the best outage performance under all the weather scenarios. It can also be noted that the outage performances for DC bias values of $\mathcal{B} = 5$ mA and $\mathcal{B} = 15$ mA are similar for all weather conditions due to the equal deviation from the optimum DC bias value of 10 mA and corresponding equal deviation in the average SNR at R.

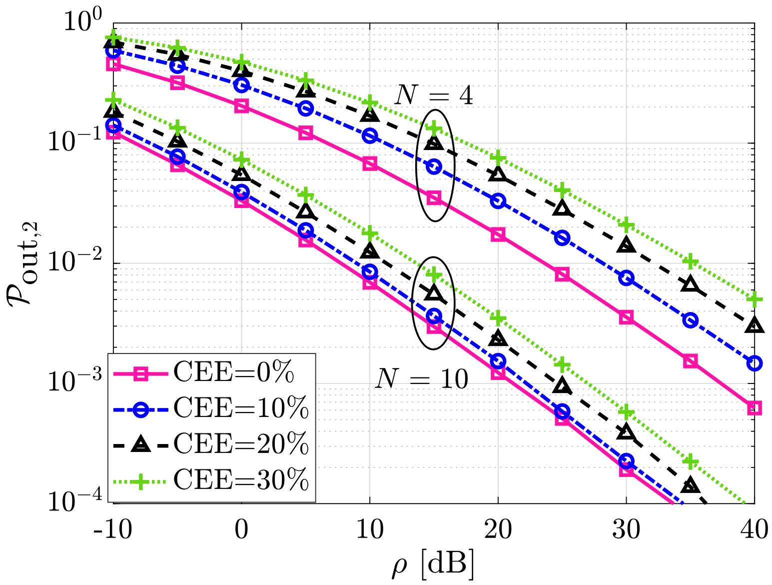

Figure 4.6: Impact of channel estimation error on the outage performance of U_2 with $w_2 = \hat{w}_2 = 0.7$.

In practical scenarios, the imperfect feedback may cause errors in acquiring the CSI at the communication nodes, especially in the IRS-assisted networks. Therefore, in Fig. 4.6, we have investigated the impact of channel estimation error (CEE) for the cascaded link between R and U_2 (i.e., R-RIRS-U_2) on the outage performance of U_2 under MT and low misalignment deviation conditions. The CEE for the cascaded R-RIRS-U_2 link can be calculated as $\text{CEE} = \mathcal{E}\left[\left|h_{\text{RU}_2} - \hat{h}_{\text{RU}_2}\right|^2\right]$, where $\hat{h}_{\text{RU}_2}$ is the estimated channel coefficient corresponding to the exact channel coefficient h_{RU_2}. We have plotted the $\mathcal{P}_{\text{out},2}$ versus ρ curves for varying CEE (0%, 10%, 20%, and 30%) values and $N = 4, 10$ in Fig. 4.6. The 0% CEE refers to the perfect CSI case.

Observation 4.2: *It can be observed from Fig. 4.6 that the outage performance deteriorates with increasing CEE and the degradation is significant for small values of N. For instance, with $N = 10$ and $N = 4$, an additional transmit SNR of about 4 dB and 8 dB, respectively, is needed to achieve an outage probability of 10^{-2} with 20% CEE as compared to the perfect CSI case.*

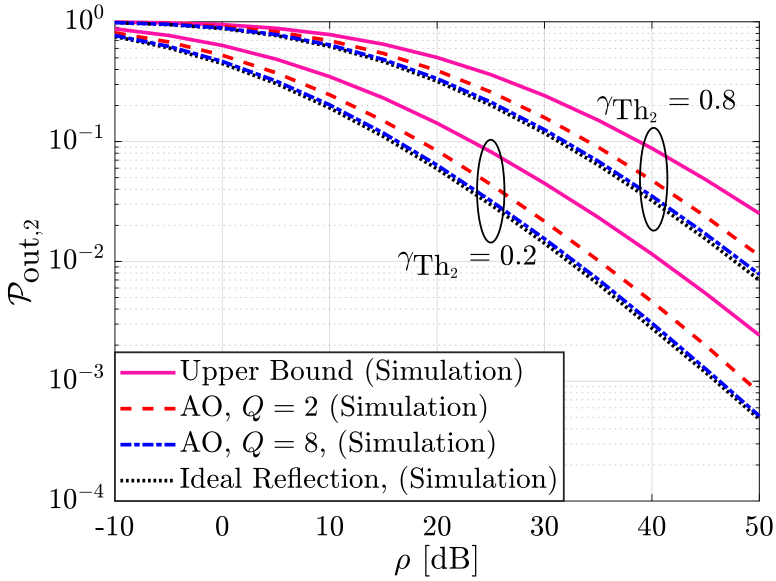

Figure 4.7: Variations of outage probability of U_2 with FSO link distance at MT and low jitter deviation with $w_2 = \hat{w}_2 = 0.7$, $\rho = 30$ dB, and $N = 10$. b). Impact of channel estimation error on the outage probability of U_2 with $w_2 = \hat{w}_2 = 0.7$.

Fig. 4.7 shows the outage performance of U_2 (assisted by RIRS) for different discrete phase shifts realized by AO algorithm 1. It is worth noting that if the net phase shift $\psi^{(n)}$ due to imperfect CSI at RIRS is uniformly distributed between $[0, 2\pi]$ (indicating the maximum randomness), the outage achieved can be considered as a upper bound. It can be clearly seen from Fig. 4.7 that by optimizing the reflection phase of each RIRS elements, the outage probability of U_2 is significantly reduced as compared to the upper bound. Further, as quantization levels Q increases from 2 to 8, the outage performance of U_2 improves and the outage performance at $Q = 8$ is very close to the ideal reflection

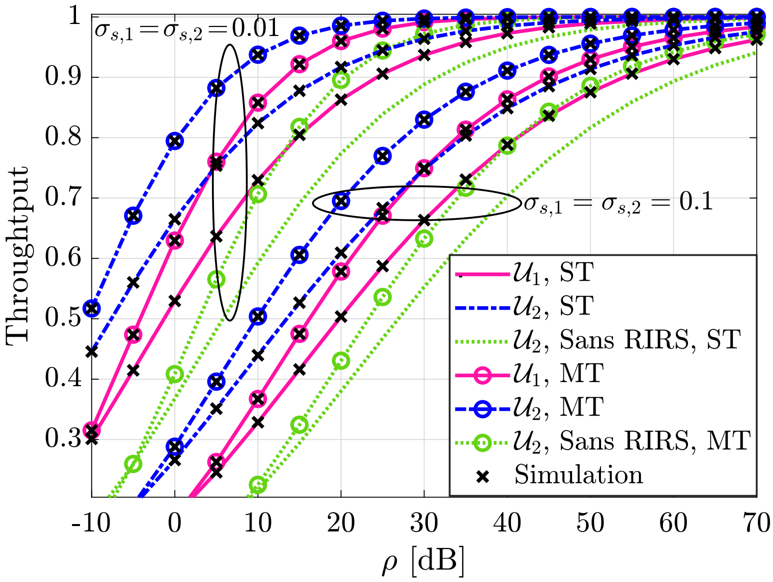

Figure 4.8: Variations of throughput of U_1 and U_2 for the considered NOMA based IRS assisted mixed FSO-RF network w.r.t transmit SNR with $w_2 = \hat{w}_2 = 0.8$, $N = 10$ and $\bar{\mathcal{R}}_1 = \bar{\mathcal{R}}_2 = 1$ bits per channel use (BPCU).

case (i.e., zero phase error).

Fig. 4.8 shows the throughput performance of U_1 and U_2 (denoted as $\mathcal{U}_1$ and $\mathcal{U}_2$, respectively) for considered NOMA-based IRS-assisted mixed FSO-RF system w.r.t the transmit SNR under different turbulence and pointing error conditions. It can be seen from Fig. 4.8 that for significant pointing error conditions (i.e., $\sigma_{s,1} = \sigma_{s,2} = 0.1$) at both the OIRS and R, the throughput performances of both the users are severely degraded (under all atmospheric turbulence conditions) in comparison with the same for negligible pointing error conditions (i.e., $\sigma_{s,1} = \sigma_{s,2} = 0.01$). For example, at $\rho = 15$ dB under MT, the $\mathcal{U}_1$ gets almost doubled (from 0.475 to 0.922) with a reduction in jitter deviation from 0.1 to 0.01. It can also be revealed from Fig. 4.8 that the throughput performance of both the users deteriorates under ST conditions, however, the impact of pointing error variations is significant as compared to the same for turbulence conditions. For the RIRS-assisted user U_2, we have compared the throughput performance of U_2 with a benchmark system without IRS and it is clear from Fig. 4.8 that use of an IRS provides notable gains in the throughput of U_2 and hence improves the power efficiency of the system. For example, to achieve the throughput of 0.6 for U_2 at $\sigma_{s,1} = \sigma_{s,2} = 0.1$ and MT, the system sans RIRS requires approximately 14 dB extra power compared to system with IRS.

Figs. 4.9(a) and 4.9(b) depict the variations of the outage probability and the system throughput, respectively, (for both the users) w.r.t to the target rates under the considered NOMA-based IRS-assisted mixed FSO-RF network. For Figs. 4.9(a) and 4.9(b), we have

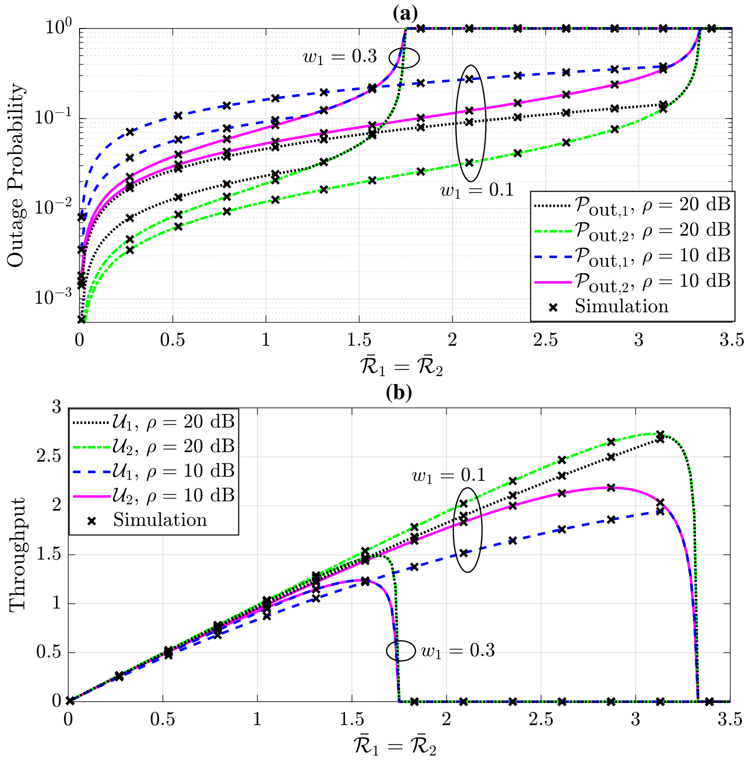

Figure 4.9: Variations of (a) Outage performance and (b) throughput w.r.t . target rate ($\bar{\mathcal{R}}_1 = \bar{\mathcal{R}}_2$) under the considered network for $N = 10$ and different values of ρ and w_1.

kept same simulation setup and we have assumed that the target rates of U_1 and U_2 are equal. We have also assumed two different values of ρ and w_1 as $\rho = 10, 20$ dB and $w_1 = 0.1, 0.3$. It can be noticed from Fig. 4.9(b) that for increasing target rate, the throughput first increases to a certain value of target rate and beyond that it quickly approaches to 0 for all values of ρ and w_1. However, the value of target rate at which throughput is 0 is independent of ρ. Since outage probability is dependent on the target rate as well, we have plotted the outage probability curves for both the users with different values of ρ and w_1 in Fig. 4.9(a). Observing the variations of outage probability w.r.t target rate, it can be deduced that the outage probability initially increases slowly w.r.t target rate, however, beyond certain value, it suddenly rises up to unity. This is why, the throughput of the system suddenly fall to 0. The values of the target rate at which throughput becomes 0 (or outage probability becomes unity) is 3.33 and 1.75 for $w_1 = 0.1$ and $w_1 = 0.3$, respectively. It can also be observed from Fig. 4.9(b) that the rate of increase in the throughput w.r.t target rate is slightly higher for larger value of ρ for all the values of w_1 and for both the users. Moreover, it can be noted from Figs. 4.9(a) and (b) that as the target rate increases, the outage as well as throughput performances of both the users are superior for $w_1 = 0.1$.

Fig. 4.10 shows the ergodic capacity performance of the considered NOMA-based

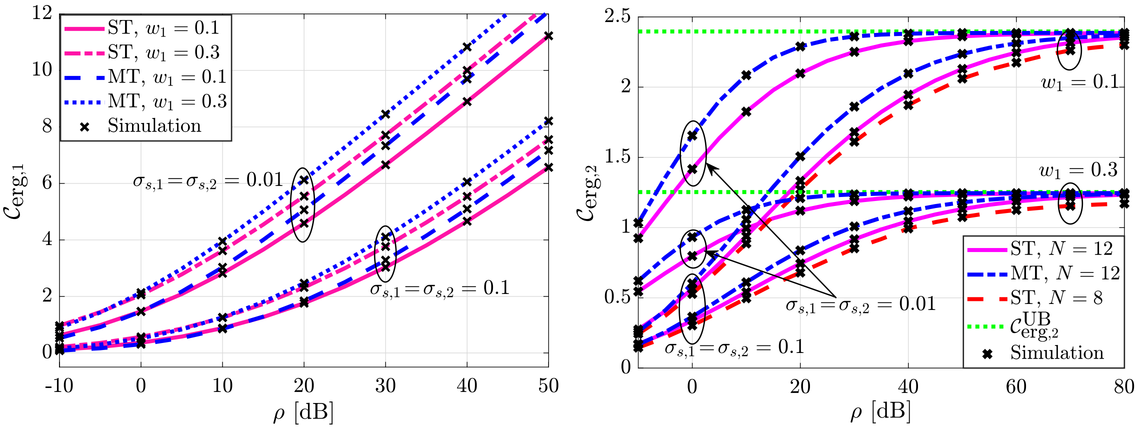

(a) Variation of ergodic capacity of U_1 w.r.t transmit SNR.

(b) Variation of ergodic capacity of U_2 w.r.t transmit SNR.

Figure 4.10: Ergodic capacity performance of the considered NOMA-based IRS-assisted mixed FSO-RF communication system a) Variation of ergodic capacity of U_1 w.r.t transmit SNR, b) Variation of ergodic capacity of U_2 w.r.t transmit SNR

IRS-assisted mixed FSO-RF system utilizing SLIPT technology under different turbulence and pointing error conditions. In Figs. 4.10(a) and (b), we have shown the variations of ergodic capacity w.r.t average transmit SNR for U_1 and U_2, respectively. It can be noticed from Fig. 4.10(a) that the ergodic performance of U_1 severely degrades for larger misalignment error conditions in comparison to the degradation for strong atmospheric turbulence. Moreover, the impact of turbulence condition is dominant at low pointing error values. It is intuitive to observe from Fig. 4.10(a) that larger power allocation to U_1 achieves better ergodic capacity. Fig. 4.10(b) also depicts that the ergodic capacity performance[3] of U_2 is superior for low pointing error conditions for all the values of w_1 considered in the figure. However, as the transmit SNR increases, the gap between the capacity values for low and high pointing error conditions reduces. This is because of the saturation in ergodic capacity of U_2 is reached at a lower value of transmit SNR under low jitter conditions. We have also plotted the upper bound on $\mathcal{C}_{\mathrm{erg},2}$ (given in (4.47)) in Fig. 4.10(b) which overlaps with the numerically obtained capacity values for high transmit SNR conditions. It shall be noted from Figs. 4.10(a) and (b) that the ergodic rate of U_1 is significantly higher as compared to that for U_2, for all values of average SNR. Moreover, due the SIC, the ergodic capacity of U_2 gets a floor in the performance.

Observation 4.3: *It can be seen from Fig. 4.10(b) that the ergodic rate of U_2 can be slightly improved by using a large size RIRS. For example, at an average SNR of* 20 *dB,* $w_1 = 0.1$*, strong turbulence, and high pointing error conditions, the ergodic rate increases from* 1.21 *to* 1.332 *with an increase in* N *from* 8 *to* 12*.*

[3]Here. the analytical values of $\mathcal{C}_{\mathrm{erg},2}$ have been obtained by numerically integrating (4.45) and (4.46).

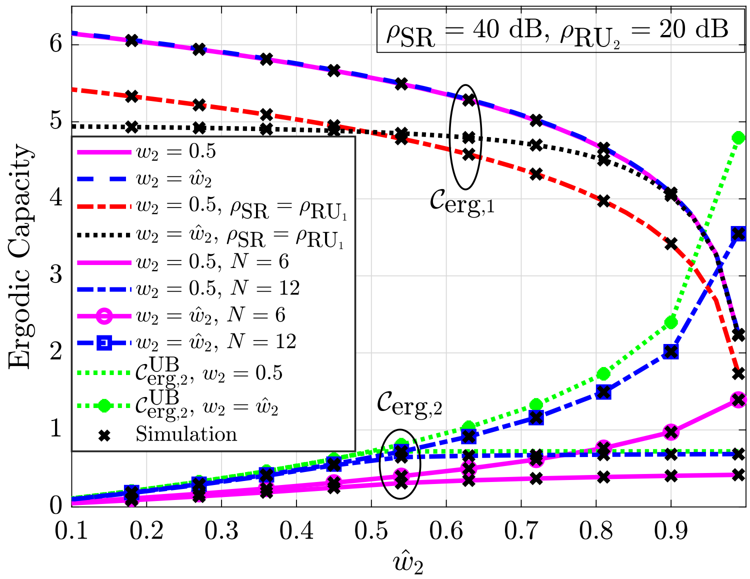

Figure 4.11: Impact of power allocation factors on the ergodic capacity OF U_1 and U_2 at MT with $\rho = 20$ dB, and $\sigma_{s,1} = \sigma_{s,2} = 0.01$.

In Fig. 4.11, we have shown the impact of power allocation factor on the ergodic capacity of both the users under moderate turbulence and low jitter deviation conditions. Specifically, we have plotted $\mathcal{C}_{\text{erg},1}$ and $\mathcal{C}_{\text{erg},2}$ w.r.t $\hat{w}_2$ under two conditions (i) similar power allocation in both FSO and RF hops (i.e., $w_2 = \hat{w}_2$), and (ii) fixed power allocation in FSO hop (i.e., $w_2 = 0.5$). It can be seen from Fig. 4.11 that under the condition (i), $\mathcal{C}_{\text{erg},1}$ (or $\mathcal{C}_{\text{erg},2}$) decreases (or increases) for increasing $\hat{w}_2$, whereas under condition (ii), $\mathcal{C}_{\text{erg},2}$ saturates at a small value after $\hat{w}_2 = 0.5$ and $\mathcal{C}_{\text{erg},1}$ is almost constant up to sufficiently high value of $\hat{w}_2$ under the condition of $\rho_{\text{SR}} = \rho_{\text{RU}_1}$. Thus, it can be deduced from Fig. 4.11 that varying the power allocation over both the hops equally can result in enhanced capacity for U_2 by keeping the sum rate constant. Further, if we increase the transmit SNR of FSO hop, i.e., $\rho_{\text{SR}} = \rho_{\text{RU}_1} + 20$ dB, the ergodic rate of U_1 behaves exactly same under both the conditions of $w_2 = \hat{w}_2$ and $w_2 = 0.5$. We have also plotted the UB on the ergodic capacity of U_2 under both the power allocation conditions and it is clear from the figure that it follows well. The impact of N on the capacity performance of U_2 can also be observed from Fig. 4.11 as larger values of N can provide significantly high capacity gains for the far user.

Fig. 4.12 compares the ergodic sum rate performance of U_1 and U_2 for the proposed NOMA-based IRS-assisted mixed FSO-RF system utilizing SLIPT with an OMA-based IRS-assisted mixed FSO-RF system as well as a mixed FSO-RF system sans IRS. The results clearly demonstrate that the ergodic sum rate is significantly higher for the proposed NOMA-based system compared than that for the OMA-based system across

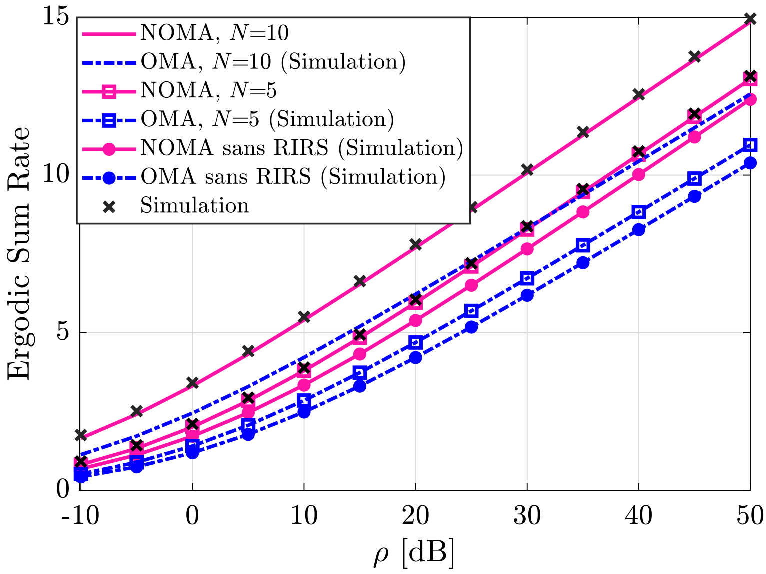

Figure 4.12: Comparison of ergodic sum rate performance for NOMA-based IRS-assisted mixed FSO-RF system utilizing SLIPT with OMA-based IRS-assisted mixed FSO-RF system as well as mixed FSO-RF system sans IRS

all ranges of SNRs. Furthermore, the integration of RIRS in both the NOMA and OMA systems leads to an additional improvement in the ergodic sum rate. Thus, it is evident that the proposed NOMA-based IRS-assisted mixed FSO-RF system with SLIPT outperforms the conventional OMA-based system and the mixed FSO-RF system without IRS. The higher ergodic sum rate achieved by NOMA, coupled with the benefits of RIRS integration, highlights the potential of this approach for future wireless communication systems.

Observation 4.4: *NOMA consistently outperforms OMA in terms of the transmit SNR requirements. This can be attributed to the higher spectrum efficiency of NOMA, enabling it to achieve better performance with lower SNR. For instance, to achieve a sum rate of* 10 *bps at* $N = 10$*, NOMA requires an SNR of approximately* 30 *dB, while OMA requires an SNR of approximately* 38 *dB. This highlights the superiority of NOMA in terms of achieving higher data rates with lower power levels.*

4.8 Summary

In this chapter, we have investigated the performance of OIRS-RIRS-aided DF relay-based mixed FSO-RF system utilizing a NOMA technique to assist two users in the RF link. The energy constraint problem of the wireless relay node is addressed by employing EH at the relay through SLIPT. Considering the instantaneously harvested power to be used by the relay for transmission over RF hop, we derived the analytical expressions of outage probability, throughput and ergodic rate for both users over $\mathcal{M}$-distributed FSO link with pointing error and Nakagami-m fading in the RF link. We also analyzed the system performance for asymptotically high transmit SNR conditions and obtained the diversity order of the system. Numerical results with useful observations were provided to see the impact of system and channel parameters on the system's performance. The integration of RIRS exhibits significant improvement in the performance of the weak user. Moreover, we also investigated the system performance for different power allocation settings over both the FSO and the RF links.

It has been shown through simulations that deployment of an OIRS with sufficient size and desired orientation improves the amount of harvested power to enable the reliable data transfer over the next hop. Furthermore, the deployment of an RIRS of suitable size and optimized reflection coefficients over RF hop ensures the sufficient received signal power, especially in the low transmit power conditions. Moreover, the simulations results show that the performance of proposed system with the practical discrete phase shifts realized using AO algorithm approaches to that of ideal phase shifts as the number of quantization levels increases.

Chapter 5

SOS for OIRS-Assisted FSO Communication System

5.1 Introduction

The efficiency of a wireless communication system degrades significantly in mobile channels with simultaneous time-variant multi-path fading and shadowing due to signal envelope variability [79]. Moreover, the temporal fluctuations in the received signal, resulting from the relative mobility of transmitter-and-receiver leads to the Doppler effect [29]. The effect of Doppler spread is more prominent at relatively lower wavelengths, e.g., as we go into mmWave communication and higher. Moreover, future 6G applications requires ultra-reliable low-latency communications, which necessitates a time-based performance evaluation. Thus, it becomes vital to characterize the dynamic temporal behaviour of fluctuations in the received envelope [107].

Conventionally, the first-order-statistics such as outage probability and bit-error-rate has been considered as a useful metric to measure link performance and it has been thoroughly studied for a variety of system models under different fading statistics. However, it captures the static behaviour of system under consideration [31]. To characterize the *dynamic behaviour* of the a system with multipath fading, the study of SOS, i.e., LCR and AOD have gained significant importance [32, 33, 34, 35, 36, 37, 38]. For example, for error control coding schemes, the statistical properties of outage time frames help the system designer to assess and implement adaptive communication systems. More importantly, it is crucial to study these performance metrics for choosing practical system design parameters, such as transmission symbol rate, interleaver depth, packet length, and time slot duration [33].

This chapter considers an FSO communication network utilizing a multi-aperture detector that performs SC to achieve spatial diversity. Assuming the inaccessibility of a direct FSO link, we consider the deployment of an OIRS to assist the communication.

The efficacy of the system under consideration is investigated by using the useful SOS. The SOS analysis is carried out in the presence of atmospheric turbulence, foggy conditions, and misalignment error. Specifically, the closed-form analytical expressions of LCR and AOD of SNR at the output of the SC receiver under non-isotropic scattering environment are eveloped. The effect of various system and channel parameters on LCR and AOD performances has been demonstrated, including the number of OIRS elements, the number of receiving apertures, Doppler shift, misalignment error and fog parameters, mean AOA, and degree of non-isotropic scattering. Further, by using FSMC model, we derive PER using the derived LCR expression. In order to have optimum packet length using FSMC model, we employ SW-ARQ protocol. The optimized packet length, which provides the maximum throughput under the SW-ARQ protocol, is also determined. Additionally, it is shown how different system settings affect PER and throughput performances.

5.1.1 State-of-the-Art

The study of SOS in terms of LCR and AOD has been extensively done in the existing literature. The LCR and AOD was investigated for the first time by Rice in his pioneering research [32]. Later on, many researchers have investigated SOS under different channel and system model [33, 34, 36, 37, 38]. The authors in [33] studied the SOS of multipath fading channels considering the non-isotropic scattering scenario under Rayleigh, Nakagami, and Rician channel distribution. In addition, the dynamic time-varying attributes of the various fading channel are well explored through SOS. In [34], the authors derived exact closed-form expressions for the LCR and AOD of the signal envelope in $\mathcal{F}$ composite fading channels for device-to-device communications. Furthermore, in [34] the response of LCR and AOD is analyzed under multipath fading as well as shadowing conditions. The study of SOS for relaying system was investigated in [36, 37, 38]. Further, the study of SOS for the diversity combing techniques was well explored in [108, 109, 110, 111, 112]. The authors in [108] obtained exact closed form expressions of LCR and AOD for output signal envelope of Selection combiner corrupted by AWGN under Rayleigh, Nakagami, and Rician fading. The authors in [109] obtained exact closed-form expressions of LCR and AOD for output signal envelope of SC, maximal ratio combining (MRC), and equal gain combining (EGC) receiver corrupted by AWGN under Nakagami fading and the impact of diversity and the number of receiving branches were analyzed. Further, in [110, 111, 112], the authors derived closed-form expressions of LCR and AOD for the interference-limited systems utilizing MRC receiver. The derived

LCR expression in [110, 111, 112] was used to obtain the PER and optimal packet length for throughput maximization by deploying the SW-ARQ transmission scheme via FSMC model. However, the authors in both [111] and [112] considered Rayleigh distribution for the desired as well as interference links. The major limitation of these diversity receiver system is that they require multiple receiving antennas leading to complexity and increased cost.

In the context of the FSO communication network, the performance analysis in terms of first-order statistics has been extensively done over past years. However, the performance analysis in terms of SOS is limited [35, 113, 114, 115]. In particular, [35] developed integral and Gauss Laguerre equations for the SOS (such as LCR and AOD) considering the multi-hop FSO links taking into account the weak atmospheric turbulence (modeled as log-normal distribution) and misalignment error. In [113], the closed-form analytical expressions of LCR and AOD are derived for a hybrid RF-FSO-RF vehicular network where RF link is modeled as Nakagami fading distribution whereas the FSO link is modeled by Gamma-Gamma fading. In [114], authors considered an AF-based multihop FSO communication system and investigated LCR and AOD under atmospheric turbulence modeled by Gamma-Gamma fading. Recently, the LCR and AOD were derived for the satellite to unmanned aerial vehicles (UAVs) FSO communication network under weak atmospheric turbulence and pointing error[115].

5.1.2 Novelity and Contributions

To the best of the authors' knowledge, there is no existing literature that examined the SOS for an IRS-assisted FSO communication network. Therefore, we present a novel framework that study SOS for OIRS-assisted FSO communication network. In order to combat fog, turbulence, and misalignment error, we employ spatial diversity technique based on SC technique where the signal with maximum received power is used for detection. Furthermore, we utilize Gamma-Gamma fading distribution for the atmospheric turbulence with fog and misalignment errors at the OIRS and PD receiver. This study is extremely beneficial for delay-sensitive applications, especially in vehicular communication scenarios.

The chapter's technical contribution is outlined as follows:

- We consider an OIRS-assisted FSO-based communication network consisting of a single-aperture transmitter and a multi-aperture receiver and derive the statistical distribution of the received SNR at a particular receiving aperture by assuming independent and non-identically distributed (INID) optical links.

- Under the impact of random fog, Gamma-Gamma distributed atmospheric turbulence, and zero-boresight misalignment errors, we derive the closed-form analytical expressions for LCR and AOD for the considered FSO-based communication network under the non-isotropic scattering environment.

- Further, using FSMC model, we derive an expression for the PER utilizing the derived LCR expression. To achieve optimum packet length using the FSMC model, we employ a SW-ARQ protocol at the link layer. The optimized packet length, which provides the maximum throughput under the SW-ARQ protocol, is also determined.

- Extensive numerical results have been provided to show the effect of various system and channel parameters such as the number of OIRS elements, the number of receiving apertures, Doppler shift, misalignment error and fog parameters, mean AoA, and degree of non-isotropic scattering on the system's performance.

5.2 System Model

We consider a down-link FSO-based communication network, where the information signal is transmitted via a single aperture transmit source (S) and received by mobile user destination (D) consisting of $\mathcal{J} = \{1, 2, \cdots, J\}$ receive apertures where the j-th receive aperture is denoted by D_j. We employ SIM technique at S, where the optical carrier or laser beam is intensity modulated using the digitally modulated RF sub-carrier. Further, non-coherent IMDD technique is employed at PD of D_j to detect the received signal. In our scenario, the direct link from S to D_j is blocked due to obstacles such as buildings, trees, and heavy vehicles. Therefore, communication between S and D_j for $j \in J$ is facilitated by an OIRS that comprises N elements capable of reflecting signals. Such situations are common in urban environments, where severe shadowing can cause connectivity issues with direct link for the signal received at the receiver.

5.2.1 Transmission Scheme

The node S uses SIM to transmit electrical message signal $x_m(t)$ at time t over the FSO link. Assume P_{S} be the transmission power available at S for transmitting the optical signal $s_m(t)$, then $s_m(t)$ is written as

$$s_m(t) = \sqrt{P_{\mathrm{S}}} \left[\delta x_m(t) + \mathcal{B}\right], \tag{5.1}$$

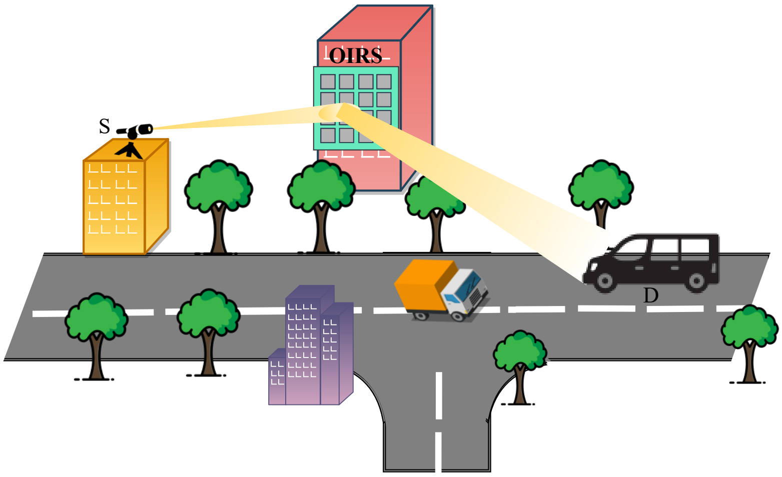

Figure 5.1: System model of OIRS-assisted multi-aperture based communication network.

where δ is the electrical to optical conversion coefficient and $\mathcal{B}$ is the DC bias that has to be added to $x_m(t)$ to ensure non-negative signal. The incoming optical signal at D_j is passed through an optical band pass filter (OBPF) that restricts the background radiations [116]. The output of the OBPF is then fed to the PD of D_j. Let the vectors $\mathbf{I}_{\mathrm{SR}}^T(t) \in \mathbb{C}^{1\times N}$ and $\mathbf{I}_{\mathrm{RD}_j}^T(t) \in \mathbb{C}^{1\times N}$ represent the channel gain vectors for S to OIRS (SR) and the OIRS to D_j (RD_j) links, respectively. Then, received signal at D_j can be given by

$$r_{\mathrm{D}_j}(t) = \eta R_{\mathrm{P}} A_{\mathrm{P}} \sqrt{P_{\mathrm{S}}}\, \mathbf{I}_{\mathrm{SR}}^T(t) \boldsymbol{\Theta} \mathbf{I}_{\mathrm{RD}_j}(t) s_m(t) + e_{\mathrm{D}_j}(t), \tag{5.2}$$

where P_{S} be the total transmit power available at S, η is the optical to electrical conversion coefficient, R_{P} and A_{P} are the responsivity and detection area of the PD; $e_{\mathrm{D}_j} \sim \mathcal{N}\left(0, \sigma_{\mathrm{D}_j}^2\right)$ is the ZM-AWGN introduced at D_j. The matrix $\boldsymbol{\Theta}$ is an $N \times N$ diagonal matrix containing the reflection coefficients of OIRS, defined as $\boldsymbol{\Theta} = \mathrm{diag}\left\{\varpi_{\mathrm{O}}^{(1)}, \cdots, \varpi_{\mathrm{O}}^{(N)}\right\}$, where reflection coefficient of n-th OIRS unit is given by $\varpi_{\mathrm{O}}^{(n)} = \left|\varpi_{\mathrm{O}}^{(n)}\right| e^{\jmath \angle \varpi_{\mathrm{O}}^{(n)}}$; $e_{\mathrm{D}_j} \sim \mathcal{N}\left(0, \sigma_{\mathrm{D}_j}^2\right)$ is the AWGN introduced at D_j that accounts for background and thermal noise. If n-th elements of $\mathbf{I}_{\mathrm{SR}}^T(t)$ and $\mathbf{I}_{\mathrm{RD}_j}^T(t)$ are represented as $I_{\mathrm{SR}}^{(n)}(t)$ and $I_{\mathrm{RD}_j}^{(n)}(t)$, respectively, we can rewrite (5.2) as

$$\begin{aligned} r_{\mathrm{D}_j}(t) = {} & \underbrace{\eta R_{\mathrm{P}} A_{\mathrm{P}} \sqrt{P_{\mathrm{S}}} \left[\sum_{n=1}^{N} \left|I_{\mathrm{SR}}^{(n)}(t)\right| \left|\varpi_{\mathrm{O}}^{(n)}\right| \left|I_{\mathrm{RD}_j}^{(n)}(t)\right| e^{\jmath \Delta\Phi^{(n)}(t)}\right] \delta x(t)}_{I_{AC}} \\ & \underbrace{+ \eta R_{\mathrm{P}} A_{\mathrm{P}} \sqrt{P_{\mathrm{S}}} \left[\sum_{n=1}^{N} \left|I_{\mathrm{SR}}^{(n)}(t)\right| \left|\varpi_{\mathrm{O}}^{(n)}\right| \left|I_{\mathrm{RD}_j}^{(n)}(t)\right| e^{\jmath \Delta\Phi^{(n)}(t)}\right] \mathcal{B}}_{I_{DC}} + e_{\mathrm{D}_j}(t), \end{aligned} \tag{5.3}$$

where $\Delta\Phi^{(n)}(t) = \angle I_{\mathrm{SR}}^{(n)}(t) + \angle I_{\mathrm{RD}_j}^{(n)}(t) - \angle\varpi_{\mathrm{O}}^{(n)}$. It may be noted that the value of reflection phase at n-th OIRS unit (i.e., $\angle\varpi_{\mathrm{O}}^{(n)}$) can be chosen through optimization-based resource allocation by maximizing a key performance metrics. Furthermore, it is reasonable to assume that for optimized phase shift values at OIRS unit, the phase difference $\Delta\Phi^{(n)}(t)$ is sufficiently small and can be neglected for the purpose of performance analysis. It can also be noted that the DC component present in received signal in (5.3) is unwanted and can be discarded using the power splitter. The AC component is used for further processing.

5.2.2 Channel Model

We consider that an FSO link suffers from the random fog, atmospheric turbulence and pointing error due to the misalignment. Therefore, amplitude of channel coefficient of the n-th FSO link is given by $\left|I_i^{(n)}\right| = \left|I_{f,i}^{(n)}\right| \left|I_{a,i}^{(n)}\right| \left|I_{p,i}^{(n)}\right|$, $i \in \{\mathrm{SR}, \mathrm{RD}_j\}$, where $\left|I_{f,i}^{(n)}\right|$, $\left|I_{a,i}^{(n)}\right|$, and $\left|I_{p,i}^{(n)}\right|$ denote the amplitudes corresponding to random fog, atmospheric turbulence, and misalignment error, respectively.

Random Fog

The channel coefficient $\left|I_{f,i}^{(n)}\right|$ exhibits path loss in foggy environment that causes extinction of the optical signal by the process of absorption and scattering. The path loss in foggy environment is random following the PDF given by [117]

$$f_{\left|I_{f,i}^{(n)}\right|}(x) = \frac{\left(v_i^{(n)}\right)^{\tau_i^{(n)}}}{\Gamma(\tau_i^{(n)})} \left[\ln\left(\frac{1}{x}\right)\right]^{\tau_i^{(n)}-1} x^{v_i^{(n)}-1}, \quad 0 < x \leq 1, \tag{5.4}$$

where the value of parameter $v_i^{(n)} = \frac{4.343}{L_i^{(n)}\zeta_i^{(n)}}$, $L_i^{(n)}$ is the position-dependent link distance, $\tau_i^{(n)} > 0$ is shape parameter, $\zeta_i^{(n)} > 0$ is the scale parameter in the range of $0 < \vartheta_i^{(n)} < \infty$, where $\vartheta_i^{(n)}$ is attenuation coefficient modelled by Gamma distribution.

Atmospheric turbulence

The atmospheric turbulence coefficient $\left|I_{a,i}^{(n)}\right|$ is modelled using Gamma-Gamma distribution and its PDF is given by

$$f_{\left|I_{a,i}^{(n)}\right|}(x) = \frac{2(\alpha_i^{(n)}\beta_i^{(n)})^{\frac{\alpha_i^{(n)}+\beta_i^{(n)}}{2}}}{\Gamma(\alpha_i^{(n)})\Gamma(\beta_i^{(n)})} x^{\frac{\alpha_i^{(n)}+\beta_i^{(n)}}{2}-1} K_{\alpha_i^{(n)}-\beta_i^{(n)}}\left(2\sqrt{\alpha_i^{(n)}\beta_i^{(n)}x}\right), \tag{5.5}$$

where the fading parameters $\alpha_i^{(n)}$ and $\beta_i^{(n)}$ depend on position dependent link distance and is associated to the effective number of large-scale cells defining the scattering process. Further, $K_v(\cdot)$ is the Bessel function of second kind and v-th order defined [68]

Pointing Error

The channel coefficient $I_{p,i}^{(n)}$ accounts for pointing loss at OIRS/D$_j$ following the PDF given by

$$f_{\left|I_{p,i}^{(n)}\right|}(x)=\frac{\left(\xi_i^{(n)}\right)^2}{\left(A_{o,i}^{(n)}\right)^{\left(\xi_i^{(n)}\right)^2}}x^{\left(\xi_i^{(n)}\right)^2-1},\ \ 0\leq I_{p,i}^{(n)}\leq A_{o,i}^{(n)}, \tag{5.6}$$

where $i\in\{\mathrm{SR},\mathrm{RD}_j\}$, $A_{o,i}^{(n)}=\left[\mathrm{erf}(r_i^{(n)})\right]^2$ is the fraction of power received at OIRS/D$_j$ where $\mathrm{erf}(\cdot)$ is the error function [68]. Further, $r_i^{(n)}=d_i^{(n)}\sqrt{\pi}/W_{z,i}^{(n)}$ with $d_i^{(n)}$ and $W_{z,i}^{(n)}$ being the radius of the receiver aperture and the beam waist, respectively; $\xi_i^{(n)}=\frac{W_{e,i}^{(n)}}{2\sigma_{s,i}^{(n)}}$ is the ratio of equivalent beam radius ($W_{e,i}^{(n)}$) and jitter deviation at OIRS/D$_j$ ($\sigma_{s,i}^{(n)}$). The parameter $\xi_i^{(n)}$ is pointing error factor, where $\xi_i^{(n)}\to 0$ corresponds to very high pointing error and $\xi_i^{(n)}\to\infty$ corresponds to very low pointing error. The equivalent beam radius is defined by

$$W_{e,i}^{(n)}=\frac{\left(W_{z,i}^{(n)}\right)^2\sqrt{\pi}\mathrm{erf}(r_i^{(n)})}{2r_i^{(n)}e^{-(r_i^{(n)})^2}}. \tag{5.7}$$

It can noted from the above discussion that the misalignment parameter $\xi_i^{(n)}$ is the function of beam waist at the receiver of i-th link. Therefore, considering the link distances of SR and RD$_j$ links, beam divergences, and incident angle of beam, we define the beam waist at the receiver of i-th link as follows.

- **Beam waist at the OIRS**

Considering elliptical beam footprint at n-th OIRS element, the beam waist is expressed as [30]

$$W_{z,\mathrm{SR}}^{(n)}=\frac{L_{\mathrm{SR}}^{(n)}\theta_{\mathrm{S}}^{(n)}}{2}\sqrt{\frac{\cos(\theta_{\mathrm{S}}^{(n)}/2)}{\cos(\phi_{\mathrm{OIRS}}^{(n)}+\theta_{\mathrm{S}}^{(n)}/2)}}, \tag{5.8}$$

where $\theta_{\mathrm{S}}^{(n)}$ is the beam divergence angle at S and $\phi_{\mathrm{OIRS}}^{(n)}$ is the incident angle of beam at OIRS.

- **Beam waist at the D$_j$**

The optical beam is perceived by D$_j$ as if it was transmitted by n-th OIRS element with divergence angle $\theta_{\mathrm{OIRS}}^{(n)}=\theta_{\mathrm{S}}\left(1+L_{\mathrm{SR}}^{(n)}/L_{\mathrm{RD}_j}^{(n)}\right)$. Considering elliptical beam footprint at D$_j$

, the beam waist at D_j is given as [30]

$$W_{z,\mathrm{D}_j} = \frac{L_{\mathrm{RD}_j}^{(n)} \theta_{\mathrm{OIRS}}^{(n)}}{2} \sqrt{\frac{\cos(\theta_{\mathrm{S}}^{(n)}/2)}{\cos(\phi_{\mathrm{D}_j}^{(n)} + \theta_{\mathrm{S}}^{(n)}/2)}}$$
$$\triangleq \frac{\left(L_{\mathrm{SR}}^{(n)} + L_{\mathrm{RD}_j}^{(n)}\right) \theta_{\mathrm{S}}^{(n)}}{2} \sqrt{\frac{\cos(\theta_{\mathrm{S}}^{(n)}/2)}{\cos(\phi_{\mathrm{D}_j}^{(n)} + \theta_{\mathrm{S}}^{(n)}/2)}}, \tag{5.9}$$

where $\phi_{\mathrm{D}_j}^{(n)}$ is the angle of incidence beam at D_j.

Further, the composite PDF of atmospheric turbulence and misalignment error, i.e., $\left|I_{ap,i}^{(n)}\right| = \left|I_{a,i}^{(n)}\right| \left|I_{p,i}^{(n)}\right|$, can be obtained as

$$f_{\left|I_{ap,i}^{(n)}\right|}(y) = \int_0^\infty \frac{1}{x} f_{\left|I_{a,i}^{(n)}\right|}\left(\frac{y}{x}\right) f_{\left|I_{p,i}^{(n)}\right|}(x) dx. \tag{5.10}$$

Substituting the PDF of $\left|I_{a,i}^{(n)}\right|$ and $\left|I_{p,i}^{(n)}\right|$ from (5.5) and (5.6), respectively, and utilizing [63, (07.34.03.0605.01)] and [63, (07.34.21.0085.01)], we get

$$f_{\left|I_{ap,i}^{(n)}\right|}(y) = \frac{\alpha_i^{(n)} \beta_i^{(n)} \left(\xi_i^{(n)}\right)^2}{A_{o,i} \Gamma\left(\alpha_i^{(n)}\right) \Gamma\left(\beta_i^{(n)}\right)} G_{1,3}^{3,0}\left(\frac{\alpha_i^{(n)} \beta_i^{(n)} y}{A_{o,i}^{(n)}} \middle| \begin{matrix} a_i^{(n)} \\ \left\{b_{i,p}^{(n)}\right\}_{p=1}^3 \end{matrix}\right), \tag{5.11}$$

where $a_i^{(n)} = \left(\xi_i^{(n)}\right)^2$, and $b_i^{(n)} = \left\{\left(\xi_i^{(n)}\right)^2 - 1, \alpha_i^{(n)} - 1, \beta_i^{(n)} - 1\right\}$.

Lemma 5.1: *The PDF of channel coefficient* $\left|I_i^{(n)}\right| = \left|I_{f,i}^{(n)}\right| \left|I_{ap,i}^{(n)}\right|$ *which accounts random fog, atmospheric turbulence and misalignment error is given as*

$$f_{\left|I_i^{(n)}\right|}(z) = \left(v_i^{(n)}\right)^{\tau_i^{(n)}} \psi_i^{(n)} G_{1+\tau_i^{(n)}, 3+\tau_i^{(n)}}^{3+\tau_i^{(n)}, 0}\left(C_i^{(n)} z \middle| \begin{matrix} a_i^{(n)}, \left\{v_i^{(n)}\right\}_1^{\tau_i^{(n)}} \\ \left\{b_{i,p}^{(n)}\right\}_{p=1}^3, \left\{v_i^{(n)} - 1\right\}_1^{\tau_i^{(n)}} \end{matrix}\right), \tag{5.12}$$

where $\psi_i^{(n)} = \frac{\alpha_i^{(n)} \beta_i^{(n)} \left(\xi_i^{(n)}\right)^2}{A_{o,i}^{(n)} \Gamma(\alpha_i^{(n)}) \Gamma(\beta_i^{(n)})}$ *and* $C_i^{(n)} = \frac{\alpha_i^{(n)} \beta_i^{(n)}}{A_{o,i}^{(n)}}$.

Proof. See Appendix A.4.1 for the proof. □

5.3 Statistical Distribution of SNR

Under this section, we obtained statistical analysis of SNR at D for the considered OIRS-assisted FSO network by obtaining the statistical distributions of the received SNR. Following (5.3), the maximum SNR of the j-th receive aperture D_j assuming $\Delta\Phi^{(n)}(t) = 0$

can be expressed as

$$\Gamma_{\mathrm{D}_j}(t) = \frac{\eta^2 R_{\mathrm{P}}^2 A_{\mathrm{P}}^2 \delta^2 P_{\mathrm{S}} \left| \sum_{n=1}^{N} \left| I_{\mathrm{SD}_j}^{(n)}(t) \right| \right|^2}{\sigma_{\mathrm{D}_j}^2} \triangleq \bar{\gamma} \left| I_{\mathrm{SD}_j}(t) \right|^2, \tag{5.13}$$

where $\left| I_{\mathrm{SD}_j}^{(n)}(t) \right| = \left| I_{\mathrm{SR}}^{(n)}(t) \right| \left| \varpi_{\mathrm{O}}^{(n)} \right| \left| I_{\mathrm{RD}_j}^{(n)}(t) \right|$, $\bar{\gamma} = \frac{\eta^2 R_{\mathrm{P}}^2 A_{\mathrm{P}}^2 \delta^2 P_{\mathrm{S}}}{\sigma_{\mathrm{D}_j}}$, and $\left| I_{\mathrm{SD}_j}(t) \right|$ is the amplitude channel coefficient of n-th received signal at D_j. For a fixed t, the PDF of $I_{\mathrm{SD}_j}^{(n)}$ can be evaluated as [89]

$$f_{\left| I_{\mathrm{SD}_j}^{(n)} \right|}(u) = \int_0^\infty \frac{1}{\left| \varpi_{\mathrm{O}}^{(n)} \right| z} f_{\left| I_{\mathrm{SR}}^{(n)} \right|} \left(\frac{u}{\left| \varpi_{\mathrm{O}}^{(n)} \right| z} \right) f_{\left| I_{\mathrm{RD}_j}^{(n)} \right|}(z) dz. \tag{5.14}$$

Substituting the PDF of $\left| I_i^{(n)} \right|$ from (5.12) in (5.14) and utilizing [63, (07.34.21.0011.01)], we get PDF of $\left| I_{\mathrm{SD}_j}^{(n)} \right|$ obtained as

$$f_{\left| I_{\mathrm{SD}_j}^{(n)} \right|}(u) = \left(v_{\mathrm{SR}}^{(n)} \right)^{\tau_{\mathrm{SR}}^{(n)}} \left(v_{\mathrm{RD}_j}^{(n)} \right)^{\tau_{\mathrm{RD}_j}^{(n)}} \frac{\psi_{\mathrm{SR}}^{(n)} \psi_{\mathrm{RD}_j}^{(n)}}{\left| \varpi_{\mathrm{O}}^{(n)} \right|}$$
$$\times G^{6+\tau_{\mathrm{SR}}^{(n)}+\tau_{\mathrm{RD}_j}^{(n)},0}_{2+\tau_{\mathrm{SR}}^{(n)}+\tau_{\mathrm{RD}_j}^{(n)},6+\tau_{\mathrm{SR}}^{(n)}+\tau_{\mathrm{RD}_j}^{(n)}} \left(\frac{C_{\mathrm{SR}}^{(n)} C_{\mathrm{RD}_j}^{(n)} u}{\left| \varpi_{\mathrm{O}}^{(n)} \right|} \middle| \begin{matrix} a_{\mathrm{SR}}^{(n)}, \left\{ v_{\mathrm{SR}}^{(n)} - 1 \right\}_1^{\tau_{\mathrm{SR}}^{(n)}}, a_{\mathrm{RD}_j}^{(n)}, \left\{ v_{\mathrm{RD}_j}^{(n)} 1 \right\}_1^{\tau_{\mathrm{RD}_j}^{(n)}} \\ \left\{ b_{\mathrm{SR},p}^{(n)} \right\}_{p=1}^{3}, \left\{ v_{\mathrm{SR}}^{(n)} - 1 \right\}_1^{\tau_{\mathrm{SR}}^{(n)}}, \left\{ b_{\mathrm{RD}_j,p}^{(n)} \right\}_{p=1}^{3}, \left\{ v_{\mathrm{RD}_j}^{(n)} - 1 \right\}_1^{\tau_{\mathrm{RD}_j}^{(n)}} \end{matrix} \right). \tag{5.15}$$

Remark 5.1: *As per the definition of Meijer-G function* $G_{p,q}^{m,n}\left(x \middle| \begin{smallmatrix} a_1,\ldots,a_p \\ b_1,\ldots,b_q \end{smallmatrix} \right)$ *defined in [63], the parameters* $m, n, p,$ *and* q *must be a natural number, i.e.,* $m, n, p, q \in \mathbb{N}$. *However, it can be observed from* (5.15) *that the parameters of Meijer-G function in* (5.15) *involve* $\tau_i^{(n)}$, $i \in \{SR, RD_j\}$, *which is the shape parameter of the random fog over* n*-th FSO link of* i*-th channel, and can take any positive real value. Therefore, it can be deduced that the PDF expression obtained in* (5.15) *are valid for positive integer values of parameter* $\tau_i^{(n)}$ *for all values of* i *and* n.

Theorem 5.1: *Considering channel coefficient* I_{SD_j} *to be the sum of* N *i.n.i.d. RVs as* $I_{SD_j} = \sum_{n=1}^{N} \left| I_{SD_j}^{(n)} \right|$, *where* $\left| I_{SD_j}^{(n)} \right|$ *is the composite channel gain of S to* n*-th OIRS element and* n*-th IRS element to* D_j *links, then the PDF and CDF of* I_{SD_j} *are given interms of* *multi-variate Fox-H function (defined in [104]) as*

$$
\begin{aligned}
f_{I_{SD_j}}(u) = {} & \prod_{n=1}^{N} \frac{\psi_{SR}^{(n)}\psi_{RD_j}^{(n)}}{\left|\varpi_O^{(n)}\right|} (v_{SR}^{(n)})^{\tau_{SR}^{(n)}} (v_{RD_j}^{(n)})^{\tau_{RD_j}^{(n)}} \\
& \times H^{0,0:6+\tau_{SR}^{(1)}+\tau_{RD_j}^{(1)},1;\cdots;6+\tau_{SR}^{(N)}+\tau_{SR}^{(N)},1}_{0,1:3+\tau_{SR}^{(1)}+\tau_{RD_j}^{(1)},6+\tau_{SR}^{(1)}+\tau_{RD_j}^{(1)};\cdots;3+\tau_{SR}^{(N)}+\tau_{RD_j}^{(N)},6+\tau_{SR}^{(N)}+\tau_{RD_j}^{(N)}} \left[\begin{array}{c|c} u\frac{C_{SR}^{(1)}C_{RD_j}^{(1)}}{\left|\varpi_O^{(1)}\right|} & \\ \cdot & -:\mathbb{P}:\{(1,1)\}_1^N \\ \cdot & \\ \cdot & (0;1,\cdots,1):\mathbb{Q} \\ u\frac{C_{SR}^{(N)}C_{RD_j}^{(N)}}{\left|\varpi_O^{(N)}\right|} & \end{array} \right],
\end{aligned}
\tag{5.16}
$$

and

$$
\begin{aligned}
\mathcal{F}_{I_{SD_j}}(u) = {} & u\prod_{n=1}^{N} \frac{\psi_{SR}^{(n)}\psi_{RD_j}^{(n)}}{\left|\varpi_O^{(n)}\right|} (v_{SR}^{(n)})^{\tau_{SR}^{(n)}} (v_{RD_j}^{(n)})^{\tau_{RD_j}^{(n)}} \\
& \times H^{0,0:6+\tau_{SR}^{(1)}+\tau_{RD_j}^{(1)},1;\cdots;6+\tau_{SR}^{(N)}+\tau_{SR}^{(N)},1}_{0,1:3+\tau_{SR}^{(1)}+\tau_{RD_j}^{(1)},6+\tau_{SR}^{(1)}+\tau_{RD_j}^{(1)};\cdots;3+\tau_{SR}^{(N)}+\tau_{RD_j}^{(N)},6+\tau_{SR}^{(N)}+\tau_{RD_j}^{(N)}} \left[\begin{array}{c|c} u\frac{C_{SR}^{(1)}C_{RD_j}^{(1)}}{\left|\varpi_O^{(1)}\right|} & \\ \cdot & -:\mathbb{P}:\{(1,1)\}_1^N \\ \cdot & \\ \cdot & (-1;1,\cdots,1):\mathbb{Q} \\ u\frac{C_{SR}^{(N)}C_{RD_j}^{(N)}}{\left|\varpi_O^{(N)}\right|} & \end{array} \right].
\end{aligned}
\tag{5.17}
$$

where

$$
\begin{aligned}
\mathbb{P} &= \left\{ a_{SR}^{(n)}, \left\{ v_{SR}^{(n)} - 1 \right\}_1^{\tau_{SR}^{(n)}}, a_{RD_j}^{(n)}, \left\{ v_{RD_j}^{(n)} - 1 \right\}_1^{\tau_{RD_j}^{(n)}} \right\}_{n=1}^{N}, \\
\mathbb{Q} &= \left\{ \left\{ b_{SR,p}^{(n)} \right\}_{p=1}^{3}, \left\{ v_{SR}^{(n)} - 1 \right\}_1^{\tau_{SR}^{(n)}}, \left\{ b_{RD_j,p}^{(n)} \right\}_{p=1}^{3}, \left\{ v_{RD_j}^{(n)} - 1 \right\}_1^{\tau_{RD_j}^{(n)}} \right\}_{n=1}^{N}.
\end{aligned}
\tag{5.18}
$$

Proof. See Appendix A.4.2 for proof. □

The PDF and CDF of SNR, Γ_{D_j} (described in (5.13)) can be derived from (5.16) and (5.17), respectively, as

$$
f_{\Gamma_{\mathrm{D}_j}}(\gamma) = \frac{1}{2\sqrt{\bar{\gamma}}\gamma^{\frac{1}{2}}} f_{I_{\mathrm{SD}_j}}\left(\left(\frac{\gamma}{\bar{\gamma}}\right)^{1/2}\right), \tag{5.19}
$$

and

$$\mathcal{F}_{\Gamma_{\mathrm{D}_j}}(\gamma) = \mathcal{F}_{I_{\mathrm{SD}_j}}\left(\left(\frac{\gamma}{\bar{\gamma}}\right)^{1/2}\right). \tag{5.20}$$

Further, the mean and variance of Γ_{D_j} can be obtained from its moments.

Lemma 5.2: *The k-th moment of SNR received at the j-th receive aperture D_j for the considered OIRS-assisted FSO communication network is given by*

$$\mathcal{E}\left\{\Gamma_{D_j}^k\right\} = \frac{1}{2\epsilon^{k+1}}\prod_{n=1}^{N}\frac{\psi_{SR}^{(n)}\psi_{RD_j}^{(n)}}{\left|\varpi_O^{(n)}\right|}(v_{SR}^{(n)})^{\tau_{SR}^{(n)}}(v_{RD_j}^{(n)})^{\tau_{RD_j}^{(n)}}$$

$$\times H^{0,1:6+\tau_{SR}^{(1)}+\tau_{RD_j}^{(1)},1;\cdots;6+\tau_{SR}^{(N)}+\tau_{SR}^{(N)},1}_{1,1:3+\tau_{SR}^{(1)}+\tau_{RD_j}^{(1)},6+\tau_{SR}^{(1)}+\tau_{RD_j}^{(1)};\cdots;3+\tau_{SR}^{(N)}+\tau_{RD_j}^{(N)},6+\tau_{SR}^{(N)}+\tau_{RD_j}^{(N)}}\left[\begin{array}{c|c}\sqrt{\frac{1}{\epsilon\bar{\gamma}}}\frac{C_{SR}^{(1)}C_{RD_j}^{(1)}}{\left|\varpi_O^{(1)}\right|} & \\ \cdot & \left(-k,\frac{1}{2},\cdots,\frac{1}{2}\right):\mathbb{P} \\ \cdot & (0;1,\cdots,1):\mathbb{Q} \\ \cdot & \\ \sqrt{\frac{1}{\epsilon\bar{\gamma}}}\frac{C_{SR}^{(N)}C_{RD_j}^{(N)}}{\left|\varpi_O^{(N)}\right|} & \end{array}\right]. \tag{5.21}$$

Proof. See Appendix A.4.3 for the proof. □

Since we employ SC receiver at D that selects the maximum of diversity branches, the end-to-end instantaneous SNR considering Γ_{D_j} as received SNR of the j-th received aperture can be obtained as

$$\Gamma_{\mathrm{D}} = \max\left(\Gamma_{\mathrm{D}_1},\Gamma_{\mathrm{D}_2},\cdots,\Gamma_{\mathrm{D}_j}\right). \tag{5.22}$$

Following Remark 5.1, it can also be noted that expressions for the PDFs and the CDFs of composite channel gain I_{SD_j} (given in (5.16) and (5.17)) and hence the SNR Γ_{D_j} (defined in (5.19) and (5.20)), respectively, are applicable only for integer values of $\tau_i^{(n)}$, for all possible settings of i and n. Furthermore, the k-th order moment of SNR (expressed in (5.21)) will have the same limitation. Since the derivation of the LCR and AOD (given in the subsequent section) utilizes the PDF and the CDF of the SNR Γ_{D_j}, the restrictions of integer valued $\tau_i^{(n)}$ will hold true for the derived expressions.

5.4 Performance Evaluation

In this section, we examine how the OIRS-assisted FSO-based communication network behaves in terms of SOS performance measure like LCR and AOD. Additionally, with SW-ARQ protocol-based data transmission, we use the FSMC model to determine the PER and ideal packet length of the system.

5.4.1 Derivation of LCR and AOD

The LCR is a measure of the rate at which the received signal falls below a given threshold in the downward direction subject to time-varying channel conditions. It can be used to quantify the frequency of signal fade events over time. In the case of OIRS-assisted FSO-based communication network, the LCR represents the temporal rate of signal fade events occurring when the received SNR at receiver D falls below a predetermined threshold that determines the sensitivity of the receiver.

If Γ_{D} is the received SNR, the LCR at D can be evaluated by Rice's formula [32] defined as

$$\mathcal{L}_{\mathrm{D}}(\gamma_{\mathrm{Th}}) = \int_0^\infty \hat{\gamma} f_{\Gamma_{\mathrm{D}}\hat{\Gamma}_{\mathrm{D}}}(\gamma_{\mathrm{Th}}, \hat{\gamma}) d\hat{\gamma}, \tag{5.23}$$

where γ_{Th} is the SNR threshold, $f_{\Gamma_{\mathrm{D}}\hat{\Gamma}_{\mathrm{D}}}(\gamma, \hat{\gamma})$ is the joint PDF of Γ_{D} and its time derivative $\hat{\Gamma}_{\mathrm{D}}$.

The time derivative of PDF of instantaneous SNR through j-th receive branch, $\hat{\Gamma}_{\mathrm{D}_j}$ is Gaussian distributed with zero mean and variance $\mathcal{V}\left\{\hat{\Gamma}_{\mathrm{D}_j}\right\}$.

Lemma 5.3: *Under non-uniform Von-Mises distribution of AOA φ_{D_j} of the signal received at D_j due to non-isotropic scattering after signal reflection from the OIRS, the variance of the $\hat{\Gamma}_{D_j}$ is given by*

$$\mathcal{V}\left\{\hat{\Gamma}_{D_j}\right\} = 2\pi^2 f_D^2\, \mathcal{E}\left\{\Gamma_{D_j}^2\right\} \left[\bar{\varepsilon}\frac{\chi[I_0(\chi)+I_2(\chi)]\cos^2\bar{\varphi}_{D_j} + 2I_1(\chi)\sin^2\bar{\varphi}_{D_j}}{2\chi I_0(\chi)} + (1-\bar{\varepsilon})\right], \tag{5.24}$$

where $\bar{\varepsilon}$ specifies the amount of directional reception, $\bar{\varphi}_{D_j}$ represents the mean AOA at D_j, f_D represents the highest value of Doppler shift due to time-varying channel, χ denotes the degree of non-isotropic scattering, and $I_p(\cdot)$ represents the Modified Bessel function of first kind with the p-th order [68].

Proof. See Appendix A.4.4 for the proof. □

Table 5.1: Several approximation scattering models derived from Von-Mises distribution [1]

Parameter	Distribution
$\chi = 0$	Uniform distribution (Isotropic scattering)
$\chi = \infty$	Impulse distribution (Highly non-isotropic scattering)
$\chi \to 0$	Cardioid distribution
$\chi \to \infty$	Normal distribution

Table 5.1 lists the different approximation scattering models that can be derived from the Von-Mises distribution. Since each OIRS element accounts for non-isotropic scattering, a large value of χ is appropriate for the considered OIRS-assisted FSO-based communication network as seen from Table 5.1.

Corollary 5.1: *Assuming high level of non-isotropic scattering χ, i.e., $\chi \to \infty$, the Bessel's function can be estimated as $I_\nu(\chi) \approx \frac{e^\chi}{\sqrt{2\pi\chi}}$, for all ν. Therefore, for $\chi \to \infty$, the variance in* (5.24) *can be approximated as*

$$\mathcal{V}\left\{\hat{\Gamma}_{D_j}\right\} \approx 2\pi^2 f_D^2 \mathcal{E}\left\{\Gamma_{D_j}^2\right\}\left[\bar{\varepsilon}\cos^2\bar{\varphi}_{D_j} + (1-\bar{\varepsilon})\right]. \tag{5.25}$$

It should be noticed that the aforementioned expression does not depend on χ.

Further, the derivative of instantaneous SNR at the output of selection combiner, $\hat{\Gamma}_{\mathrm{D}}$ is given by

$$\hat{\Gamma}_{\mathrm{D}} = \hat{\Gamma}_{\mathrm{D}_j}, \text{ if } \Gamma_{\mathrm{D}_j} = \max\left(\{\Gamma_{\mathrm{D}_r}\}_{r=1}^{J}\right). \tag{5.26}$$

The joint PDF of Γ_{D} and $\hat{\Gamma}_{\mathrm{D}}$ can be obtained from jont CDF $\mathcal{F}_{\Gamma_{\mathrm{D}}\hat{\Gamma}_{\mathrm{D}}}(\gamma,\hat{\gamma})$ as

$$\begin{aligned}\mathcal{F}_{\Gamma_{\mathrm{D}}\hat{\Gamma}_{\mathrm{D}}}(\gamma,\hat{\gamma}) &= \Pr\left[\Gamma_{\mathrm{D}} < \gamma, \hat{\Gamma}_{\mathrm{D}} < \hat{\gamma}\right] \\ &= \sum_{j=1}^{J}\Pr\left[\Gamma_{\mathrm{D}_j} < \gamma, \hat{\Gamma}_{\mathrm{D}_j} < \hat{\gamma}, \Gamma_{\mathrm{D}_j} = \max\left(\{\Gamma_{\mathrm{D}_r}\}_{r=1}^{J}\right)\right]. \end{aligned} \tag{5.27}$$

Since Γ_{D_j} and $\hat{\Gamma}_{\mathrm{D}_j}$ are independent for all $j = 1, \cdots, J$, (5.27) can be written as

$$\begin{aligned}\mathcal{F}_{\Gamma_{\mathrm{D}}\hat{\Gamma}_{\mathrm{D}}}(\gamma,\hat{\gamma}) &= \sum_{j=1}^{J}\Pr\left[\hat{\Gamma}_{\mathrm{D}_j} < \hat{\gamma}\right]\Pr\left[\Gamma_{\mathrm{D}_j} < \gamma, \Gamma_{\mathrm{D}_j} = \max\left(\{\Gamma_{\mathrm{D}_r}\}_{r=1}^{J}\right)\right] \\ &= \sum_{j=1}^{J}\mathcal{F}_{\hat{\Gamma}_{\mathrm{D}_j}}(\hat{\gamma})\int_0^\gamma f_{\Gamma_{\mathrm{D}_j}}(x)\prod_{r=1,k\neq j}^{J}\mathcal{F}_{\Gamma_{\mathrm{D}_r}}(x)dx. \end{aligned} \tag{5.28}$$

Taking the derivative of (5.28) with respect to (w.r.t.) Γ_{D} and $\hat{\Gamma}_{\mathrm{D}}$, we get joint PDF,

$f_{\Gamma_{\mathrm{D}}\hat{\Gamma}_{\mathrm{D}}}(\gamma,\hat{\gamma})$ as

$$f_{\Gamma_{\mathrm{D}}\hat{\Gamma}_{\mathrm{D}}}(\gamma,\hat{\gamma}) = \sum_{j=1}^{J} f_{\hat{\Gamma}_{\mathrm{D}_j}}(\hat{\gamma}) f_{\Gamma_{\mathrm{D}_j}}(\gamma) \prod_{r=1,k\neq j}^{J} \mathcal{F}_{\Gamma_{\mathrm{D}_r}}(\gamma). \tag{5.29}$$

Substituting (5.29) in (5.23) and using the fact $\int_0^{\infty} \hat{\gamma} f_{\hat{\Gamma}_{\mathrm{D}_j}}(\hat{\gamma}) d\hat{\gamma} = \sqrt{\frac{\mathcal{V}\{\hat{\Gamma}_{\mathrm{D}_j}\}}{2\pi}}$, we get

$$\mathcal{L}_{\mathrm{D}}(\gamma_{\mathrm{Th}}) = \sum_{j=1}^{J} f_{\Gamma_{\mathrm{D}_j}}(\gamma_{\mathrm{Th}}) \frac{\sqrt{\mathcal{V}\left\{\hat{\Gamma}_{\mathrm{D}_j}\right\}}}{\sqrt{2\pi}} \prod_{r=1,k\neq j}^{J} \mathcal{F}_{\Gamma_{\mathrm{D}_r}}(\gamma_{\mathrm{Th}}). \tag{5.30}$$

Using (5.19), (5.20), and (5.24) in (5.30), we can obtain the closed form expression of LCR.

Further, we define the AOD as the average time duration over which the received signal power falls below a certain threshold level. AOD is often used as a measure of the temporal variability of a wireless channel. For the considered OIRS-assisted FSO-based communication network with multi-aperture receiver employing SC, the AOD can be mathematically defined as

$$\mathcal{T}_{\mathrm{D}}(\gamma_{\mathrm{Th}}) = \frac{\mathcal{F}_{\Gamma_{\mathrm{D}}}(\gamma_{\mathrm{Th}})}{\mathcal{L}_{\mathrm{D}}(\gamma_{\mathrm{Th}})}. \tag{5.31}$$

where $\mathcal{F}_{\Gamma_{\mathrm{D}}}(\gamma)$ is the CDF of Γ_{D} defined as

$$\begin{aligned}\mathcal{F}_{\Gamma_{\mathrm{D}}}(\gamma) &= \Pr\left(\Gamma_{\mathrm{D}_1} < \gamma, \Gamma_{\mathrm{D}_2} < \gamma, \cdots, \Gamma_{\mathrm{D}_J} < \gamma\right) \\ &= \prod_{j=1}^{J} \mathcal{F}_{\Gamma_{\mathrm{D}_j}}(\gamma) \end{aligned} \tag{5.32}$$

Substituting (5.20) in (5.32), we can obtain CDF of Γ_{D}. Further, utilizing the LCR and CDF expressions obtained in (5.30) and (5.32), respectively, the closed-form expression of AOD can be obtained.

5.4.2 PER Computation under SW-ARQ Protocol

To provide reliable communication between the two nodes, error control strategies are used, out of which SW-ARQ is the one which is more appropriate and widely used for packet transmission. In SW-ARQ, after transmitting the data packet, the source node first waits for the receiver acknowledgement and then sends the next data packet. However, if no acknowledgement is received, the data packet is re-transmitted. In our work, we use the SW-ARQ scheme in the data-link layer for packet transmission and thereafter, we derive the expression of PER for uncoded transmission while considering the FSMC model. In general, PER describes the performance of the based communication network and is considered as a crucial QoS measure while designing the data link layer protocol. In contrast to the general definition of the PER, where the packet is referred to as error packet when atleast one bit error occurs. Under FSMC model, the PER is determined using the user's LCR, which takes into account the time variations as well as channel correlations [112]. Then, the PER at D_j with SNR threshold γ_{Th} is given as [112]

$$\mathcal{P}_{\mathrm{p,D}}(\gamma_{\mathrm{Th}}) = \mathcal{F}_{\Gamma_{\mathrm{D}}}(\gamma_{\mathrm{Th}}) \exp\left(-T_{P_{\mathrm{D}}} \frac{\mathcal{L}_{\mathrm{D}}(\sqrt{\gamma_{\mathrm{Th}}})}{\mathcal{F}^c_{\Gamma_{\mathrm{D}}}(\gamma_{\mathrm{Th}})}\right), \tag{5.33}$$

where $\mathcal{F}^c_{\Gamma_{\mathrm{D}}}(\cdot) = 1 - \mathcal{F}_{\Gamma_{\mathrm{D}_j}}(\cdot)$ is the CCDF of Γ_{D_j}, $T_{P_{\mathrm{D}}} = m_{\mathrm{T}} T_{S_{\mathrm{D}}}$ is the total packet duration, m_{T} represents symbols in a packet, and $T_{S_{\mathrm{D}}}$ denotes the length of each symbol present in the transmitted packet. Substituting (5.17) and (5.30) in (5.33), we can obtain the analytical expression of PER.

Apart from PER, throughput can be considered as an another performance metric for the FSMC model when employing the SW-ARQ protocol. The system throughput for a given packet and using the SW-ARQ protocol can be given as

$$\mathcal{U}_{\mathrm{D}}(m_{\mathrm{T}}) = \frac{m_{\mathrm{T}} \mathcal{R}_{\mathrm{D}}}{(m_{\mathrm{T}} + m_{\mathrm{O}})} \left(1 - \mathcal{P}^e_{\mathrm{D}}(\gamma_{\mathrm{Th}})\right), \tag{5.34}$$

where $\mathcal{R}_{\mathrm{D}} = \frac{1}{T_{S_{\mathrm{D}}}}$ denotes the data rate of D with m_{OV} being the number of overhead symbols. Later, in Section V (Refer Fig. 5.8(c)), it has been shown that throughput as a function of m_{T} follows a concave downward trend when N and $\mathcal{R}_{\mathrm{D}}$ are varied. Thus, by computing the first derivative of (5.34), we find the maximum value of throughput and optimized m_{T}. Using (5.33) in (5.34), and then differentiating w.r.t. m_{T}, we get

$$\begin{aligned} \frac{\partial \mathcal{U}_{\mathrm{D}}(m_{\mathrm{T}})}{\partial m_{\mathrm{T}}} &= \left[-\mathcal{L}_{\mathrm{D}}(\sqrt{\gamma_{\mathrm{Th}}}) m_{\mathrm{T}} + \mathcal{R}_{\mathrm{D}} \mathcal{F}^c_{\Gamma_{\mathrm{D}_j}}(\gamma_{\mathrm{Th}}) - \frac{m_{\mathrm{T}} \mathcal{R}_{\mathrm{D}} \mathcal{F}^c_{\Gamma_{\mathrm{D}}}(\gamma_{\mathrm{Th}})}{m_{\mathrm{T}} + m_{\mathrm{OV}}} \right] \\ &\times \frac{\exp\left(-\frac{m_{\mathrm{T}} T_{S_{\mathrm{D}}} \mathcal{L}_{\mathrm{D}}(\sqrt{\gamma_{\mathrm{Th}}})}{\mathcal{F}^c_{\Gamma_{\mathrm{D}}}}\right)}{m_{\mathrm{T}} + m_{\mathrm{OV}}}. \end{aligned} \tag{5.35}$$

Further, m_{T} from (5.35) is obtained as

$$m^*_{\mathrm{T}} = \frac{m_{\mathrm{OV}}}{2} \left(\sqrt{1 + \frac{4 \mathcal{F}^c_{\Gamma_{\mathrm{D}}}(\gamma_{\mathrm{Th}})}{m_{\mathrm{OV}} \mathcal{L}_{\mathrm{D}}(\sqrt{\gamma_{\mathrm{Th}}}) T_{S_{\mathrm{D}}}}} - 1 \right), \tag{5.36}$$

where m^*_{T} represents the optimized symbols per packet that maximizes the throughput.

Table 5.2: System Specifications

Parameter	Value
Wavelength (λ)	1550
Optical-to-electrical conversion coefficient (η)	0.9
Diameter of PD	20 cm
Responsivity of PD (R_{P})	0.9
Equivalent beam radius at n-th OIRS element (W_{eq})	0.1733
Equivalent beam radius at PD of D_j (W_{eq})	0.2287
Jitter deviation under weak pointing error (σ_s)	0.01, 0.013
Jitter deviation under weak pointing error (σ_s)	0.08, 0.15
Noise power (σ_{D}^2)	1

Table 5.3: Weather and atmospheric conditions

Weather conditions of FSO link			
Scenario	Visibility (V)	τ	ζ
Thick Fog	0.2 km	6	23
Moderate Fog	0.5 km	5	12
Light Fog	0.77 km	2	13
Clear Sky	10 km	2	0.745×10^{-3}
Atmospheric Turbulence Conditions			
ST	$\alpha = 3.98$, $\beta = 1.70$		
MT	$\alpha = 5.42$, $\beta = 3.79$		
WT	$\alpha = 11.3$, $\beta = 10$		

5.5 Numerical Evaluation

In this section, we provide some useful insights of SOS for the considered OIRS-assisted FSO-based communication network. The simulation values are taken as follows. Table 5.2 describes the system parameters and Table 5.3 describes the parameters related to atmospheric turbulence, and foggy conditions, respectively. The transmit power (P_{S}) is set to 5 dB, Doppler shift (f_{D}) is set to 50 Hz, number of reflecting elements (N) is set to 50, and number of receive apertures (J) is set to 3, unless otherwise defined.

In Figs. 5.2(a) and 5.2(b), we examine the variations of LCR and AOD, respectively, w.r.t. the fade threshold γ_{Th} for the considered OIRS-assisted FSO-based communication network under different turbulence and pointing error conditions (i.e., low pointing error ($\sigma_{s,\text{SR}} = 0.01$ and $\sigma_{s,\text{RD}_j} = 0.013$) and high pointing error ($\sigma_{s,\text{SR}} = 0.08$ and $\sigma_{s,\text{RD}_j} = 0.15$)). As seen from Fig. 5.2(a), there is a threshold at which the received signal variations are at their highest level. For small and large values of the threshold, the variations approach zero. Further, it can also be observed that LCR increases as the atmospheric turbulence increases and that the range of fade threshold for which LCR occurs increases as the severity of atmospheric turbulence increases. This implies that the channel becomes

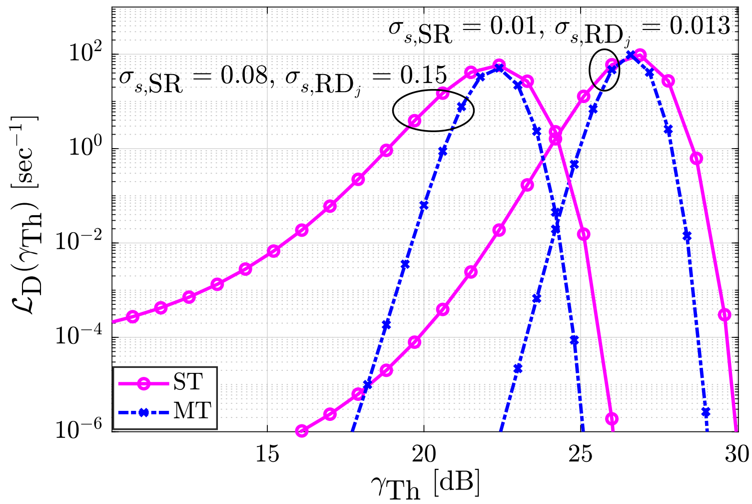

(a) LCR versus γ_{Th}

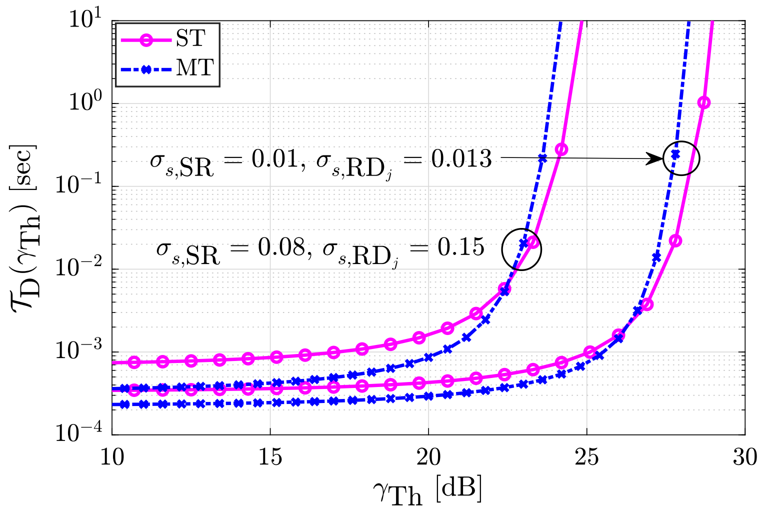

(b) AOD versus γ_{Th}

Figure 5.2: (a) LCR and (b) AOD versus SNR fade threshold for different atmospheric turbulence and misalignment parameters with $J = 3$.

highly variable, that can lead to frequent signal fading and can reduce the signal quality. Further, we can observe the LCR degradation with the decrease in the pointing error. Moreover, for low pointing error, the LCR curves shifts to the right and the threshold for which maximum LCR occurs increases under all condition of atmospheric turbulence. Moreover, we can observe from Fig. 5.2(b), that there is an exponential increase in AOD w.r.t. fade threshold, which implies that the duration for which the network stays in fade becomes longer with an increase in fade threshold. Moreover, AOD increases with an increase in atmospheric turbulence and pointing error.

Observation 5.1: *Fig. 5.2 clearly depicts that the LCR and AOD are significantly affected by pointing error and atmospheric turbulence and the impact of misalignment error on the parameters is severe compared to atmospheric turbulence. For example, to obtain the LCR*

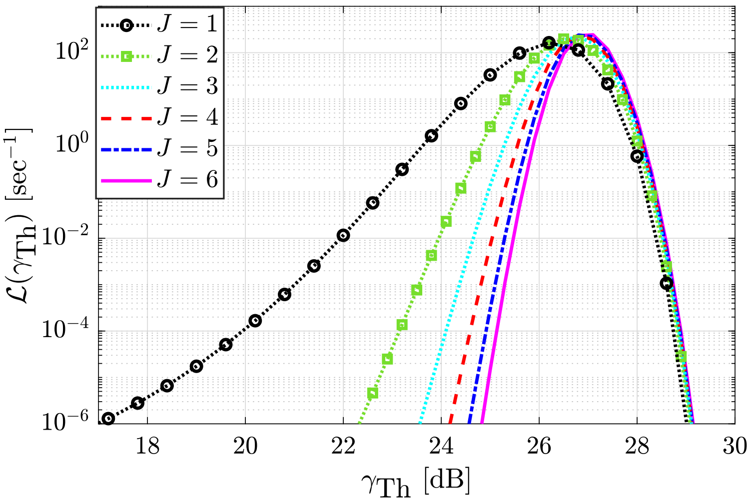

(a) LCR versus γ_{Th}

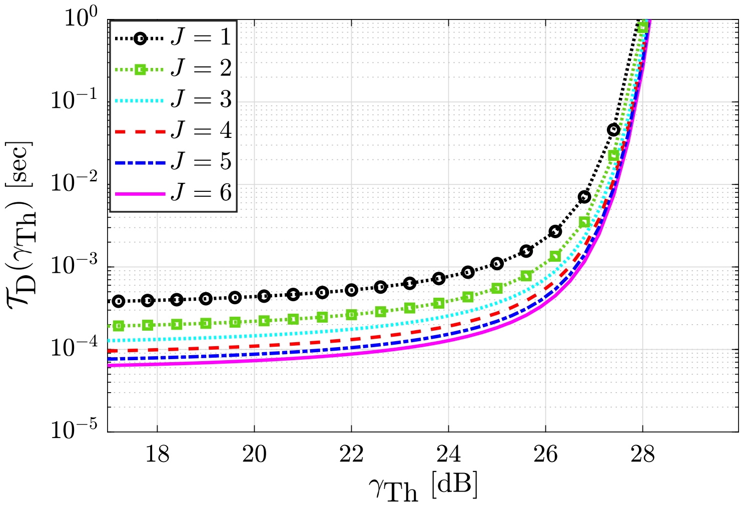

(b) AOD versus γ_{Th}

Figure 5.3: (a) LCR and (b) AOD versus fade threshold for different values of J with $N = 50$ under moderate turbulence and low jitter deviation.

of 10^{-3} *sec*$^{-1}$ *at high pointing error, the SNR threshold increases from* 13 *dB to* 19 *dB with the decrease in the severity of atmospheric turbulence and threshold increase from* 13 *dB to* 21 *dB with the decrease in the severity of pointing error.*

Figs. 5.3(a) and 5.3(b) represent the variation of LCR and AOD, respectively w.r.t SNR threshold for different values of J (i.e., number of receiver apertures) for the considered OIRS-assisted FSO-based communication network with multi-aperture receiver employing SC. It can be clearly observed from Fig. 5.3(a) that the number of receiving apertures has significant impact on the LCR. The SC technique selects the best copy of the transmitted signal based on the received signal strength and reduce the impact of fading on the received signal. Therefore, LCR becomes low and curves become narrower with an increase in J, i.e., the fades occur rarely with increase in J. For example, at $\gamma_{\mathrm{Th}} = 24$ dB, the LCR reduces from 2×10^{-2} sec^{-1} to 1.03×10^{-4} sec^{-1} with an increase in J from 2 to

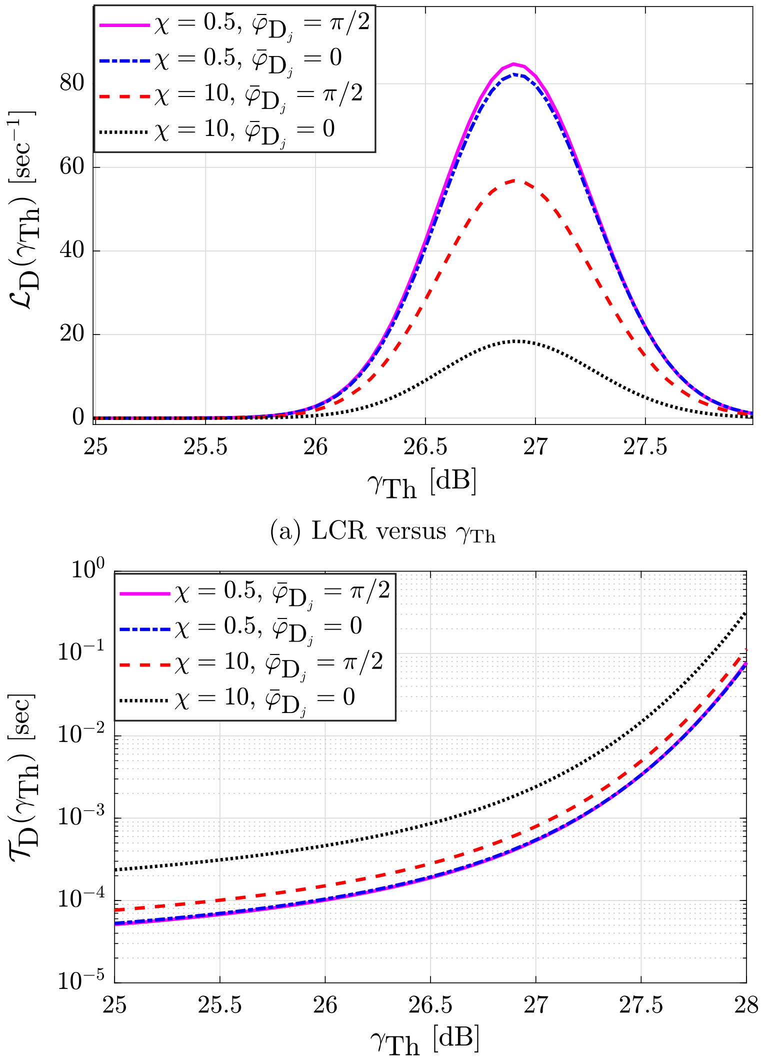

(a) LCR versus γ_{Th}

(b) AOD versus γ_{Th}

Figure 5.4: (a) LCR and (b) AOD versus fade threshold for different values of χ with θ_P with $N = 50$ and $J = 3$ under moderate turbulence, and low jitter deviation.

3. Moreover, as the number of receive aperture increases, the rate (by which the LCR decreases) reduces. This implies the maximum performance gain can be obtained with a few number of receive apertures. On the other hand, it can be observed from Fig. 5.3(b) that the AOD reduces as the number of receive apertures increases. For example, at $\gamma_{\mathrm{Th}} = 24$ dB, the AOD reduces from 7.23×10^{-4} sec to 2.6×10^{-4} sec with increase in J from 1 to 3. Moreover, it can be observed from Fig. 5.3 that the worst performance in terms of LCR and AOD is obtained at $J = 1$. Further, it is necessary to study the impact of parameters related to non-isotropic scattering χ (defines degree of non-isotropic scattering) and $\bar{\varphi}_{\mathrm{D}_j}$ (mean AOA of scattered components at D_j) for the considered OIRS-assisted FSO-based communication network. Therefore, in Figs. 5.4(a) and 5.4(b), we present the variation of LCR and AOD, respectively, w.r.t SNR threshold for different values of χ and

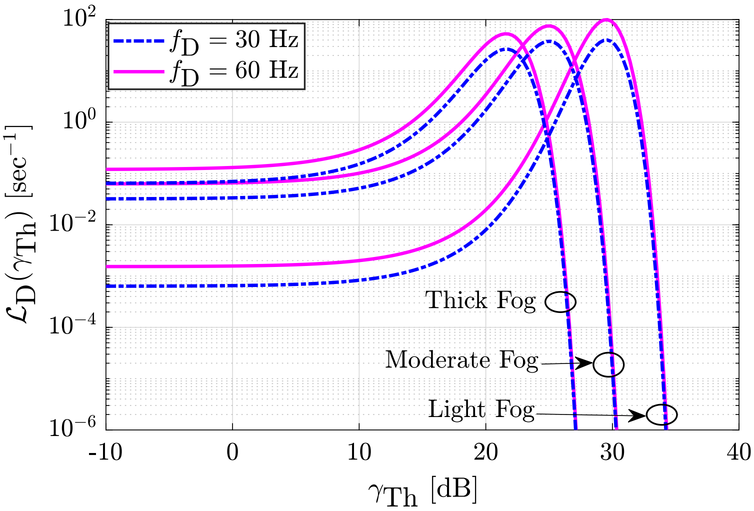

(a) LCR versus $\gamma_{\rm Th}$

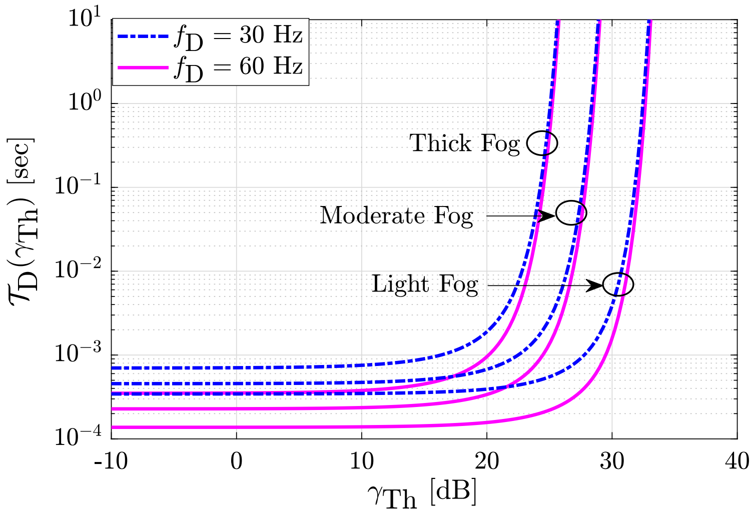

(b) AOD versus $\gamma_{\rm Th}$

Figure 5.5: (a) LCR and (b) AOD versus fade threshold for different values of Fog parameters and Doppler frequency with $N = 50$ and $J = 3$ under weak turbulence and low jitter deviation.

$\bar{\varphi}_{\mathrm{D}_j}$. It can be seen from Fig. 5.4(a) that LCR decreases as χ increases. This is because of the fact that as χ increases, the spread of the beam after reflection through OIRS reduces. Further, LCR is minimum when the $\chi = 10$ and $\bar{\varphi}_{\mathrm{D}_j} = 0$ i.e., beam becomes highly collimated and the maximum power is collected by the PD. Moreover, the maximum SNR threshold is unaffected due to the variation of χ and $\bar{\varphi}_{\mathrm{D}_j}$. On the other hand, it can be observed from Fig. 5.4(b) that the average duration for which system remain in fade decreases with an increase in χ and $\bar{\varphi}_{\mathrm{D}_j}$. However, the impact of $\bar{\varphi}_{\mathrm{D}_j}$ is negligible at higher values of χ. Figs. 5.5(a) and 5.5(b) represent the variation of LCR and AOD, respectively, w.r.t SNR threshold for different Doppler shifts. The system performance is also observed under different foggy environments, i.e., light fog ($\tau = 2$, $\zeta = 13$), moderate fog ($\tau = 5$, $\zeta = 12$), and thick fog ($\tau = 6$, $\zeta = 23$). Since foggy conditions occur under weak atmospheric turbulence, we analyze the impact of fog on the system's performance under weak atmosphere turbulence conditions ($\alpha = 11.3$ and $\beta = 10$). It can be seen from Fig. 5.5(a) that the peak SNR threshold or the receiver sensitivity reduces as the density of fog increases. This is due to the greater signal power loss caused by the severe fog conditions. The results show that during conditions of heavy fog, the performance is low and the maximum LCR is obtained. In contrast, Fig. 5.5(b) shows that the average duration for which system is in fade/outage increases as the fog density increases i.e. AOD increases. Further, it can be observed from Figs. 5.5(a) and 5.5(b) that the increase in Doppler shift f_{D} results in increasing the LCR without affecting the maximum SNR threshold, however, the fades vanish more quickly. This is because of the fact that the increase in users's speed results in more rapid signal fluctuations. Moreover, the impact of Doppler shift at high SNR threshold is unnoticeable.

Observation 5.2: *The presence of fog in the wireless channel can cause severe attenuation and scattering of the signal, resulting in a decrease in the signal power level. This reduction in signal power level can cause an increase in the LCR, as the signal is more likely to cross the threshold level. For example, at SNR threshold $\gamma_{Th} = 20$ dB and $f_D = 30$ Hz, the LCR values under thick, moderate, and light fog are obtained as 18 sec^{-1}, 1.7 sec^{-1}, and 6.8×10^{-4}, respectively, and the corresponding AOD values as 1.8×10^{-3} sec, 6.7×10^{-4} sec, and 3.8×10^{-4} sec, respectively.*

In Figs. 5.6(a) and 5.6(b), we examine the performance of LCR and AOD w.r.t. transmit power P_{S} for different values of N (i.e., number of OIRS elements) and γ_{Th}. It can be seen from Fig. 5.6(a) that LCR reduces exponentially with the transmit power and becomes constant with higher values of transmit power since the signal is less likely to cross the threshold level. Moreover, LCR curves shift towards left with an increase in the number of OIRS elements. Also, LCR increases with an increase in γ_{Th} for a given transmitter power. It can also be observed from Fig. 5.6(b) that AOD reduces exponentially with an increase in the transmit power. This is because the signal is generally above the threshold level, and it takes a longer time for it to fall below the threshold level. Therefore, a high signal power can result in a shorter AOD. Further, it can noted from Figs. 5.6(a) and 5.6(b) that for high transmit power, both LCR and AOD are independent of the fade threshold and depends on the number of IRS elements.

Observation 5.3: *From Fig. 5.6, we notice a significant performance improvement with the number of reflecting elements. For example, at $P_S = 5$ dB and $\gamma_{Th} = 15$ dB,*

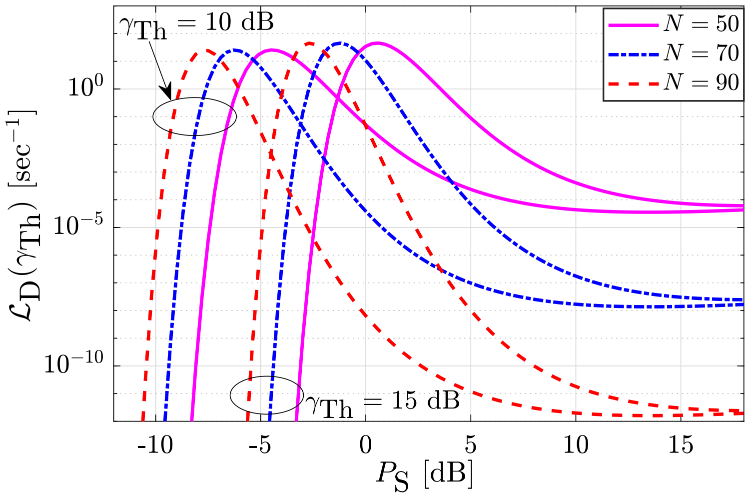

(a) LCR versus $P_{\rm S}$

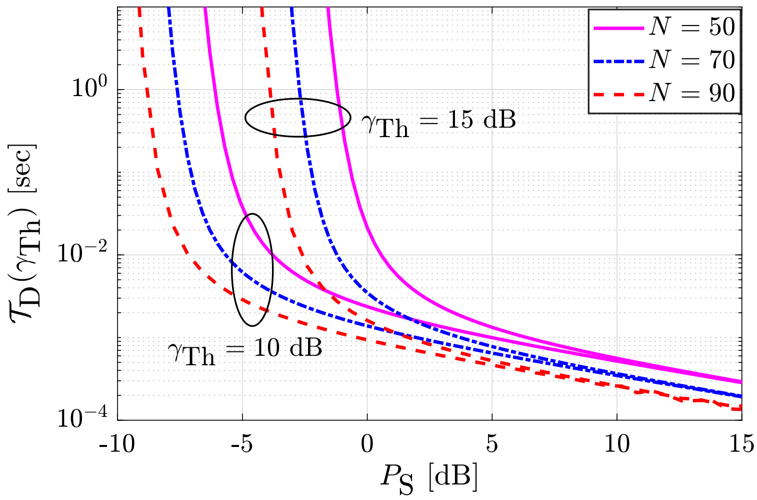

(b) AOD versus $P_{\rm S}$

Figure 5.6: (a) LCR (b) AOD versus transmit power ($P_{\rm S}$) for different values of fade threshold and number of reflecting elements with $J = 2$ under weak turbulence and low jitter deviation.

with increase in N from 50 to 70, the LCR drops from 5.7×10^{-5} sec^{-1} to 8.25×10^{-9} sec^{-1} and the corresponding AOD values reduces from 1.3 millisec to 0.7 millisec. Using a large-sized OIRS enables the system to perform for a larger range of fade threshold while maintaining low LCR and very low AOD values.

Further, Fig. 5.7 shows the PER performance of the considered OIRS-assisted FSO-based communication network with multi-aperture receiver employing SW-ARQ protocol under FSMC model. We have shown the PER performance w.r.t. $P_{\rm S}$ for different values of fade threshold $\gamma_{\rm Th}$ and number of reflecting elements (N). It can be observe from Fig. 5.7 that PER decreases with increase in $P_{\rm S}$ and the saturates to certain value at high transmit power. However, the PER saturation value varies for different values of N. It is clear from the figure that system's performance degrades significantly with

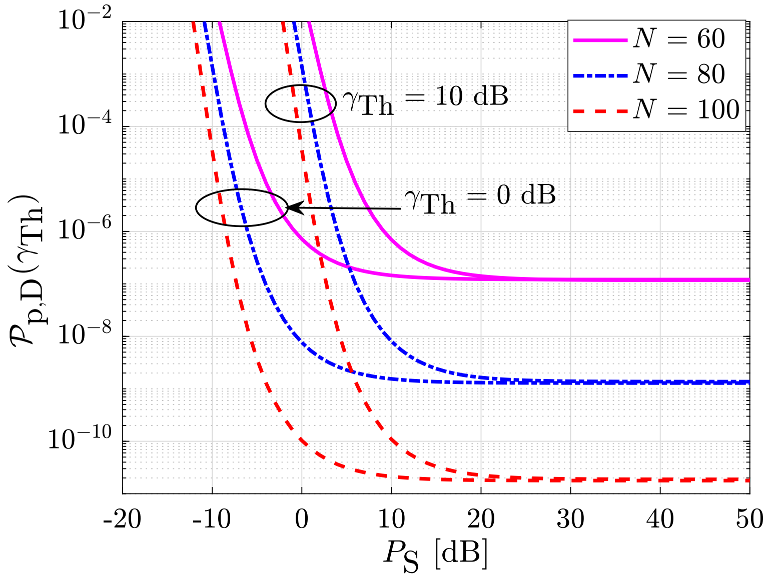

Figure 5.7: PER performance versus transmit power (P_{S}) for different values of fade threshold (γ_{Th}) and number of reflecting elements (N) with $J = 3$ under moderate turbulence and low jitter deviation.

increase in fade threshold for low to moderate values of transmit power. However, for high transmit power, the PER performance for different γ_{Th} becomes almost equal. Further, as the N increases, the PER performance become superior. For example, $P_{\mathrm{S}} = 10$ dB and $\gamma_{\mathrm{Th}} = 10$ dB, PER achieved for N equal to 60, 80, and 100 is 6.9×10^{-7}, 8.04×10^{-9}, and 1.09×10^{-10}, respectively.

Remark 5.2: *It can be observed from Fig. 5.6 and Fig. 5.7, that at high transmit power, the system's performance interms of LCR, AOD, and PER depends on numbers of reflecting elements of OIRS (N) and is independent of the fade threshold (γ_{Th}).*

Figure 5.8 illustrates the impact of varying packet length (m_{T}), data rates ($\mathcal{R}_{\mathrm{D}}$), and the number of OIRS elements (N) on the normalized throughput ($\bar{\mathcal{U}}_{\mathrm{D}} = \mathcal{U}_{\mathrm{D}}(m_{\mathrm{T}})/\mathcal{R}_{\mathrm{D}}$). The overhead symbols under the ARQ transmission policy were set to $m_{\mathrm{OV}} = 100$ symbols for all curves in the figure. The results show that with increase in the data rate, $\bar{\mathcal{U}}_{\mathrm{D}}$ also increases. The normalized throughput is a decreasing exponential function of the inverse data rate, which is equivalent to an increasing exponential function of the data rate, as evident from the (5.34). Moreover, the figure reveals that there is an optimal m_{T}^* at which $\bar{\mathcal{U}}_{\mathrm{D}}$ is maximum. Specifically, with $N = 50$ and data rates $\mathcal{R}_{\mathrm{D}} = \{1, 5, 10\}$K symbols per sec (sps), m_{T}^* is calculated using (5.36) and were found to be 618, 1441, and 2057 symbols, respectively. On a similar note, with $N = 60$ and $\mathcal{R}_{\mathrm{D}} = \{1, 5, 10\}$K sps, the value of m_{T}^* were found to be 618, 1441, and 2057 symbols, respectively. These results closely match the simulation results. Moreover, an increase in the number of reflecting elements leads to a significant improvement in the normalized throughput at all data rates.

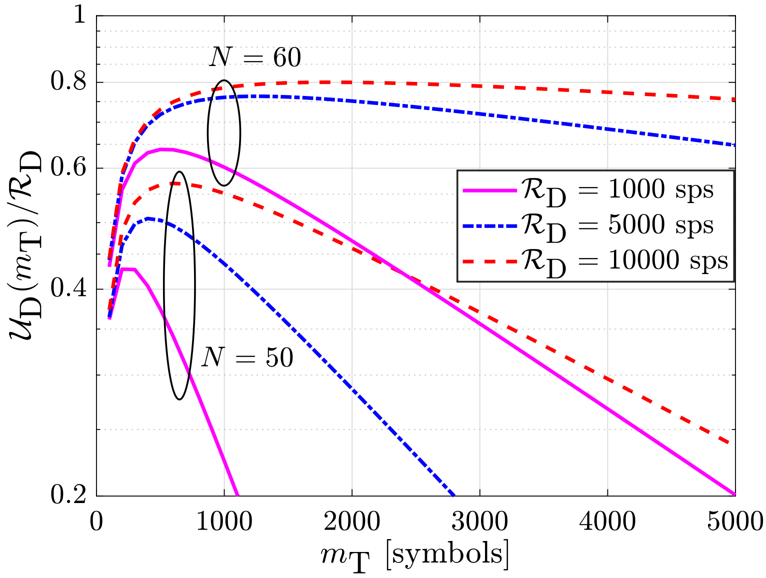

Figure 5.8: Variation of normalized throughput w.r.t. length of data packet for different values of N and $\mathcal{R}_{\mathrm{D}}$ under moderate turbulence and low jitter deviation.

Notably, the optimal packet length increases with an increase in both the data rate and the number of OIRS reflecting elements. As a result, to improve the performance of the system, the system designer must always choose an optimal packet length and a more number of reflecting elements.

5.6 Summary

This chapter has studied the SOS of a noise-limited OIRS-assisted FSO-based communication network with SC diversity technique. The SOS has characterized how long and how often the system has experienced fading. Specifically, in this chapter, we have derived the closed-form expressions of the LCR and AOD for the considered system under the atmospheric turbulence modeled using Gamma-Gamma distribution along with random fog and pointing error. Under the FSMC model, we have also evaluated the PER and optimal packet length with SW-ARQ protocol-based information transfer. Furthermore, we have investigated the effect of various system and channel parameters, including the number of OIRS elements and receiving apertures, Doppler shift, misalignment error, fog parameters, mean AOA, and degree of non-isotropic scattering, etc., on the system's performance. Finally, we have shown that the introduction of OIRS into the FSO communication network can improve the system performance in terms of SOS.

Chapter 6

SOS for IRS-Assisted Multiuser RF Communication Network

6.1 Introduction

In addition to multipath fading, interference is another critical factor that affects the performance of the communication system. RF wireless communication usually suffers from CCI resulting from unlicensed devices operating in the same sub-band or due to the frequency reuse of available spectrum to serve multiple users simultaneously [79, 80, 118]. As the density of users increases, the vigorous reuse of frequency channels for high spectrum resources results in severe CCI and degrades the quality of the desired performance [79]. Furthermore, the unplanned allocation of resources has the potential to degrade overall system performance by increasing interference [119]. Therefore, it is important to consider the impact of interference in RF communication networks.

In this chapter, we consider a downlink multi-user communication network empowered by an IRS with base station (BS) employing the OFDMA scheme. The performance of the considered system is evaluated in terms of SOS in the presence of multiple co-channel interferers. In particular, we develop the analytical expressions of LCR and AOD of the received signal envelope at a desired user by considering a generalized fading model as κ-μ distribution. The impact of various system and channel parameters such as number of reflecting elements, amplitude of reflection coefficients, number of interferers, Doppler frequencies of desired and interfering users, and different channel fading environments has been shown on the LCR and AOD performances. Moreover, we derive an expression for asymptotic LCR under high transmit power conditions. It has been shown that the asymptotic LCR is independent of the threshold and transmit power. In addition, we consider a SW-ARQ protocol for reliable data packet transmission and derive the expressions for PER and throughput by utilizing the FSMC model. The optimal packet length is also determined which maximizes the throughput under SW-ARQ protocol.

The impact of various system parameters is also shown on the PER and throughput performances.

6.1.1 State-of-the-Art

The study of SOS in terms of LCR and AOD has been extensively done in the existing literature for the RF-based communication system. The LCR and AFD was investigated for the first time by Rice in his pioneering research [32]. Later on, many researchers have investigated SOS under different channel and system model [33, 34, 36, 37, 38]. The authors in [33] studied the SOS of multipath fading channels considering the non-isotropic scattering scenario under Rayleigh, Nakagami, and Rician channel distribution. In addition, the dynamic time-varying attributes of the various fading channel are well explored through SOS. In [34], the authors derived exact closed-form expressions for the LCR and AOD of the signal envelope in $\mathcal{F}$ composite fading channels for device-to-device communications. Furthermore, in [34] the response of LCR and AOD is analyzed under multipath fading as well as shadowing conditions. The study of SOS for relaying system was investigated in [36, 37, 38]. The authors in [108] obtained exact closed form expressions of LCR and AOD for output signal envelope of Selection combiner corrupted by AWGN under Rayleigh, Nakagami, and Rician fading.

To combat fading and the effect of CCI, multiple diversity combining receivers, such as SC, MRC, and EGC have been widely studied, especially in an interference-limited systems [109, 110, 111, 112]. The authors in [109] obtained exact closed-form expressions of LCR and AOD for output signal envelope of SC, MRC, and EGC receiver corrupted by AWGN under Nakagami fading and the impact of diversity and the number of receiving branches were analyzed. Further, in [110, 111, 112], the authors derived closed-form expressions of LCR and AOD for the interference-limited systems utilizing MRC receiver. The derived LCR expression in [111, 112] was used to obtain the PER and optimal packet length for throughput maximization by deploying the SW-ARQ transmission scheme via FSMC model. However, the authors in both [111] and [112] considered Rayleigh distribution for the desired as well as interference links. The major limitation of these diversity receiver system is that they require multiple receiving antennas leading to complexity and increased cost.

6.1.2 Novelity and Contributions

From the above works [28, 29, 74, 75, 76, 77, 82, 78, 79, 80] that considered IRS, only few works have taken CCI for system analysis. However, in a real-world scenario, most wireless communication systems are interference-limited. For example, the wireless communication system is interference-limited due to the large traffic in the urban areas. None of the previous studies that considered IRS have analyzed SOS. To the best of the authors' knowledge, SOS in terms of LCR and AOD for IRS-assisted network without CCI was first explored in [120] for the noise-limited IRS-assisted network under Nakagami and Rician fading. There is no reported work that studied the SOS for IRS-assisted network in the presence of CCI. This chapter presents a novel framework that considers the IRS-assisted multiuser communication system with multiple co-channel interferers. Furthermore, we utilize a more generalized κ-μ fading distribution for the desired and interferers links that has not been considered previously for the IRS-assisted system. The scope of the study is highly useful for Delay-Sensitive Applications in dynamic RF systems.

The main contributions of this work are as follows:

- We consider a downlink IRS-assisted multi-user communication network, employing OFDMA scheme at the source to analyze the SOS at a user. The effect of CCI is considered by assuming multiple interferers moving with unequal velocities under the practical assumption of INID channels.

- We derive the analytical expressions for the SOS in terms of LCR and AOD for the considered IRS-assisted RF communication system under interference-limited scenario by following the κ-μ fading distribution for all the desired as well interfering links. Moreover, we derive the analytical expressions for asymptotic LCR for high transmit power conditions.

- For reliable packet transmission, we employ the SW-ARQ scheme at the link layer of the considered IRS-assisted RF system and derive the expressions for PER and throughput using the FSMC model. Furthermore, the optimal packet length of the data packet is determined which maximizes the throughput under SW-ARQ protocol.

- Through numerical results, we have shown the impact of various system and channel parameters such as the number of reflecting elements of IRS, minimum reflection amplitude, number of interferers, Doppler shifts due to the movement of desired as well as interfering users, and the severity of channel fading on system's performance.

6.2 System Model

In this Section, we describe the system setup for the considered multi-user RF communication network assisted by IRS and introduce the channel model for the desired and the interference links.

6.2.1 System Setup

As shown in Fig. 6.1, we consider a multi-user downlink RF communication network in urban environment consisting of a single BS and J desired user equipment (DUE) represented by set $\mathbb{J} = \{1, \cdots, J\}$ and each DUE is equipped with single antenna. The communication between BS and the DUE_j, $j \in \mathbb{J}$, takes place through an IRS consisting of N reflecting meta-surfaces in the form of a planar array that operates in the far-field region [1]. We consider that there is no direct link between BS and DUE because of blockage due to buildings, trees and heavy vehicles, as considered [118, 119] . This type of scenario exists in the urban environment where the received signal at a user experiences connectivity problem through the direct link due to deep shadowing. We also consider that the communication between BS and DUE_j is affected by CCI which is caused by L interfering user equipment (IUE) denoted by a set $\mathbb{L} = \{1, \cdots, L\}$. It may be noted that the L IUE produce CCI because of the transmission of their data over the same sub-band (utilized by the DUE_j) due to the frequency reuse. To facilitate multi-user communication, we employ OFDMA scheme (i.e., allocating a portion of the entire bandwidth/transmit power to each user) to simultaneously support multi-users due to its flexibility in resource allocation design and the ability to leverage multi-user diversity. The total available bandwidth ($\mathcal{B}$) is divided into $K(\geq J)$ mutually orthogonal spectrum bands/sub-carriers represented by a set $\mathbb{K} = \{1, \cdots, K\}$ with a sub-band spacing of $\Delta f = \frac{\mathcal{B}}{K}$. It is assumed that the BS serves a single DUE in one sub-band. Let DUE_j is served in k-th sub-band, $k \in \mathbb{K}$, for notational convenience, we denote the k-th sub-band as the j-th sub-band in the sequel of this chapter.

The location of BS and DUE_j in 3-D Cartesian coordinate system is given as $\mathcal{X}_{\mathrm{B}} \triangleq (x_{\mathrm{B}}, y_{\mathrm{B}}, z_{\mathrm{B}})$ and $\mathcal{X}_{\mathrm{D}_j} \triangleq \left(x_{\mathrm{D}_j}, y_{\mathrm{D}_j}, 0\right)$, respectively. We assume that the IRS is mounted on the facet of a high-rise building such that it lies in the 3-D Cartesian coordinate system with center at $\mathcal{X}_{\mathrm{R}} \triangleq (x_{\mathrm{R}}, y_{\mathrm{R}}, z_{\mathrm{R}})$. Without loss of generality, we consider that the distance of BS (or DUE_j) from each reflecting element of IRS is equal to the distance

[1] We consider that the distance between BS/DUE and each element of the IRS to be greater than 5λ, where λ is the operating wavelength, therefore BS/DUE are in the far-field region of the IRS [121].

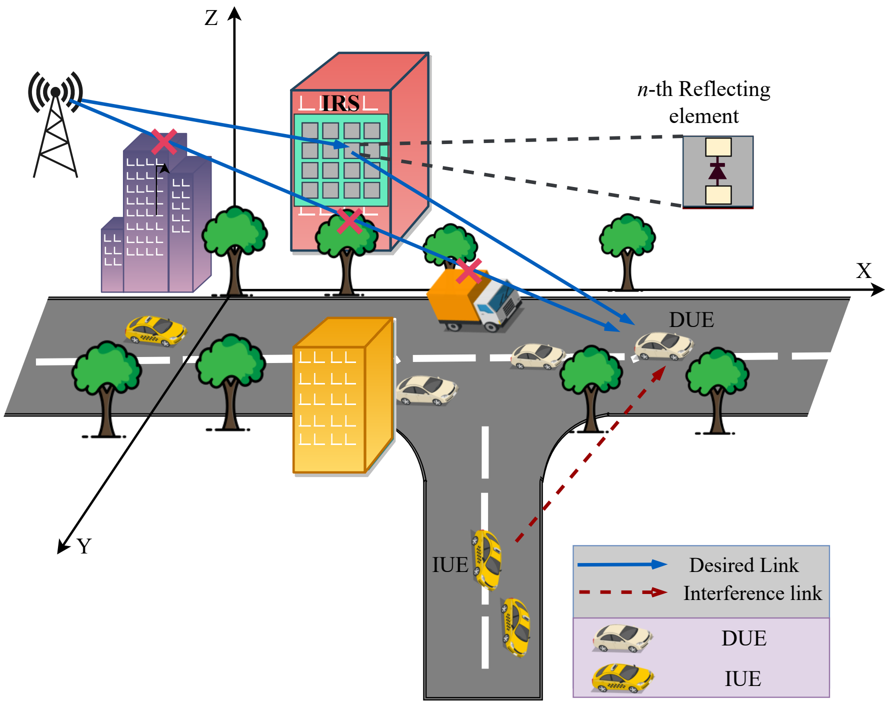

Figure 6.1: Block diagram of IRS-assisted RF network in urban environment.

calculated from the center of IRS. Therefore, we can write the distances of BS-IRS and IRS-DUE$_j$ links as $d_{\mathrm{BR}} = \|\mathcal{X}_{\mathrm{B}} - \mathcal{X}_{\mathrm{R}}\| = \sqrt{(x_{\mathrm{B}} - x_{\mathrm{R}})^2 + (y_{\mathrm{B}} - y_{\mathrm{R}})^2 + (z_{\mathrm{B}} - z_{\mathrm{R}})^2}$ and $d_{\mathrm{RD}_j} = \|\mathcal{X}_{\mathrm{R}} - \mathcal{X}_{\mathrm{D}_j}\| = \sqrt{(x_{\mathrm{R}} - x_{\mathrm{D}_j})^2 + (y_{\mathrm{R}} - y_{\mathrm{D}_j})^2 + z_{\mathrm{R}}^2}$, respectively. The location of IUE$_\ell$, $\ell \in \mathbb{L}$, in the X-Y plane is given by $\mathcal{X}_{\mathrm{I}_\ell} \triangleq (x_{\mathrm{I}_\ell}, y_{\mathrm{I}_\ell}, 0)$ and the distance between IUE$_\ell$ and DUE$_j$ can be obtained as $d_{\mathrm{I}_\ell \mathrm{D}_j} = \|\mathcal{X}_{\mathrm{I}_\ell} - \mathcal{X}_{\mathrm{D}_j}\| = \sqrt{(x_{\mathrm{I}_\ell} - x_{\mathrm{D}_j})^2 + (y_{\mathrm{I}_\ell} - y_{\mathrm{D}_j})^2}$.

In general, the IRS is assumed to be linked to a smart controller that is in charge of adjusting the reflection amplitudes and/or phase shifts of each element using a feedback connection to exchange information with the BS. The phase shift of the reflection coefficient at each reflecting element is assumed to take a discrete set of values from 0 to 2π. Let the reflection coefficients of IRS are represented by a diagonal matrix $\mathbf{\Theta} = \mathrm{diag}\left[\varpi_{\mathrm{R}}^{(1)}, \varpi_{\mathrm{R}}^{(2)}, \cdots, \varpi_{\mathrm{R}}^{(N)}\right]$, where $\varpi_{\mathrm{R}}^{(n)} = |\varpi_{\mathrm{R}}^{(n)}| e^{-\jmath \angle \varpi_{\mathrm{R}}^{(n)}}$ is the reflection coefficient of n-th reflecting element with $|\varpi_{\mathrm{R}}^{(n)}| \in [0, 1]$ being the amplitude of reflection and $\angle \varpi_{\mathrm{R}}^{(n)} \in [0, 2\pi]$ is the phase shift. The value of $|\varpi_{\mathrm{R}}^{(n)}|$ corresponding to practical phase shift is given by [74, (5)].

6.2.2 Transmission Scheme

Let P_{B} is the total power available at the BS to serve all the DUE. The total power is distributed to J sub-bands such that $\sum_{j \in \mathbb{J}} P_{\mathrm{D}_j} \leq P_{\mathrm{B}}$, where P_{D_j} is the transmit power used over the j-th sub-band. Let the vectors $\mathbf{h}_{\mathrm{BR}}^T \in \mathbb{C}^{1 \times N}$ and $\mathbf{h}_{\mathrm{RD}_j}^T \in \mathbb{C}^{1 \times N}$ denote the channel vectors of the BS-IRS and the IRS-DUE$_j$ links, respectively, the signal received by DUE$_j$ can be given by

$$r_{\mathrm{D}_j} = \sqrt{P_{\mathrm{D}_j}}\, \mathbf{h}_{\mathrm{BR}}^T \boldsymbol{\Theta} \mathbf{h}_{\mathrm{RD}_j} s_{\mathrm{D}_j} + \mathbf{g}_{\mathrm{ID}_j}^T\, \mathbf{s}_{\mathrm{I}} + e_{\mathrm{D}_j}, \tag{6.1}$$

where s_{D_j} is the unit-norm symbol transmitted in the j-th sub-band; vector $\mathbf{s}_{\mathrm{I}} = [s_{\mathrm{I}_1}, s_{\mathrm{I}_2}, \cdots, s_{\mathrm{I}_L}]^T$ contains the unit-energy interference data received from all the active IVE; and $e_{\mathrm{D}_j} \sim \mathcal{N}\left(0, \sigma_{\mathrm{D}_j}^2\right)$ is the AWGN noise at DUE$_j$. The vector $\mathbf{g}_{\mathrm{ID}_j}^T \in \mathbb{C}^{1\times L}$ denotes the interference channel vector at DUE$_j$ containing the channel coefficients of all the interfering links to j-th DUE with ℓ-th element defined as $\sqrt{P_{\mathrm{I}_\ell}}\rho_{\mathrm{I}_\ell \mathrm{D}_j} g_{\mathrm{I}_\ell \mathrm{D}_j}$, where P_{I_ℓ} is the transmit power of IUE$_\ell$, $\rho_{\mathrm{I}_\ell \mathrm{D}_j} = \sqrt{\rho_0 d_{\mathrm{I}_\ell \mathrm{D}_j}^{-\mathrm{e}}}$ and $g_{\mathrm{I}_\ell \mathrm{D}_j}$ represent the path loss component and complex channel coefficient of IUE$_\ell$-DUE$_j$ link, respectively, with ρ_0 being the path loss at a reference distance of 1 m and e denoting the path loss exponent which determines the slope of path loss characteristics. Further, if we define the n-th elements of $\mathbf{h}_{\mathrm{BR}}^T$ and $\mathbf{h}_{\mathrm{RD}_j}^T$ as $\rho_{\mathrm{BR}} h_{\mathrm{BR}}^{(n)}$ and $\rho_{\mathrm{RD}_j} h_{\mathrm{RD}_j}^{(n)}$, respectively, where $\rho_{\mathrm{BR}} = \sqrt{\rho_0 d_{\mathrm{BR}}^{-\mathrm{e}}}$ and $\rho_{\mathrm{RD}_j} = \sqrt{\rho_0 d_{\mathrm{RD}_j}^{-\mathrm{e}}}$ represent the path loss components of BS-IRS and IRS-DUE$_j$ links, respectively, we can rewrite (6.1) as

$$\begin{aligned} r_{\mathrm{D}_j} &= \sqrt{P_{\mathrm{D}_j}} \rho_{\mathrm{BR}} \rho_{\mathrm{RD}_j} \left(\sum_{n=1}^{N} h_{\mathrm{BR}}^{(n)} \varpi_{\mathrm{R}}^{(n)} h_{\mathrm{RD}_j}^{(n)} \right) s_{\mathrm{D}_j} + \sum_{\ell=1}^{L} \sqrt{P_{\mathrm{I}_\ell}} \rho_{\mathrm{I}_\ell \mathrm{D}_j} g_{\mathrm{I}_\ell \mathrm{D}_j} s_{\mathrm{I}_\ell} + e_{\mathrm{D}_j}, \\ &\triangleq \sum_{n=1}^{N} X_{\mathrm{D}_j}^{(n)} s_{\mathrm{D}_j} + \sum_{\ell=1}^{L} Y_{\mathrm{I}_\ell \mathrm{D}_j} s_{\mathrm{I}_\ell} + e_{\mathrm{D}_j}. \end{aligned} \tag{6.2}$$

6.2.3 Channel Model

We consider κ-μ distribution to model multipath fading for the desired as well as interference links. This model was discovered to efficiently capture the small-scale fluctuations of a fading signal in non-homogeneous environment [122, 123]. Moreover, κ-μ distribution model fits experimental data better than several commonly used fading distributions [123]. Physically, κ-μ fading model addresses signal consisting of clusters of multipath scattered waves with random phases that are propagating in a non-homogeneous environment. Each cluster has a dominant component with arbitrary strength. The parameter κ denotes the ratio of power of dominant components and total scattered waves, and μ is the total number of clusters. For a complex channel coefficient h_{AB}, the amplitude $|h_{\mathrm{AB}}|$ follows κ-μ distribution with parameters $(\kappa_{\mathrm{AB}}, \mu_{\mathrm{AB}}, \Omega_{\mathrm{AB}})$ with the

PDF given by [123]

$$f_{|h_{\mathrm{AB}}|}(h) = \frac{2h^{\mu_{\mathrm{AB}}}}{\kappa_{\mathrm{AB}}^{\frac{\mu_{\mathrm{AB}}-1}{2}}} \frac{\mu_{\mathrm{AB}} \left(\Lambda_{\mathrm{AB}}\right)^{\frac{\mu_{\mathrm{AB}}+1}{2}}}{\exp\left(\kappa_{\mathrm{AB}}\mu_{\mathrm{AB}}\right)} \exp\left(-\mu_{\mathrm{AB}}\Lambda_{\mathrm{AB}}h^2\right) I_{\mu_{\mathrm{AB}}-1}\Big(2\mu_{\mathrm{AB}}h\sqrt{\kappa_{\mathrm{AB}}\Lambda_{\mathrm{AB}}}\Big), \quad (6.3)$$

where $\Lambda_{\mathrm{AB}} = \frac{1+\kappa_{\mathrm{AB}}}{\Omega_{\mathrm{AB}}}$, $\Omega_{\mathrm{AB}} = \mathcal{E}\left\{|h_{\mathrm{AB}}|^2\right\}$ corresponds to mean power of $|h_{\mathrm{AB}}|$ and $I_v(\cdot)$ is the modified Bessel function of the first kind and order v. The l-th moment of h_{AB} following κ-μ distribution is given by

$$\mathcal{E}\left\{|h_{\mathrm{AB}}|^l\right\} = \frac{\Gamma(\mu_{\mathrm{AB}} + l/2)\left(\Omega_{\mathrm{AB}}\right)^{l/2}}{\Gamma(\mu_{\mathrm{AB}})\left[(1+\kappa_{\mathrm{AB}})\mu_{\mathrm{AB}}\right]^{l/2}\exp(\kappa_{\mathrm{AB}}\mu_{\mathrm{AB}})} \, {}_1F_1\left(\mu_{\mathrm{AB}} + \frac{l}{2}; \mu_{\mathrm{AB}}; \kappa_{\mathrm{AB}}\mu_{\mathrm{AB}}\right), \quad (6.4)$$

where $\Gamma(\cdot)$ is the gamma function defined in [68, (8.31)] and ${}_1F_1(\cdot;\cdot;\cdot)$ is the Kummer confluent hypergeometric function defined in [63, (07.20.02.0001.01)]. Furthermore, the parameters κ_{AB} and μ_{AB} are related to each other as

$$\mu_{\mathrm{AB}} = \frac{\Omega_{\mathrm{AB}}^2}{\mathcal{V}\left\{|h_{\mathrm{AB}}|^2\right\}} \frac{1+2\kappa_{\mathrm{AB}}}{\left(1+\kappa_{\mathrm{AB}}\right)^2}. \quad (6.5)$$

Substituting (6.5) in (6.4) and further solving for $l = 6$, κ_{AB} can be obtained through

$$\kappa_{\mathrm{AB}}^{-1} = \frac{\sqrt{2}\mathcal{V}\left\{|h_{\mathrm{AB}}|^2\right\}}{\sqrt{2\mathcal{E}^2\left\{|h_{\mathrm{AB}}|^4\right\} - \Omega_{\mathrm{AB}}^2\mathcal{E}\left\{|h_{\mathrm{AB}}|^4\right\} - \Omega_{\mathrm{AB}}\mathcal{E}\left\{|h_{\mathrm{AB}}|^6\right\}}} - 2. \quad (6.6)$$

The κ-μ distribution is a generic fading distribution that incorporates the Rayleigh ($\mu = 1$ and $\kappa \to 0$), Nakagami ($\mu \geq 1$ and $\kappa \to 0$), and Rician ($\mu = 1$ and $\kappa \geq 0$) distributions, which are some of the well-known and widely used fading distributions.

6.3 Statistical Distribution of SINR

In this section, we derive the CDF of the SINR at DUE_j for the considered IRS-assisted multi-user RF network by obtaining the statistical distributions of the combined desired and the interfering signals. Following (6.2), the SINR at DUE_j can be expressed as

$$\Gamma_{\mathrm{D}_j} = \frac{\left|\sum_{n=1}^{N} X_{\mathrm{D}_j}^{(n)}\right|^2}{\left|\sum_{\ell=1}^{L} Y_{\mathrm{I}_\ell \mathrm{D}_j}\right|^2 + \sigma_{\mathrm{D}_j}^2} \triangleq \frac{\left|X_{\mathrm{D}_j}\right|^2}{\left|Y_{\mathrm{ID}_j}\right|^2 + \sigma_{\mathrm{D}_j}^2}, \quad (6.7)$$

where $X_{\mathrm{D}_j} \triangleq \sum_{n=1}^{N} X_{\mathrm{D}_j}^{(n)}$ is the combined envelope of received desired signal and $Y_{\mathrm{ID}_j} = \sum_{\ell=1}^{L} Y_{\mathrm{I}_\ell \mathrm{D}_j}$ is the combined envelope of received interference signal. If we assume that total interference power at a DUE dominates the noise power, i.e., interference-limited scenario, the CDF of the received SINR $\Gamma_{\mathrm{D}_j} \simeq \frac{\left|X_{\mathrm{D}_j}\right|^2}{\left|Y_{\mathrm{ID}_j}\right|^2}$ at DUE$_j$ can be evaluated as

$$\mathcal{F}_{\Gamma_{\mathrm{D}_j}}(\gamma) = \int_0^{\infty} \mathcal{F}_{\left|X_{\mathrm{D}_j}\right|^2}(\gamma v) f_{\left|Y_{\mathrm{ID}_j}\right|^2}(v) dv, \tag{6.8}$$

where $\mathcal{F}_X(\cdot)$ represents the CDF of RV X. In the subsequent part of this section, we derive the statistical distributions of the combined desired and the interfering signals.

6.3.1 Modelling and Statistical Characterization of Combined Desired Signal $X_{\mathbf{D}_j}$

If the perfect CSI of all the links is available, the reflection phase shift at each reflecting element can be configured to cancel out the phase difference of BS-IRS and IRS-DUE$_j$ links for achieving the maximum received signal power. With this assumption, the n-th combined desired signal component can be written as $X_{\mathrm{D}_j}^{(n)} = \sqrt{P_{\mathrm{D}_j}} \rho_{\mathrm{BR}} \rho_{\mathrm{RD}_j} |\varpi_{\mathrm{R}}^{(n)}| \left|h_{\mathrm{BR}}^{(n)}\right| \left|h_{\mathrm{RD}_j}^{(n)}\right|$. Since the channel amplitudes $\left|h_{\mathrm{BR}}^{(n)}\right|$ and $\left|h_{\mathrm{RD}_j}^{(n)}\right|$ are INID RVs, the X_{D_j} will represent a sum of N INID RVs and for large N, according to Lyapunov central limit theorem [124], X_{D_j} will converge in a Normal distributed RV provided the Lyapunov condition is satisfied for any $\delta > 0$ as

$$\mathcal{U}_\delta = \lim_{N\to\infty} \frac{\sum_{n=1}^{N} \mathcal{E}\left\{\left|X_{\mathrm{D}_j}^{(n)} - \mathcal{E}\left\{X_{\mathrm{D}_j}^{(n)}\right\}\right|^{2+\delta}\right\}}{\left(\sum_{n=1}^{N} \mathcal{V}\left\{X_{\mathrm{D}_j}^{(n)}\right\}\right)^{1+\frac{\delta}{2}}} = 0. \tag{6.9}$$

Thus, X_{D_j} is approximated as Gaussian distribution with mean $\mathcal{E}\left\{X_{\mathrm{D}_j}\right\}$ and variance $\mathcal{V}\left\{X_{\mathrm{D}_j}\right\}$, which can be obtained as

$$\mathcal{E}\{X_{\mathrm{D}_j}\} = \sqrt{P_{\mathrm{D}_j}} \rho_{\mathrm{BR}} \rho_{\mathrm{RD}_j} \sum_{n=1}^{N} |\varpi_{\mathrm{R}}^{(n)}| \mathcal{E}\left\{\left|h_{\mathrm{BR}}^{(n)}\right|\right\} \mathcal{E}\left\{\left|h_{\mathrm{RD}_j}^{(n)}\right|\right\}, \tag{6.10}$$

and

$$\begin{aligned}\mathcal{V}\{X_{\mathrm{D}_j}\} &= \sum_{n=1}^{N} \left[\mathcal{E}\left\{\left|X_{\mathrm{D}_j}^{(n)}\right|^2\right\} - \mathcal{E}^2\left\{\left|X_{\mathrm{D}_j}^{(n)}\right|\right\}\right] \\ &= P_{\mathrm{D}_j} \rho_{\mathrm{BR}}^2 \rho_{\mathrm{RD}_j}^2 \sum_{n=1}^{N} \left(|\varpi_{\mathrm{R}}^{(n)}|\right)^2 \left[\mathcal{E}\left\{\left|h_{\mathrm{BR}}^{(n)}\right|^2\right\} \mathcal{E}\left\{\left|h_{\mathrm{RD}_j}^{(n)}\right|^2\right\} - \mathcal{E}^2\left\{\left|h_{\mathrm{BR}}^{(n)}\right|\right\} \mathcal{E}^2\left\{\left|h_{\mathrm{RD}_j}^{(n)}\right|\right\}\right],\end{aligned} \tag{6.11}$$

where moments of $\left|h_{\mathrm{BR}}^{(n)}\right|$ and $\left|h_{\mathrm{RD}_j}^{(n)}\right|$ can be obtained from (6.4). Now, since X_{D_j} follows Gaussian distribution, the $\left|X_{\mathrm{D}_j}\right|^2$ will follow non-central chi-square distribution with one degree of freedom (DoF) and the CDF of $\left|X_{\mathrm{D}_j}\right|^2$ can be given by [82]

$$\mathcal{F}_{\left|X_{\mathrm{D}_j}\right|^2}(u) = 1 - Q_{\frac{1}{2}}\left(\frac{\mathcal{E}\left\{X_{\mathrm{D}_j}\right\}}{\sqrt{\mathcal{V}\left\{X_{\mathrm{D}_j}\right\}}}, \frac{\sqrt{u}}{\sqrt{\mathcal{V}\left\{X_{\mathrm{D}_j}\right\}}}\right), \tag{6.12}$$

where $Q_p(a,b)$ is the Marcum Q-function [125].

6.3.2 Modelling and Statistical Characterization of Combined Interference Signal Y_{ID_j}

Since the channel coefficient of the link between IUE$_\ell$ and DUE$_j$, i.e., $g_{\mathrm{I}_\ell\mathrm{D}_j}$ follows κ-μ distribution with parameters $\left(\kappa_{\mathrm{I}_\ell\mathrm{D}_j}, \mu_{\mathrm{I}_\ell\mathrm{D}_j}, \Omega_{\mathrm{I}_\ell\mathrm{D}_j}\right)$, the RV $\mathrm{Y}_{\mathrm{I}_\ell\mathrm{D}_j} \triangleq \sqrt{P_{\mathrm{I}_\ell}}\rho_{\mathrm{I}_\ell\mathrm{D}_j} g_{\mathrm{I}_\ell\mathrm{D}_j}$ will also follow κ-μ distribution with parameters $\left(\kappa_{\mathrm{I}_\ell\mathrm{D}_j}, \mu_{\mathrm{I}_\ell\mathrm{D}_j}, P_{\mathrm{I}_\ell}\rho^2_{\mathrm{ID}_j}\Omega_{\mathrm{I}_\ell\mathrm{D}_j}\right)$. Furthermore, the RV $Y_{\mathrm{ID}_j} \triangleq \sum_{\ell=1}^{L} \mathrm{Y}_{\mathrm{I}_\ell\mathrm{D}_j}$ can also be approximated by another $\kappa-\mu$ distributed RV with parameters $\left(\kappa_{\mathrm{ID}_j}, \mu_{\mathrm{ID}_j}, \Omega_{\mathrm{ID}_j}\right)$ [122, 126], where $\Omega_{\mathrm{ID}_j} = \mathcal{E}\left\{Y^2_{\mathrm{ID}_j}\right\}$ and the parameters κ_{ID_j} and μ_{ID_j} can be calculated by using (6.5) and (6.6).

The l-th moment of the sum RV can be obtained as

$$\mathcal{E}\left\{Y^l_{\mathrm{ID}_j}\right\} = \sum_{l_1=0}^{l}\sum_{l_2=0}^{l_1}\cdots\sum_{l_{L-1}=0}^{l_{L-2}}\binom{l}{l_1}\binom{l_1}{l_2}\cdots\binom{l_{L-2}}{l_{L-1}}\mathcal{E}\left\{Y^{l-l_1}_{\mathrm{I}_\ell\mathrm{D}_j}\right\}\mathcal{E}\left\{Y^{l_1-l_2}_{\mathrm{I}_\ell\mathrm{D}_j}\right\}\cdots\mathcal{E}\left\{Y^{l_{L-1}}_{\mathrm{I}_\ell\mathrm{D}_j}\right\}. \tag{6.13}$$

The PDF of $\left|Y_{\mathrm{ID}_j}\right|^2$ can now be expressed as

$$f_{\left|Y_{\mathrm{ID}_j}\right|^2}(v) = \left(\frac{v}{\kappa_{\mathrm{ID}_j}}\right)^{\frac{\mu_{\mathrm{ID}_j}-1}{2}} \frac{\mu_{\mathrm{ID}_j}\left(\Lambda_{\mathrm{ID}_j}\right)^{\frac{\mu_{\mathrm{ID}_j}+1}{2}}}{\exp\left(\kappa_{\mathrm{ID}_j}\mu_{\mathrm{ID}_j}\right)} \exp\left(-\mu_{\mathrm{ID}_j}\Lambda_{\mathrm{ID}_j}v\right) I_{\mu_{\mathrm{ID}_j}-1}\left(2\mu_{\mathrm{ID}_j}\sqrt{\kappa_{\mathrm{ID}_j}\Lambda_{\mathrm{ID}_j}}\right). \tag{6.14}$$

Substituting (6.12) and (6.14) into (6.8) and using the power series expansions $Q_p(a,b) = 1 - e^{-a^2/2}\sum_{k_1=0}^{\infty}\frac{1}{k_1!}\left(\frac{a^2}{2}\right)^{k_1}\frac{\gamma(p+k_1,b^2/2)}{\Gamma(p+k)}$ [125, (2.12)] and $I_v(z) = \sum_{k_2=0}^{\infty}\frac{1}{k_2!\Gamma(v+k_2+1)}\left(\frac{z}{2}\right)^{v+2k_2}$ [67, (8.445)], we get

$$\mathcal{F}_{\Gamma_{\mathrm{D}_j}}(\gamma) = \exp\left(-\kappa_{\mathrm{ID}_j}\mu_{\mathrm{ID}_j} - \frac{\mathcal{E}^2\left\{X_{\mathrm{D}_j}\right\}}{2\mathcal{V}\left\{\mathrm{D}_j\right\}}\right)\sum_{k_1=0}^{\infty}\sum_{k_2=0}^{\infty}\frac{1}{k_1!}\left(\frac{\mathcal{E}^2\left\{X_{\mathrm{D}_j}\right\}}{2\mathcal{V}\left\{X_{\mathrm{D}_j}\right\}}\right)^{k_1}\frac{\mathcal{J}_{\mathrm{D}_j}(k_2)\mathcal{H}_{\mathrm{D}_j}(k_1,k_2;\gamma)}{\Gamma\left(k_1+\frac{1}{2}\right)}. \tag{6.15}$$

where

$$\mathcal{J}_{\mathrm{D}_j}(k_2) = \frac{\mu_{\mathrm{ID}_j}^{\mu_{\mathrm{ID}_j}+2k_2}\kappa_{\mathrm{ID}_j}^{k_2}}{k_2!\,\Gamma\left(\mu_{\mathrm{ID}_j}+k_2\right)}\left(\Lambda_{\mathrm{ID}_j}\right)^{\mu_{\mathrm{ID}_j}+k_2} \tag{6.16}$$

and

$$\mathcal{H}_{\mathrm{D}_j}(k_1,k_2;\gamma)=\int_0^{\infty} v^{\mu_{\mathrm{ID}_j}+k_2-1}\exp\left(-\Lambda_{\mathrm{ID}_j}\mu_{\mathrm{ID}_j}v\right)\gamma\left(k_1+\frac{1}{2},\frac{\gamma\, v}{2\mathcal{V}\left\{X_{\mathrm{D}_j}\right\}}\right)dv. \tag{6.17}$$

The integral in (6.17) can be evaluated by utilizing [67, (6.455.2)] and the closed-form expression of $\mathcal{H}_{\mathrm{D}_j}(k_1,k_2;\gamma)$ is given by

$$\mathcal{H}_{\mathrm{D}_j}(k_1,k_2;\gamma)=\frac{\left(\frac{\gamma}{2\mathcal{V}\left\{X_{\mathrm{D}_j}\right\}}\right)^{k_1+\frac{1}{2}}\Gamma\left(\mu_{\mathrm{ID}_j}+k_1+k_2+\frac{1}{2}\right)}{\left(k_1+\frac{1}{2}\right)\left(\frac{\gamma}{2\mathcal{V}\left\{X_{\mathrm{D}_j}\right\}}+\Lambda_{\mathrm{ID}_j}\mu_{\mathrm{ID}_j}\right)^{\mu_{\mathrm{ID}_j}+k_1+k_2+\frac{1}{2}}}$$
$$\times\ {}_2F_1\left(1,\mu_{\mathrm{ID}_j}+k_1+k_2+\frac{1}{2};k_1+\frac{3}{2};\frac{\frac{\gamma}{2\mathcal{V}\left\{X_{\mathrm{D}_j}\right\}}}{\left(\frac{\gamma}{2\mathcal{V}\left\{X_{\mathrm{D}_j}\right\}}+\Lambda_{\mathrm{ID}_j}\mu_{\mathrm{ID}_j}\right)}\right). \tag{6.18}$$

where ${}_2F_1(\cdot;\cdot;\cdot)$ is the Gauss Hypergeometric function defined in [63, (07.23.02.0001.01)]. Therefore, the analytical expression of $\mathcal{F}_{\Gamma_{\mathrm{D}_j}}(\gamma)$ for the considered interference-limited IRS-assisted RF network can be obtained by using (6.18) in (6.15).

6.4 Performance Evaluation

In this Section, we analyze the system performance in terms of SOS like LCR and AOD for the considered interference-limited RF communication network assisted by IRS. Moreover, we derive the PER and optimal packet length of the considered IRS-assisted network with SW-ARQ protocol based data transmission by utilizing the FSMC model.

6.4.1 Calculation of LCR and AOD

The LCR is defined as the mean rate at which the received signal (in the time-varying channel conditions) crosses a particular threshold in downward direction. More specifically, the LCR gives the temporal rate of outage events. For the considered interference-limited network, the LCR may be described as the temporal rate of outage events when the envelope of received SINR falls below a predefined threshold (determining the receiver sensitivity). If $Z_{\mathrm{D}_j}\triangleq\sqrt{\Gamma_{\mathrm{D}_j}}=\frac{X_{\mathrm{D}_j}}{Y_{\mathrm{ID}_j}}$ is the the envelope of received SINR, the derivative $\dot{Z}_{\mathrm{D}_j}$ can be obtained as

$$\dot{Z}_{\mathrm{D}_j}=\frac{1}{Y_{\mathrm{ID}_j}}\left(\dot{X}_{\mathrm{D}_j}-Z_{\mathrm{D}_j}\dot{Y}_{\mathrm{ID}_j}\right), \tag{6.19}$$

where $\dot{X}_{\mathrm{D}_j}$ is the time derivative of X_{D_j} following the Gaussian distribution with zero mean and variance $\mathcal{V}\left\{\dot{X}_{\mathrm{D}_j}\right\}$.

Lemma 6.1: *Considering the non-isotropic scattering for the signal received at DUE$_j$ through the reflection from the IRS, and assuming the non-uniform distribution for angle of arrival (AoA) φ_{D_j} at DUE$_j$, the variance of the $\dot{X}_{D_j}$ is given by*

$$\mathcal{V}\left\{\dot{X}_{D_j}\right\} = 2\pi^2 f_{D_j}^2 \mathcal{E}\left\{X_{D_j}^2\right\} \frac{\chi[I_0(\chi) + I_2(\chi)]\cos^2\varphi_{D_{j,p}} + 2I_1(\chi)\sin^2\varphi_{D_{j,p}}}{2\chi I_0(\chi)}, \tag{6.20}$$

where $\varphi_{D_{j,p}}$ is the mean AoA at DUE$_j$, f_{D_j} denotes the maximum Doppler frequency shift due to the movement of DUE$_j$, χ defines the degree of non-isotropic scattering, and $I_x(\cdot)$ represents the x-th order Bessel function of first kind [68].

Proof. See Appendix A.5.1 for the proof. □

It may noted from Table 5.1 that a large value of χ is suitable for the considered IRS-assisted system model.

Corollary 6.1 *Since for large χ, i.e., $\chi \to \infty$, the Bessel's function can be approximated as $I_x(\chi) \approx \frac{e^\chi}{\sqrt{2\pi\chi}}$, for all x. Thus, for $\chi \to \infty$, the variance in (6.20) can be approximated as*

$$\mathcal{V}\left\{\dot{X}_{D_j}\right\} \approx 2\pi^2 f_{D_j}^2 \mathcal{E}\left\{X_{D_j}^2\right\}\cos^2\varphi_{D_{j,p}}. \tag{6.21}$$

It may be noted that the above expression is independent of χ.

Similarly, $\dot{Y}_{\mathrm{ID}_j}$ is the time derivative of Y_{ID_j} following the Gaussian distribution with zero mean and variance

$$\mathcal{V}\left\{\dot{Y}_{\mathrm{ID}_j}\right\} = \sum_{\ell=1}^{L} \mathcal{V}\left\{\dot{Y}_{\mathrm{I}_\ell \mathrm{D}_j}\right\} = 2\pi^2 \sum_{\ell=1}^{L}\left(f_{I_\ell}^2 + f_{\mathrm{D}_j}^2\right)\frac{P_{\mathrm{I}_\ell}\rho_{\mathrm{I}_\ell \mathrm{D}_j}^2 \Omega_{\mathrm{I}_\ell \mathrm{D}_j}}{\mu_{\mathrm{I}_\ell \mathrm{D}_j}(1+\kappa_{\mathrm{I}_\ell \mathrm{D}_j})}, \tag{6.22}$$

with f_{I_ℓ} being the maximum Doppler frequency shift due to IUE$_\ell$ [127, 6]. Therefore, the LCR at DUE$_j$ can be evaluated by putting $z = \sqrt{\gamma_{\mathrm{Th}}}$ in the Rice's formula [32] defined as

$$\mathcal{L}_{\mathrm{D}_j}(z) = \int_0^\infty \dot{z} f_{Z_{\mathrm{D}_j}\dot{Z}_{\mathrm{D}_j}}(z,\dot{z})d\dot{z}, \tag{6.23}$$

which can further be simplified by using the joint PDF properties [128] as

$$\begin{aligned}\mathcal{L}_{\mathrm{D}_j}(z) &= \int_0^\infty \left(\int_0^\infty \dot{z}\, f_{\dot{Z}_{\mathrm{D}_j}|Z_{\mathrm{D}_j},Y_{\mathrm{ID}_j}}(\dot{z}|z,y)d\dot{z}\right) f_{Z_{\mathrm{D}_j}|Y_{\mathrm{ID}_j}}(z|y) f_{Y_{\mathrm{ID}_j}}(y)\,dy \\ &\triangleq \int_0^\infty \mathcal{I}_{\mathrm{D}_j}(z,y) f_{Z_{\mathrm{D}_j}|Y_{\mathrm{ID}_j}}(z|y) f_{Y_{\mathrm{ID}_j}}(y)\,dy\end{aligned} \tag{6.24}$$

where $f_{A|B,C}(\cdot|\cdot,\cdot)$ and $f_{A|B}(\cdot|\cdot)$ represent the conditional PDFs. It is clear from (6.19) and the discussion thereafter that if Z_{D_j} and Y_{ID_j} are known, $\dot{Z}_{\mathrm{D}_j}$ follows the Gaussian distribution with zero mean and variance $\mathcal{V}\left\{\dot{Z}_{\mathrm{D}_j}|Z_{\mathrm{D}_j}=z, Y_{\mathrm{D}_j}=y\right\}$ defined as

$$\mathcal{V}\Big\{\dot{Z}_{\mathrm{D}_j}|Z_{\mathrm{D}_j}{=}z, Y_{\mathrm{D}_j}{=}y\Big\}=\frac{1}{y^2}\mathcal{V}\Big\{\dot{X}_{\mathrm{D}_j}\Big\}+\frac{z^2}{y^2}\mathcal{V}\Big\{\dot{Y}_{\mathrm{ID}_j}\Big\}. \tag{6.25}$$

Since for a zero mean Gaussian RV (X) having variance σ_X^2, we have $\int_0^\infty x f_X(x)dx = \frac{1}{\sqrt{2\pi}}\sigma_X$. Hence, the term $\mathcal{I}_{\mathrm{D}_j}(z,y)$ in (6.24) can be given as

$$\mathcal{I}_{\mathrm{D}_j}(z,y) = \frac{1}{y\sqrt{2\pi}}\sqrt{\mathcal{V}\Big\{\dot{X}_{\mathrm{D}_j}\Big\} + z^2\mathcal{V}\Big\{\dot{Y}_{\mathrm{ID}_j}\Big\}}. \tag{6.26}$$

Substituting (6.26) in (6.24) along with the use of $f_{Z_{\mathrm{D}_j}|Y_{\mathrm{D}_j}}(z|y) = y f_{X_{\mathrm{D}_j}}(zy)$, we have

$$\mathcal{L}_{\mathrm{D}_j}(z){=}\frac{1}{\sqrt{2\pi}}\sqrt{\mathcal{V}\Big\{\dot{X}_{\mathrm{D}_j}\Big\}{+}z^2\mathcal{V}\Big\{\dot{Y}_{\mathrm{ID}_j}\Big\}}\int_0^\infty f_{X_{\mathrm{D}_j}}(zy)f_{Y_{\mathrm{ID}_j}}(y)dy. \tag{6.27}$$

Since $X_{\mathrm{D}_j} \sim \mathcal{N}\left(\mathcal{E}\left\{X_{\mathrm{D}_j}\right\}, \mathcal{V}\left\{X_{\mathrm{D}_j}\right\}\right)$ and Y_{ID_j} follows κ-μ distribution with parameters $\left(\kappa_{\mathrm{ID}_j}, \mu_{\mathrm{ID}_j}, \Omega_{\mathrm{ID}_j}\right)$, we utilize the Gaussian PDF [129, (2.1.4)] and κ-μ PDF (from (6.3)) in (6.27) along with the use of power series expansion of $I_v(\cdot)$ to get

$$\mathcal{L}_{\mathrm{D}_j}(z){=}\exp\left(-\kappa_{\mathrm{ID}_j}\mu_{\mathrm{ID}_j}-\frac{\mathcal{E}^2\left\{X_{\mathrm{D}_j}\right\}}{2\mathcal{V}\left\{X_{\mathrm{D}_j}\right\}}\right)\sqrt{\frac{\mathcal{V}\left\{\dot{X}_{\mathrm{D}_j}\right\}{+}z^2\mathcal{V}\left\{\dot{Y}_{\mathrm{ID}_j}\right\}}{\pi^2\mathcal{V}\left\{X_{\mathrm{D}_j}\right\}}}\sum_{k_3=0}^{\infty}\mathcal{J}_{\mathrm{D}_j}(k_3)\mathcal{G}_{\mathrm{D}_j}(k_3;z), \tag{6.28}$$

where

$$\mathcal{G}_{\mathrm{D}_j}(k_3;z) = \int_0^\infty y^{2\left(\mu_{\mathrm{ID}_j}+k_3\right)-1}\exp\left(-\left[\frac{z^2}{2\mathcal{V}\{X_{\mathrm{D}_j}\}}+\Lambda_{\mathrm{ID}_j}\mu_{\mathrm{ID}_j}\right]y^2+\frac{\mathcal{E}\left\{X_{\mathrm{D}_j}\right\}}{\mathcal{V}\{X_{\mathrm{D}_j}\}}zy\right)dy. \tag{6.29}$$

The integral in (6.29) can be solved by utilizing [67, (3.462,1)] to produce (6.30) by

$$\mathcal{G}_{\mathrm{D}_j}(k_3;z) = \frac{\Gamma\left(2\mu_{\mathrm{ID}_j}+2k_3\right)}{\left[2\left(\frac{z^2}{2\mathcal{V}\left\{X_{\mathrm{D}_j}\right\}}+\Lambda_{\mathrm{ID}_j}\mu_{\mathrm{ID}_j}\right)\right]^{\left(\mu_{\mathrm{ID}_j}+k_3\right)}}\exp\left(\frac{\left(\frac{\mathcal{E}\left\{X_{\mathrm{D}_j}\right\}}{\mathcal{V}\left\{X_{\mathrm{D}_j}\right\}}z\right)^2}{8\left(\frac{z^2}{2\mathcal{V}\left\{X_{\mathrm{D}_j}\right\}}+\Lambda_{\mathrm{ID}_j}\mu_{\mathrm{ID}_j}\right)}\right)$$
$$\times D_{-2\left(\mu_{\mathrm{ID}_j}+k_3\right)}\left(\frac{-\frac{\mathcal{E}\left\{X_{\mathrm{D}_j}\right\}}{\mathcal{V}\left\{X_{\mathrm{D}_j}\right\}}z}{\sqrt{2\left(\frac{z^2}{2\mathcal{V}\left\{X_{\mathrm{D}_j}\right\}}+\Lambda_{\mathrm{ID}_j}\mu_{\mathrm{ID}_j}\right)}}\right). \tag{6.30}$$

where $D_v(\cdot)$ is the Parabolic cylinder function defined in [68]. Using (6.30) in (6.28) along with the substitution of $z = \sqrt{\gamma_{\mathrm{Th}}}$, the expression for the LCR for a given threshold SINR (i.e. $\mathcal{L}_{\mathrm{D}_j}(\sqrt{\gamma_{\mathrm{Th}}})$) can be obtained. To get further insights about the second order statistical behavior of the considered IRS-assisted RF network, we derive asymptotic expression of LCR at DUE$_j$ by utilizing high transmit power conditions, which may be defined as $\tilde{\mathcal{L}}_{\mathrm{D}_j}(z) \triangleq \lim_{P_{\mathrm{D}_j}\to\infty} \mathcal{L}_{\mathrm{D}_j}(z)$. It shall be noted that the ratio $\frac{\mathcal{V}\left\{\dot{Y}_{\mathrm{ID}_j}\right\}}{\mathcal{V}\left\{X_{\mathrm{D}_j}\right\}} \to 0$ for $P_{\mathrm{D}_j} \to \infty$, whereas the ratio $\frac{\mathcal{V}\left\{\dot{X}_{\mathrm{D}_j}\right\}}{\mathcal{V}\left\{X_{\mathrm{D}_j}\right\}}$ is a constant. Therefore, $\tilde{\mathcal{L}}_{\mathrm{D}_j}(z)$ can be obtained from (6.28) as

$$\tilde{\mathcal{L}}_{\mathrm{D}_j}(z) = \exp\left(-\kappa_{\mathrm{ID}_j}\mu_{\mathrm{ID}_j} - \frac{\mathcal{E}^2\left\{X_{\mathrm{D}_j}\right\}}{2\mathcal{V}\left\{X_{\mathrm{D}_j}\right\}}\right)\sqrt{\frac{\mathcal{V}\left\{\dot{X}_{\mathrm{D}_j}\right\}}{\pi^2\mathcal{V}\left\{X_{\mathrm{D}_j}\right\}}}\sum_{k_3=0}^{\infty}\mathcal{J}_{\mathrm{D}_j}(k_3)\tilde{\mathcal{G}}_{\mathrm{D}_j}(k_3;z), \tag{6.31}$$

where $\tilde{\mathcal{G}}_{\mathrm{D}_j}(k_3;z) = \lim_{P_{\mathrm{D}_j}\to\infty} \mathcal{G}_{\mathrm{D}_j}(k_3;z)$. Utilizing high transmit power conditions (i.e., $P_{\mathrm{D}_j} \to \infty$) in (6.30) followed by the use of $D_v(0) = \frac{2^{v/2}\sqrt{\pi}}{\Gamma\left(\frac{1-v}{2}\right)}$ [63, (07.41.03.0001.01)], we get

$$\tilde{\mathcal{G}}_{\mathrm{D}_j}(k_3;z) = \frac{\Gamma\left(2\mu_{\mathrm{ID}_j} + 2k_3\right)\sqrt{\pi}}{\Gamma\left(\mu_{\mathrm{ID}_j} + k_3 + \frac{1}{2}\right)\left(4\Lambda_{\mathrm{ID}_j}\mu_{\mathrm{ID}_j}\right)^{(\mu_{\mathrm{ID}_j}+k_3)}}. \tag{6.32}$$

Remark 6.1: *It can be noticed from* (6.31) *that asymptotically LCR expression for the considered IRS-assisted system with CCI is independent of outage threshold and transmit power. The asymptotic LCR is function of channel parameters of κ-μ distribution of the desired as well as interference links. Moreover, the asymptotic LCR depends on the number of IRS elements and amplitude of reflection at each reflecting elements.*

Furthermore, we define the AOD as the average time duration for which the received signal remains below a particular threshold. In other words, AOD gives the time span over which the a node remains in outage. For the considered interference-limited RF communication network, the AOD can be mathematically defined as

$$\mathcal{T}_{\mathrm{D}_j}(\gamma_{\mathrm{Th}}) = \frac{\mathcal{F}_{\Gamma_{\mathrm{D}_j}}(\gamma_{\mathrm{Th}})}{\mathcal{L}_{\mathrm{D}_j}(\sqrt{\gamma_{\mathrm{Th}}})}. \tag{6.33}$$

Using the CDF and LCR expressions given in (6.15) and (6.28), respectively, the analytical expression of AOD can be obtained for the considered IRS-assisted RF network.

6.4.2 Calculation of PER under SW-ARQ Protocol

One of the most basic error control strategies for providing reliable communication between two wireless nodes is ARQ. SW-ARQ is one of the widely used data packet transmission protocol where the source node waits for the receiver's response about the transmitted data packet. If the source gets the acknowledgment from the receiver, then only the next data packet is transmitted, otherwise the current data packet is re-transmitted. Due to the popularity of this scheme in the practical communication systems, we employ SW-ARQ scheme in the link layer of the considered IRS-assisted system with CCI for reliable transmission of packets and derive the expression for PER by considering FSMC model. The PER is an important QoS measure for link layer designs which describes the performance of a RF communication system. In general, a packet will be termed as error packet iff there exists at least one bit error in the packet. For FSMC based model, the PER at a user can be evaluated using the LCR of that user which considers the time variations and correlations of the channel [112]. Thus, for the considered network, the PER at DUE$_j$ having an SINR threshold of γ_{Th} can be evaluated as [112]

$$\mathcal{P}_{\mathrm{p,D}_j}(\gamma_{\mathrm{Th}}) = 1 - \mathcal{F}^c_{\Gamma_{\mathrm{D}_j}}(\gamma_{\mathrm{Th}}) \exp\left(-T_{P_{\mathrm{D}_j}} \frac{\mathcal{L}_{\mathrm{D}_j}(\sqrt{\gamma_{\mathrm{Th}}})}{\mathcal{F}^c_{\Gamma_{\mathrm{D}_j}}(\gamma_{\mathrm{Th}})}\right), \tag{6.34}$$

where $\mathcal{F}^c_{\Gamma_{\mathrm{D}_j}}(\cdot) = 1 - \mathcal{F}_{\Gamma_{\mathrm{D}_j}}(\cdot)$ is the complementary CDF of Γ_{D_j}, $T_{P_{\mathrm{D}_j}} = m_{\mathrm{T}} T_{S_{\mathrm{D}_j}}$ is the total duration of the packet with m_{T} representing the number of symbols per data packet and $T_{S_{\mathrm{D}_j}}$ being the finite duration of each symbol in the packet transmitted over j-th sub-band. Substituting (6.18) and (6.30) in (6.34), the analytical expression of PER can be obtained. Another important performance metric for FSMC based model using SW-ARQ protocol is the *throughput*. For a given data packet length (i.e., m_{T}), the throughput of the system with SW-ARQ protocol can be obtained as

$$\mathcal{U}_{\mathrm{D}_j}(m_{\mathrm{T}}) = \frac{m_{\mathrm{T}} \mathcal{R}_{\mathrm{D}_j}}{(m_{\mathrm{T}} + m_{\mathrm{O}})} \left(1 - \mathcal{P}_{\mathrm{p,D}_j}(\gamma_{\mathrm{Th}})\right), \tag{6.35}$$

where $\mathcal{R}_{\mathrm{D}_j} = \frac{1}{T_{S_{\mathrm{D}_j}}}$ is the data rate of DUE$_j$ and m_{OV} is the number of overhead symbols. It is shown in the numerical results section (Refer Fig. 6.7(c)) that the throughput is a concave downward function of m_{T} for different values of N and $\mathcal{R}_{\mathrm{D}_j}$. Thus, we analytically find the optimum value of m_{T} that maximizes the throughput by equating the first derivative of (6.35) to zero. Using (6.34) in (6.35), followed by differentiation w.r.t. m_{T}, we get

$$\frac{\partial \mathcal{U}_{\mathrm{D}_j}(m_{\mathrm{T}})}{\partial m_{\mathrm{T}}} = \left[-\mathcal{L}_{\mathrm{D}_j}(\sqrt{\gamma_{\mathrm{Th}}}) m_{\mathrm{T}} + \mathcal{R}_{\mathrm{D}_j} \mathcal{F}^c_{\Gamma_{\mathrm{D}_j}}(\gamma_{\mathrm{Th}}) \frac{m_{\mathrm{T}} \mathcal{R}_{\mathrm{D}_j} \mathcal{F}^c_{\Gamma_{\mathrm{D}_j}}(\gamma_{\mathrm{Th}})}{m_{\mathrm{T}} + m_{\mathrm{OV}}} \right] \frac{\exp\left(-\frac{m_{\mathrm{T}} T_{S_{\mathrm{D}_j}} \mathcal{L}_{\mathrm{D}_j}(\sqrt{\gamma_{\mathrm{Th}}})}{\mathcal{F}^c_{\Gamma_{\mathrm{D}_j}}}\right)}{m_{\mathrm{T}} + m_{\mathrm{OV}}}. \tag{6.36}$$

Further, equating (6.36) to 0 and solving for m_{T}, we get

$$m_{\mathrm{T}}^{*}=\frac{m_{\mathrm{OV}}}{2}\left(\sqrt{1+\frac{4\mathcal{F}_{\Gamma_{\mathrm{D}_j}}^{c}(\gamma_{\mathrm{Th}})}{m_{\mathrm{OV}}\mathcal{L}_{\mathrm{D}_j}(\sqrt{\gamma_{\mathrm{Th}}})T_{S_{\mathrm{D}_j}}}}-1\right), \tag{6.37}$$

where m_{T}^{*} is the optimum number of symbols per data packet.

6.5 Numerical Results

In this section, we obtain the the numerical results of LCR, AOD, PER and the throughput for the considered IRS-assisted RF communication network in the presence of CCI. The locations of the BS and the IRS are assumed to be $\mathcal{X}_{\mathrm{B}} \triangleq (-15, 2, 25)$ and $\mathcal{X}_{\mathrm{R}} \triangleq (20, 0, 20)$, respectively, and the location of j-th DUE at a particular time instant is taken as $\mathcal{X}_{\mathrm{D}_j} \triangleq (35, 5, 0)$. The values of path loss exponent e and average received power ρ_0 due to path loss at a reference distance of 1 m are assumed to be 2 and -10 dB, respectively, and all the distances are measured in meters (m). Except for Fig. 6.5, we have considered two interferers (i.e., $L = 2$) with distances $d_{\mathrm{I}_1\mathrm{D}_j} = 60$ m and $d_{\mathrm{I}_2\mathrm{D}_j} = 66$ m. The values of $\varphi_{\mathrm{D}_{j,p}}$ and χ are taken as $\pi/4$ and 10, respectively, in all figures. Unless stated, the values of the transmit power (P_{D_j}), maximum Doppler frequency due to DUE$_j$ (f_{D_j}), number of reflecting elements (N), and minimum reflection amplitude (ϖ_{min}) are taken as 5 dB, 60 Hz 50, and 0.8 respectively.

In Figs. 6.2(a) and 6.2(b), we present the variations of the LCR and the AOD, respectively, w.r.t. the outage threshold γ_{Th} for different fading parameters of the BS-IRS and IRS-DUE links under the considered RF communication network with 2 IUE. It can be noticed from Fig. 6.2(a) that the received signal fluctuations are maximum at a particular threshold SINR (say Γ_{Th}^{*}), which increases with increase in fading parameters of BS-IRS and IRS-DUE links. The fluctuations approach to zero for very small and very large values of γ_{Th}. It shall be noted that for any $\gamma_{\mathrm{Th}} < \Gamma_{\mathrm{Th}}^{*}$, the larger values of fading parameters provide lower LCR, whereas the reverse holds true for $\gamma_{\mathrm{Th}} > \Gamma_{\mathrm{Th}}^{*}$. For example, at $\gamma_{\mathrm{Th}} = 15$ dB and $\kappa_{\mathrm{BR}} = \kappa_{\mathrm{RD}_j} = 1$, increasing $\mu_{\mathrm{BR}}, \mu_{\mathrm{RD}_j}$ from 0.5 to 1 results in an LCR decrease from 100 sec^{-1} to 45 sec^{-1}, whereas for $\gamma_{\mathrm{Th}} = 25$ dB, the same change in fading parameters increases the LCR from 35 sec^{-1} to 60 sec^{-1}. Further, it can be observed from Fig. 6.2(b) that the AOD increases exponentially with outage threshold, which depicts that the system spends a longer time in fade for larger γ_{Th}.

Observation 6.1: *It can be deduced from Fig. 6.2 that increasing γ_{Th} may result in lower LCR values but the amount of time taken in each fade will be quiet high. For example, with*

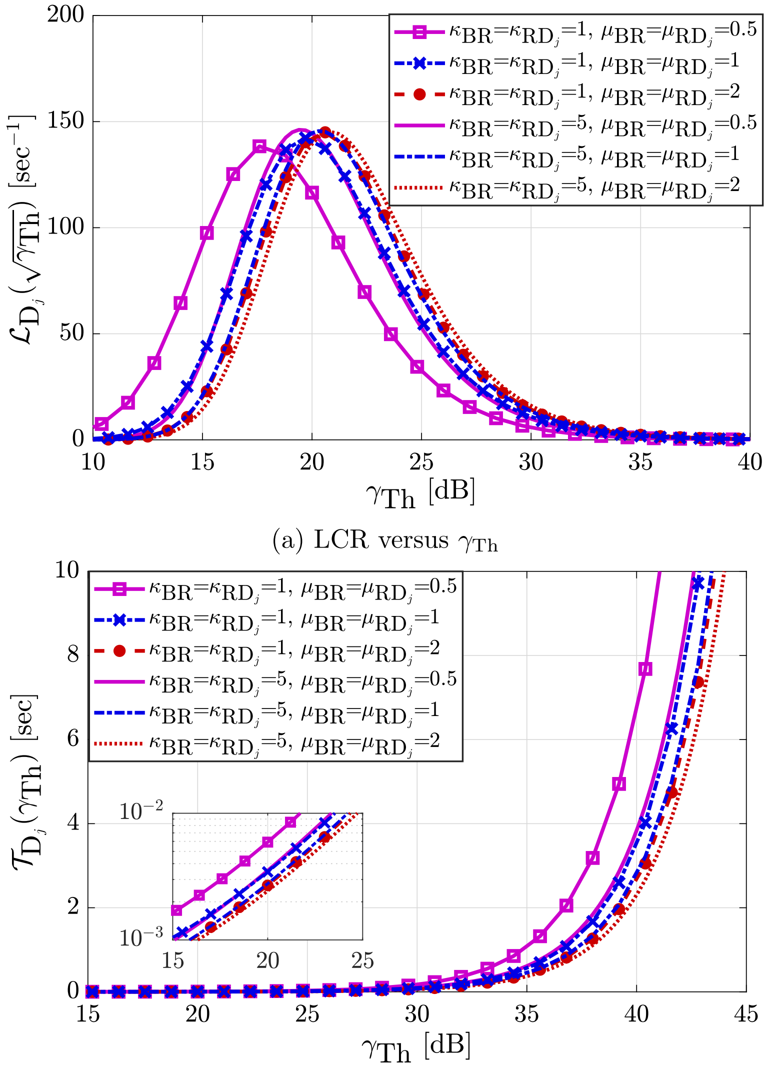

(a) LCR versus γ_{Th}

(b) AOD versus γ_{Th}

Figure 6.2: (a) LCR and (b) AOD versus SINR outage threshold for different fading parameters of BS-IRS and IRS-DUE$_j$ links with $\Omega_{\text{BR}} = \Omega_{\text{RD}_j} = 10$ and $L = 2$ having $f_{\text{I}_1\text{D}_j} = 60$ Hz, $f_{\text{I}_2\text{D}_j} = 50$ Hz. The fading parameters for interference links are $(\kappa_{\text{I}_\ell\text{D}_j}, \mu_{\text{I}_\ell\text{D}_j}, \Omega_{\text{I}_\ell\text{D}_j}) = (1, 1, 10)$ and $P_{\text{I}_\ell\text{D}_j} = 5$ dB for $\ell = 1, 2$.

$\kappa_{BR} = \kappa_{RD_j} = 5$ and $\mu_{BR} = \mu_{RD_j} = 2$, the LCR of 50 per sec is achieved at $\gamma_{Th} = 16.7$ and 26.6 dB, but the AOD for the corresponding LCR values are 0.00108 sec and 0.0207 sec. Moreover, it can also be noted from Fig. 6.2(b) that although increasing the fading parameters result in reduction in the AOD, the impact of parameter μ dominates over that of parameter κ.

In Figs. 6.3(a) and 6.3(b), we have investigated the impact of number of reflecting elements of IRS for different values of minimum reflection amplitude on the LCR and AOD, respectively. It can be observed from Fig. 6.3(a) that the LCR curves shifts to the right for increasing N for all values of ϖ_{min} considered in the figure. This implies that a given amount of level crossings will occur at a higher values of γ_{Th} for larger N. For the

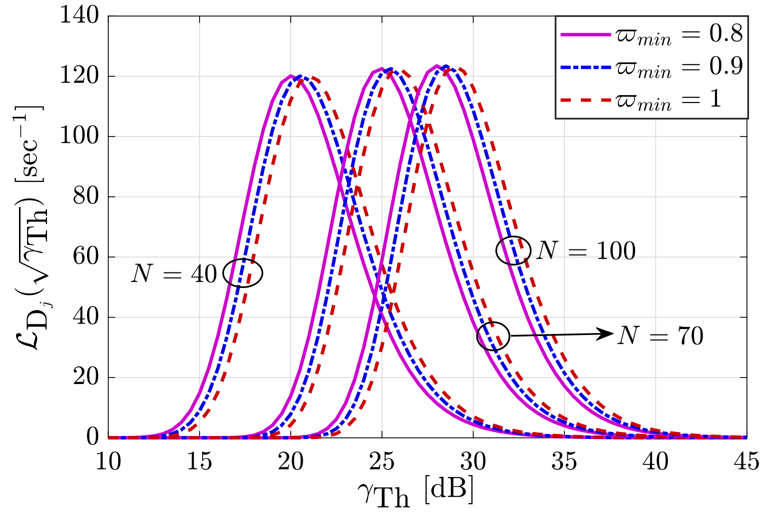

(a) LCR versus γ_{Th}

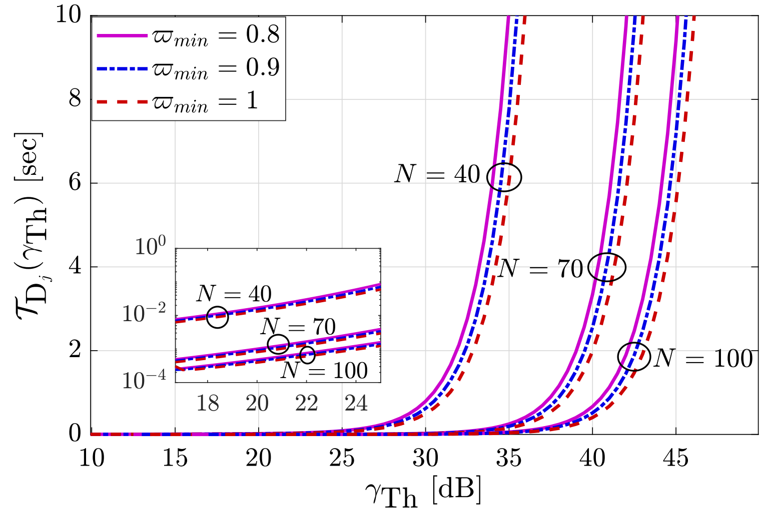

(b) AOD versus γ_{Th}

Figure 6.3: (a) LCR and (b) AOD performance for varying N, ϖ_{min}, and $L = 2$ with $\kappa_{\mathrm{BR}} = \kappa_{\mathrm{RD}_j} = \kappa_{\mathrm{I}_\ell \mathrm{D}_j} \to 0$, $\mu_{\mathrm{BR}} = \mu_{\mathrm{I}_1\mathrm{D}_j} = 1$, $\mu_{\mathrm{RD}_j} = \mu_{\mathrm{I}_2\mathrm{D}_j} = 2$, $\Omega_{\mathrm{BR}} = \Omega_{\mathrm{RD}_j} = \Omega_{\mathrm{I}_\ell\mathrm{D}_j} = 1$. The power distribution at IUE are $P_{\mathrm{I}_1\mathrm{D}_j} = -10$ dB, $P_{\mathrm{I}_2\mathrm{D}_j} = -5$ dB with Doppler frequencies $f_{\mathrm{I}_1\mathrm{D}_j} = 60$ Hz, $f_{\mathrm{I}_2\mathrm{D}_j} = 50$ Hz.

case of ideal reflection (i.e., $\varpi_{min} = 1$), the maximum LCR values for $N = 40, 70$, and 100 are obtained at a threshold SINR of 21 dB, 26 dB, and 29 dB, respectively. It can also be observed that the peak LCR value is almost same for all N and ϖ_{min}. Moreover, it may be noted from Fig. 6.3 that for a given threshold ($> \Gamma^{*}_{\mathrm{Th}}$), the LCR increases but the corresponding AOD reduces significantly. For example, at $\gamma_{\mathrm{Th}} = 35$ dB and $\varpi_{min} = 0.8$, the LCR values are 0.34, 6.5, and 17 sec^{-1} for $N = 40, 70$, and $N = 100$, respectively, whereas the AOD values are 10 sec, 0.2486 sec, and 0.036 sec, respectively. It can be intuitively inferred from Figs. 6.3(a) and 6.3(b) that the N has significant impact on LCR and AOD performances. Using a large-sized IRS allows the system to operate over a wider range of outage threshold with low LCR and very low AOD values.

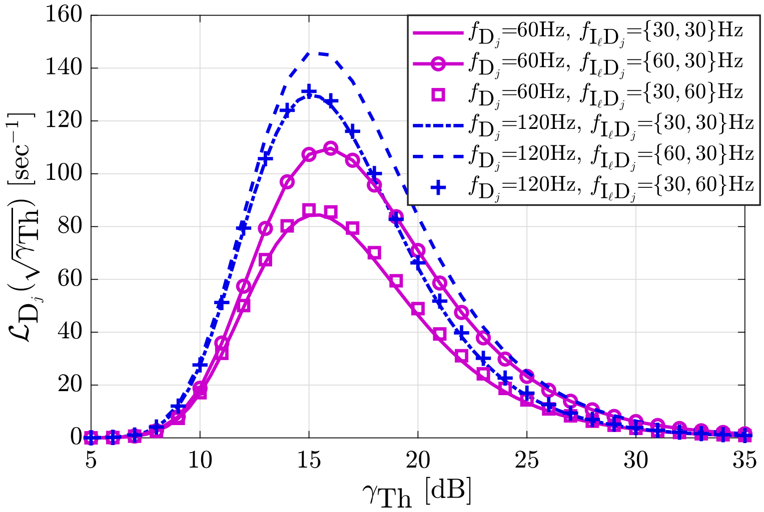

(a) LCR versus γ_{Th}

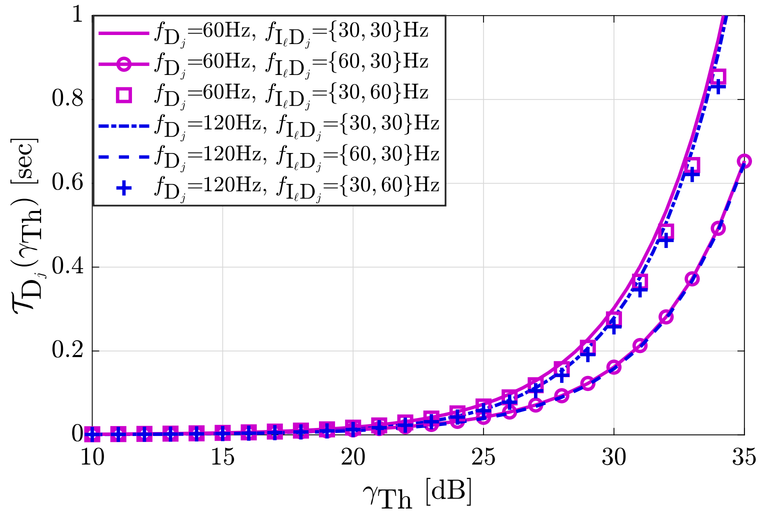

(b) AOD versus γ_{Th}

Figure 6.4: LCR and (b) AOD versus SINR outage threshold for different values of f_{D_j} and $f_{\mathrm{I}_\ell\mathrm{D}_j}$ ($\kappa_{\mathrm{BR}} = \kappa_{\mathrm{RD}_j} = \kappa_{\mathrm{I}_\ell\mathrm{D}_j} \to 0$, $\mu_{\mathrm{BR}} = 1$, $\mu_{\mathrm{RD}_j} = 2$, $\mu_{\mathrm{I}_1\mathrm{D}_j} = 1$, $\mu_{\mathrm{I}_2\mathrm{D}_j} = 2$, $\Omega_{\mathrm{BR}} = \Omega_{\mathrm{RD}_j} = \Omega_{\mathrm{I}_\ell\mathrm{D}_j} = 0$ dB, $P_{\mathrm{I}_1\mathrm{D}_j} = 2$ dB, $P_{\mathrm{I}_2\mathrm{D}_j} = -5$ dB).

In Fig. 6.4, we have shown the impact of Doppler frequencies f_{D_j} and $f_{\mathrm{I}_\ell\mathrm{D}_j}$ resulting from different speeds of j-th DUE and ℓ-th IVE, respectively. It can be seen from Fig. 6.4 that the LCR increases with an increase in f_{D_j} for all the values of outage threshold and $f_{\mathrm{I}_\ell\mathrm{D}_j}$, whereas the corresponding AOD value decreases by increasing the f_{D_j}. This refers that the received SINR experiences more fluctuations for a fast moving user however, the fluctuations lasts for a smaller amount of time as compared to the slowly moving DUE. Furthermore, the impact of varying Doppler frequencies of IUE is shown in Fig. 6.4 for a constant f_{D_j} with 2 IUE having transmit powers $P_{\mathrm{I}_1\mathrm{D}_j} = 2$ dB, $P_{\mathrm{I}_2\mathrm{D}_j} = -5$ dB. It can be seen from Fig. 6.4 that LCR increases significantly with an increase in Doppler frequency of IUE$_1$ ($f_{\mathrm{I}_1\mathrm{D}_j}$), however, the effect of change in Doppler frequency of IUE$_2$ ($f_{\mathrm{I}_2\mathrm{D}_j}$) on LCR performance is almost negligible. The intuitive reason for this behavior is the transmit power distribution among the IUE. The movement of an IUE with higher transmit power will dominate the variations in the LCR performance for all values of outage threshold. On the other hand, the impact of Doppler frequencies on AOD is shown in Fig. 6.4(b). It can be noticed from Fig. 6.4(b) that for a given value of f_{D_j}, the AOD reduces significantly by increasing the Doppler frequency of an IUE with more transmit power, whereas very small reduction in AOD values is observed if the Doppler frequency of an IUE with small transmit power is increased by the same amount. Finally, it can be deduced from Fig. 6.4 that the impact of variations in Doppler frequencies of IUE is significant on both LCR as well as AOD, for medium to high range of thresholds, whereas the impact of variations in f_{D_j} is noteworthy only in the LCR performance. These findings can be utilized to choose the proper system margin for a practical mobile system. It's worth mentioning that the Doppler shift has a significant impact on the outage rate as compared to the duration of the outage.

Figs. 6.5(a) and 6.5(b) illustrate the impact of L, i.e., the number of co-channel interferers on LCR and AOD, respectively. It can be seen from Fig. 6.5(a) that the LCR curve gets narrower with higher peak for increasing L for all values of P_{D_j} considered in the figure. This implies that for more IUE present in the network, the received signal envelope is affected by large amount of fluctuations per second over low threshold regime. With an increase in L, not only the threshold (Γ^*_{Th}) at which the LCR attains maximum shifts towards left, but also the maximum value of LCR increases significantly. For example, at $P_{\mathrm{D}_j} = 3$ dB, the values of Γ^*_{Th} for $L = 1, 2$, and $L = 3$ are 23 dB, 17 dB, and 14 dB, respectively, and the corresponding LCR values are 55 sec^{-1}, 77 sec^{-1}, and 115 sec^{-1}, respectively. Further, it may also be noted from 6.5(a) that for higher transmit power values, a desired LCR is obtained at a higher threshold SINR, for all values of L considered here. From Fig. 6.5(b), we can observe that AOD performance degrades significantly by putting more IUE in the network for all values of P_{D_j}.

Observation 6.2: *It can be clearly seen from Fig. 6.5(b) that the rate of rise of AOD curve w.r.t. threshold is quite large for $L = 2, 3$ as compared to $L = 1$. This implies that a small increase in SINR threshold (or the transmit power of DUE$_j$), the AOD will increase significantly over moderate to high threshold regime. For example, at $P_{D_j} = 5$ dB and $\gamma_{Th} = 30$ dB, the AOD values for $L = 1, 2$, and $L = 3$ are .0336 sec, 0.46 sec, and 4.68 sec, respectively.*

Fig. 6.6(a) shows the variations of LCR w.r.t. transmit power for different values of

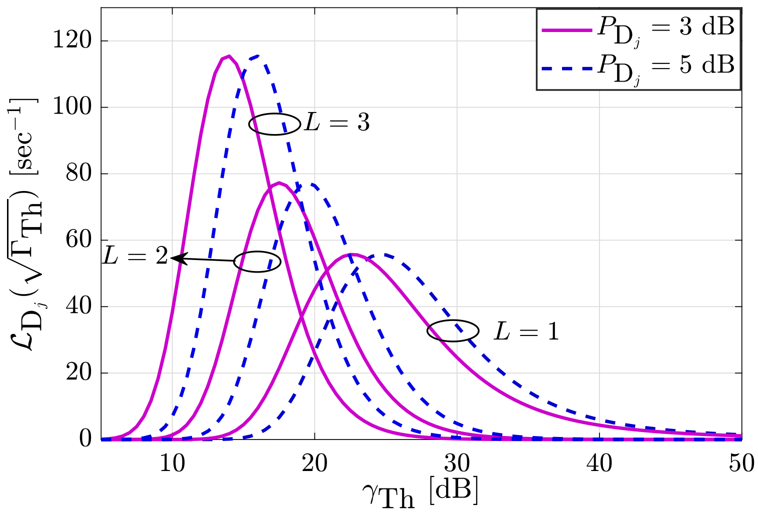

(a) LCR versus γ_{Th}

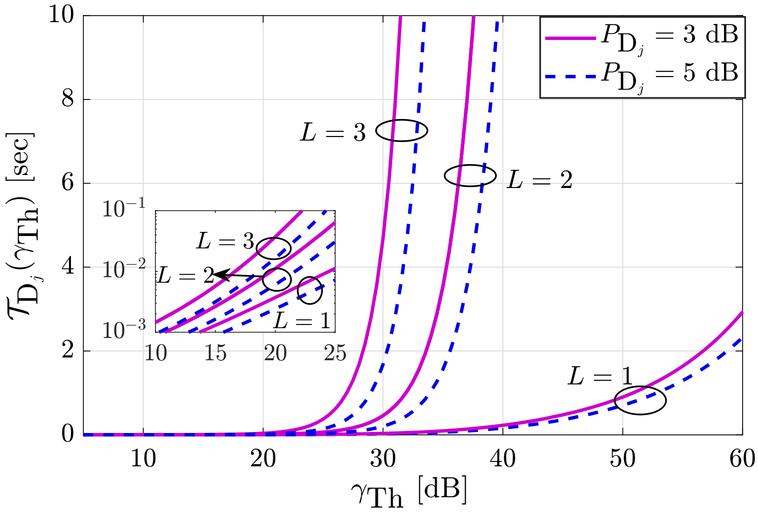

(b) AOD versus γ_{Th}

Figure 6.5: (a) LCR and (b) AOD versus SINR outage threshold by varying L with $(\kappa_{\mathrm{BR}}, \mu_{\mathrm{BR}}, \Omega_{\mathrm{BR}}) = (0, 1, 0)$, $(\kappa_{\mathrm{RD}_j}, \mu_{\mathrm{RD}_j}, \Omega_{\mathrm{RD}_j}) = (0, 1, 0)$. The fading parameters for the interference links are $(\kappa_{\mathrm{I}_\ell \mathrm{D}_j}, \mu_{\mathrm{I}_\ell \mathrm{D}_j}, \Omega_{\mathrm{I}_\ell \mathrm{D}_j}) = (0, 1, 0)$, $P_{\mathrm{I}_\ell \mathrm{D}_j} = -5$ dB, and $f_{\mathrm{I}_\ell \mathrm{D}_j} = 50$ Hz for $\ell = 1, 2, 3$.).

SINR outage threshold. As outage threshold increases, LCR decreases for low values of transmit power and reverse holds true for high values of transmit power. In Fig. 6.6(a), we have also shown the asymptotic LCR for very high transmit power conditions. It can be observed that asymptotic LCR approaches the analytical value at high transmit power. Moreover, the asymptotic LCR is independent of transmit power and SINR threshold which is well explained in Remark 6.1. Indeed, the high transmit power performance depends on channel fading distribution parameters and number of IRS elements. Further, Fig. 6.6(b) shows AOD variations w.r.t. the transmit power and it can be noticed that AOD decreases with an increase in transmit power and saturates at high transmit power. Moreover, AOD increases with an increase in outage threshold which is evident from

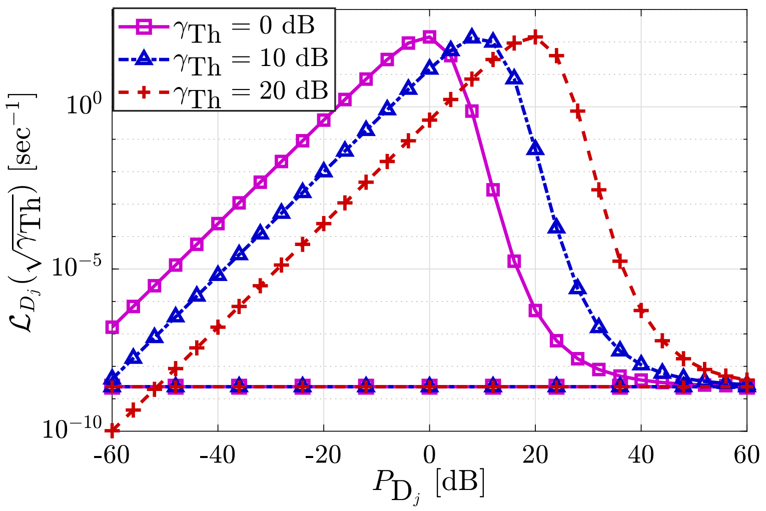

(a) LCR versus Transmit power

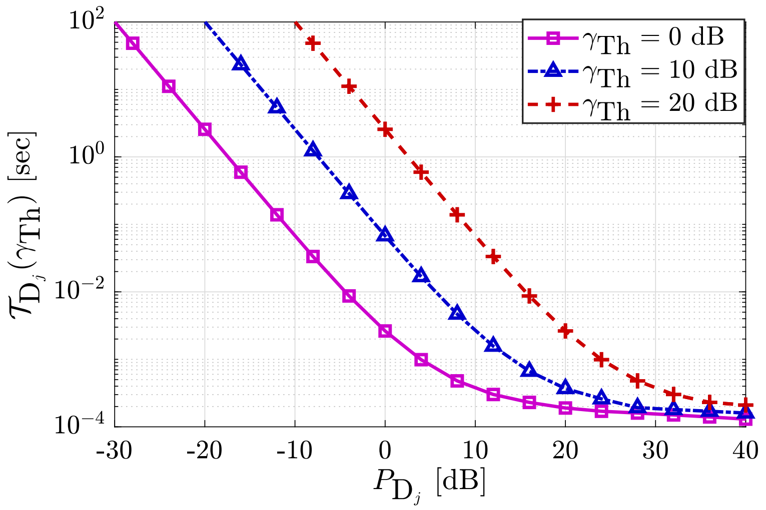

(b) AOD versus Transmit power

Figure 6.6: (a) LCR and (b) AOD versus transmit power by varying γ_{Th} with $(\kappa_{\mathrm{BR}}, \mu_{\mathrm{BR}}, \Omega_{\mathrm{BR}}) = (2, 2, 10)$, $(\kappa_{\mathrm{RD}_j}, \mu_{\mathrm{RD}_j}, \Omega_{\mathrm{RD}_j}) = (2, 2, 10)$, and $L = 2$ having $f_{\mathrm{I}_1\mathrm{D}_j} = 60$ Hz, $f_{\mathrm{I}_2\mathrm{D}_j} = 50$ Hz. The fading parameters for the interference links are $(\kappa_{\mathrm{I}_\ell\mathrm{D}_j}, \mu_{\mathrm{I}_\ell\mathrm{D}_j}, \Omega_{\mathrm{I}_\ell\mathrm{D}_j}) = (1, 1, 10)$ and $P_{\mathrm{I}_\ell\mathrm{D}_j} = 20$ dB for $\ell = 1, 2$.

Figs. 6.2-6.4. Further, we have shown the PER and throughput performance of the considered IRS-assisted RF communication system employing SW-ARQ protocol under FSMC model with multiple co-channel IUE in Fig. 6.7. We have shown the PER versus transmit power performance of a DUE in Fig. 6.7(a) for different values of outage threshold and Doppler frequencies of DUE and IUE (i.e., f_{D_j} and $f_{\mathrm{I}_\ell\mathrm{D}_j}$, respectively). The total duration of the packet is set as $T_{P_{\mathrm{D}_j}} = 0.5$ sec. It can be observed from Fig. 6.7(a) that for all the values of outage threshold and Doppler frequencies considered in the figure, the PER curves saturates to certain value, however, the saturation value of PER is slightly higher for larger f_{D_j}. Furthermore, the PER performance for a slowly moving DUE (i.e., lower f_{D_j}) is superior than that of a fast moving DUE (i.e., higher f_{D_j}) under all the

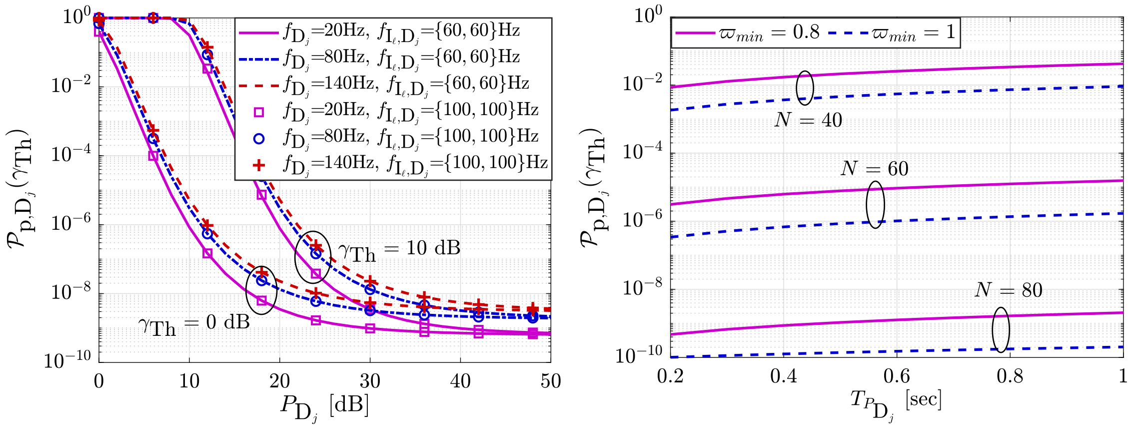

(a) PER performance with transmit power for different values of SINR threshold and varying Doppler frequencies of DUE and IUE with $N = 50$ and $\varpi_{min} = 0.8$.

(b) PER performance with packet duration for different values of N and ϖ_{min} with $P_{\mathrm{D}_j} = 20$ dB, $\gamma_{\mathrm{Th}} = 15$ dB, $f_{\mathrm{I}_1\mathrm{D}_j} = 60$ Hz, and $f_{\mathrm{I}_2\mathrm{D}_j} = 50$ Hz.

Figure 6.7: PER performance of considered system employing SW-ARQ protocol under FSMC model having 2 IUE with transmit powers $P_{\mathrm{I}_1\mathrm{D}_j} = 20$ dB and $P_{\mathrm{I}_1\mathrm{D}_j} = 10$ dB. The channel parameters for all the links involved are considered to be same, i.e., $(\kappa_{\mathrm{BR}}, \mu_{\mathrm{BR}}, \Omega_{\mathrm{BR}}) = (\kappa_{\mathrm{RD}_j}, \mu_{\mathrm{RD}_j}, \Omega_{\mathrm{RD}_j}) = (\kappa_{\mathrm{I}_\ell\mathrm{D}_j}, \mu_{\mathrm{I}_\ell\mathrm{D}_j}, \Omega_{\mathrm{I}_\ell\mathrm{D}_j}) = (1, 1, 15)$ for $\ell = 1, 2$.

threshold and transmit power conditions.

Observation 6.3: *It can also be seen from Fig. 6.7(a) that the PER performance degrades with an increase in γ_{Th} for all the values of f_{D_j} and $f_{I_\ell D_j}$ considered here. For example, at $P_{D_j} = 20$ dB and $\gamma_{Th} = 0$ dB, a PER of 3.5×10^{-9}, 1.32×10^{-8}, and 2.3×10^{-8} is obtained for $f_{D_j} = 20$, 80, and 140 Hz, respectively, whereas for the same values of f_{D_j} and P_{D_j}, the PER values are 7.8×10^{-7}, 2.99×10^{-6}, and 5.23×10^{-6}, respectively for $\gamma_{Th} = 10$ dB. It is interesting to note that PER curves do not change with any sort of variations in $f_{I_\ell D_j}$, $\ell = 1, 2$, for all the values of γ_{Th} and P_{D_j} considered in the figure, which refers that movement of IUE does not really affect the PER of the desired user under the considered parameter settings.*

Fig. 6.7(b) depicts the impact of total packet duration (i.e., $T_{P_{\mathrm{D}_j}}$) on the PER for different values of N and ϖ_{min}. It can be noticed from Fig. 6.7(a) that the PER increases very slowly with $T_{P_{\mathrm{D}_j}}$ for all the values of N and ϖ_{min} considered in the figure. This refers that the probability of at least one-bit error increases slightly for a longer packet duration due to the increased channel fluctuations during the packet length. Furthermore, it is clear from Fig. 6.7(b) that the PER value reduces dramatically for larger N for all values of $T_{P_{\mathrm{D}_j}}$. For example, with $\varpi_{min} = 0.8$ and $T_{P_{\mathrm{D}_j}} = 0.6$, a PER of 5.479×10^{-3}, and 1.52×10^{-10} is obtained for $N = 40$, 60, and 80, respectively. Moreover, the deviation in minimum reflection amplitude (ϖ_{min}) from the ideal conditions (i.e., $\varpi_{min} = 1$) deteriorates the PER performance of the system over all values of $T_{P_{\mathrm{D}_j}}$ and N.

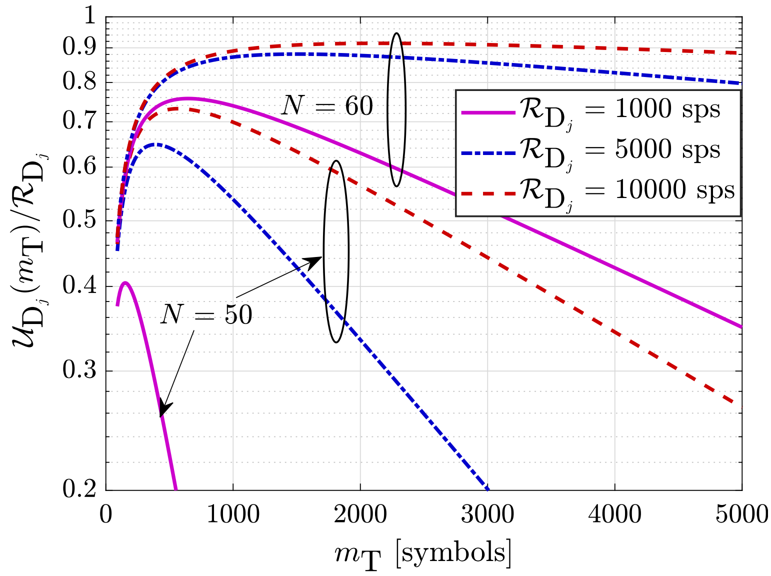

Figure 6.8: Normalized throughput versus data packet length for different values of N and $\mathcal{R}_{\mathrm{D}_j}$ with $P_{\mathrm{D}_j} = 20$ dB, $\gamma_{\mathrm{Th}} = 15$ dB, $f_{\mathrm{I}_1\mathrm{D}_j} = 60$ Hz, and $f_{\mathrm{I}_2\mathrm{D}_j} = 50$ Hz. The channel parameters for all the links involved are considered to be same, i.e., $(\kappa_{\mathrm{BR}}, \mu_{\mathrm{BR}}, \Omega_{\mathrm{BR}}) = (\kappa_{\mathrm{RD}_j}, \mu_{\mathrm{RD}_j}, \Omega_{\mathrm{RD}_j}) = (\kappa_{\mathrm{I}_\ell\mathrm{D}_j}, \mu_{\mathrm{I}_\ell\mathrm{D}_j}, \Omega_{\mathrm{I}_\ell\mathrm{D}_j}) = (1, 1, 15)$ for $\ell = 1, 2$.

Fig. 6.8 shows the variation of normalized throughput $(\mathcal{U}_{\mathrm{D}_j}(m_{\mathrm{T}})/\mathcal{R}_{\mathrm{D}_j})$ by varying packet length (m_{T}) for different data rates $(\mathcal{R}_{\mathrm{D}_j})$ and number of reflecting elements (N). The overhead symbols under the ARQ transmission policy are set as $m_{\mathrm{Ov}} = 100$ symbols for all the curves shown in the figure. It can be observed from Fig. 6.8 that the normalized throughput increases with an increase in data rate. It is also clear from (6.35) that the normalized throughput is a decaying exponential function of inverse data rate, which is equivalent to a rising exponential function of the data rate. Further, increase in N results in significant improvement in normalized throughput at all date rates. It is also worth noting that optimal value of packet length increases with an increase in data rate as well number of IRS reflecting elements. Thus choosing optimal packet length, high data rate and more number of reflecting elements is optimum choice to improve the system's performance.

Observation 6.4: *It can be observed from Fig. 6.8 that there exists some optimum packet length (m^*_T) at which normalized throughput is maximum. In particular, for $N = 50$, the values of m^*_T obtained using the analytical expression in* (6.37) *at data rate* 1000 *symbols per sec (sps),* 5000 *sps, and* 10000 *sps are as* 618*,* 1441*, and* 2057 *symbols, respectively. Similarly, for $N = 60$ the value of m^*_T at data rates* 1000 *sps,* 5000 *sps, and* 10000 *sps are obtained as* 618*,* 1441*, and* 2057 *symbols, respectively. The figure clearly shows that these values match the simulation results extremely well.*

6.6 Summary

In general, the importance of first-order statistics, such as outage, is of great interest in RF communication networks, however, the duration and rate for which the system remains in outage contribute to choosing system design parameters. Therefore, in this chapter, we have studied the SOS of IRS-assisted RF communication system in the presence of multiple interferers. We have derived the analytical expressions of LCR and AOD for the considered system utilizing non-identical κ-μ distribution for the desired and interference links. We have also obtained asymptotic expressions of LCR under high transmit power conditions. Moreover, the PER and optimal packet length of the considered IRS-assisted network have been derived with SW-ARQ protocol-based data transmission under the FSMC model. Moreover, the impact of various system and channel parameters, such as number of reflecting elements of IRS, minimum amplitude of reflection, number of co-channel interferers, and Doppler shift due to desired and interfering users has been investigated on the system's performance.

Chapter 7

Conclusion and Future Scope

In this chapter, we conclude the thesis by summarizing the accomplished work and suggesting some potential further research topics.

7.1 Conclusion

In this dissertation, we presented a comprehensive evaluation of a mixed FSO-RF communication system that combines the advantages of both technologies while addressing their individual limitations. The thesis investigates the performance of a DF relay-based mixed FSO-RF system with SLIPT to overcome power constraints. We derived statistical distribution of SNR and analytical expressions for various performance metrics such as outage probability, bit-error rate, ergodic capacity, and effective capacity. Furthermore, the thesis explores the potential of IRS to enhance the performance of the RF link, especially in urban areas with blockage issues. We investigated performance of on-off control IRS-assisted mixed FSO-RF system interms outage probability, average bit-error rate, and ergodic capacity. Moreover, we integreted integrates the concept of NOMA to the relay-based FSO-RF communication to assist multiple users. We considerd the deployment of an OIRS in the FSO link as well as RF IRS in vicinity of user with poor channel conditions and adopts SLIPT technology for energy harvesting at relay. The system's performance is evaluated in terms of outage probability, throughput, and ergodic rate.

The thesis also highlights the importance of studying SOS to capture the *dynamic behavior* of the system under multipath fading. In particular we have investigated the LCR and AOD for the OIRS-assisted FSO network in the presence of random fog, atmospheric turbulence, and pointing error. We also investigated the SOS for the IRS-assisted RF communication network with CCI.

Overall, this research contributes to the understanding and advancement of mixed FSO-RF communication systems by addressing power constraints, atmospheric turbulence, limited coverage range, and the use of IRS and NOMA.

7.2 Future Scope

The work presented in this dissertation can be extended by integrating the mixed FSO-RF communication system into the space-airborne-terrestrial (SAT) networks. The evolution of space and aerial platforms is confirming the advent of SAT wireless frameworks through its integration into terrestrial networks. It can be a promising solution for building a fully globally connected architecture for next-generation communication networks. Moreover, space and aerial platforms are primarily based on the scarce RF bands with limited capacity. To address the RF spectrum scarcity issue and deliver a Terabit-per-second (Tb/s) data rate, we can applied FSO technology as prescribed in this dissertation. For example, in May 2018, the German Aerospace Center registered a world record of achieving 13.16 Tb/s using FSO transmissions in a GEO-equivalent turbulent channel. As a result, FSO link is more desired for space-air communication because of low absorption and scattering loss in the space environment. Due to the numerous advantages of FSO, these SAT networks can be designed for satisfying the QoS requirements of terrestrial users for different applications.

Also, the evolving real-time services require an intelligent global network that can adapt according to the service requirements. Moreover, the inherent characteristics of space and aerial platforms, when deployed, can fulfill this time varying demand of the terrestrial users by dynamic utilization of resources and scheduling according to the user's needs, especially in the disaster-affected areas, emergency scenarios, smart cities, etc. Furthermore, by utilizing IRS into the SAT communication network, the high path losses over long propagation distances can be compensated.

The aid of IRS-assisted SAT network promises to bring a revolutionary changes including:

- Reduced deployment cost against conventional satellite networks,
- 360-degree coverage to cover a number of applications,
- Boost the communication performance of SATCN with limited resources by selecting an appropriate system model.

Chapter A

Appendix

A.1 Detailed Proofs of Chapter 2

A.1.1 Proof of Lemma 2.1

The PDF of Γ_{E} can be derived by differentiating $F_{\Gamma_{\mathrm{E}}}(\gamma)$ with the help of [63, 07.34.20.0017.02] as

$$f_{\Gamma_{\mathrm{E}}}(\gamma)=\frac{K\gamma^{-1}}{\Gamma(m)}\left[\sum_{n=0}^{\infty}\frac{(-1)^n}{n!}\left(\frac{m}{\bar{\gamma}'_{\mathrm{D}}}\right)^{m+n}\times\sum_{r=1}^{\infty}\Upsilon_r G_{5,9}^{7,2}\left(\frac{(\alpha\beta\Psi)^2\gamma}{16\varkappa_{FSO}}\left|\begin{matrix}0,1,\mathbb{A},m+n+1\\ m+n,\mathbb{B},0,1\end{matrix}\right.\right)\right.$$
$$\left.+\Gamma\left(m,\frac{m}{\bar{\gamma}'_{\mathrm{D}}}\right)\sum_{r=1}^{\infty}\Upsilon_r G_{4,8}^{6,2}\left(\frac{(\alpha\beta\Psi)^2\gamma}{16\varkappa_{FSO}}\left|\begin{matrix}0,1,\mathbb{A}\\ \mathbb{B},0,1\end{matrix}\right.\right)\right]. \tag{A.1.1}$$

Substituting (A.1.1) in (2.36), expressing $\ln\left(1+\frac{e}{2\pi}\gamma\right)=G_{2,2}^{1,2}\left(\frac{e}{2\pi}\gamma\left|\begin{matrix}1,1\\1,0\end{matrix}\right.\right)$ from [63, 07.34.03.0456.01], and using [63, 07.34.20.0017.02], we get (2.37).

A.2 Detailed Proofs of Chapter 3

A.2.1 Proof of Lemma 3.1

Considering the reflection amplitudes of each reflecting elements to be identical, i.e., $|\varpi_{\mathrm{R}}^{(n)}|=|\varpi_{\mathrm{R}}|$, $\forall n$, we can write (3.14) as

$$\gamma_{\mathrm{D}}(\mathbf{f}_\ell)=\rho_{\mathrm{R}}\left|W_\ell\right|^2, \tag{A.2.1}$$

where

$$W_\ell=\frac{1}{\sqrt{D}}\underbrace{\sum_{i=(\ell-1)D+1}^{\ell D}H^{(n)}e^{j\psi^{(n)}}}_{D\text{ Terms}}=\frac{1}{\sqrt{D}}\underbrace{\sum_{j=0}^{D-1}H^{((\ell-1)D+1+j)}e^{j\psi^{((\ell-1)D+1+j)}}}_{D\text{ Terms}}, \tag{A.2.2}$$

where $j = n - (1-\ell)D - 1$. Further, considering phase error as Generalized uniform distributed, obtaing the PDF of W_ℓ becomes difficult. Therefore, we obtain a lower bound of the performance of an IRS-assisted by considering phase error to be distributed as $U \sim (-\pi, \pi)$. Under, this assumption the PDF of W_ℓ can be obtained from [103] with some RV transformation as

$$f_{|W_\ell|^2}(v) = \sum_{u_0=0}^{m_1-1} \cdots \sum_{u_{D-1}=0}^{m_1-1} \prod_{j=0}^{D-1} Z_j \frac{2\left(\frac{Dm_1m_2}{\Omega_1\Omega_2}\right)^{\frac{(\nu+1)}{2}}}{(\nu-1)!} v^{\frac{\nu-1}{2}} K_{\nu-1}\left(2\sqrt{\frac{Dm_1m_2}{\Omega_1\Omega_2}v}\right), \quad \text{(A.2.3)}$$

where $\nu = D(m_1+m_2-1) - \sum_{j=0}^{D-1} u_j$ and $Z_j = \frac{(m_2)_{m_1-1-u_j}(1-m_2)_{u_j}}{(m_1-1-u_j)!u_j!}$. Moreover, the CDF of $|W_\ell|^2$ can be derived by $\int_0^v f_{|W_\ell|^2}(z)\,dz$ along with the use of [68, Eq. 6.561.8] as

$$\mathcal{F}_{|W_\ell|^2}(v) = \sum_{u_0=0}^{m_1-1} \cdots \sum_{u_{D-1}=0}^{m_1-1} \prod_{j=0}^{D-1} Z_j \left[1 - \frac{2\left(\frac{Dm_1m_2}{\Omega_1\Omega_2}\right)^{\frac{\nu}{2}}}{(\nu-1)!} v^{\frac{\nu}{2}} K_{\nu}\left(2\sqrt{\frac{Dm_1m_2}{\Omega_1\Omega_2}v}\right)\right], \quad \text{(A.2.4)}$$

From the definition of W_ℓ in (A.2.2) and the assumption of g_i and h_i following Nakagami-m distribution with parameters $(m_1, \Omega_1/m_1)$ and $(m_2, \Omega_2/m_2)$, respectively, it is straightforward to write that $\mathcal{E}\left\{|W_\ell|^2\right\} = \Omega_1\Omega_2$. Now we can write the CDF of $\gamma_{\mathrm{D}}(\mathbf{f}_\ell)$ given in (3.12) as

$$\begin{aligned}\mathcal{F}_{\gamma_{\mathrm{D}}(\mathbf{f}_\ell)}(\gamma) &= \Pr\left\{\rho_{\mathrm{R}}|W_\ell|^2 \le \gamma\right\}, \\ &= \mathcal{F}_{|W_\ell|^2}\left(\frac{\gamma}{\rho_{\mathrm{R}}}\right).\end{aligned} \quad \text{(A.2.5)}$$

Using (A.2.4) in (A.2.5), we get (3.18).

A.2.2 Proof of Lemma 3.2

As $\rho_{\mathrm{RD}} \to \infty$, the argument of the modified Bessel's function in (3.18) tends to zero. Following [68], we utilize two different approximations of $K_\nu(x)$ for $x \to 0$ as $K_1(x) \approx x^{-1} + 0.5x\ln(0.5x)$ and $K_\nu(x) \approx 0.5\left\{(2x^{-1})^\nu\Gamma(\nu) - (2x^{-1})^{\nu-2}\Gamma(\nu-1)\right\}$ with $\nu = 1$ and $\nu > 1$, respectively. Using these asymptotic values in (3.18), we get (3.22).

A.2.3 Proof of Lemma 3.3

Utilizing the $\bar{\gamma}_{\mathrm{R}}^{(q)} \to \infty$ in (3.31) along with the asymptotic expression of Meijer's-G function from [63, (07.34.06.0006.01)], we get (3.34). Further, asymptotic bit-error-rate $\tilde{\mathcal{P}}_{\mathrm{RF}}$ for the IRS-assisted RF hop can be obtained using asymptotic expression of Bessel function and then using [68, (3.371)] in (3.32), we get (3.35)

A.2.4 Proof of Lemma 3.4

From (1.3) $\mathcal{Q}_1$ can be written as

$$\mathcal{Q}_1 = \mathcal{E}\left\{\ln\left(1+\Lambda\gamma_{\mathrm{R}}^{(q)}\right)\right] = \mathcal{E}\left\{\ln\left(1+\Lambda\bar{\gamma}_{\mathrm{R}}^{(q)}I^q\right)\right\}, \tag{A.2.6}$$

Since, $\ln(1+x) \approx \ln(x)$ when $x \to \infty$, the asymptotic expression of $\mathcal{Q}_1$ in (A.2.6) considering high SNR conditions i.e., $\bar{\gamma}_{\mathrm{R}}^{(q)} \to \infty$ can be accurately lower-bounded as follows

$$\lim_{\bar{\gamma}_{\mathrm{R}}^{(q)}\to\infty} \mathcal{Q}_1 = \tilde{\mathcal{Q}}_1 = \ln\left(\bar{\gamma}_{\mathrm{R}}^{(q)}\right) + \frac{1}{\Lambda}\int_0^\infty \frac{\mathcal{F}'_{I^q}(i)}{i}di, \tag{A.2.7}$$

where $\mathcal{F}'_{I^q}(i)$ is the CCDF of I_q which can be obtained using (3.39) by linear transformation as $\mathcal{F}'_{I^q}(i) = \mathcal{F}'_{\gamma_{\mathrm{R}}^{(q)}}\left(\bar{\gamma}_{\mathrm{R}}^{(q)}i\right)$. Further, utilizing [63, (07.34.21.0086.01)] in (A.2.7), we get (3.44). Further, $\tilde{\mathcal{Q}}_2 = \lim_{\bar{\gamma}\to\infty}\mathcal{Q}_2$, can be obtained from (3.41) by utilizing high SNR asymptotic expansion of Bessel function expression and then using [63, (07.34.21.0086.01)], we get (3.45).

A.3 Detailed Proofs of Chapter 4

A.3.1 Proof of Theorem 4.1

From (4.23), $\mathcal{P}_{\mathrm{out},1}$ can be evaluated based on different range of values for γ'_{U_1} as

$$\mathcal{P}_{\mathrm{out},1} = \underbrace{\int_0^{\frac{C_2}{C_1}} \mathcal{F}_{\gamma_{\mathrm{R}}}\left(\frac{C_2}{u}\right) f_{\gamma'_{\mathrm{U}_1}}(u)du}_{\mathcal{D}_1} + \underbrace{\int_{\frac{C_2}{C_1}}^\infty \mathcal{F}_{\gamma_{\mathrm{R}}}(C_1) f_{\gamma'_{\mathrm{U}_1}}(u)du}_{\mathcal{D}_2}. \tag{A.3.1}$$

Substituting (4.17) along with the PDF of γ'_{U_1} in (A.3.1), we get

$$\mathcal{D}_1 = \frac{K_{\mathrm{eq}}m_0^{m_0}}{\bar{\gamma}'^{m_0}_{\mathrm{U}_1}\Omega_0^{m_0}\Gamma(m_0)}\sum_{r_1=1}^{\infty}\sum_{r_2=1}^{\infty}\Upsilon_r\int_0^{\frac{C_2}{C_1}} u^{m_0-1}\exp\left(-\frac{m_0}{\bar{\gamma}'_{\mathrm{U}_1}\Omega_0}u\right) G_{5,13}^{12,1}\left(\frac{\Psi_{\mathrm{eq}}}{\mu_{\mathrm{eq}}}\frac{C_2}{u}\middle|\begin{matrix}1,\mathbb{P}\\ \mathbb{Q},0\end{matrix}\right)du, \tag{A.3.2}$$

and

$$\mathcal{D}_2 = \frac{K_{\mathrm{eq}}m_0^{m_0}}{\bar{\gamma}'^{m_0}_{\mathrm{U}_1}\Omega_0^{m_0}\Gamma(m_0)}\sum_{r_1=1}^{\infty}\sum_{r_2=1}^{\infty}\Upsilon_r\int_{\frac{C_2}{C_1}}^\infty u^{m_0-1}\exp\left(-\frac{m_0}{\bar{\gamma}'_{\mathrm{U}_1}\Omega_0}u\right) G_{5,13}^{12,1}\left(\frac{\Psi_{\mathrm{eq}}}{\mu_{\mathrm{eq}}}C_1\middle|\begin{matrix}1,\mathbb{P}\\ \mathbb{Q},0\end{matrix}\right)du, \tag{A.3.3}$$

Substituting $e^{-x} = G_{0,1}^{1,0}\left(x \,\middle|\, {- \atop 0}\right)$ [63, (07.34.03.0228.01)] along with use of property of Meijer's-G function from [63, (07.34.17.0012.01)], and then using the primary definition of the Meijer's G function from [63, (07.34.02.0001.01)], (A.3.2) can be evaluated as

$$\mathcal{D}_1 = \frac{K_{\rm eq} m_0^{m_0}}{\bar{\gamma}_{\rm U_1}^{\prime m_0} \Omega_0^{m_0} \Gamma(m_0)} \sum_{r_1=1}^{\infty} \sum_{r_2=1}^{\infty} \Upsilon_r \frac{1}{(2\pi\jmath)^2} \int_{\ell_1} \int_{\ell_2} \frac{\Gamma(-s_1)\Gamma(-s_2) \prod_{l=1}^{12} \Gamma(a_l + s_2)}{\prod_{k=1}^{4} \Gamma(b_k + s_2) \Gamma(1 - s_2)} \left(\frac{C_2}{C_1}\right)^{m_0+s_1+s_2}$$
$$\times \left(\frac{m_0}{\bar{\gamma}_{\rm U_1}' \Omega_0}\right)^{s_1} \left(\frac{\mu_{\rm eq}}{\Psi_{\rm eq} C_2}\right)^{s_2} \frac{\Gamma(m_0+s_1+s_2)}{\Gamma(m_0+s_1+s_2+1)} ds_2\, ds_1, \tag{A.3.4}$$

where $a_l \in \mathbb{Q}$ and $b_k \in \mathbb{P}$. Using the definition of the bivariate Fox-H function [104, 2.55] in (A.3.4), we get (4.25). Similarly, using [68, 3.381.3] in (A.3.3), we get (4.26).

A.3.2 Proof of Theorem 4.2

From (4.27), $\mathcal{P}_{\rm out,2}$ can be evaluated for different range of $\gamma_{\rm U_2}'$ as

$$\mathcal{P}_{\rm out,2} = \underbrace{\int_0^{\frac{C_4}{C_3}} \mathcal{F}_{\gamma_{\rm R}}\left(\frac{C_4}{u}\right) f_{\gamma_{\rm U_2}'}(u) du}_{\mathcal{H}_1} + \underbrace{\int_{\frac{C_4}{C_3}}^{\infty} \mathcal{F}_{\gamma_{\rm R}}(C_3) f_{\gamma_{\rm U_2}'}(u) du}_{\mathcal{H}_2}. \tag{A.3.5}$$

Substituting (4.17) along with the PDF of $\gamma_{\rm U_2}'$ in (A.3.5), we get

$$\mathcal{H}_1 = 2K_{\rm eq} \sum_{r_1=1}^{\infty} \sum_{r_2=1}^{\infty} \Upsilon_r \sum_{u_1=0}^{m_1-1} \cdots \sum_{u_N=0}^{m_1-1} \prod_{n=1}^{N} \frac{Z_n \mathcal{C}_o^{\frac{\nu+1}{2}}}{\Gamma(\nu)} \int_0^{\frac{C_4}{C_3}} u^{\frac{\nu-1}{2}} K_{\nu-1}\left(2\sqrt{\mathcal{C}_o u}\right) G_{5,13}^{12,1}\left(\frac{\Psi_{\rm eq}}{\mu_{\rm eq}} \frac{C_4}{u} \,\middle|\, {1, \mathbb{P} \atop \mathbb{Q}, 0}\right) du, \tag{A.3.6}$$

and

$$\mathcal{H}_2 = 2K_{\rm eq} \sum_{r_1=1}^{\infty} \sum_{r_2=1}^{\infty} \Upsilon_r \sum_{u_1=0}^{m_1-1} \cdots \sum_{u_N=0}^{m_1-1} \prod_{n=1}^{N} Z_n \frac{\mathcal{C}_o^{\frac{\nu+1}{2}}}{\Gamma(\nu)} G_{5,13}^{12,1}\left(\frac{\Psi_{\rm eq}}{\mu_{\rm eq}} C_3 \,\middle|\, {1, \mathbb{P} \atop \mathbb{Q}, 0}\right) \int_{\frac{C_4}{C_3}}^{\infty} u^{\frac{\nu-1}{2}} K_{\nu-1}\left(2\sqrt{\mathcal{C}_o u}\right) du. \tag{A.3.7}$$

where $\mathcal{C}_o = \frac{m_1 m_2}{\left|\varpi_{\rm R}^{(n)}\right| \bar{\gamma}_{\rm U_2}' \Omega_1 \Omega_2}$. Expressing Bessel function in terms of meijer's-G function as $K_{a-b}(2\sqrt{x}) = x^{-\frac{a+b}{2}} G_{0,2}^{2,0}\left(x \,\middle|\, {- \atop a,b}\right)$ [63, (07.34.03.0605.01)] along with use of property of Meijer's-G function given in [63, (07.34.17.0012.01)], followed by the use of the primary definition of Meijer-G function [63, (07.34.02.0001.01)], we can evaluate (A.3.6) as

$$\mathcal{H}_1 = 2K_{\rm eq} \sum_{r_1=1}^{\infty} \sum_{r_2=1}^{\infty} \Upsilon_r \sum_{u_1=0}^{m_1-1} \cdots \sum_{u_N=0}^{m_1-1} \prod_{n=1}^{N} \frac{Z_n \mathcal{C}_o}{\Gamma(\nu)} \frac{1}{(2\pi\jmath)^2} \int_{\ell_3} \int_{\ell_4} \frac{\Gamma(\nu-1-s_3)\Gamma(-s_3)\Gamma(-s_4) \prod_{l=1}^{12} \Gamma(a_l + s_4)}{\prod_{k=1}^{4} \Gamma(b_k + s_4) \Gamma(1 - s_4)}$$

$$\times \mathcal{C}_o^{s_3}\left(\frac{\mu_{\rm eq}}{\Psi_{\rm eq}C_4}\right)^{s_4}\left(\frac{C_4}{C_3}\right)^{s_3+s_4+1}\frac{\Gamma(s_3+s_4+1)}{\Gamma(s_3+s_4+2)}\,ds_4\,ds_3, \tag{A.3.8}$$

where $a_l \in \mathbb{Q}$ and $b_k \in \mathbb{P}$. Using the definition of the bivariate Fox-H function [104, 2.55] in (A.3.8), we get (4.29). Similarly, solving the integral $\mathcal{H}_2$ defined in (A.3.7) using [68, 6.561.8], we get (4.30).

A.3.3 Proof of Lemma 4.1

The high SNR asymptotic expansion of the bivariate Fox H-function can be obtained from the Mellin-Barnes integral expansion of the Fox H-function. The asymptotic values can be calculated by evaluating the residue of the respective integrands that are close to the contour, particularly, the maximum pole on the left for small Fox's H-function argument and the minimum pole on the right for large ones [130]. To evaluate the asymptotic expression of $\mathcal{D}_1$, we can rewrite $\mathcal{D}_1$ (from (A.3.4)) in form of Mellin–Barnes integrals as

$$\mathcal{D}_1=\frac{K_{\rm eq}m_0^{m_0}}{\bar{\gamma}_{\rm U_1}'^{m_0}\Omega_0^{m_0}\Gamma(m_0)}\sum_{r_1=1}^{\infty}\sum_{r_2=1}^{\infty}\Upsilon_r\frac{1}{(2\pi\jmath)^2}\int_{\ell_1}\mathcal{I}_1(s_1)\int_{\ell_2}\mathcal{I}_2(s_2)\,\mathcal{I}_3(s_1,s_2)\,ds_2ds_1, \tag{A.3.9}$$

$$\text{wherein}\quad \mathcal{I}_1(s_1)=\Gamma(-s_1)\left(\frac{m_0}{\bar{\gamma}_{\rm U_1}'\Omega_0}\right)^{s_1},\quad \mathcal{I}_2(s_2)=\frac{\Gamma(-s_2)\prod_{l=1}^{12}\Gamma(a_l+s_2)}{\prod_{k=1}^{4}\Gamma(b_k+s_2)\Gamma(1-s_2)}\left(\frac{\mu_{\rm eq}}{\Psi_{\rm eq}C_2}\right)^{s_2}$$
$$\text{and}\quad \mathcal{I}_3(s_1,s_2)=\left(\frac{C_2}{C_1}\right)^{m_0+s_1+s_2}\frac{\Gamma(m_0+s_1+s_2)}{\Gamma(m_0+s_1+s_2+1)}. \tag{A.3.10}$$

For high transmit SNR conditions, i.e., $\rho\to\infty$, and hence $\mu_{\rm eq}\to\infty$, the bivariate Fox's H-function can be evaluated at the highest poles on the left of contour ℓ_2 (i.e., residue at $s_2=-s_1-m_0$) as

$$\begin{aligned}\int_{\ell_2}\mathcal{I}_2(s_2)\mathcal{I}_3(s_1,s_2)ds_2 &\approx 2\pi\jmath\text{Res}\left[\mathcal{I}_2(s_2)\mathcal{I}_3(s_1,s_2),-m_0-s_1\right]\\ &=2\pi\jmath\lim_{s_2\to-m_0-s_1}(s_1+s_2+m_0)\mathcal{I}_2(s_2)\mathcal{I}_3(s_1,s_2)\\ &=2\pi\jmath\frac{\Gamma(s_1+m_0)\prod_{l=1}^{12}\Gamma(a_l-m_0-s_1)}{\prod_{k=1}^{4}\Gamma(b_k-m_0-s_1)\Gamma(1+m_0+s_1)}\left(\frac{\mu_{\rm eq}}{\Psi_{\rm eq}C_2}\right)^{-m_0-s_1}\\ &\triangleq\mathcal{I}_4(s_1).\end{aligned} \tag{A.3.11}$$

Using (A.3.11) in (A.3.9), we can write $\mathcal{D}_1$ for high SNR conditions as

$$\tilde{\mathcal{D}}_1=\frac{K_{\rm eq}m_0^{m_0}}{\bar{\gamma}_{\rm U_1}'^{m_0}\Omega_0^{m_0}\Gamma(m_0)}\sum_{r_1=1}^{\infty}\sum_{r_2=1}^{\infty}\frac{\Upsilon_r}{2\pi\jmath}\int_{\ell_1}\mathcal{I}_1(s_1)\mathcal{I}_4(s_1). \tag{A.3.12}$$

Similarly, we can apply residue approach in (A.3.12) by computing the residue at the dominant pole on the right of contour ℓ_1 (i.e., at $s_1 = \tilde{a}_l - m_0$, where $\tilde{a}_l = \min\{\mathbb{Q}\}$) as

$$\int_{\ell_1} \mathcal{I}_1(s_1)\mathcal{I}_4(s_1)ds_1 \approx 2\pi\jmath \operatorname{Res}[\mathcal{I}_1(s_1)\, \mathcal{I}_4(s_1), \tilde{a}_l - m_0]$$
$$= 2\pi\jmath \lim_{s_1 \to \tilde{a}_l - m_0} (\tilde{a}_l - m_0 - s_1)\mathcal{I}_1(s_1)\mathcal{I}_4(s_1). \quad \text{(A.3.13)}$$

Substituting $\mathcal{I}_1(s_1)$ and $\mathcal{I}_4(s_1)$ from (A.3.10) and (A.3.11), respectively, in (A.3.13), and using the final result in (A.3.12), we get (4.31). Furthermore, by applying the asymptotic expansion of Meijer's-G function [63, (07.34.06.0006.01)] in (4.26), we get (4.32).

A.3.4 Proof of Lemma 4.2

To evaluate the asymptotic expression of $\mathcal{H}_1$, we consider $\mathcal{H}_1$ in form of Mellin–Barnes integrals (from (A.3.8)) as

$$\mathcal{H}_1 = 2K_{\text{eq}} \sum_{r_1=1}^{\infty}\sum_{r_2=1}^{\infty} \Upsilon_r \sum_{u_1=0}^{m_1-1}\cdots\sum_{u_N=0}^{m_1-1}\prod_{n=1}^{N} \frac{Z_n\mathcal{C}_o}{\Gamma(\nu)} \frac{1}{(2\pi\jmath)^2} \int_{\ell_3} \mathcal{K}_1(s_3) \int_{\ell_4} \mathcal{K}_2(s_4)\mathcal{K}_3(s_3,s_4)ds_4 s_3, \quad \text{(A.3.14)}$$

where $\mathcal{K}_1(s_3) = \Gamma(\nu-1-s_3)\Gamma(-s_3)\mathcal{C}_o^{s_3}$, $\mathcal{K}_2(s_4) = \dfrac{\Gamma(-s_4)\prod_{l=1}^{12}\Gamma(a_l+s_4)}{\prod_{k=1}^{4}\Gamma(b_k+s_4)\Gamma(1-s_4)}\left(\dfrac{\mu_{\text{eq}}}{\Psi_{\text{eq}}C_4}\right)^{s_4}$,

$$\text{and} \quad \mathcal{K}_3(s_3,s_4) = \left(\frac{C_4}{C_3}\right)^{s_3+s_4+1} \frac{\Gamma(s_3+s_4+1)}{\Gamma(s_3+s_4+2)}. \quad \text{(A.3.15)}$$

For high transmit SNR conditions, i.e., $\rho \to \infty$, and hence $\mu_{\text{eq}} \to \infty$, the bivariate Fox's H-function can be evaluated at the highest poles on the left of contour ℓ_4 (i.e., residue at $s_4 = -s_3 - 1$) as

$$\int_{\ell_4} \mathcal{K}_2(s_4)\mathcal{K}_3(s_3,s_4)ds_4 \approx 2\pi\jmath \operatorname{Res}[\mathcal{K}_2(s_4)\mathcal{K}_3(s_3,s_4), -1-s_3]$$
$$= 2\pi\jmath \lim_{s_4 \to -1-s_3} (s_3+s_4+1)\mathcal{K}_2(s_4)\mathcal{K}_3(s_3,s_4)$$
$$= 2\pi\jmath \frac{\Gamma(1+s_3)\prod_{l=1}^{12}\Gamma(-1+a_l-s_3)}{\prod_{k=1}^{4}\Gamma(-1+b_k-s_3)\Gamma(2+s_3)}\left(\frac{\mu_{\text{eq}}}{\Psi_{\text{eq}}C_4}\right)^{-1-s_3}$$
$$\triangleq \mathcal{K}_4(s_3). \quad \text{(A.3.16)}$$

Using (A.3.16) in (A.3.14), we have

$$\tilde{\mathcal{H}}_1 = 2K_{\text{eq}} \sum_{r_1=1}^{\infty}\sum_{r_2=1}^{\infty} \Upsilon_r \sum_{u_1=0}^{m_1-1}\cdots\sum_{u_N=0}^{m_1-1}\prod_{n=1}^{N} \frac{Z_n\mathcal{C}_o}{\Gamma(\nu)} \frac{1}{2\pi\jmath} \int_{\ell_3} \mathcal{K}_1(s_3)\mathcal{K}_4(s_3)ds_3. \quad \text{(A.3.17)}$$

Similarly, we can apply residue approach in (A.3.17) by computing the residue at the dominan pole on the right of contour ℓ_3, (i.e., at $s_3 = \tilde{a}_l - 1$) as

$$\int_{\ell_1} \mathcal{K}_1(s_3)\ \mathcal{K}_4(s_3) ds_3 \approx 2\pi \jmath\ \mathrm{Res}[\mathcal{K}_3(s_3)\ \mathcal{K}_4(s_3), \tilde{a}_l - 1]$$
$$= 2\pi \jmath \lim_{s_3 \to \tilde{a}_l - 1} (\tilde{a}_l - 1 - s_3) \mathcal{K}_1(s_3) \mathcal{K}_4(s_3). \tag{A.3.18}$$

Substituting $\mathcal{K}_1(s_3)$ and $\mathcal{K}_4(s_3)$ from (A.3.15) and (A.3.16), respectively, in (A.3.18), we get (4.35). Similarly, by applying asymptotic Meijer's-G function expansion in (4.30), we get (4.36).

A.3.5 Proof of Lemma 4.3

The CDF of end-to-end instantaneous SNR of S-R-U$_1$ link, i.e., Γ_{E_1} is given by

$$\mathcal{F}_{\Gamma_{\mathrm{E}_1}}(\gamma) = \Pr\left[\min\left(w_1 \gamma_{\mathrm{R}}, \hat{w}_1 \gamma_{\mathrm{R}} \gamma'_{\mathrm{U}_1}\right) \leq \gamma\right] = \Pr\left[\min\left(\gamma_{\mathrm{R}}, \gamma_{\mathrm{R}} \gamma''_{\mathrm{U}_1}\right) \leq \frac{\gamma}{w_1}\right], \tag{A.3.19}$$

where $\gamma''_{\mathrm{U}_1} = \frac{\hat{w}_1}{w_1} \bar{\gamma}'_{\mathrm{U}_1} |h_{\mathrm{RU}_1}|^2$. Note that when $0 \leq \gamma''_{\mathrm{U}_1} < 1$, then $\Gamma_{\mathrm{E}_1} = \gamma_{\mathrm{R}} \gamma''_{\mathrm{U}_1}$, whereas, when $\gamma''_{\mathrm{U}_1} \geq 1$, then $\Gamma_{\mathrm{E}_1} = \gamma_{\mathrm{R}}$. Accounting this, we can transform (A.3.19) as

$$\mathcal{F}_{\Gamma_{\mathrm{E}_1}}(\gamma) = \int_0^1 \mathcal{F}_{\gamma_{\mathrm{R}}}\left(\frac{\gamma}{w_1 u}\right) f_{\gamma''_{\mathrm{U}_1}}(u) du + \int_1^\infty \mathcal{F}_{\gamma_{\mathrm{R}}}\left(\frac{\gamma}{w_1}\right) f_{\gamma''_{\mathrm{U}_1}}(u) du. \tag{A.3.20}$$

Taking the derivative of (A.3.20) to obtain $f_{\Gamma_{\mathrm{E}_1}}(\gamma)$ and substituting it in (4.42), we get

$$\mathcal{C}_{\mathrm{erg},1} = \underbrace{\int_0^\infty \ln(1+\Lambda\gamma) \int_0^1 \frac{1}{w_1 u} f_{\gamma_{\mathrm{R}}}\left(\frac{\gamma}{w_1 u}\right) f_{\gamma''_{\mathrm{U}_1}}(u) du d\gamma}_{\mathcal{L}_{11}}$$
$$+ \underbrace{\int_0^\infty \ln(1+\Lambda\gamma) \int_1^\infty \frac{1}{w_1} f_{\gamma_{\mathrm{R}}}\left(\frac{\gamma}{w_1}\right) f_{\gamma''_{\mathrm{U}_1}}(u) du d\gamma}_{\mathcal{L}_{12}}, \tag{A.3.21}$$

where PDF of γ_{R} can be obtained using [63, (07.34.20.0011.02] and [63, (07.34.03.0001.01)] in (4.17) as

$$f_{\gamma_{\mathrm{R}}}(\gamma) = K_{\mathrm{eq}} \sum_{r_1=1}^{\infty} \sum_{r_2=1}^{\infty} \Upsilon_r G_{4,12}^{12,0}\left(\frac{\Psi_{\mathrm{eq}}}{\mu_{\mathrm{eq}}}\gamma \middle| \begin{matrix} \mathbb{P} - 1 \\ \mathbb{Q} - 1 \end{matrix}\right). \tag{A.3.22}$$

Substituting (A.3.22) along with the PDF of γ''_{U_1} (from (4.18)) in (A.3.21), followed by the use of $\ln(1+\Lambda\gamma) = G_{2,2}^{1,2}\left(\Lambda\gamma \middle| \begin{matrix} 1,1 \\ 1,0 \end{matrix}\right)$ [63, (07.34.03.0456.01)] and [63, (07.34.21.0011.01)], we can write $\mathcal{L}_{11}$ as

$$\mathcal{L}_{11}=\frac{K_{\text{eq}} m_0^{m_0}}{\hat{w}_1 \bar{\gamma}_{\text{U}_1}^{\prime m_0} \Omega_0^{m_0} \Gamma(m_0)} \sum_{r_1=1}^{\infty}\sum_{r_2=1}^{\infty} \Upsilon_r \int_0^1 u^{m_0-2} \exp\left(-\frac{w_1 m_0 u}{\hat{w}_1 \bar{\gamma}_{\text{U}_1}^{\prime} \Omega_0}\right) G_{6,14}^{14,1}\left(\frac{\Psi_{\text{eq}} u^{-1}}{w_1 \mu_{\text{eq}} \Lambda} \middle| \begin{matrix} -1,0,\mathbb{P}-1 \\ \mathbb{Q}-1,-1,-1 \end{matrix}\right) du. \tag{A.3.23}$$

To solve the above integral, we first use $e^{-x} = G_{0,1}^{1,0}\left(x \,\middle|\, \begin{smallmatrix} - \\ 0 \end{smallmatrix}\right)$ [63, (07.34.03.0228.01)] and then utilize the primary definition of the Meijer's-G function [63, (07.34.02.0001.01)]. After that, we evaluate the integral for u and apply the definition of the bivariate Fox-H function [104, 2.55] to get (4.43). To solve the term $\mathcal{L}_{12}$ in (A.3.21), we substitute the PDFs of γ_{R} and $\gamma_{\text{U}_1}^{\prime\prime}$ with the use of $\ln(1+\Lambda\gamma) = G_{2,2}^{1,2}\left(\Lambda\gamma \middle| \begin{matrix} 1,1 \\ 1,0 \end{matrix}\right)$ and solve the two integrals (w.r.t γ and u) by using [63, (07.34.21.0011.01)] and [68, 3.381,3] to get (4.44).

The CDF of end-to-end instantaneous SNR of S-R-U$_2$ link, i.e., $\mathcal{F}_{\Gamma_{\text{E}_2}}(\gamma)$ can be expressed as

$$\mathcal{F}_{\Gamma_{\text{E}_2}}(\gamma)= \Pr\left[\min\left(\frac{w_2\gamma_{\text{R}}}{w_1\gamma_{\text{R}}+1}, \frac{\hat{w}_2\gamma_{\text{R}}\gamma_{\text{U}_2}^{\prime}}{\hat{w}_1\gamma_{\text{R}}\gamma_{\text{U}_2}^{\prime}+1}\right) \le \gamma\right] = \Pr\left[\gamma_{\text{R}} \le \max\left(\omega_1(\gamma), \frac{\omega_2(\gamma)}{\gamma_{\text{U}_2}^{\prime}}\right)\right], \tag{A.3.24}$$

where $\omega_1(\gamma) = \frac{\gamma}{w_2 - w_1\gamma}$, and $\omega_2(\gamma) = \frac{\gamma}{(\hat{w}_2 - \hat{w}_1\gamma)}$. The CDF $\mathcal{F}_{\Gamma_{\text{E}_2}}(\gamma)$ can further be evaluated for different range of $\gamma_{\text{U}_2}^{\prime}$ as

$$\mathcal{F}_{\Gamma_{\text{E}_2}}(\gamma)= \int_0^{\frac{\omega_2(\gamma)}{\omega_1(\gamma)}} \mathcal{F}_{\gamma_{\text{R}}}\left(\frac{\omega_2(\gamma)}{u}\right) f_{\gamma_{\text{U}_2}^{\prime}}(u)du + \int_{\frac{\omega_2(\gamma)}{\omega_1(\gamma)}}^{\infty} \mathcal{F}_{\gamma_{\text{R}}}(\omega_1(\gamma)) f_{\gamma_{\text{U}_2}^{\prime}}(u)du. \tag{A.3.25}$$

Taking the derivative of (A.3.25) to obtain $f_{\Gamma_{\text{E}_2}}(\gamma)$ and substituting it in (4.42), we get

$$\mathcal{C}_{\text{erg},2} = \underbrace{\int_0^{\infty} \frac{\ln(1+\Lambda\gamma)\hat{w}_2}{(\hat{w}_2 - \hat{w}_1\gamma)^2} \int_0^{\frac{\omega_2(\gamma)}{\omega_1(\gamma)}} \frac{1}{u} f_{\gamma_{\text{R}}}\left(\frac{\omega_2(\gamma)}{u}\right) f_{\gamma_{\text{U}_2}^{\prime}}(u)dud\gamma}_{\mathcal{L}_{21}}$$
$$+ \underbrace{\int_0^{\infty} \frac{\ln(1+\Lambda\gamma)w_2}{(w_2 - w_1\gamma)^2} f_{\gamma_{\text{R}}}(\omega_1(\gamma)) \int_{\frac{\omega_2(\gamma)}{\omega_1(\gamma)}}^{\infty} f_{\gamma_{\text{U}_2}^{\prime}}(u)dud\gamma}_{\mathcal{L}_{22}}. \tag{A.3.26}$$

Substituting (A.3.22) along with the PDF of $\gamma_{\text{U}_2}^{\prime}$ (from (4.19)) in (A.3.26), followed by the use of $K_{a-b}(2\sqrt{x}) = x^{-\frac{a+b}{2}} G_{0,2}^{2,0}\left(x \,\middle|\, {- \atop a,b}\right)$ [63, (07.34.03.0605.01)], we can write $\mathcal{L}_{21}$ as

$$\mathcal{L}_{21} = 2K_{\text{eq}} \sum_{r_1=1}^{\infty} \sum_{r_2=1}^{\infty} \Upsilon_r \sum_{u_1=0}^{m_1-1} \cdots \sum_{u_N=0}^{m_1-1} \prod_{n=1}^{N} \frac{Z_n}{\Gamma(\nu)} \int_0^{\infty} \frac{\ln(1+\Lambda\gamma)\hat{w}_2}{(\hat{w}_2 - \hat{w}_1\gamma)^2}$$
$$\times \int_0^{\frac{\omega_2(\gamma)}{\omega_1(\gamma)}} \frac{1}{u} G_{0,2}^{2,0}\left(\mathcal{C}_o u \,\middle|\, {- \atop \nu-1, 0}\right) G_{4,12}^{12,0}\left(\frac{\Psi_{\text{eq}}\omega_2(\gamma)}{\mu_{\text{eq}} u} \,\middle|\, {\mathbb{P}-1 \atop \mathbb{Q}1}\right) du d\gamma. \tag{A.3.27}$$

The above integral can be solved by utilizing the primary definition of the Meijer's-G function [63, (07.34.02.0001.01)] and then evaluating the integral for u and applying the definition of the bivariate Fox-H function [43, 2.55] to get (4.45). To solve the term $\mathcal{L}_{22}$ in (A.3.26), we substitute the PDFs of γ_{R} and γ'_{U_2} with the use of [68, (3.381.3)] and get (4.46).

A.4 Detailed Proofs of Chapter 5

A.4.1 Proof of Lemma 5.1

The PDF of channel coefficient $I_i^{(n)} = I_{f,i}^{(n)} I_{ap,i}^{(n)}$ which accounts random fog, atmospheric turbulence and misalignment error can be obtained as [89]

$$f_{I_i^{(n)}}(z) = \int_0^{\infty} \frac{1}{y} f_{I_{f,i}^{(n)}}\left(\frac{z}{y}\right) f_{I_{ap,i}^{(n)}}(y) dy. \tag{A.4.1}$$

Substituting the PDF of $I_{f,i}^{(n)}$ and $I_{ap,i}^{(n)}$ from (5.4) and (5.11), respectively, along with the use definition of Meijer-G function from [63, Eq. 07.34.02.0001.01], we get

$$f_{I_i^{(n)}}(z) = \frac{\left(v_i^{(n)}\right)^{\tau_i^{(n)}} \psi_i^{(n)}}{\Gamma(\tau_i^{(n)})} z^{v_i^{(n)}-1} \frac{1}{2\pi\jmath} \int_{\mathcal{L}} \left(C_i^{(n)}\right)^{\ell} \frac{\prod_{p=1}^{3} \Gamma\left(b_{i,p}^{(n)} - \ell\right)}{\Gamma\left(a_i^{(n)} - \ell\right)} \int_0^{\infty} \left[\ln\left(\frac{u}{z}\right)\right]^{\tau_i^{(n)}-1} u^{\ell - v_i^{(n)}} du d\ell, \tag{A.4.2}$$

where $\jmath = \sqrt{-1}$ is the imaginary number, $\psi_i^{(n)} = \frac{\left(\xi_i^{(n)}\right)^2}{A_o \Gamma(\alpha_i^{(n)})\Gamma(\beta_i^{(n)})}$ and $C_i^{(n)} = \frac{\alpha_i^{(n)}\beta_i^{(n)}}{A_o}$. Substituting $\ln\left(\frac{u}{z}\right) = y$ and using [67, (3.351.3)], we can solve the inner integral as

$$f_{I_i^{(n)}}(z) = \frac{\left(v_i^{(n)}\right)^{\tau_i^{(n)}}}{\Gamma(\tau_i^{(n)})} \psi_i^{(n)} z^{v_i^{(n)}-1}$$

$$\times \frac{1}{2\pi\jmath}\int_{\mathcal{L}} \frac{\prod_{p=1}^{3}\Gamma\left(b_{i,p}^{(n)}-\ell\right)\left[\Gamma\left(v_i^{(n)}-1-\ell\right)\right]^{\tau_i^{(n)}}\Gamma\left(\tau_i^{(n)}\right)}{\Gamma\left(a_i^{(n)}-\ell\right)\left[\Gamma\left(v_i^{(n)}-\ell\right)\right]^{\tau_i^{(n)}}}\left(C_i^{(n)}\right)^{\ell} z^{\ell-v_i^{(n)}+1}d\ell. \quad \text{(A.4.3)}$$

Applying the definition of Meijer-G function from [63, Eq. 07.34.02.0001.01], we get (5.12).

A.4.2 Proof of Theorem 5.1

The PDF of $I_{\mathrm{SD}_j}=\sum_{n=1}^{N} I_{\mathrm{SD}_j}^{(n)}$ can be obtained by determining the inverse lapace transform of moment generating function (MGF) as

$$f_{I_{\mathrm{SD}_j}}(z)=\mathcal{L}^{-1}\left[\prod_{n=1}^{N} M_{I_{\mathrm{SD}_j}^{(n)}}(s)\right], \quad \text{(A.4.4)}$$

where $M_{I_{\mathrm{SD}_j}^{(n)}}(s)$ is the MGF of RV $I_{\mathrm{SD}_j}^{(n)}$ given by

$$M_{I_{\mathrm{SD}_j}^{(n)}}(s)=\int_0^{\infty} e^{-su} f_{I_{\mathrm{SD}_j}^{(n)}}(u)du. \quad \text{(A.4.5)}$$

Utilizing the PDF of $I_{\mathrm{SD}_j}^{(n)}$ given in (5.15) in the above equation and utilizing the definition of meijer-G function followed by the use of [67, (3.381.4)], we get $M_{I_{\mathrm{SD}_j}^{(n)}}(s)$ given by

$$M_{I_{\mathrm{SD}_j}^{(n)}}(s)=\frac{1}{2\pi\jmath}\left(v_{\mathrm{SR}}^{(n)}\right)^{\tau_{\mathrm{SR}}^{(n)}}\left(v_{\mathrm{RD}_j}^{(n)}\right)^{\tau_{\mathrm{RD}_j}^{(n)}}\frac{\psi_{\mathrm{SR}}^{(n)}\psi_{\mathrm{RD}_j}^{(n)}}{\left|\varpi^{(n)}\right|}\int_{\mathcal{L}_n}\frac{\prod_{p=1}^{3}\Gamma\left(b_{\mathrm{SR},p}^{(n)}-\ell_n\right)\left[\Gamma\left(v_{\mathrm{SR}}^{(n)}-1-\ell_n\right)\right]^{\tau_{\mathrm{SR}}^{(n)}}}{\Gamma\left(a_{\mathrm{SR}}^{(n)}-\ell_n\right)\left[\Gamma\left(v_{\mathrm{SR}}^{(n)}-\ell_n\right)\right]^{\tau_{\mathrm{SR}}^{(n)}}}$$
$$\times\frac{\prod_{p=1}^{3}\Gamma\left(b_{\mathrm{RD}_j,p}^{(n)}-\ell_n\right)\left[\Gamma\left(v_{\mathrm{RD}_j}^{(n)}-1-\ell_n\right)\right]^{\tau_{\mathrm{RD}_j}^{(n)}}}{\Gamma\left(a_{\mathrm{RD}_j}^{(n)}-\ell_n\right)\left[\Gamma\left(v_{\mathrm{RD}_j}^{(n)}-\ell_n\right)\right]^{\tau_{\mathrm{RD}_j}^{(n)}}}\left(\frac{C_{\mathrm{SR}}^{(n)}C_{\mathrm{RD}_j}^{(n)}}{\left|\varpi^{(n)}\right|}\right)^{\ell_n}\Gamma(\ell_n+1)s^{-1-\ell_n}\,d\ell_n. \quad \text{(A.4.6)}$$

Substituting (A.4.6) in (A.4.4), we get

$$f_{I_{\mathrm{SD}_j}}(u)=\frac{1}{(2\pi\jmath)^N}\prod_{n=1}^{N}\left(v_{\mathrm{SR}}^{(n)}\right)^{\tau_{\mathrm{SR}}^{(n)}}\left(v_{\mathrm{RD}_j}^{(n)}\right)^{\tau_{\mathrm{RD}_j}^{(n)}}\frac{\psi_{\mathrm{SR}}^{(n)}\psi_{\mathrm{RD}_j}^{(n)}}{\left|\varpi^{(n)}\right|}$$
$$\times\int_{\mathcal{L}_n}\frac{\prod_{p=1}^{3}\Gamma\left(b_{\mathrm{SR},p}^{(n)}-\ell_n\right)\left[\Gamma\left(v_{\mathrm{SR}}^{(n)}-1-\ell_n\right)\right]^{\tau_{\mathrm{SR}}^{(n)}}\prod_{p=1}^{3}\Gamma\left(b_{\mathrm{RD}_j,p}^{(n)}-\ell_n\right)\left[\Gamma\left(v_{\mathrm{RD}_j}^{(n)}-1-\ell_n\right)\right]^{\tau_{\mathrm{RD}_j}^{(n)}}\Gamma(\ell_n+1)}{\Gamma\left(a_{\mathrm{SR}}^{(n)}-\ell_n\right)\left[\Gamma\left(v_{\mathrm{SR}}^{(n)}-\ell_n\right)\right]^{\tau_{\mathrm{SR}}^{(n)}}\Gamma\left(a_{\mathrm{RD}_j}^{(n)}-\ell_n\right)\left[\Gamma\left(v_{\mathrm{RD}_j}^{(n)}-\ell_n\right)\right]^{\tau_{\mathrm{RD}_j}^{(n)}}}$$

$$\times\left(\frac{C_{\mathrm{SR}}^{(n)}C_{\mathrm{RD}_j}^{(n)}}{\left|\varpi^{(n)}\right|}\right)^{\ell_n}\left(\frac{1}{2\pi\jmath}\int_{\mathcal{L}} s^{-\sum_{n=1}^{N}\ell_n-1}e^{su}ds\right)d\ell_n. \tag{A.4.7}$$

Solving the inner integral given in (A.4.7) using [67, (8.315.1)] and using the definition of multi-variate-Fox H function from [104, (A.1)], we get (5.16). Further, the CDF of h_{SD_j} can be derived using

$$\mathcal{F}_{I_{\mathrm{SD}_j}}(z)=\mathcal{L}^{-1}\left[\prod_{n=1}^{N}\frac{M_{I_{\mathrm{SD}_j}^{(n)}}(s)}{s}\right]. \tag{A.4.8}$$

Utilizing (A.4.6) in the above equation followed by the use of [67, (8.315.1)] and the definition of multi-variate-Fox H function from [104, A.1], we get (5.21).

A.4.3 Proof of Lemma 5.2

The k-th moment of SNR at D_j can be obtained as$\mathcal{E}\left\{\Gamma_{\mathrm{D}_j}^k\right\} = \int_0^\infty \gamma^k f_{\Gamma_{\mathrm{D}_j}}(\gamma)d\gamma$ Substituting (5.19) along with the use of [104, A.1], we get

$$\mathcal{E}\left\{\Gamma_{\mathrm{D}_j}^k\right\}=\frac{1}{2\sqrt{\bar{\gamma}}}\prod_{n=1}^{N}\frac{\psi_{\mathrm{SR}}^{(n)}\psi_{\mathrm{RD}_j}^{(n)}}{\left|\varpi^{(n)}\right|}(v_{\mathrm{SR}}^{(n)})^{\tau_{\mathrm{SR}}^{(n)}}(v_{\mathrm{RD}_j}^{(n)})^{\tau_{\mathrm{RD}_j}^{(n)}}\left(\frac{1}{2\pi\jmath}\right)^N$$
$$\times\int_{\mathcal{L}_n}\frac{\prod_{p=1}^{3}\Gamma\left(b_{\mathrm{SR},p}^{(n)}-\ell_n\right)\left[\Gamma\left(v_{\mathrm{SR}}^{(n)}-1-\ell_n\right)\right]^{\tau_{\mathrm{SR}}^{(n)}}}{\Gamma\left(a_{\mathrm{SR}}^{(n)}-\ell_n\right)\left[\Gamma\left(v_{\mathrm{SR}}^{(n)}-\ell_n\right)\right]^{\tau_{\mathrm{SR}}^{(n)}}}\frac{\prod_{p=1}^{3}\Gamma\left(b_{\mathrm{RD}_j,p}^{(n)}-\ell_n\right)\left[\Gamma\left(v_{\mathrm{RD}_j}^{(n)}-1-\ell_n\right)\right]^{\tau_{\mathrm{RD}_j}^{(n)}}}{\Gamma\left(a_{\mathrm{RD}_j}^{(n)}-\ell_n\right)\left[\Gamma\left(v_{\mathrm{RD}_j}^{(n)}-\ell_n\right)\right]^{\tau_{\mathrm{RD}_j}^{(n)}}}$$
$$\times\left(\frac{C_{\mathrm{SR}}^{(n)}C_{\mathrm{RD}_j}^{(n)}}{\sqrt{\bar{\gamma}}\left|\varpi^{(n)}\right|}\right)^{\ell_n}\left(\int_0^\infty\gamma^k\gamma^{\frac{1}{2}\sum_{n=1}^{N}\ell_n}d\gamma\right)d\ell_n. \tag{A.4.9}$$

The inner integral in (A.4.9) can be solved using final value theorem $\lim_{x\to\infty}\int_0^x f(t)dt = \lim_{s\to 0}F(s)=F(\epsilon)$ where ϵ is nearly zero ($\approx 10^{-6}$). Therefore

$$\int_0^\infty\gamma^{k+\frac{1}{2}\sum_{n=1}^{N}\ell_n}d\gamma=\left(\frac{1}{\epsilon}\right)^{k+1+\frac{1}{2}\sum_{n=1}^{N}s_n}\Gamma\left(k+1+\frac{1}{2}\sum_{n=1}^{N}s_n\right). \tag{A.4.10}$$

Substituting (A.4.10) in (A.4.9) and utilizing the definition of multivariate Fox-H function from [104, A.1], we get (5.21).

A.4.4 Proof of Lemma 5.3

The variance of the derivative of Γ_{D_j} is obtained using [1] as

$$\mathcal{V}\left\{\hat{\Gamma}_{\mathrm{D}_j}\right\}=\frac{1}{\jmath^2}\frac{d^2\mathcal{Z}_{\Gamma_{\mathrm{D}_j}}(\bar{\tau})}{d\tau^2}\bigg|_{\tau=0}, \tag{A.4.11}$$

where $\mathcal{Z}_{\Gamma_{\mathrm{D}_j}}(\tau)$ defines the ACF of Γ_{D_j} at time lag $\bar{\tau}$. Assuming Γ_{D_j} to be a bandpass and wide-sense stationary Gaussian RP (due to the CLT), the ACF of Γ_{D_j} can be given by following [131, 2.22] as

$$\mathcal{Z}_{\Gamma_{\mathrm{D}_j}}(\bar{\tau}) = \frac{\mathcal{E}\left\{\Gamma_{\mathrm{D}_j}^2\right\}}{2}\mathcal{E}\left\{\exp\left(\jmath\, 2\pi\tau f_{\mathrm{D}_j}\cos\varphi_{\mathrm{D}_j}\right)\right\}. \tag{A.4.12}$$

Since the reflected signal through the ORIS forms a highly collimated beam, we consider a non-isotropic scattering environment at D_j with the AoA φ_{D_j} following the Von-Mises distribution. The Von-Mises distribution is an appropriate model to characterize the non-isotropic scattering environment because of its versatility of addressing wide range of scenarios [1, 131]. The unified PDF of φ_{D_j} considering non-isotropic/isotropic scattering model is given by

$$f_{\varphi_{\mathrm{D}_j}}\left(\varphi_{\mathrm{D}_j}\right) = \bar{\varepsilon}\frac{\exp\left[\chi\cos\left(\varphi_{\mathrm{D}_j} - \bar{\varphi}_{\mathrm{D}_j}\right)\right]}{2\pi I_0(\chi)} + (1-\bar{\varepsilon})\frac{1}{2\pi}, \quad \varphi_{\mathrm{D}_j} \in [-\pi,\, \pi). \tag{A.4.13}$$

where $\bar{\varepsilon}$ specifies the amount of directional reception. For $\bar{\varepsilon} = 1$, (A.4.13) reduces to non-isotropic scattering model, whereas, for $\bar{\varepsilon} = 0$, (A.4.13) simplifies to is isotropic scattering model. Utilizing $f_{\varphi_{\mathrm{D}_j}}\left(\varphi_{\mathrm{D}_j}\right)$ from (A.4.13), (A.4.12) can be re-written by solving the expectation over φ_{D_j} as

$$\mathcal{Z}_{\Gamma_{\mathrm{D}_j}}(\bar{\tau}) = \frac{\mathcal{E}\left\{\Gamma_{\mathrm{D}_j}^2\right\}}{2}\left[\bar{\varepsilon}\frac{I_0\left(\sqrt{\chi^2 - 4\pi^2\bar{\tau}^2 f_{\mathrm{D}}^2 + \jmath 4\pi\chi\bar{\tau} f_{\mathrm{D}}\cos(\bar{\varphi}_{\mathrm{D}_j})}\right)}{I_0(\chi)} + (1-\bar{\varepsilon})J_0\left(2\pi f_{\mathrm{D}}\bar{\tau}\right)\right]. \tag{A.4.14}$$

where $J_0(\cdot)$ is the zeroth order Bessel function [67]. Further, substituting (A.4.14) in (A.4.11) and utilizing $\frac{dI_\nu(z)}{dz} = \frac{1}{2}\left(I_{\nu-1}(z) + I_{\nu+1}(z)\right)$ and $\frac{dJ_\nu(z)}{dz} = \frac{1}{2}\left(I_{\nu-1}(z) - J_{\nu+1}(z)\right)$ [63], we get (5.24).

A.5 Detailed Proofs of Chapter 6

A.5.1 Proof of Lemma 6.1

The variance of the derivative of X_{D_j} can be calculated by following [1] as

$$\mathbb{V}\left\{\dot{X}_{\mathrm{D}_j}\right\} = \frac{1}{\mathrm{j}^2}\frac{d^2\mathcal{Z}_{X_{\mathrm{D}_j}}(\bar{\tau})}{d\bar{\tau}^2}\bigg|_{\bar{\tau}=0}, \tag{A.5.1}$$

where $\mathrm{j} = \sqrt{-1}$, $\mathcal{Z}_{X_{\mathrm{D}_j}}(\bar{\tau})$ defines the ACF of X_{D_j} at time lag $\bar{\tau}$. Assuming X_{D_j} to be a bandpass and wide-sense stationary Gaussian random process (due to the CLT), the ACF of X_{D_j} can be given by following [131, 2.22] as

$$\mathcal{Z}_{X_{\mathrm{D}_j}}(\bar{\tau}) = \frac{\mathcal{E}\left\{X_{\mathrm{D}_j}^2\right\}}{2}\mathcal{E}\left\{\exp\left(\mathrm{j}\, 2\pi\bar{\tau} f_{\mathrm{D}_j}\cos\varphi_{\mathrm{D}_j}\right)\right\}. \tag{A.5.2}$$

Since, the reflected signal through the IRS forms a highly collimated beam, we consider a non-isotropic scattering environment at DVE$_j$ with the AoA φ_{D_j} following the von Mises distribution. The von Mises distribution is suitable for modelling the non-isotropic scattering because of its versatility of addressing many scenarios [1, 131]. The PDF of φ_{D_j} is given by

$$f_{\varphi_{\mathrm{D}_j}}(\varphi_{\mathrm{D}_j}) = \frac{\exp[\chi\cos(\varphi_{\mathrm{D}_j} - \varphi_{\mathrm{D}_{j,p}})]}{2\pi I_0(\chi)}, \quad \varphi_{\mathrm{D}_j} \in [-\pi,\, \pi). \tag{A.5.3}$$

Using the PDF from (A.5.3), we can rewrite (A.5.2) by evaluating the expectation over φ_{D_j} as

$$\mathcal{Z}_{X_{\mathrm{D}_j}}(\bar{\tau}) = \frac{\mathcal{E}\left\{X_{\mathrm{D}_j}^2\right\}}{2}\frac{I_0\left(\sqrt{\chi^2 4\pi^2\bar{\tau}^2 f_{\mathrm{D}_j}^2 + \mathrm{j}4\pi\chi\bar{\tau} f_{\mathrm{D}_j}\cos(\varphi_{\mathrm{D}_{j,p}})}\right)}{I_0(\chi)}. \tag{A.5.4}$$

Further, substituting (A.5.4) in (A.5.1) and utilizing $\frac{dI_\nu(z)}{dz} = \frac{1}{2}\left(I_{\nu-1}(z) + I_{\nu+1}(z)\right)$ [63], we get (6.20).

Chapter B

List of Publications

Journal

- A. Girdher, A. Bansal, and A. Dubey, "Second-Order Statistics for IRS-Assisted Multiuser Vehicular Network With Co-Channel Interference," *IEEE Trans. Intell. Vehicles*,vol. 8, no. 2, pp. 1800 - 1812, Feb 2023.

- A. Girdher, A. Bansal, and A. Dubey, "On the performance of SLIPT-enabled DF relay-aided hybrid OW/RF network," *IEEE Sys. J.*, vol. 16, no. 4, pp. 5973-5984, Dec. 2022.

- A. Girdher, A. Bansal, M. R. Bhatnagar, and A. Dubey, "Performance Evaluation of IRS-Assisted One-Bit Control Based Mixed FSO-RF Communication System," *IEEE J. Optical Commun. Netw.* (Under Review)

- A. Girdher, A. Bansal, and A. Dubey, "Generalized Analytical Framework for SLIPT-Enabled OIRS-RIRS-Aided Mixed FSO-RF Communication System Using NOMA," *IEEE Trans. Commun.* (Under Review)

- A. Girdher, A. Bansal, and A. Dubey, "Second-Order Statistics for RIS-Assisted Optical Wireless communication system with Selection Combining" *IEEE Trans. Vehi. Tech.* (Under Review)

Conference Proceeding

- A. Girdher, A. Bansal, and A. Dubey, "Analyzing SLIPT for DF Based Mixed FSO-RF Communication System," *in Proc. IEEE Int. Conf. Telecommunications (ICT)*, London, UK, Jun., 2021.

- A. Girdher, A. Bansal, and A. Dubey, "Level Crossing Rate and Average Fade Duration of RIS-Assisted RF Communication System," *in Proc. IEEE India Council (INDICON)*, Guwahati, India, Oct., 2021.

- A. Girdher, A. Bansal, M. R. Bhatnagar, and A. Dubey, “IRS-Assisted Mixed FSO-RF Communication System with On-Off Controlling,” *in Proc. IEEE Int. Conf. Advanced Networks Telecommunications Sys. (ANTS), Women-in-Engg.*, Gandinagar, India, 2022.

References

[1] A. Abdi, J. A. Barger, and M. Kaveh, "A parametric model for the distribution of the angle of arrival and the associated correlation function and power spectrum at the mobile station," *IEEE Transactions on vehicular technology*, vol. 51, pp. 425–434, Aug. 2002.

[2] M. Giordani, M. Polese, M. Mezzavilla, S. Rangan, and M. Zorzi, "Toward 6g networks: Use cases and technologies," *IEEE Communications Magazine*, vol. 58, pp. 55–61, Mar. 2020.

[3] B. Ji, Y. Han, S. Liu, F. Tao, G. Zhang, Z. Fu, and C. Li, "Several key technologies for 6g: Challenges and opportunities," *IEEE Communications Standards Magazine*, vol. 5, pp. 44–51, Jun. 2021.

[4] I. F. Akyildiz, A. Kak, and S. Nie, "6g and beyond: The future of wireless communications systems," *IEEE access*, vol. 8, pp. 133995–134030, Jul. 2020.

[5] M. Z. Chowdhury, M. Shahjalal, S. Ahmed, and Y. M. Jang, "6g wireless communication systems: Applications, requirements, technologies, challenges, and research directions," *IEEE Open Journal of the Communications Society*, vol. 1, pp. 957–975, Jul. 2020.

[6] M. Z. Chowdhury, M. T. Hossan, A. Islam, and Y. M. Jang, "A comparative survey of optical wireless technologies: Architectures and applications," *ieee Access*, vol. 6, pp. 9819–9840, Jan. 2018.

[7] A. Jahid, M. H. Alsharif, and T. J. Hall, "A contemporary survey on free space optical communication: Potentials, technical challenges, recent advances and research direction," *Journal of Network and Computer Applications*, p. 103311, 2022.

[8] H. Kaushal and G. Kaddoum, "Optical communication in space: Challenges and mitigation techniques," *IEEE Commun. surveys & Tuts.*, vol. 19, pp. 57–96, Aug. 2016.

[9] A. Niaz, F. Qamar, M. Ali, R. Farhan, and M. K. Islam, "Performance analysis of chaotic FSO communication system under different weather conditions," *Transactions on Emerging Telecommunications Technologies*, vol. 30, p. e3486, Feb. 2019.

[10] H. Kaushal, V. Jain, S. Kar, H. Kaushal, V. Jain, and S. Kar, "Free-space optical channel models," *Free space optical communication*, pp. 41–89, Jan. 2017.

[11] F. Yang, J. Cheng, and T. A. Tsiftsis, "Free-space optical communication with nonzero boresight pointing errors," *IEEE Trans. Commun.*, vol. 62, pp. 713–725, Feb. 2014.

[12] Q. Huang, M. Lin, W.-P. Zhu, J. Cheng, and M.-S. Alouini, "Uplink massive access in mixed RF/FSO satellite-aerial-terrestrial networks," *IEEE Trans. Commun.*, vol. 69, pp. 2413–2426, Apr. 2021.

[13] A. Dochhan, J. Poliak, J. Surof, M. Richerzhagen, H. Kelemu, and R. Mata Calvo, "13.16 tbit/s free-space optical transmission over 10.45 km for geostationary satellite feeder-links," 05 2019.

[14] E. Research, "Emergen research." https://www.emergenresearch.com/industry-report/free-space-optics-communication-technology-market/".

[15] E. Times, "IIT Guwahati FSO system." https://economictimes.indiatimes.com/news/science/iit-guwahati-develops-free-space-optical-communication-system/articleshow/79365963.cms.

[16] M. Electric, "Mitsubishi electric." https://www.mitsubishielectric.com/news/2022/0531-a.html.

[17] S. Nikoletseas, Y. Yang, and A. Georgiadis, *Wireless power transfer algorithms, technologies and applications in ad-hoc communication networks*. Springer, 2016.

[18] J. Ren, J. Hu, D. Zhang, H. Guo, Y. Zhang, and X. Shen, "RF energy harvesting and transfer in cognitive radio sensor networks: Opportunities and challenges," *IEEE Commun. Mag.*, vol. 56, pp. 104–110, Jan. 2018.

[19] X. Lu, P. Wang, D. Niyato, D. I. Kim, and Z. Han, "Wireless networks with RF energy harvesting: A contemporary survey," *IEEE Commun. Surveys & Tuts.*, vol. 17, pp. 757–789, Nov. 2014.

[20] T. D. Ponnimbaduge Perera, D. N. K. Jayakody, S. K. Sharma, S. Chatzinotas, and J. Li, "Simultaneous wireless information and power transfer (SWIPT): Recent advances and future challenges," *IEEE Commun. Surveys & Tuts.*, vol. 20, pp. 264–302, Dec. 2018.

[21] H.-V. Tran, G. Kaddoum, and C. Abou-Rjeily, "Collaborative RF and lightwave power transfer for next-generation wireless networks," *IEEE Commun. Mag.*, vol. 58, pp. 27–33, Feb. 2020.

[22] S. Ma, F. Zhang, H. Li, F. Zhou, Y. Wang, and S. Li, "Simultaneous lightwave information and power transfer in visible light communication systems," *IEEE Trans. Wireless Commun.*, vol. 18, pp. 5818–5830, Dec. 2019.

[23] P. D. Diamantoulakis, G. K. Karagiannidis, and Z. Ding, "Simultaneous lightwave information and power transfer (SLIPT)," *IEEE Trans. Green Commun. & Netw.*, vol. 2, pp. 764–773, Mar. 2018.

[24] C. Abou-Rjeily, G. Kaddoum, and G. K. Karagiannidis, "Ground-to-air FSO communications: When high data rate communication meets efficient energy harvesting with simple designs," *Opt. Express*, vol. 27, pp. 34079–34092, Nov. 2019.

[25] M. D. Renzo, M. Debbah, D.-T. Phan-Huy, A. Zappone, M.-S. Alouini, C. Yuen, V. Sciancalepore, G. C. Alexandropoulos, J. Hoydis, H. Gacanin, *et al.*, "Smart radio environments empowered by reconfigurable ai meta-surfaces: An idea whose time has come," *EURASIP Journal on Wireless Communications and Networking*, vol. 2019, no. 1, pp. 1–20, 2019.

[26] Q. Wu and R. Zhang, "Towards smart and reconfigurable environment: Intelligent reflecting surface aided wireless network," *IEEE communications magazine*, vol. 58, pp. 106–112, Jan. 2020.

[27] E. Basar, M. Di Renzo, J. De Rosny, M. Debbah, M. Alouini, and R. Zhang, "Wireless communications through reconfigurable intelligent surfaces," *IEEE Access*, vol. 7, pp. 116753–116773, Aug. 2019.

[28] Q. Wu, S. Zhang, B. Zheng, C. You, and R. Zhang, "Intelligent reflecting surface aided wireless communications: A tutorial," *IEEE Trans. Commun.*, Jan. 2021.

[29] E. Basar, "Reconfigurable intelligent surfaces for doppler effect and multipath fading mitigation," *arXiv preprint arXiv:1912.04080*, Dec. 2019.

[30] A. R. Ndjiongue, T. M. Ngatched, O. A. Dobre, A. G. Armada, and H. Haas, "Analysis of RIS-based terrestrial-FSO link over GG turbulence with distance and jitter ratios," *J. of Lightwave Technol.*, vol. 39, pp. 6746–6758, Aug. 2021.

[31] R. Annavajjala and J. Zhang, "Level crossing rates and average outage durations of sinr with multiple co-channel interferers," in *Proc. Military Commun. Conf. (MILCOM)*, pp. 1233–1238, IEEE, Oct. 2010.

[32] S. O. Rice, "Statistical properties of a sine wave plus random noise," *The Bell System Technical Journal*, vol. 27, pp. 109–157, Jan. 1948.

[33] A. Abdi, K. Wills, H. A. Barger, M. . Alouini, and M. Kaveh, "Comparison of the level crossing rate and average fade duration of rayleigh, rice and nakagami fading models with mobile channel data," in *Proc. 52nd Veh. Technol. Conf.*, vol. 4, pp. 1850–1857 vol.4, Sep. 2000.

[34] S. K. Yoo, S. L. Cotton, P. C. Sofotasios, S. Muhaidat, and G. K. Karagiannidis, "Level crossing rate and average fade duration in $\mathcal{F}$ composite fading channels," *IEEE Wireless Commun. Lett.*, vol. 9, no. 3, pp. 281–284, 2020.

[35] C. B. Issaid and M.-S. Alouini, "Level crossing rate and average outage duration of free space optical links," *IEEE Trans. Commun.*, vol. 67, pp. 6234–6242, May 2019.

[36] R. N. de Souza, E. E. B. Olivo, C. R. N. da Silva, L. C. de Freitas Ferreira, and J. C. S. Santos Filho, "On second-order statistics of full-duplex relaying," *IEEE Commun. Lett.*, vol. 25, no. 4, pp. 1104–1108, 2020.

[37] M. S. Gilan, M. Y. Manesh, and A. Mohammadi, "Level crossing rate and average fade duration of amplify and forward relay channels with cochannel interference," in *Proc. 22th European Wireless Conf.*, pp. 1–5, VDE, 2016.

[38] Z. Hadzi-Velkov, N. Zlatanov, and G. K. Karagiannidis, "Level crossing rate and average fade duration of the multihop rayleigh fading channel," in *Proc. IEEE Int. Conf. Commun. (ICC)*, pp. 4451–4455, IEEE, May 2008.

[39] M. Z. Chowdhury, M. K. Hasan, M. Shahjalal, M. T. Hossan, and Y. M. Jang, "Optical wireless hybrid networks: Trends, opportunities, challenges, and research directions," *IEEE Commun. Surveys & Tuts.*, vol. 22, pp. 930–966, Jan. 2020.

[40] N. T. P. Van, S. F. Hasan, X. Gui, S. Mukhopadhyay, and H. Tran, "Three-step two-way decode and forward relay with energy harvesting," *IEEE Commun. Lett.*, vol. 21, pp. 857–860, Apr. 2017.

[41] A. Girdher, A. Bansal, and A. Dubey, "Analyzing SLIPT for DF based mixed FSO-RF communication system," in *2021 28th International Conference on Telecommunications (ICT)*, pp. 1–7, IEEE, Aug. 2021.

[42] N. Sharma, A. Bansal, and P. Garg, "Relay selection in mixed RF/FSO system using DF relaying," *Photonic Netw. Commun.*, vol. 33, pp. 143–151, Apr. 2017.

[43] H. Liang, Y. Li, M. Miao, C. Gao, and X. Li, "Unified performance analysis of MIMO mixed RF/FSO relaying system," *Applied Sciences*, vol. 11, p. 3054, Jan. 2021.

[44] E. Zedini, I. S. Ansari, and M.-S. Alouini, "Performance analysis of mixed nakagami-m and gamma-gamma dual-hop FSO transmission systems," *IEEE Photonics Journal*, vol. 7, pp. 1–20, Feb. 2015.

[45] E. Zedini, H. Soury, and M.-S. Alouini, "On the performance analysis of dual-hop mixed FSO/RF systems," *IEEE Trans. Wireless Commun.*, vol. 15, pp. 3679–3689, May 2016.

[46] B. Ashrafzadeh, E. Soleimani-Nasab, M. Kamandar, and M. Uysal, "A framework on the performance analysis of dual-hop mixed FSO-RF cooperative systems," *IEEE Trans. Commun.*, vol. 67, pp. 4939–4954, Jul. 2019.

[47] Y. Zhang, J. Zhang, L. Yang, B. Ai, and M. S. Alouini, "On the performance of dual-hop systems over mixed FSO/mmWave fading channels," *IEEE Open J. Commun. Society*, vol. 1, pp. 477–489, Apr. 2020.

[48] M. A. Amirabadi and V. T. Vakili, "Performance analysis of a novel hybrid FSO/RF communication system," *IET Optoelectronics*, vol. 14, pp. 66–74, Nov. 2019.

[49] U. Anushree and V. Jagadeesh, "Outage performance analysis of hybrid FSO/RF system using rayleigh and k-distribution," in *Advances in Communication, Signal Processing, VLSI, and Embedded Systems*, pp. 69–78, Springer, Dec. 2020.

[50] Q. Sun, Z. Zhang, Y. Zhang, M. López-Benítez, and J. Zhang, "Performance analysis of dual-hop wireless systems over mixed FSO/RF fading channel," *IEEE Access*, vol. 9, pp. 85529–85542, Jun. 2021.

[51] S. Anees and M. R. Bhatnagar, "Performance of an amplify-and-forward dual-hop asymmetric RF-FSO communication system," *J. Opt. Commun. Netw.*, vol. 7, pp. 124–135, Feb. 2015.

[52] N. Singhal, A. Bansal, and A. Kumar, "Performance evaluation of decode-and-forward-based asymmetric simo-rf/fso system with misalignment errors," *IET communications*, vol. 11, no. 14, pp. 2244–2252, 2017.

[53] L. Yang, M. O. Hasna, and I. S. Ansari, "Unified performance analysis for multiuser mixed η - μ and $\mathcal{M}$ - distribution dual-hop RF/FSO systems," *IEEE Trans. Commun.*, vol. 65, pp. 3601–3613, Aug. 2017.

[54] H. Lei, Z. Dai, I. S. Ansari, K.-H. Park, G. Pan, and M.-S. Alouini, "On secrecy performance of mixed rf-fso systems," *IEEE Photonics Journal*, vol. 9, no. 4, pp. 1–14, 2017.

[55] J. Zhang, H. Ran, X. Pan, G. Pan, and Y. Xie, "Outage analysis of wireless-powered relaying FSO-RF systems with nonlinear energy harvesting," *Optics Commun.*, vol. 477, p. 126309, Dec. 2020.

[56] J. Chen, L. Yang, W. Wang, H. Yang, Y. Liu, M. O. Hasna, and M. Alouini, "A novel energy harvesting scheme for mixed FSO-RF relaying systems," *IEEE Trans. Veh. Techol.*, vol. 68, pp. 8259–8263, Aug. 2019.

[57] M. I. Petković, G. T. Dordević, and D. N. Milić, "BER performance of IM/DD FSO system with OOK using APD receiver," *Radioengineering*, vol. 23, pp. 480–487, Apr. 2014.

[58] G. K. Varotsos, H. E. Nistazakis, W. Gappmair, H. G. Sandalidis, and G. S. Tombras, "DF relayed subcarrier FSO links over malaga turbulence channels with phase noise and non-zero boresight pointing errors," *Applied Sciences*, vol. 8, p. 664, May 2018.

[59] I. S. Ansari, F. Yilmaz, and M.-S. Alouini, "Performance analysis of free-space optical links over Málaga turbulence channels with pointing errors," *IEEE Trans. Wireless Commun.*, vol. 15, pp. 91–102, Aug. 2016.

[60] M. Abramowitz, I. A. Stegun, *et al.*, *Handbook of mathematical functions: with formulas, graphs, and mathematical tables*, vol. 55. National bureau of standards Washington, DC, 1972.

[61] A. Jurado-Navas, J. M. Garrido-Balsells, J. F. Paris, A. Puerta-Notario, and J. Awrejcewicz, "A unifying statistical model for atmospheric optical scintillation," *Numerical simulations of physical and engineering processes*, vol. 181, pp. 181–205, Sep. 2011.

[62] I. S. Ansari, F. Yilmaz, and M. Alouini, "Performance analysis of FSO links over unified gamma-gamma turbulence channels," in *Proc. IEEE Veh. Technol. Conf. (VTC), Glasgow, Scotland*, pp. 1–5, May 2015.

[63] Wolfram, "The wolfram functions site." https://functions.wolfram.com/.

[64] A. Jurado-Navas, J. M. Garrido-Balsells, J. F. Paris, M. Castillo-Vázquez, and A. Puerta-Notario, "Impact of pointing errors on the performance of generalized atmospheric optical channels," *Optics Express*, vol. 20, pp. 12550–12562, May 2012.

[65] Z. Jing, Z. Shang-hong, Z. Wei-hu, and C. Ke-fan, "Performance analysis for mixed FSO/RF nakagami-m and exponentiated weibull dual-hop airborne systems," *Optics Commun.*, vol. 392, pp. 294–299, Jun. 2017.

[66] T. Rakia, H.-C. Yang, F. Gebali, and M.-S. Alouini, "Optimal design of dual-hop VLC/RF communication system with energy harvesting," *IEEE Commun. Lett.*, vol. 20, pp. 1979–1982, Oct. 2016.

[67] Y. A. Brychkov, O. Marichev, and A. Prudnikov, *Integrals and Series, vol 3: more special functions*. Gordon and Breach science publishers Philadelphia, PA, 1986.

[68] A. Jeffrey and D. Zwillinger, *Table of integrals, series, and products*. Elsevier, 2007.

[69] L. Chen and W. Wang, "Effective capacity of MIMO free-space optical systems over gamma–gamma turbulence channels," *Optics Commun.*, vol. 382, pp. 450–454, Jan. 2017.

[70] I. I. Kim, B. McArthur, and E. J. Korevaar, "Comparison of laser beam propagation at 785 nm and 1550 nm in fog and haze for optical wireless communications," in *Optical Wireless Commun. III*, vol. 4214, pp. 26–37, International Society for Optics and Photonics, Feb. 2001.

[71] E. Basar, "Reconfigurable intelligent surface-based index modulation: A new beyond mimo paradigm for 6g," *IEEE Transactions on Communications*, vol. 68, no. 5, pp. 3187–3196, 2020.

[72] G. Zhou, C. Pan, H. Ren, K. Wang, M. Di Renzo, and A. Nallanathan, "Robust beamforming design for intelligent reflecting surface aided miso communication systems," *IEEE Wireless Communications Letters*, vol. 9, pp. 1658–1662, Jun. 2020.

[73] X. Yu, D. Xu, D. W. K. Ng, and R. Schober, "Power-efficient resource allocation for multiuser miso systems via intelligent reflecting surfaces," in *GLOBECOM 2020-2020 IEEE Global Communications Conference*, pp. 1–6, IEEE, 2020.

[74] S. Abeywickrama, R. Zhang, Q. Wu, and C. Yuen, "Intelligent reflecting surface: Practical phase shift model and beamforming optimization," *IEEE Trans. Commun.*, vol. 68, pp. 5849–5863, Jun. 2020.

[75] Q. Wu and R. Zhang, "Beamforming optimization for wireless network aided by intelligent reflecting surface with discrete phase shifts," *IEEE Trans. Commun.*, vol. 68, pp. 1838–1851, Dec. 2020.

[76] J. Zhang, J. Liu, S. Ma, C.-K. Wen, and S. Jin, "Large system achievable rate analysis of ris-assisted MIMO wireless communication with statistical csit," *IEEE Trans. Wireless Commun.*, Mar. 2021.

[77] L. Yang, Y. Yang, D. B. da Costa, and I. Trigui, "Performance analysis of an interference-limited ris-aided network," *arXiv preprint arXiv:2011.07479*, Nov. 2020.

[78] L. Yang, P. Li, Y. Yang, S. Li, I. Trigui, and R. Ma, "Performance analysis of ris-aided networks with co-channel interference," *IEEE Commun. Lett.*, pp. 1–1, Oct. 2021.

[79] Y. Chen, Y. Wang, J. Zhang, and Z. Li, "Resource allocation for intelligent reflecting surface aided vehicular communications," *IEEE Trans. Veh. Technol.*, vol. 69, pp. 12321–12326, Jul. 2020.

[80] N. Agrawal, A. Bansal, K. Singh, and C.-P. Li, "Performance evaluation of ris-assisted uav-enabled vehicular communication system with multiple non-identical interferers," *IEEE Transactions on Intelligent Transportation Systems*, 2021.

[81] L. Yang, W. Guo, and I. S. Ansari, "Mixed dual-hop FSO-RF communication systems through reconfigurable intelligent surface," *IEEE Commun. Lett.*, vol. 24, pp. 1558–1562, July 2020.

[82] A. Sikri, A. Mathur, P. Saxena, M. R. Bhatnagar, and G. Kaddoum, "Reconfigurable intelligent surface for mixed fso-rf systems with co-channel interference," *IEEE Commun. Lett.*, vol. 25, pp. 1605–1609, Feb. 2021.

[83] G. D. Verma, A. Mathur, Y. Ai, and M. Cheffena, "Mixed dual-hop IRS-assisted FSO-RF communication system with H-ARQ protocols," *IEEE Commun. Lett.*, vol. 26, pp. 384–388, Nov. 2021.

[84] A. Sikri, A. Mathur, and G. Kaddoum, "Signal space diversity-based distributed ris-aided dual-hop mixed rf-fso systems," *IEEE Communications Letters*, vol. 26, no. 5, pp. 1066–1070, 2022.

[85] M. A. Khalighi and M. Uysal, "Survey on free space optical communication: A communication theory perspective," *IEEE communications surveys & tutorials*, vol. 16, no. 4, pp. 2231–2258, 2014.

[86] A. Girdher, A. Bansal, and A. Dubey, "On the performance of SLIPT-enabled DF relay-aided hybrid OW/RF network," *IEEE Systems Journal*, Jan. 2022.

[87] Z. Ding and H. V. Poor, "A simple design of IRS-NOMA transmission," *IEEE Comm. Lett.*, vol. 24, pp. 1119–1123, Feb. 2020.

[88] Y. Zeng and R. Zhang, "Millimeter wave mimo with lens antenna array: A new path division multiplexing paradigm," *IEEE Transactions on Communications*, vol. 64, no. 4, pp. 1557–1571, 2016.

[89] A. Papoulis and S. U. Pillai, *Probability, Random variables, and Stochastic processes.* Tata McGraw-Hill Education, 2002.

[90] M. Najafi and R. Schober, "Intelligent reflecting surfaces for free space optical communications," in *2019 IEEE Global Communications Conference (GLOBECOM)*, pp. 1–7, IEEE, 2019.

[91] M. Najafi, B. Schmauss, and R. Schober, "Intelligent reflecting surfaces for free space optical communication systems," *IEEE Trans. Commun.*, vol. 69, pp. 6134–6151, May 2021.

[92] O. Maraqa, A. S. Rajasekaran, S. Al-Ahmadi, H. Yanikomeroglu, and S. M. Sait, "A survey of rate-optimal power domain NOMA with enabling technologies of future wireless networks," *IEEE Comm. Sur. & Tut.*, vol. 22, pp. 2192–2235, Aug. 2020.

[93] H. Jia, J. Zhong, M. N. Janardhanan, and G. Chen, "Ergodic capacity analysis for FSO communications with UAV-equipped irs in the presence of pointing error," in *2020 IEEE 20th International Conference on Communication Technology (ICCT)*, pp. 949–954, IEEE, 2020.

[94] H. Ajam, M. Naja, V. Jamali, and R. Schober, "Channel modeling for IRS-assisted FSO systems," in *2021 IEEE Wireless Communications and Networking Conference (WCNC)*, pp. 1–7, IEEE, 2021.

[95] L. Yang, W. Guo, D. B. da Costa, and M.-S. Alouini, "Free-space optical communication with reconfigurable intelligent surfaces," *arXiv preprint arXiv:2012.00547*, 2020.

[96] J. Zhu, Y. Huang, J. Wang, K. Navaie, and Z. Ding, "Power efficient IRS-assisted NOMA," *IEEE Trans. Commun.*, vol. 69, pp. 900–913, Oct. 2020.

[97] X. Yue and Y. Liu, "Performance analysis of intelligent reflecting surface assisted NOMA networks," *IEEE Trans. Wireless Commun.*, vol. 21, pp. 2623–2636, Oct. 2021.

[98] J. Zuo, Y. Liu, Z. Qin, and N. Al-Dhahir, "Resource allocation in intelligent reflecting surface assisted NOMA systems," *IEEE Trans. Commun.*, vol. 68, pp. 7170–7183, Feb. 2020.

[99] R. Li, T. Chen, L. Fan, and A. Dang, "Performance analysis of a multiuser dual-hop amplify-and-forward relay system with FSO/RF links," *J. Opt. Commun. Netw.*, vol. 11, pp. 362–370, Jul. 2019.

[100] M. V. Jamali and H. Mahdavifar, "Uplink non-orthogonal multiple access over mixed RF-FSO systems," *IEEE Trans. Wireless Commun.*, vol. 19, pp. 3558–3574, Feb. 2020.

[101] N. Ben Halima and H. Boujemaa, "Optimal power allocation and harvesting duration for mixed RF/FSO using non orthogonal multiple access," *Optical and Quantum Electronics*, vol. 52, pp. 1–21, Sep. 2020.

[102] Y. Zhuang and J. Zhang, "Secrecy performance analysis for a NOMA based FSO-RF system with imperfect CSI," *J. of Optical Commun. and Networking*, vol. 14, pp. 500–510, July 2022.

[103] S. A. Tegos, D. Tyrovolas, P. D. Diamantoulakis, C. K. Liaskos, and G. K. Karagiannidis, "On the distribution of the sum of double-nakagami-m random vectors and application in randomly reconfigurable surfaces," *IEEE Trans. Veh. Technol.*, vol. 71, July 2022.

[104] A. M. Mathai, R. K. Saxena, and H. J. Haubold, *The H-function: Theory and Applications.* Springer, 2009.

[105] Q. Wu, Y. Zeng, and R. Zhang, "Joint trajectory and communication design for multi-UAV enabled wireless networks," *IEEE Trans. Wireless Commun.*, vol. 17, no. 3, pp. 2109–2121, 2018.

[106] N. Gupta, S. Agarwal, and D. Mishra, "Joint trajectory and velocity-time optimization for throughput maximization in energy-constrained UAV," *IEEE Internet Things J.*, vol. 9, no. 23, pp. 24516–24528, 2022.

[107] X. Cheng, C. Wang, B. Ai, and H. Aggoune, "Envelope level crossing rate and average fade duration of nonisotropic vehicle-to-vehicle Rician fading channels," *IEEE Trans. Intell. Transp. Syst.*, vol. 15, pp. 62–72, Aug. 2014.

[108] X. Dong and N. C. Beaulieu, "Average level crossing rate and average fade duration of selection diversity," *IEEE Commun. Lett.*, vol. 5, pp. 396–398, Oct. 2001.

[109] C.-D. Iskander and P. T. Mathiopoulos, "Analytical level crossing rates and average fade durations for diversity techniques in nakagami fading channels," *IEEE Trans. Commun.*, vol. 50, pp. 1301–1309, Nov. 2002.

[110] L. Yang and M.-S. Alouini, "On the average outage rate and average outage duration of wireless communication systems with multiple cochannel interferers," *IEEE Trans. wireless Commun.*, vol. 3, pp. 1142–1153, Jul. 2004.

[111] A. O. Ali, C. M. Yetis, and M. Torlak, "Optimal packet length for throughput maximization in correlated multi-user channels," in *Proc. IEEE Int. Conf. Commun. (ICC)*, pp. 1–6, IEEE, May 2016.

[112] A. O. D. Ali, C. M. Yetis, and M. Torlak, "Novel expressions and applications for the level crossing rate of maximal ratio combining in the presence of cochannel interferers," *IEEE Trans. Veh. Technol.*, vol. 66, pp. 9793–9808, Jun. 2017.

[113] C. Stefanovic, M. Pratesi, and F. Santucci, "Second order statistics of mixed RF-FSO relay systems and its application to vehicular networks," in *Proc. IEEE Int. Conf. Commun. (ICC), Shanghai, China*, pp. 1–6, July 2019.

[114] C. Stefanovic, S. Panic, V. Bhatia, and N. Kumar, "On second-order statistics of the composite channel models for uav-to-ground communications with uav selection," *IEEE Open J. Commun. Society*, vol. 2, pp. 534–544, Mar. 2021.

[115] H. D. Le and A. T. Pham, "Level crossing rate and average fade duration of satellite-to-UAV FSO channels," *IEEE Photonics J.*, vol. 13, pp. 1–14, Feb. 2021.

[116] W. O. Popoola and Z. Ghassemlooy, "Bpsk subcarrier intensity modulated free-space optical communications in atmospheric turbulence," *Journal of Lightwave technology*, vol. 27, pp. 967–973, Apr. 2009.

[117] M. A. Esmail, H. Fathallah, and M.-S. Alouini, "On the performance of optical wireless links over random foggy channels," *IEEE Access*, vol. 5, pp. 2894–2903, Feb. 2017.

[118] K. Eshteiwi, G. Kaddoum, B. Selim, and F. Gagnon, "Impact of co-channel interference and vehicles as obstacles on full-duplex V2V cooperative wireless network," *IEEE Transactions on Vehicular Technology*, vol. 69, no. 7, pp. 7503–7517, 2020.

[119] Y. Zhu, B. Mao, Y. Kawamoto, and N. Kato, "Intelligent reflecting surface-aided vehicular networks toward 6G: Vision, proposal, and future directions," *IEEE Vehicular Technology Magazine*, vol. 16, no. 4, pp. 48–56, 2021.

[120] A. Girdher, A. Bansal, and A. Dubey, "Level crossing rate and average fade duration of ris-assisted rf communication system," in *Proc. IEEE 18th India Council Int. Conf. (INDICON)*, pp. 1–6, Dec. 2021.

[121] W. Tang, M. Z. Chen, X. Chen, J. Y. Dai, Y. Han, M. Di Renzo, Y. Zeng, S. Jin, Q. Cheng, and T. J. Cui, "Wireless communications with reconfigurable intelligent surface: Path loss

modeling and experimental measurement," *IEEE Transactions on Wireless Communications*, vol. 20, pp. 421–439, Sep. 2020.

[122] J. Santos Filho and M. Yacoub, "Highly accurate κ-μ approximation to sum of m independent non-identical ricean variates," *Electronics Lett.*, vol. 41, pp. 338–339, Apr. 2005.

[123] M. D. Yacoub, "The κ-μ distribution and the η-μ distribution," *IEEE Antennas Propag. Mag.*, vol. 49, no. 1, pp. 68–81, 2007.

[124] P. Billingsley, *Probability and measure.* Wiley series in probability and mathematical statistics, Wiley, 3rd ed ed., 1995.

[125] S. András, A. Baricz, and Y. Sun, "The generalized marcum $q-$ function: an orthogonal polynomial approach," *arXiv preprint arXiv:1010.3348*, Oct. 2010.

[126] D. B. Da Costa and M. D. Yacoub, "Accurate approximations to the sum of generalized random variables and applications in the performance analysis of diversity systems," *IEEE Trans. Commun.*, vol. 57, pp. 1271–1274, May 2009.

[127] S. L. Cotton, "Second-order statistics of κ-μ shadowed fading channels," *IEEE Trans. Veh. Technol.*, vol. 65, pp. 8715–8720, Dec. 2015.

[128] J. Zhang, F. Jin, Z. Tan, H. Wang, Q. Huang, and L. Hanzo, "Performance analysis of high-speed railway communication systems subjected to co-channel interference and channel estimation errors," *IET Commun.*, vol. 8, pp. 1151–1157, May 2014.

[129] P. Beckmann, *Probability in Communication Engineering.* San Diego, CA, USA: Hartcourt Brace & World, 1967.

[130] H. Chergui, M. Benjillali, and S. Saoudi, "Performance analysis of project-and-forward relaying in mixed MIMO-pinhole and rayleigh dual-hop channel," *IEEE Commun. Lett.*, vol. 20, pp. 610–613, Mar. 2016.

[131] G. L. Stüber and G. L. Stèuber, *Principles of mobile communication*, vol. 2. Springer, 1996.